Durham University

Durham E-Theses

Spatial and Temporal Distribution of Groundwater Recharge in the West Bank Using Remote Sensing and GIS Techniques

KHALAF, ADLA,JAMIL

How to cite:

KHALAF, ADLA,JAMIL (2010) *Spatial and Temporal Distribution of Groundwater Recharge in the West Bank Using Remote Sensing and GIS Techniques*, Durham theses, Durham University. Available at Durham E-Theses Online: http://etheses.dur.ac.uk/442/

Use policy

The full-text may be used and/or reproduced, and given to third parties in any format or medium, without prior permission or charge, for personal research or study, educational, or not-for-profit purposes provided that:

- a full bibliographic reference is made to the original source
- a link is made to the metadata record in Durham E-Theses
- the full-text is not changed in any way

The full-text must not be sold in any format or medium without the formal permission of the copyright holders.

Please consult the full Durham E-Theses policy for further details.

Academic Support Office, The Palatine Centre, Durham University, Stockton Road, Durham, DH1 3LE
e-mail: e-theses.admin@durham.ac.uk Tel: +44 0191 334 6107
http://etheses.dur.ac.uk

Spatial and Temporal Distribution of Groundwater Recharge in the West Bank Using Remote Sensing and GIS Techniques

Thesis submitted for the Degree of Doctor of Philosophy

Department of Geography

Durham University

Adla J. Khalaf

September, 2010

Spatial and Temporal Distribution of Groundwater Recharge in the West Bank Using Remote Sensing and GIS Techniques

Adla Khalaf

Abstract

Estimating groundwater recharge to aquifer systems is a very important element in assessing the water resources of the West Bank. Of particular interest is the sustainable yield of the aquifers. Previous studies have developed analytical recharge models that are based on the long-term annual rainfall data. These models have been shown to be inadequate and changes over shorter periods, e.g. monthly estimates, must be known in order to study the temporal distribution of recharge.

The approach used in this research integrates data derived from satellite images (e.g. land cover, evapotranspiration, rainfall, and digital elevation model) with hydrogeological data in a Geographic Information System (GIS) model to identify and map the surface recharge areas. The Surface Energy Balance Algorithm for Land (SEBAL) is applied to time series of remote sensing MODerate Resolution Imaging Spectroradiometer (MODIS) level 3 data of reflectance and surface temperature measurements to estimate monthly evapotranspiration; precipitation is derived from the monthly data sets of the Tropical Rainfall Measuring Mission (TRMM); runoff is given assumed values of 0.75 mm month^{-1} and 0.4 mm month^{-1} for the months of January and February, respectively. Recharge is quantified from November until March by applying the water balance method where evapotranspiration estimates and runoff are subtracted from precipitation. Results show good agreement between data reported in the literature and remote sensing-based analysis. Empirical models that are based on long term rainfall measurements suggest recharge values between 800 and 836 MCM yr^{-1} while the remote sensing based model results estimate recharge to be 700 MCM yr^{-1}. The Western, North-Eastern, and Eastern Aquifer Basins receive 30%, 23%, and 47% of the total calculated recharge while percentages available in the literature provide 49%, 22%, and 29%, respectively. Discrepancies are mainly due to lack of field data, the overestimation of actual evapotranspiration, and underestimation of TRMM precipitation values.

The recharge map indicates that the most effective groundwater recharge zones are located in the north and west of the area that is characterised by thick and well developed soil deposits, heavy vegetation, and a sub-humid climate with the potential of significant recharge occurring during the wet season. Some areas in the east include concentration of drainage and stream flows which increase the ability of to recharge the groundwater system. The least effective areas are in the south and south-west region that is more arid with much less recharge, mainly due to its isolated thin soil deposits.

A sensitivity analysis was carried out to demonstrate the impact of land cover change on groundwater and natural recharge. The assessment involved the use of land covers of 1994 and 2004 with the same fixed parameters of evapotranspiration, precipitation, drainage, slope, soil, and geology. Results show a decrease in high and intermediate high recharge areas from 40.25 km^2 and 2462.25 km^2 in year 1994 to 15.5 km^2 and 1994 km^2 in 2004, respectively. This illustrates the extent of land cover/land use change influence on recharge and calls for integrated plans and strategies to preserve recharge at least at its current rates.

TABLE OF CONTENTS

Abstract.....ii
Symbols and Constants.....xiv
Declaration.....xvi
Statement of Copyright.....xvi
Acknowledgments.....xvii

Chapter 1: Introduction **1**
1.1 Background 1
1.2 Research Questions, Aims, and Objectives 5
1.2.1 Research Questions 5
1.2.2 Aim of Research 6
1.2.3 Research Objectives 6
1.3 Research Approach 7
1.4 Thesis Structure 7

Chapter 2: Study Area; Attributes and Processes Affecting Aquifer Recharge **10**
2.1 Geographic Location 10
2.2 Meteorological Data 11
2.3 Hydro-Climatology 13
2.3.1 Rainfall 14
2.3.2 Air Temperature 17
2.3.3 Relative Humidity 20
2.3.4 Evaporation 21
2.4 Recharge 22
2.4.1 Previous Recharge Estimates 23
2.4.2 Recharge Mechanism in the West Bank 24
2.4.2.1 Rainfall Recharge 25
2.4.2.2 Recharge from Wadi Losses 26
2.4.2.3 Urban Recharge 27
2.4.2.4 Irrigation Losses: 27
2.5 Relief, Drainage, and Geomorphology 31
2.5.1 Relief 31
2.5.2 Surface Water Runoff 33
2.6 Unsaturated Zone 36
2.7 Geology 36
2.8 Soil 37
2.9 Vegetation and Land Use 38
2.10 Conclusion 41

Chapter 3: Data Sources and Methodology: Previous and Current Study **42**
3.1 Introduction 42
3.2 Satellite Data Sets 43
3.3 SPOT Data 46
3.4 MODIS Data 47
3.4.1 MODIS Level 3 (8-day) Products 47
3.5 Landsat TM5 Data 50
3.4.1 Processing Landsat TM5 Data 50

3.6 ASTER GDEM Data 51
3.6.1 ASTER GDEM Characteristics 52
3.6.2 Geo-referencing ASTER GDEM 54
3.6.3 Slope Map Generation 54
3.7 TRMM Data 55
3.7.1 Geo-Referencing TRMM 58
3.8 Methodological Framework 60
3.9 Field Research 65
3.10 Summary 65

Chapter 4: Regional Scale Evapotranspiration Modelling using Remote Sensing and SEBAL Processing 67
4.1 Introduction 67
4.2 Steps and Equations in SEBAL Algorithm 69
4.2.1 Net Radiation (Rn) 70
4.2.1.1 Instantaneous Short Wave Radiation (K↓) 70
4.2.1.2 Instantaneous Incoming Long Wave Radiation (L↓) 72
4.2.1.3 Instantaneous Outgoing Long Wave Radiation (L↑) 73
4.2.1.4 Surface Emissivity (εo) 73
4.2.2 Soil Heat Flux (Go) 74
4.2.3 Sensible Heat Flux (H) 75
4.3 Evapotranspiration Up-Scaling 77
4.3.1 Evaporative Fraction 77
4.3.2 Daily Net Radiation 78
4.3.3 Daily Actual Evapotranspiration (ETa-day) 79
4.3.4 Monthly Actual Evapotranspiration 79
4.4 MODIS and Landsat Calibration and Atmospheric Correction 80
4.4.1 Calibration for Reflective Solar Bands 81
4.4.1.1 Reflective Solar Bands for MODIS Level 1B, Bands 1 and 2 81
4.4.1.2 Reflective Solar Bands for Landsat TM5, Bands 3 and 4 83
4.4.1.3 MODIS Level 3 Surface Reflectance (MOD09Q1) 85
4.4.2 Calibration for Radiance Values 86
4.4.2.1 Thermal Emissive Bands for MODIS Level 1B, Bands 31 and 32 86
4.4.2.2 Thermal Emissive Band for Landsat TM5, Band 6 87
4.4.2.3 MODIS Level 3 Land Surface Temperature and Emissivity (MOD11A2) 88
4.4.3 Atmospheric Correction 88
4.5 Procedural Steps in SEBAL Processing 89
4.5.1 MODIS Level 1B and Level 3 and Landsat TM5 89
4.6 Assumptions and Uncertainties Induced by of SEBAL Algorithm 96
4.7 Further Validation 97
4.8 Conclusion 98

Chapter 5: Local Scale Evapotranspiration Modelling 99
5.1 Introduction 99
5.2 Local Scale Evapotranspiration Methods 101
5.2.1 Penman-Monteith Equation 102
5.2.1.1 Model Inputs and Calculation Procedures 104
5.2.1.1.1 Mean Saturation Vapour Pressure (es) 104

5.2.1.1.2Slope of Saturation Vapour Pressure Curve (Δ) 105
5.2.1.1.3Actual Vapour Pressure (ea) 105
5.2.1.1.4Vapour Pressure Deficit (es-ea) 105
5.2.1.1.5 Soil Heat Flux (G) 105
5.2.1.1.6 Net Radiation (Rn) 106
5.2.2 Thornthwaite Method 108
5.2.3 Grindley's Soil Moisture Deficit Model 109
5.3 Crop Evapotranspiration (PEc) 109
5.4 Results and Discussion 110
5.4.1 Monthly Penman-Monteith 110
5.4.2 Thornthwaite Method 117
5.4.3 Soil Moisture Deficit 119
5.5 Summary 123

Chapter 6: Land Cover Classification 126
6.1 Introduction 126
6.2 Change Detection 127
6.3 Image Classification 128
6.3.1 SPOT-2 HRV Classification 137
6.3.2 SPOT-5 HRG Classification 141
6.4 Change Detection 142
6.4.1 Results 142
6.4.2 Normalized Difference Vegetation Index (NDVI) 146
6.4.2.1 SPOT Images NDVI 147
6.4.2.2 MODIS Images NDVI 150
6.5 Accuracy Assessment 153
6.6 Classification Validation 155
6.7 Conclusion 156

Chapter 7: Spatial and Temporal Distribution of Evapotranspiration 158
7.1 Introduction 158
7.2 SEBAL Monthly Evapotranspiration 159
7.3 SEBAL Model Results 162
7.3.1 Monthly ET Results 162
7.3.2 Net Radiation (Rn) 163
7.3.3 Soil Heat Flux (Go) 164
7.3.4 Relationship between NDVI and Surface Temperature (Ts) 167
7.3.5 Relationship between ET and Surface Biophysical Variables 167
7.4 SEBAL Model Validation 170
7.4.1 Validation to Ground Estimates 170
7.4.2 Validation Using Land Cover 175
7.5 Correlation of MODIS with Landsat Sensor 177
7.5.1 Inter-Comparison of Ts, NDVI, and ET by MODIS and Landsat 181
7.6 Discussion 183
7.7 SEBAL Calibration 187
7.8 Conclusion 189

Chapter 8: Rainfall and Surface Recharge Mapping and Modelling 191

8.1 Introduction 191
8.2 Surface Recharge Modelling 192
8.2.1 Rainfall and Surface Recharge Modelling 193
8.2.2 Modelling and Mapping Recharge 196
8.2.2.1 Precipitation 198
8.2.2.2 Evapotranspiration 199
8.2.2.3 Geology 200
8.2.2.4 Soil Type 201
8.2.2.5 Slope 202
8.2.2.6 Land Cover 203
8.2.2.7 Drainage Density 204
8.3 Surface Recharge Modelling 205
8.3.1 Recharge Rates Results 205
8.4 SEBAL Evapotranspiration 209
8.5 TRMM Precipitation Estimates 210
8.5.1 Results 210
8.5.2 TRMM Validation 212
8.6 Recharge Mapping Discussion 216
8.6.1 Sensitivity Analysis 220
8.7 Recharge Sustainability 221
8.8 Refinements of Precipitation-Recharge Model Estimates 227
8.9 Conclusion 229

Chapter 9: Conclusions and Recommendations 233
9.1 Introduction 233
9.2 Summary of Methodology and Results 234
9.3 Evaluation of Research Aims 238
9.4 Limitations of Remote Sensing Application 240
9.5 Recommendations for Future Research 242
9.6 Conclusion 244

References 246

LIST OF APPENDICES

Appendix 1.1: Monthly Air Temperatures for the West Bank (2004) I
Appendix 1.2: Mean Monthly Rainfall (mm month-1) for the West Bank (2004) II
Appendix 1.3: Mean Monthly Relative Humidity (%) for the West Bank (2004) III
Appendix 1.4: Mean Monthly Wind Speed (km $hour^{-1}$) for the West Bank (2004) IV
Appendix 2.1: Psychometric constant (γ) for different altitudes (z) V
Appendix 2.2: Slope of vapour pressure curve (Δ) for different temperatures (T) VI
Appendix 2.3: Number of the day in the year (J) VII
Appendix 2.4: Penman-Monteith evapotranspiration calculations for Jenin VIII
Appendix 2.5: Penman-Monteith evapotranspiration calculations for Ramallah X
Appendix 2.6: Penman-Monteith evapotranspiration calculations for Hebron XII
Appendix 2.7: Penman-Monteith evapotranspiration calculations for Jericho XIV
Appendix 3.1: SEBAL code for MATLAB-based processing of MODIS L1B XVI
Appendix 3.2: SEBAL code for MATLAB-based processing of Landsat TM5 XX

LIST OF FIGURES

Figure 1.1: Shared aquifer basins 2
Figure 2.1: Location of the West Bank 10
Figure 2.2: Main weathering stations 11
Figure 2.3: Annual rainfall map 14
Figure 2.4: Annual rainfall variation for key stations of the West Bank 16
Figure 2.5: Mean monthly rainfall for year 2004 16
Figure 2.6: Annual rainfall distribution for Jerusalem station 17
Figure 2.7: Mean monthly air temperature for 2004 18
Figure 2.8: Mean annual temperature 18
Figure 2.9: Mean annual temperature variation for Jerusalem station 19
Figure 2.10: Regional warming exemplified by temperature elevation in Jerusalem ... 20
Figure 2.11: Mean monthly relative humidity for 2004 21
Figure 2.12: Mean annual potential evaporation 22
Figure 2.13: Rainfed agriculture recharge 26
Figure 2.14: Indirect recharge 26
Figure 2.15: Urban recharge 27
Figure 2.16: Recharge model for monthly estimates 31
Figure 2.17: Digital Elevation Model 32
Figure 2.18: Wadis of the West Bank 35
Figure 2.19: Geological map of the West Bank 37
Figure 2.20: Different land cover types 40
Figure 3.1: Methodology flowchart 44
Figure 3.2: NASA Warehouse Inventory Search Tool 49
Figure 3.3: USGS Global Visualization Viewer 50

Figure 3.4: ASTER GDEM tile selection 52
Figure 3.5: ASTER slope map 54
Figure 3.6: Exporting geo-referenced images using ArcGIS 60
Figure 3.7: Sites covered for land cover detection 61
Figure 4.1: Schematic of SEBAL computations 69
Figure 4.2: Main SEBAL equation 70
Figure 4.3: Soil heat flux 74
Figure 4.4: Aerodynamic heat transfer 75
Figure 4.5: Concept of temperature difference 77
Figure 4.6: Correction of MODIS and Landsat DN values 81
Figure 4.7: Relationship between dn** and scaled integers 82
Figure 4.8: Relationship between thermal emissive radiance and its scaled integer 86
Figure 4.9: ERDAS Imagine defining rasters and functions 90
Figure 4.10: MATLAB interface 92
Figure 4.11: Geo-referencing ET MODIS Level 3 product 95
Figure 5.1: A schematic model for local scale evapotranspiration estimation 101
Figure 5.2: Characteristics of the hypothetical reference crop 103
Figure 5.3: Typical Kc for different types of full grown crops 110
Figure 5.4: Linear regression between Epan and Penman-Monteith 112
Figure 5.5: Crop evapotranspiration against Epan measurements 116
Figure 5.6: Relationship between Pan and Thornthwaite estimates 118
Figure 5.7: Soil moisture deficit results 122
Figure 6.1: Steps used to extract land cover maps 130
Figure 6.2: SPOT scenes 131
Figure 6.3: SPOT classification 132
Figure 6.4: SPOT classification on governorate scale 135
Figure 6.5: Homogeneity and spectral similarity of land covers 139
Figure 6.6: Concept of convolution 141
Figure 6.7: Supervised classification of 1994 and 2004 142
Figure 6.8: Land cover change 143
Figure 6.9: Land cover change by governorate 145
Figure 6.10: Har Homa settlement between 1997 and 2007 146
Figure 6.11: SPOT NDVI variation over ten years period 147
Figure 6.12: Rainfall graph for Jerusalem 149
Figure 6.13: Seasonal and spatial varaition of NDVI 151
Figure 6.14: Manual land cover classification 156
Figure 7.1: Study concept 159
Figure 7.2: MODIS geographical coverage of the West Bank 162
Figure 7.3: Evapotranspiration cycle over 2004 163
Figure 7.4: Distribution of daily net radiation and ET 164
Figure 7.5: Relationship between NDVI and Go/Rn 166
Figure 7.6: Regression between NDVI and Ts 167

Figure 7.7: SEBAL ET and Ts relation 168
Figure 7.8: SEBAL ET and NDVI relation 169
Figure 7.9: Relationship between SPOT-derived NDVI and ET 169
Figure 7.10: Monthly ET estimates 171
Figure 7.11: Correlation between ET derived by SEBAL and SMD 173
Figure 7.12: SPOT land cover classification and MODIS ET maps 177
Figure 7.13: ET maps derived from Landsat TM5 and MODIS.....178
Figure 7.14: Landsat TM5 and MODIS histograms 179
Figure 7.15: Comparison between MODIS and Landsat images and histograms 180
Figure 8.1: A schematic of the water budget 194
Figure 8.2: Methodology flowchart for actual groundwater zones mapping 197
Figure 8.3: Relation between TRMM derived precipitation and rain gauges.....198
Figure 8.4: Recharge/ land cover maps 208
Figure 8.5: Sprinkled vegetation 209
Figure 8.6: Comparison between TRMM and rain gauge data 211
Figure 8.7: Mean annual TRMM rain gauge rainfall.....213
Figure 8.8: Average annual variations of RMSE (%) 215
Figure 8.9: Actual areas of recharge in January 217
Figure 8.10: Recharge and land cover maps 218
Figure 8.11: Recharge maps 221
Figure 8.12: Recharge using different land cover maps 223
Figure 8.13: High recharge areas in 1994 and 2004 224
Figure 8.14: Land cover change impact on recharge in Ramallah 225
Figure 8.15: Jenin land cover classification 226

LIST OF TABLES

Table 1.1: Recharge-Rainfall coefficients 4
Table 2.1: Mean sunshine duration for some stations in the West Bank 13
Table 2.2: Number of rainfall days in key stations of the West Bank 15
Table 2.3: Pan evaporation quantities in the West Bank for 2004 21
Table 2.4: Recharge estimates of the Mountain Aquifer 29
Table 2.5: Eastwards and westwards wadis runoff 34
Table 2.6: Runoff data from 1996-1997 35
Table 2.7: Main soil types in the West Bank 38
Table 3.1: General characteristics of satellite data sets 45
Table 3.2: General characteristics of SPOT satellite data.....46
Table 3.3: Reflectance and land surface temperature and emissivity of MODIS 48
Table 3.4: Landsat TM5 image characteristics 51
Table 3.5: ASTER GDEM characteristics 53
Table 3.6: Comparison of ASTER GDEM with other DEMs 53

Table 3.7: TRMM gridded data products 56
Table 4.1: Determination of intermediate radiation balance parameters 72
Table 4.2: MODIS Level 1B reflectance calibration scales 83
Table 4.3: Landsat TM post calibration 84
Table 4.4: Solar exoatmospheric spectral irradiances 85
Table 4.5: Science data sets for MOD09Q1 85
Table 4.6: MODIS radiance calibration scales 87
Table 4.7: Landsat TM5 thermal band calibration 88
Table 4.8: Science data sets for MOD11A2 88
Table 4.9: Specifications of projection system used in Palestine 94
Table 5.1: PE values derived by Penman-Monteith equation 111
Table 5.2: Relation between Epan adjustments and Penman-Monteith 114
Table 5.3: Thornthwaite calculations and relation to Pan measurements 117
Table 5.4: Calculation of soil moisture deficit 120
Table 6.1: Land cover classification results 143
Table 6.2: Climatic variables for 1994 and 2004 148
Table 6.3: Characteristics of Terra-MODIS data 150
Table 6.4: Monthly range of NDVI for 2004 153
Table 6.5: Comparison of classification accuracy 154
Table 6.6: Manually delineated land use vs supervised land cover classification 155
Table 7.1: MODIS 8-day reflectance products 160
Table 7.2: MODIS 8-day land surface temperature and emissivity products 161
Table 7.3: Comparison between conventional and SEBAL ET 170
Table 7.4: Variation of Ts, NDVI, Rn, and ET 182
Table 8.1: Weighing scheme for precipitation parameter 199
Table 8.2: Weighing scheme for evapotranspiration parameter 199
Table 8.3: Weighing scheme for geology parameter 200
Table 8.4: Weighing scheme for soil type parameter 202
Table 8.5: Weighing scheme for slope parameter 203
Table 8.6: Weighing scheme for land cover parameter 204
Table 8.7: Weighing scheme for drainage parameter 204
Table 8.8: Recharge mapping weighing values 205
Table 8.9: Recharge estimations from November to January 206
Table 8.10: Comparison of recharge with published figures 207
Table 8.11: Sensitivity model weighing values 220
Table 8.12: Recharge areas change on governorate scale 225
Table 9.1: Recharge areas change on governorate scale 238

LIST OF EQUATIONS

Equation 2.1: 19
Equation 3.1: 62
Equation 4.1: 70
Equation 4.2: 70
Equation 4.3: 71
Equation 4.4: 71
Equation 4.5: 71
Equation 4.6: 71
Equation 4.7: 72
Equation 4.8: 73
Equation 4.9: 73
Equation 4.10: 73
Equation 4.11: 73
Equation 4.12: 74
Equation 4.13: 74
Equation 4.14: 75
Equation 4.15: 75
Equation 4.16: 75
Equation 4.17: 76
Equation 4.18: 76
Equation 4.19: 76
Equation 4.20: 77
Equation 4.21: 77
Equation 4.22: 78
Equation 4.23: 78
Equation 4.24: 78
Equation 4.25: 78
Equation 4.26: 78
Equation 4.27: 78
Equation 4.28: 79
Equation 4.29: 79
Equation 4.30: 80
Equation 4.31: 80
Equation 4.32: 82
Equation 4.33a: 82
Equation 4.33b: 82
Equation 4.34: 83
Equation 4.35: 84
Equation 4.36: 84
Equation 4.37: 86

Equation 4.38a: 86
Equation 4.38b: 86
Equation 4.39: 87
Equation 5.1: 102
Equation 5.2: 102
Equation 5.3: 103
Equation 5.4: 103
Equation 5.5: 103
Equation 5.6: 104
Equation 5.7: 104
Equation 5.8: 104
Equation 5.9: 105
Equation 5.10: 105
Equation 5.11: 106
Equation 5.11a: 106
Equation 5.12: 106
Equation 5.12a: 106
Equation 5.12b: 106
Equation 5.12c: 107
Equation 5.12d: 107
Equation 5.12e: 107
Equation 5.12f: 107
Equation 5.12g: 107
Equation 5.12h: 108
Equation 5.12i: 108
Equation 5.13: 108
Equation 5.13a: 109
Equation 5.13b: 109
Equation 5.14: 110
Equation 5.15: 114
Equation 6.1: 136
Equation 6.2: 136
Equation 7.1: 163
Equation 7.2: 177
Equation 8.1: 194

Symbols and constants, their units and definitions

Symbol	Unit	Definition
ET	mm	Evapotranspiration
ET_a	mm	Actual evapotranspiration
ET_o	mm	Reference evapotranspiration
G_o	Wm^{-2}	Soil heat flux
H	Wm^{-2}	Sensible heat flux
Rn	Wm^{-2}	Net radiation
λE	Wm^{-2}	Latent heat flux
SMD	mm	Soil Moisture Deficit
DEM	m	Digital Elevation Model
NDVI	-	Normalized Difference Vegetation Index
LAI	$m^2\ m^{-2}$	Leaf Index Area
Λ	-	Evaporative fraction
P	mm	Precipitation
Ts	°C	Land surface temperature
Ta	°C	Air temperature
ΔT	°C	Temperature difference
LST	°C	Land surface temperature
VIS	µm	Visible band
NIR	µm	Near-infrared band
TIR	µm	Thermal infrared band
$K\downarrow$	Wm^{-2}	Incident shortwave radiation
$K\uparrow$	$Wm^{-2}\ sr^{-1}\ \mu m^{-1}$	Reflected shortwave radiation
$L\downarrow$	Wm^{-2}	Incident longwave radiation
$L\uparrow$	$Wm^{-2}\ sr^{-1}\ \mu m^{-1}$	Outgoing longwave radiation
σ	$Wm^{-2}\ K^{-4}$	Stefan-Boltzmann constant (5.67×10^{-8})
c_p	$JKg^{-1}\ K^{-1}$	Air specific heat capacity (1004)
k_b	JK^{-1}	Boltzmann's gas constant (1.381×10^{-23})
k	-	Von Karman constant (0.41)
Gsc	$1367\ W\ m^{-2}$	Global solar constant
r_p	-	Planetary reflectance
r_a	-	Atmospheric reflectance
α	-	Albedo
d_s	m	Earth-sun distance
d_r	m	Inverse Earth-sun distance
λ	µm	Band wavelength
φ	Rad	Sun zenith angle
JD	days	Julian day (Day of the year)
ε_o	-	Surface emissivity
ε_a	-	Atmospheric emissivity
T_B	K	Brightness temperature
t	s (hrs)	Local time
δ	Rad	Solar declination

$\omega_{(x)}$	Rad	Solar hour angle
$t_{(x)}$	Rad	Decimal hours
ø	Rad	Solar zenith angle
E_o	-	Eccentricity factor
Lat/lon	Degrees	Latitude/Longitude
τ	-	Transmissivity
τ^2	-	Two-way transmissivity
e_s	kPa	Saturated vapour pressure
e_a	kPa	Actual vapour pressure
e_d	kPa	Vapour pressure deficit
Δ	kPa	Slope of vapour pressure curve
γ	kPa °C	Psychometric constant
z	m	Vertical height
z_{oh}	m	Roughness length of momentum transfer
z_{om}	m	Roughness length of heat transfer
K_p	-	Pan coefficient
K_c	-	Crop coefficient

Declaration

The material contained in this thesis has not been previously submitted by the candidate for a degree in this or any other University.

Statement of Copyright

The copyright of this thesis rests with the author. No quotation from it should be published without her prior written consent and information derived from it should be acknowledged.

Acknowledgments

I would like to thank my father, mother, and brother and his family for their support throughout the course of this research. My uttermost thanks go to Dr. Shaddad Attili, for his extraordinary support and encouragement; it wouldn't have been possible without you.

My gratitude goes out to my supervisors, Prof. Danny Donoghue, Prof. Tim Burt, and Dr. Louise Bracken for their guidance and advice. My immense appreciations go to Brijesh K. Bava for his support and valuable friendship; I extremely value your encouragement and care throughout, you have greatly influenced my life. Many thanks to my colleagues and friends Rushil Ranchod and Diana Martin; I wouldn't have endured it without your friendship and coffee breaks. Also, I would like to thank my best friends: Amjad Abu El Ezz, Mohammad Tayeh, Hadi El Amine, Lama Omar, Mohammad Jabary, Razan Abu Obeid, Tamador Khalid, Alia Alsaadi, Samantha Smail and Fuad Hosban, Peter Byrne, and Bill and Diane Williamson.

Finally, I would like to thank the Geography Department in Durham University for sponsoring my PhD study, Clemens Messerschmid for providing me with significant reports and documents, and Deeb Abdul Ghafour for the water data and shapefiles.

Chapter One

Introduction

1.1 Background

Future water security is considered a serious cause of concern for the Palestinians. Israelis and Palestinians in the Occupied Palestinian Territory (OPT) share the same water resources. These resources are: the West Bank Mountain Aquifer System; the Jordan River System; and the Coastal Aquifer as illustrated in Figure 1.1. The Mountain Aquifer is a shared Israeli-Palestinian groundwater resource lying under both Israel and the West Bank. It is the only remaining water resource for Palestinians, as they are denied access to the Jordan River, and one of the important groundwater resources for Israel. Nearly the entire Palestinian population in the West Bank is dependent on its springs and wells for domestic, agricultural, and industrial uses. However, Israel has two other main water resources which are Lake Tiberias and the Coastal Aquifer. Despite that, Israel is continuing to over-abstract water for its own usage far in excess of the aquifer's yearly sustainable yield. The greatest part of the Aquifer's recharge area is situated in the West Bank where rainfall and snowfall is infiltrated and flows northwards and westwards towards Israel and towards the Jordan River in the east.

However, Israel is restricting Palestinian water usage and exploiting Palestinian water resource since its occupation of the Territory in 1967. Currently, Israel uses more than 80% of the water from the Mountain Aquifer (more than 400 MCM yr^{-1}) as well as all of the surface water available from the diverted Jordan River which supplies up to 650 MCM yr^{-1} (Amnesty International, 2009).

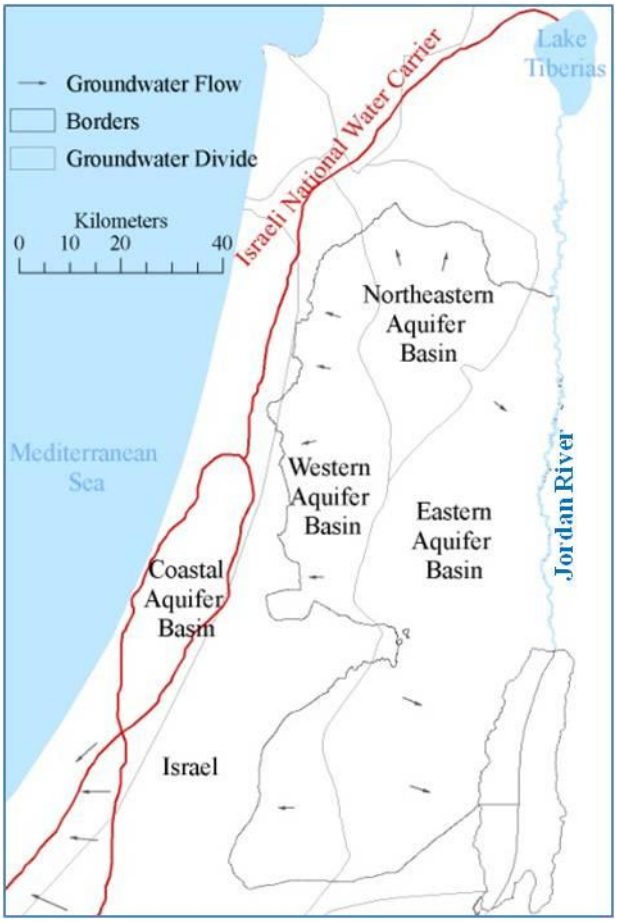

Figure 1.1: Shared Aquifer Basins, the Mountain Aquifer System and Coastal Aquifer

During its occupation, Israel has over exploited Palestinian water resources and arbitrarily built its settlements over the West Bank. Problems have become more complicated in recent years as some Palestinians have been drilling unlicensed wells in the face of water shortage, along with increased poverty. Therefore, urgent measures are required to ensure the aquifers sustainability and prevent further damage to the water resources. According to Amnesty International (2009), Palestinian consumption in the OPT is about 70 litres a day per capita, which is less than the 100 litres per capita per day recommended water consumption by the World Health Organization (WHO). Israeli daily per capita consumption is around 300 litres; about four times as much. According to the World Bank (2007), the overall Palestinian water extraction from the Mountain Aquifer in the West Bank has dropped from 138.2 MCM in year 1999 to 113.5 MCM in 2007. This reduction is due to the drop in the level of the water tables caused by Israeli over-abstraction and low annual rainfall.

Two main problems are facing the aquifer system in the West Bank: pollution and over-abstraction. Pollution originates from four main sources: domestic wastewater, solid wastewater leachate, industrial effluents, and runoff from agricultural activities. Quality measurements of groundwater in the West Bank have shown that the nitrate level in some areas exceeds the permissible level (50 mg l^{-1}) (Amnesty International, 2009). Nitrates in groundwater are an indicator of pollution from fertilizers and/or wastewater. Future estimates predict that groundwater quality will deteriorate with the expected population growth, if adequate measurements are not taken to prevent pollution (SUSMAQ, 2001).

The second dilemma is over-abstraction of the aquifer systems. All the water resources in the region are currently utilized up to, and in some cases, beyond their full sustainable potential. Any increase in overall abstraction may cause permanent damage to water quality and sustainable yield. There is already a serious concern about over-pumping from the Jordan River and from the Coastal Aquifer (UNEP, 2003). Thus, sustainable management of water resources must be a joint venture, based on reasonable and equitable allocation and principles of environmental protection, as opposed to the current situation, which is essentially one of physical domination and oppression.

In addition, rapid land use change and its associated impacts significantly affect the aquifers. One means of protection is to preserve the aquifers recharge and prevent any land uses that would harm its replenishment. Understanding the regional recharge mechanism is therefore becoming a critical factor in assessing the current water resources and predicting the potential future resources as well. Due to the Israeli occupation of the West Bank and the abnormal political status since 1967, the number of groundwater management studies by Palestinian researchers and hydrologists has been limited. Israeli water-related data with regard to the aquifer basins and the water research studies by Israeli hydrologists are not accessible to the public. Most of them are either written in Hebrew or published in the form of internal reports. The absence of studies and adequate protection plans to preserve the aquifers and their recharge areas suggest an urgent need to conserve and develop these aquifers in order to sustain them from any deterioration.

In previous studies, annual recharge has been calculated as a percentage of the long-term annual average rainfall over the basin as a whole, regardless of the nature of outcropping formations or the spatial distribution of rainfall, climate conditions, wadi flows, land use or relief. It is assumed here that the hydrogeology plays a key role in the differentiation of the recharge coefficients. Different authors have come to very different conclusions (Table 1.1).

Table 1.1: Recharge-Rainfall coefficients from different studies in Palestine

Author	% of recharge from Rainfall
Scarpa (1994)	20
ANTEA (1998)	20
Blake & Goldschmidt (1947)	22-25
CDM (1997)	20-30
Arad & Michaeli (1967)	6-48
Goldschmidt (1955)	34
Rofe & Raffety (1963, 1965)	20-55
Guttman & Zukerman (1995)	25-60

The problem with these studies is that they use a percentage of recharge from the annual rainfall (except for Guttman & Zukerman (1995) who take percentages for 3 ranges of rainfall) and they neglect the effect of geology and hydrogeology when they estimate the recharge on aquifer outcrops. In this research, however, these problems are avoided and recharge models are developed for monthly periods.

This study is constrained by paucity of field data (such as rainfall, evapotranspiration, and land cover) and limited ground stations and spatial coverage. Access to large areas of the West Bank is denied by the Israeli military forces and movement is restricted between its different parts. Access to field measurement records prior to the establishment of the Palestinian Authority in 1995, has been declined by the Israeli authorities and data after this date are incomplete (see Chapter 2). Therefore, this research will attempt to establish an integrated remote sensing and GIS model to quantify and estimate the areal spatial distribution of groundwater recharge over the West Bank area using satellite remote sensing.

1.2 Research Questions, Aims, and Objectives

1.2.1 Research Questions

Recharge calculations have been based on either long-term annual rainfall formulas (Goldschmidt, 1955; Goldschmidt and Jacobs, 1958; Tahel, 1988; Assaf *et al*., 1993; Guttman and Zuckerman, 1995 Ba'ba', 1996; Bachmat, 1995; Rofe and Raffety, 1965) or models based on local scale measurements (SUSMAQ, 2003). Both approaches lack the spatial and temporal distribution of data inputs required such as actual evapotranspiration and precipitation which have yielded to overestimation of recharge rates (SUSMAQ, 2001). Surface Energy Balance Algorithm for Land (SEBAL) is one of the models used to estimate regional actual evapotranspiration. It uses surface temperature and reflectance to infer surface fluxes and estimate latent heat flux. It has been validated with field experiments in a number of regions. However, SEBAL has not been validated in arid and semi-arid areas beyond the wet season. This research will try to apply SEBAL algorithm and validate its seasonal variation over the West Bank region. Based on the regional distribution of SEBAL and precipitation derived from the Tropical Rainfall Measuring Mission (TRMM), a temporal and spatial estimation of recharge is obtained. As a result, the following research questions have been generated to understand recharge mechanism within the region and estimate its rates over the twelve months period of 2004.

1. To what extent can the satellite data and its acquisition help to provide reasonable estimates of water balance parameters at regional scale?
2. Can satellite measurements, combined with meteorological data, be used to determine the regional distribution of evapotranspiration?
3. Can satellite sensors detect rainfall/precipitation in semi-arid regions such as the West Bank?
4. Can the estimates derived from the well established SEBAL algorithm be used as an input to the hydrological models needed to assess water resources?
5. Are there suitable satellite sensors that can provide reasonable estimates of ET, precipitation and other related hydrological parameters?
6. To what extent do the spatial distribution of ET and precipitation help to predict recharge in the West Bank aquifers?

7. What other factors impact recharge in the area?
8. How does land cover/land use change impact recharge?

1.2.2 Aim of Research

The aim of this research is to use remote sensing data sets to help improve the estimation and mapping of regional groundwater recharge across the West Bank. Such inputs include evapotranspiration (ET), precipitation (P), land cover, and Digital Elevation Model (DEM).

1.2.3 Research Objectives

The following objectives are proposed to achieve the research aim:

1. To estimate evapotranspiration and understand its spatial and temporal over the West Bank area.
    a. To assess the advantages and limitations of the satellite-based models of evapotranspiration such as the SEBAL algorithm.
    b. To study the feasibility of using NASA's MODIS level 3 (8-day) products (1 km) to compute the spatially distributed evapotranspiration.
    c. Validate MODIS evapotranspiration estimates with those derived from Landsat TM datasets.
    d. Validate the spatial estimates of evapotranspiration with results obtained from the soil moisture deficit method through the application of three conventional methods: Penman-Monteith, Thornthwaite, and pan evaporation.
2. Estimate the regional precipitation over the twelve months of 2004 using satellite microwave (TRMM sensor) datasets.
    a. Validate TRMM-derived precipitation estimates with rain gauge measurements to assess its accuracy.
3. Use multispectral satellite data to derive high quality land cover maps (SPOT data) to help establish land cover change in the West Bank.
    a. Validate land cover maps with the ET spatial estimates.

4. Use GIS to apply water balance modelling to estimate and map groundwater recharge.

1.3 Research Approach

The research approach adopted in this study is based on remote sensing data and GIS analysis. The methodology does not require complex hydrogeologic modelling or detailed knowledge of soil characteristics, vegetation cover, or land-use practices. A simple numerical model is used where the water balance method is applied and recharge is estimated by subtracting ET estimates and runoff from precipitation. Surface Energy Balance Algorithm for Land (SEBAL) is used to estimate ET which involves multiplication of daily net radiation and evaporative fraction. The net radiation data and evaporative fraction are obtained from MODIS 8-day product satellite imagery for each pixel value. Since runoff patterns are unpredictable and exact numbers have not been found yet, a value of 1.0 mm month^{-1} and 0.5 mm month^{-1} over the area is proposed for January and February, respectively. Precipitation is derived from the monthly data sets of the Tropical Rainfall Measuring Mission (TRMM). Recharge is quantified from November until March as they are considered the winter season.

Mapping actual recharge areas involves integrating seven parameters: precipitation, evapotranspiration, geology, soil type, slope, land cover, and drainage density. Other factors such as the saturated zone, water tables, well extraction, and discharge are outside the scope of this study. Each recharge parameter is assumed to be an independent variable and given a weighing value. The weight represents the relative importance of each parameter classes vis-a-vis recharge where all parameters are assumed to have the same level of significance to recharge. The final step includes spatial analysis to identify the most significant groundwater recharge zones.

1.4 Thesis Structure

The second chapter of this thesis provides a definition of the study area and a detailed description including its geography, climate, hydro-climatology, geomorphology, and vegetation.

Chapter three describes the remote sensing data sets used in the recharge estimation and mapping model. MODIS Level 3 (8-day) product data are employed to estimate the regional estimates of evapotranspiration (ET) and Landsat TM5 images are used to validate MODIS results. Monthly precipitation is derived from TRMM data sets of the same year covering the whole West Bank area. SPOT land cover classification and ASTER DEM has been selected as additional inputs to ET and precipitation to map the actual recharge areas in addition to available GIS data such as geology, soil type, and wadis. A detailed description of images calibration, processing, and geo-referencing is also given.

Chapter Four describes the Surface Energy Balance Algorithm for Land (SEBAL) and the procedures used to employ satellite data to estimate regional estimates of different parameters such as albedo (α), Normalized Difference Vegetation Index (NDVI), and surface temperature (Ts). The decision to use SEBAL is taken based on the fact that it requires minimal field data and is one of the most accurate methods for spatial ET modelling over heterogeneous landscapes (Mekonnen, 2005; Bastiannssen *et al*., 1998). The operational methods for running SEBAL algorithm using MATLAB are described. Its estimates are compared to local-scale ET modelling using three approaches: Penman-Monteith, Thornthwaite, and Pan measurements as described in Chapter Five.

Chapter Six describes SPOT classification and the derivation of land cover maps. It discusses the different image enhancements for better classification. Also, this chapter quantifies the changes in land cover in 1994 and 2004 in order to study its impact on the recharge process.

Chapter Seven discusses the different regional model parameters and validates ET estimates with ground measurements and land cover maps. Moreover, an inter-relation of MODIS with the Landsat sensor is carried out to study the consistency of SEBAL performance for the different satellite sensors.

Chapter Eight reviews previous recharge studies and provides a detailed approach to quantifying and mapping recharge. It compares previous results with those estimated in this research and discusses the outcome discrepancies. Validation of TRMM is carried out by comparing estimates with rain gauge measurements. In addition, two sensitivity

analyses are carried out: one presents the degree to which recharge mapping is affected by the use of remote sensing-derived data only excluding other field data such as geology and soil type and the second demonstrates the impact of land cover change on groundwater and natural recharge. Chapter Eight also discusses the possible model refinements for better estimation of recharge.

Chapter Nine evaluates the research objectives, provides conclusions and recommendations, and suggests further research.

Each chapter includes its relevant literature review, methodology, results, and discussion.

Chapter Two

Study Area; Attributes and Processes Affecting Aquifer Recharge

2.1 Geographic Location

The West Bank is located between latitude 31° 20’ 00’’ and 32° 38’ 00’’ N and longitude 34° 53’ 00’’ and 35° 31’ 00’’ E (see Figure 2.1). It lies on the west bank of the Jordan River in the Middle East. To the west, north, and the south the West Bank shares borders with Israel, and to the east across the Jordan River, is Jordan. After the 1967 Arab-Israeli War, the June 4th, 1967 Armistice Line between Israel and Jordan defines its current interim boundary. The name “West Bank” was first used by the Jordanians at the time of their annexation of the region. The term literally means “the West bank of the Jordan River” where the Kingdom of Jordan being the East bank of the River Jordan.

The West Bank covers an area of 5842 km^2 including East Jerusalem and North West part of the Dead Sea within the border of 4th June, 1967. The average width of the West Bank from East to West is about 40 km, and its maximum length from North to South is approximately 130 km.

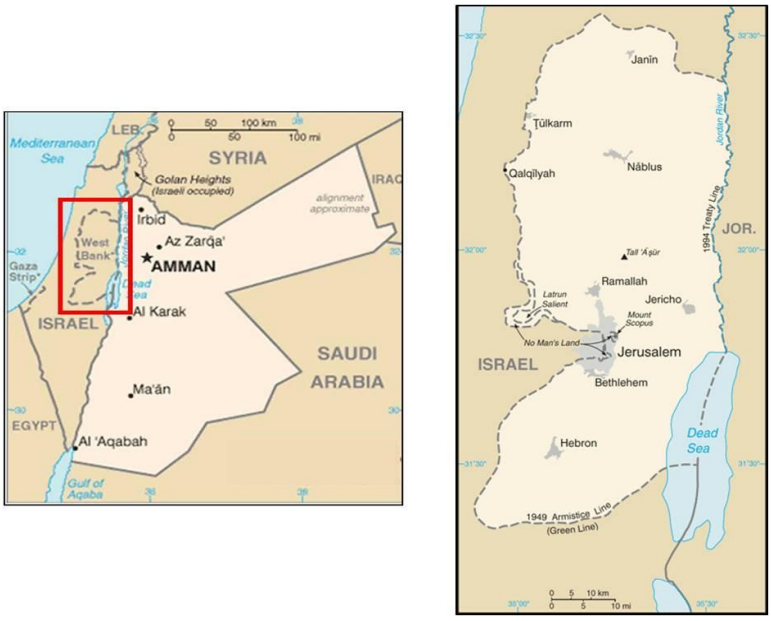

Figure 2.1: Location of the West Bank (www.cia.gov)

The West Bank is selected as a study area for its intrinsic scientific interest and the political sensitivity of water resources in the region. For successful negotiations between the two parties for sustainable management of disputed groundwater aquifers, an investigation of recharge mechanism is required. Therefore, an understanding of the regional water balance including evaporative losses and recharge may help in water resources management and land use planning.

2.2 Meteorological Data

In 1958, the Palestinian Meteorological Office established a limited number of air monitoring stations in the West Bank. After the Arab Israeli War in June 1967, the Israeli forces destroyed the installed stations and their infrastructure. After the creation of the Palestinian Authority, it became a priority to establish a meteorological service office with a defined mission to cope with the requirements of the State, the establishment of a Palestinian airport, and serve the aviation, maritime navigation and the daily needs of the Palestinian people and its institutions (www.pmd.ps). In mid-1998, the Palestinian Meteorological Office started issuing its daily bulletins of three hourly rainfall, air temperature, wind speed, relative humidity, sunshine duration, and pressure at six meteorological stations: Jenin, Tulkarm, Ramallah, Jericho, Bethlehem, and Hebron (shown in Figure 2.2 below).

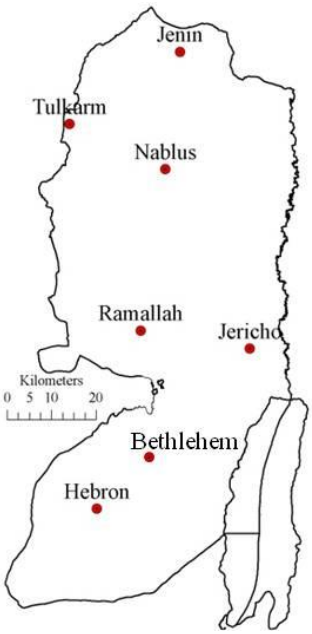

Figure 2.2: Main weathering stations

However, such plan is highly constrained by several factors that account for the limited network and so limited spatial coverage. The political instability in the area, damage to stations' equipments by the Israeli forces, outdated equipments, economic deteriorations, and lack of external funding are the main causes. Also, the geographical distribution of the six stations may be not representative for all the West Bank and more station installations are required. According to the installation and control of these stations, three historical periods are discussed:

a. The Jordanian Administration of the West Bank (1948-1967): five agricultural weather stations are installed to record data for agricultural purposes including rainfall, temperature, humidity, wind speed, and sunshine. These stations are located in El Arroub, Maythalun, Beit Qad (currently known as Jenin station), Tulkarm (Al-Hussein Agricultural School), and Al Far'a. Another three meteorological stations are established by the Jordanian Ministry of Transportation; these are the Jerusalem, Hebron and Jericho meteorological stations. These meteorological stations make full observations and have records of rainfall, evaporation, relative humidity, sunshine, wind direction and speed, maximum and minimum temperatures and air pressure. In addition, 100 more traditional rain gauges are installed at schools, mosques, and other places to measure rainfall. Within the Rofe & Raffety study (1963-1965), 12 hydrometric gauge stations are installed to measure the flood flow runoff on their streams.

b. The Israeli Administration (1967-1993): only one additional meteorological station is installed in the city of Nablus. They kept 5 hydrometric stations of the 12 stations installed by Jordan before 1967, while they ignored the remaining ones. They also ignored 30 rain gauges of those traditional stations installed before 1967.

c. The Palestinian Authority Administration (1993-current): All the previous stations and pre-measured data were transferred to the Palestinian Authority. There is much inaccuracy in these data for several reasons such as: lack of experienced technicians to measure and record the meteorological data from their gauge stations and lack of responsible persons to work with the technicians to monitor their accuracy. There are gaps in the data resulting from political

instability especially when curfews and strikes are imposed by Israel which prevent the workers from travelling to collect such on-site data. After 1994, four electronic weather stations are installed at Tulkram, Bir Zeit, Ramallah and Bethlehem Cities of the West Bank. These electronic stations are measuring all meteorological parameters every half-hour.

As a result, the most complete historical records to be used for this research start from 1998 and those archived data of Jerusalem station provided by the Israeli Meteorological Service.

2.3 Hydro-Climatology

The upland areas of the West Bank have a Mediterranean climate, with cool, wet winters and mild summers. The lower Jordan Valley, the Dead Sea region, has a different climate ranging between dry and extreme desert conditions. Rainfall occurs mostly in the north and west of the West Bank during winter and spring months, but mostly from December to March, and can be severe. During the remainder of the year, the climate is temperate, with the highest temperatures in the months of July and August. Palestine receives an average of seven hours of sunshine a day during the winter and thirteen hours during the summer. Table 2.1 below shows figures of sunshine durations in some of the West Bank stations.

Table 2.1: Mean Sunshine Duration for Some Stations in the West Bank (hr day^{-1})

Month	Jerusalem	Jericho	Nablus	Hebron	Jenin	Tubas
January	5.4	5.5	4.7	4.7	5.4	5.7
February	7.1	5.9	4.8	4.8	5.6	6.0
March	7.4	7.7	6.4	6.4	6.8	7.5
April	9.4	9.3	8.2	8.1	7.8	8.7
May	11.4	9.4	8.9	9.0	9.7	10.3
June	12.4	11.8	8.4	8.3	11.3	11.6
July	12.1	11.7	9.6	9.6	11.1	11.7
August	11.8	11.6	10.9	10.9	10.0	11.0
September	10.1	10.5	10.2	10.3	9.1	9.9
October	7.3	8.7	9.8	9.8	8.1	8.5
November	6.5	6.5	7.0	7.0	6.8	7.3
December	5.9	5.6	4.5	4.7	5.4	6.2

Source: Palestinian Meteorological Office Website (www.pmd.ps)

2.3.1 Rainfall

There are four climatic zones within the West Bank as shown in Figure 2.3 (ARIJ, 1997; Hughes and Mansour, 2005):

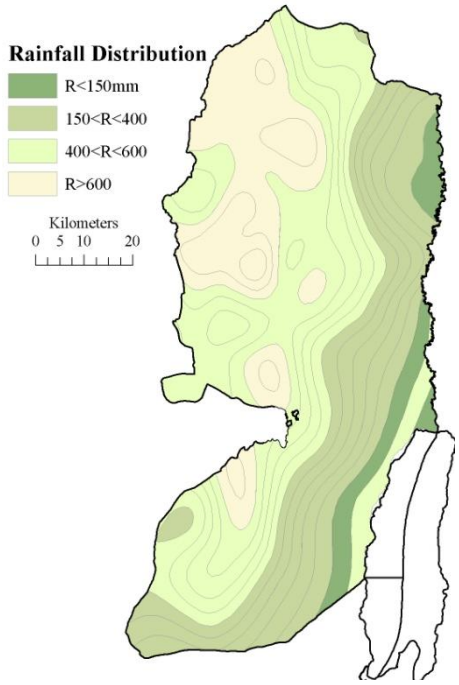

Figure 2.3: Annual rainfall map (Source: Palestinian Water Authority)

i. Rainfall less than 150 mm year^{-1}: South east of the West Bank; is the lowest area (412 m below sea level) with a semi-tropical climate.

ii. Rainfall greater than 150 mm year^{-1}and less than 400 mm year^{-1}: The Eastern Aquifer Basin and the southern part of the Western Aquifer Basin. Elevations range from 200 m below sea level to 800 m above sea level and is considered a semi-arid region.

iii. Rainfall greater than 400 mm year^{-1} and less than 600 mm year^{-1}: Central part of the Western Aquifer Basin and the North-eastern Aquifer Basin. This predominantly area ranges in elevation from more than 400 m to 1000 m above sea level. The mountain hills in this area are considered the main catchment area of the groundwater aquifer basins.

iv. Rainfall greater than 600 mm year^{-1} and less than 1200 mm year^{-1}: The north part of the Western Aquifer Basin considered as a Semi-Coastal region. It is an

extension of the Mediterranean coastal region with elevation ranging between 100 m to 400 m above sea level.

Rainfall has a critical importance for Palestinians as it replenishes groundwater supplies in the West Bank. Rainfall decreases from north to south and from west to east. Rain averages 900 mm per year in the north and west to 100 mm per year in south and east (PASSIA, 2003), and the eastern third of the territory is arid and dry, with warm winters and hot summers.

The West Bank is characterised by its Mediterranean climate except for the Jordan Valley (Eastern part of the West Bank) which is considered to be a semi-arid to arid area. The rainy season starts in the second half of autumn (mid-October) and continues until the end of April. Heavy rain is limited to fewer than 50 days, with around 70% of the rain falling during November to February (PASSIA, 2003).

Table 2.2: Number of rainfall days in key stations of the West Bank

Station	Year							
Location	1997	1998	1999	2000	2001	2002	2003	2004
Jenin	74	49	35	48	38	no data	64	51
Tulkarm	77	62	39	61	44	no data	no data	50
Nablus	62	68	42	61	49	no data	64	58
Jericho	50	32	23	32	24	no data	41	35
Jerusalem	59	32	no data	no data	35	no data	48	no data
Hebron	54	40	31	54	48	no data	49	42

Source: Palestinian Central Bureau of Statistics (2004)

Table 2.2 shows the variation in the number of rainfall days at different years and at different stations. For example, the highest number of rainfall days in Tulkarm station is 77 days in 1997 while in 1999 it is 39 days only. In year 2004, Nablus receives 58 days of rainfall, Hebron 42 days, and Jericho receives the least with 35 days. Nonetheless, the north and west parts of the West Bank (such as Jenin, Tulkarm, and Nablus) are the areas receiving highest rainfall as illustrated in Figure 2.4.

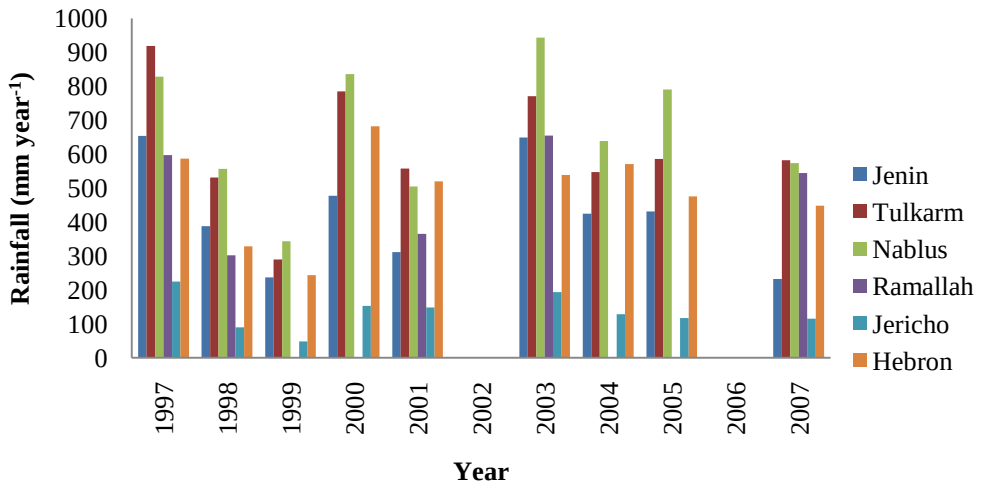

Figure 2.4: Annual rainfall variation for key stations of the West Bank

Rainfall in the year 1997 records 918.4 mm in Tulkarm station and 224.6 mm in Jericho while in 1999 rainfall is 290 mm in Tulkarm and 48.7 mm in Jericho. These variations in climate as well as in the hydrogeological characteristics results in variation of groundwater recharge and water infiltration.

The mean monthly data of 2004 (Figure 2.5) indicates that January has the highest amount of rainfall, while the quantity of rainfall halts starting the summer season from May until September. The total quantities of rainfall range between 638.5 mm in Nablus station and 128.5 mm in Jericho.

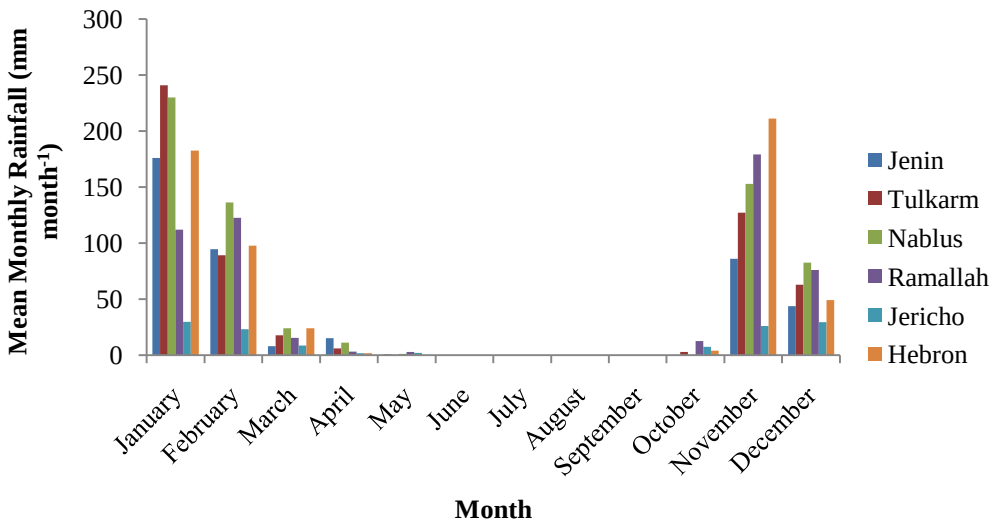

Figure 2.5: Mean monthly rainfall for year 2004 (PCBS, 2004)

However, historical annual rainfall data of the Jerusalem station from 1964 to 2004 (Figure 2.6) indicates that the mean annual rainfall for the year 2004 is below the average that is estimated (approximately 590 mm).

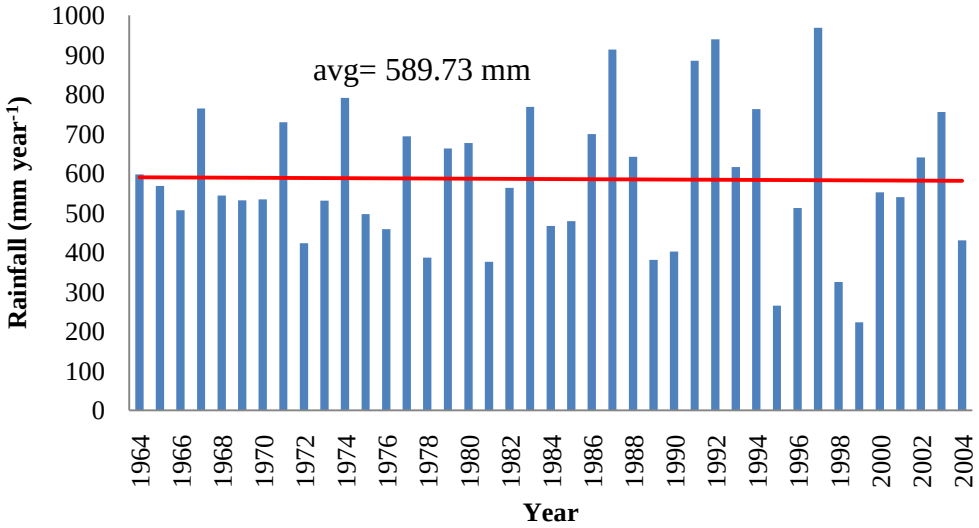

Figure 2.6: Annual rainfall distribution for Jerusalem station

Though as rainfall is one of the key factors controlling recharge (along with other factors such as evapotranspiration, vegetation, and soil), it is expected that its estimates in 2004 are less than the previous year or the long-term average annual recharge.

2.3.2 Air Temperature

Topography and distance from the Mediterranean Sea play an important role in the temperature variations of the West Bank. For instance, Tulkarm (North West) receives more marine effects than Jericho as it is more open to the sea. On the other hand, the eastern heights affect the wind and rain distribution over the Jordan Valley preventing the marine effects and cold air from reaching it; thus increasing temperature and decreasing rainfall.

Summer temperatures in the West Bank reach 35 °C and in the winter drop to 0 °C. Time series indicate that the annual mean, the annual mean maximum, and the annual mean minimum air temperatures over the period 1975-1996 in Hebron station (south) are between 15.4°, 19.6°, and 11.2 °C, respectively (PCBS website). While in Jericho, it was recorded that the annual mean, annual mean maximum, and annual mean minimum

air temperatures over the same period, 1975-1996, were 22.7°, 29.6°, and 15.7 °C, respectively.

For the year 2004, the main findings indicate that January is the coldest month of the year, in which the lowest temperature recorded a monthly mean of 7.7 °C at the Hebron station. July is the hottest month recording a monthly mean temperature of 32.4 °C at the Jericho station. Figures 2.7 and 2.8 illustrate the monthly and annual dynamic of air temperature of the main stations of the West Bank.

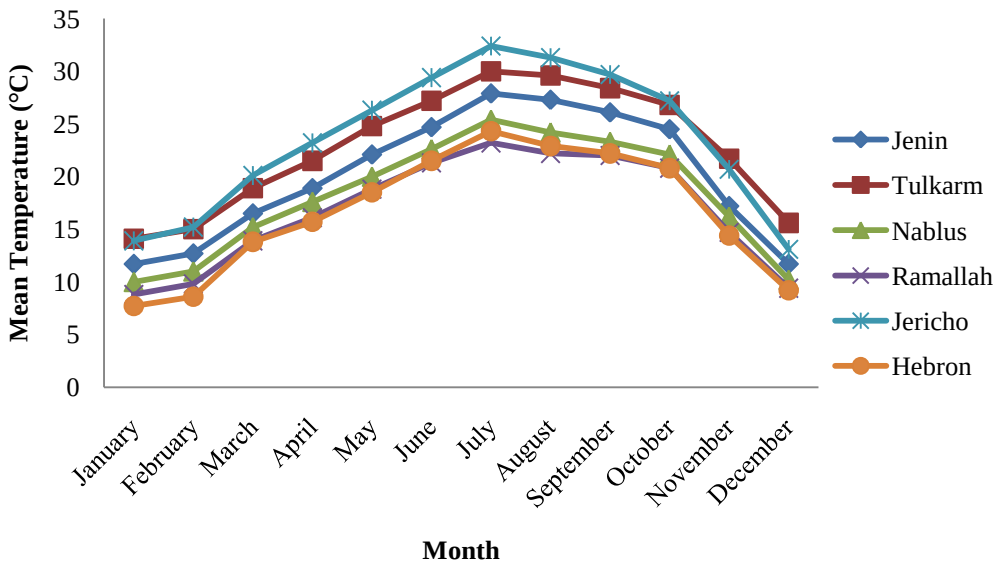

Figure 2.7: Mean monthly air temperature for year 2004

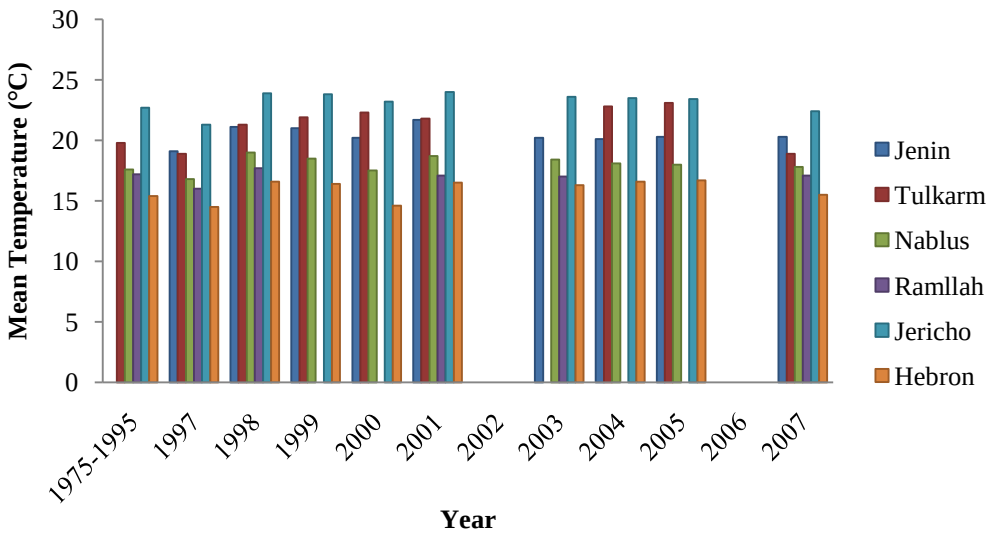

Figure 2.8: Mean annual temperature

Historical records of mean annual air temperature for the Jerusalem Station, from 1964 to 2004, demonstrate that the year 2004 is above the average mean annual temperature values, where the average for the fifty years is 17.47 °C (Figure 2.9 below).

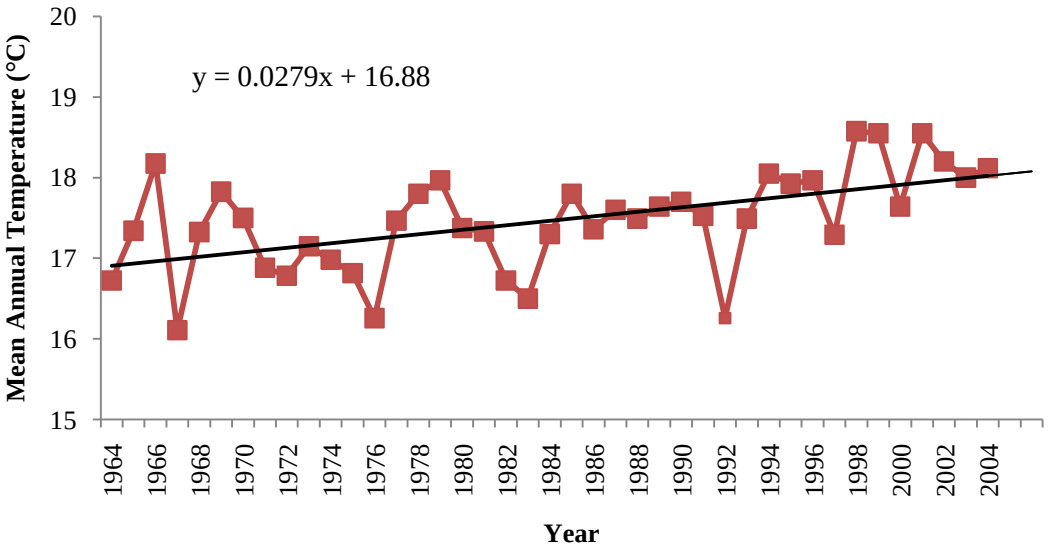

Figure 2.9: Mean Annual Temperature Variation for Jerusalem Station over 50 Years

To further illustrate the warming conditions in the area, the percentage of temperature departure for Jerusalem station is calculated as

$$\% \text{ departure } dr = (ti-tr)/tr * 100 \qquad (2.1)$$

where ti is the mean annual station temperature and tr is the mean annual regional temperature. Variation in annual temperature over the last 20-years (1985-2004) has been tested against the preceding 20-years period.

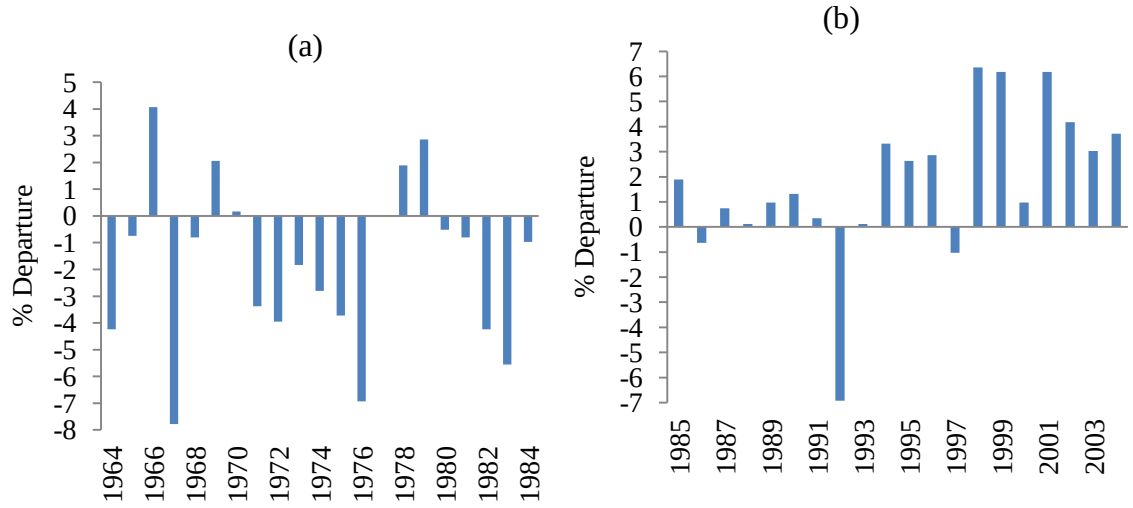

Figure 2.10: Regional Warming Exemplified by Temperature Elevation in Jerusalem Station (1964-2004): (a) 1964-1984 and (b) 1985-2004

Figure 2.10 clearly illustrates that temperature departures are showing positive deviations from the long-term average in the last twenty years, while in the preceding years they were negative. Elevation in regional temperature ranges approximately between 1-6%, signifying an increase in temperature at around 0.2-1.05°C, with a mean value of 0.32°C and a standard deviation of 0.53°C. An increase reaching such range is considered high over a twenty years period which may cause further water stress problems in the area.

2.3.3 Relative Humidity

The average annual relative humidity is 60% reaching its highest rates during the months of January and February. In May, however, humidity levels are at their lowest. Night dew may occur in up to 180 days per year.

In 2004, the annual mean of relative humidity is between 53% in Jericho station and 68% in Ramallah station as illustrated in Figure 2.11 below (PCBS, 2004).

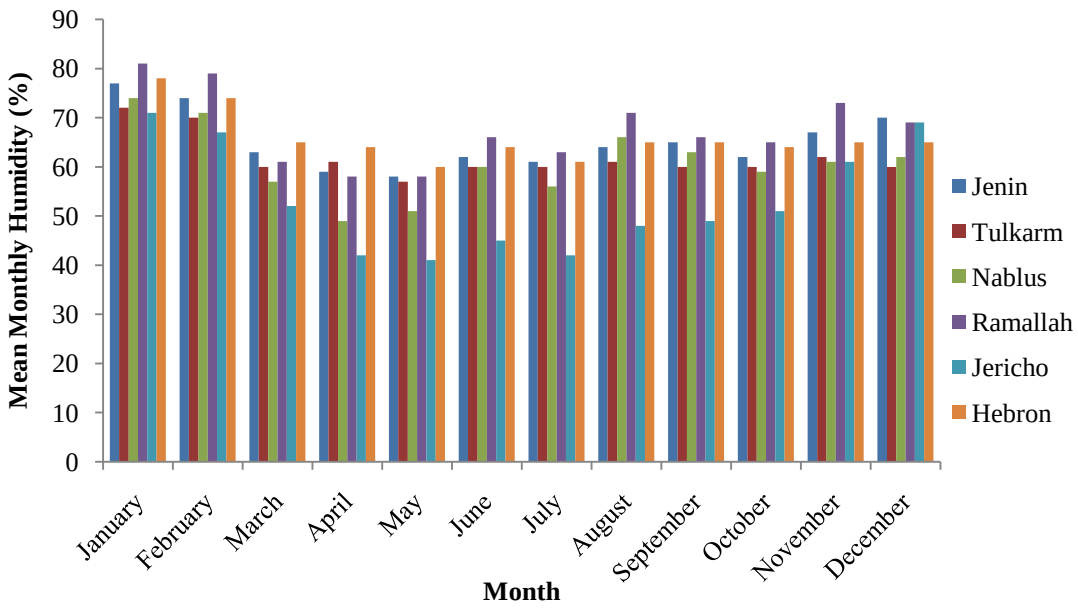

Figure 2.11: Mean monthly relative humidity for year 2004

2.3.4 Evaporation

Potential evaporation reaches its highest values in the south east at 2300 mm year-1 and in the north at 1850 mm year-1 (Hughes and Mansour, 2005). It is high in summer due to the rise in temperatures, intensive sunshine and low humidity. The mean monthly evaporation rates ranges are highest in the three months from June to August, reaching its highest in July at 310.9 mm at the Jericho station (Table 2.3) (PCBS, 2004).

Table 2.3: Pan Evaporation quantities in the West Bank for the Year 2004 (mm month^{-1})

Month	Station				
	Jenin	Nablus	Ramallah	Jericho	Hebron
January	61.1	70.1	84.7	62.3	76.9
February	78.2	77.8	76.4	78.4	95.8
March	132.4	150.6	153.6	143.9	178.5
April	176.3	180.2	185.5	200.2	153.7
May	237.2	228.4	233.5	248.9	195.0
June	258.5	239.2	268.2	279.3	240.5
July	291.0	265.5	216.0	310.9	233.2
August	259.1	223.6	277.0	271.4	216.2
September	191.3	200.7	243.0	219.1	202.3
October	143.4	151.7	184.0	150.9	156.8
November	57.0	112.6	107.0	87.1	113.9
December	58.4	81.4	79.0	58.3	111.5
Total	**1943.9**	**1981.8**	**2107.9**	**2110.7**	**1974.3**

Evaporation is measured through the use of Class-A pan. Long term evaporation records are not available, but the available average annual estimates from 1973-1984 and from 1997-2007 indicate that Tulkarm Station has the lowest annual mean of potential evaporation values, while the Jericho Station has the highest annual means (Figure 2.12 (PCBS, 2007)).

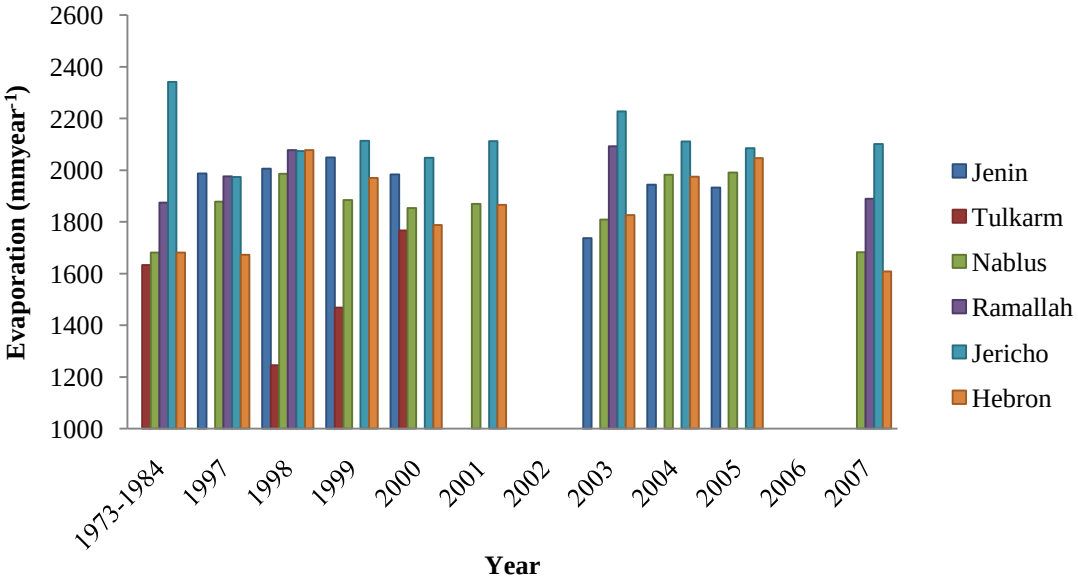

Figure 2.12: Mean annual potential evaporation

2.4 Recharge

Groundwater recharge is the long-term average residual between precipitation (P) and evapotranspiration (ET). Both quantities can be estimated from remote sensing data. Precipitation can be estimated from cloud temperature data using certain algorithms (e.g. Herman *et al*., 1997) in combination with precipitation data from meteorological stations on the ground. The Famine Early Warning Systems Network (FEWS 2006) offers such data at a 10-day temporal resolution for all of Africa. The Special Sensor Microwave Imager (SSM/I) and Tropical Rainfall Measuring Mission (TRMM) also provide global data on rainfall that can be used as a source for precipitation data (Milewski *et al*., 2009; Milewski *et al*., 2009). Evapotranspiration can be derived from multispectral satellite data via the surface energy balance using the dry and wet pixels: the dry pixels heat up to higher temperatures than wet pixels which has large amount of water available for evaporative cooling. The radiation data can then be related to evapotranspiration and the fraction of net radiation energy consumed by evaporating

water estimated. Groundwater recharge from rivers, streams, and wetlands, under certain circumstances, can also be inferred from remote sensing through anomalies in temperature or electrical conductivity. In arid environments, evaporation is mostly through plants in the form of transpiration. This increases salinity in groundwater and hence the electrical conductivity. In contrast, freshly infiltrated water beneath a stream has a low conductivity. This subsurface electrical conductivity and type of groundwater can be detected by airborne electromagnetic methods (Paine and Collins, 2003).

The soil moisture balance can also be used as an indicator of recharge. It requires some information on the field capacity of a soil which can be estimated on the basis of the soil type in addition to average ET and P to account for water storage in the soil. Hyperspectral satellite information and gamma radiation counts from airborne platforms can help in identifying the soil type and moisture content (Rainey *et al*., 2003; Cook *et al*., 1996). European Space Agency's (ESA) Soil Moisture and Ocean Salinity (SMOS) mission (www.esa.int) is to observe the soil moisture over the Earth's land. The moisture reported relates to 1-2 meters but the use of this type of data requires substantial modelling (Brunner *et al*., 2006).

The spatial distribution of recharge may be heterogeneous even if the distribution of precipitation is homogeneous (Brunner *et al*., 2006). In arid areas, depressions, where water collects and infiltrates, are often the dominant factor of recharge (Leduc *et al*., 2001). The temporal behaviour can be identified by remote sensing such as radar data or multispectral characterization (McCarthy *et al*., 2004; Roshier and Rumbachs 2004). Their density and distribution are considered indicative of the spatial distribution of recharge.

2.4.1 Previous Recharge Estimates

Estimation of recharge and its spatial variation is an important issue in preserving the aquifers replenishment and hence maintaining and increasing the amount of water draining into these aquifers. While previous recharge estimates have been calculated as a percentage of long-term mean rainfall, they overlooked many recharge variables such as land use/land cover, actual evapotranspiration, rainfall distribution, topography, and

geology. The failure to account for such parameters leads to estimation inaccuracies and therefore, recharge may be less than estimated (SUSMAQ, 2001).

All the work on the West Bank recharge estimate has been directed towards producing empirical formulae that describe the relationship between rainfall and recharge (Goldschmidt, 1955; Goldschmidt and Jacobs, 1958; Tahel, 1988; Assaf *et al*., 1993; Guttman and Zuckerman, 1995 Ba'ba', 1996; Bachmat, 1995), except that of Rofe and Raffety (1965) who used the Penman (1948) soil moisture approach (see Chapter 5). Such an approach did not allow for the identification of recharge processes such as the indirect recharge to wadis or the impact of land use change on recharge.

A more recent study has been developed for the recharge calculation on the regional scale by the British Geological Survey in coordination with the Palestinian Water Authority and SUSMAQ project team, based on an object oriented model. This model calculates recharge at nodes held on grids where four different types of calculations have been used on corresponding nodes. For instance, recharge at nodes in the sub-humid area (northwest) of the West Bank is calculated using the Soil Moisture Deficit (SMD) method where it is calculated as the excess quantity of water from rainfall after accounting for runoff, potential evapotranspiration, and soil moisture deficit. While in the arid area in the southeast of the West Bank, the wetting threshold method is used as soil moisture is rarely at its field capacity and no runoff is generated. In urban and agricultural areas, urban recharge and irrigation recharge are applied on corresponding nodes. Though the model calculated recharge in a detailed manner, it lacks the spatial distributed data required by the model of evaporation and rainfall. Moreover, the model uses the potential evapotranspiration while the actual evapotranspiration values ought to be used instead.

2.4.2 Recharge Mechanism in the West Bank

The Mountain Aquifer system comprises three basins: the Western Aquifer, Eastern Aquifer, and the North-Eastern Aquifer basins. The geological structure indicates a defined groundwater divide between the Western Aquifer and the Eastern Aquifer basins, and between the Western and the North-Eastern Aquifer basins (see Figure 1.2). The Mountain Aquifer creates an upland area comprising of limestone with subordinate

lithologies. A major Eocene sedimentary basin exists in the north-west of the Aquifer. Direct rainfall recharge occurs in the permeable limestone and indirect recharge is routed via the ephemeral influent wadi flow. The limestone aquifer is comprised of four distinct hydraulic zones: the Shallow Aquifer, Upper Aquifer, Lower Aquifer, and the Deep Aquifer. The Mountain Aquifer is recharged within the West Bank and flows west towards the Mediterranean Sea, spring discharges in Israel, and the Jordan River.

There are two main types of recharge: direct and indirect recharge. Direct recharge is the amount of rainfall that percolates through the surface into the water table. Indirect recharge is the water that reaches the water table by other routes including runoff to surface water courses and subsequent infiltration and localized recharge due to ponding. As aridity increases towards the south and southeast, direct recharge is likely to become important in terms of total recharge to the aquifer (Lerner *et al*., 1990).

The main recharge processes (illustrated in Figures 2.13-2.15) operating in the West Bank are (Hughes and Mansour, 2005).

2.4.2.1 Rainfall Recharge

Rainfall is the main component of recharge; however, other components may be locally significant such as urban recharge and wadi infiltration. The amount of recharge depends on rainfall intensity and temporal distribution, evapotranspiration, runoff, soil thickness and soil type, vegetation cover, slope, and the unsaturated zone. In the sub-humid area in the north and west of the West Bank, the amount of direct recharge is dependent on soil processes and how much evapotranspiration occurs from plants. While in the arid areas covering the East and Southeast of the study area, recharge is more complex. The long-term average rainfall is lower, rainfall is concentrated in more intense events, and soil is less well developed. These factors indicate that the soil moisture deficit is high and direct recharge rarely occurs (Lloyd, 1980). In the semi-arid areas, rainfall occurs in sufficient quality to reduce soil moisture deficit and increases as a result of infiltration.

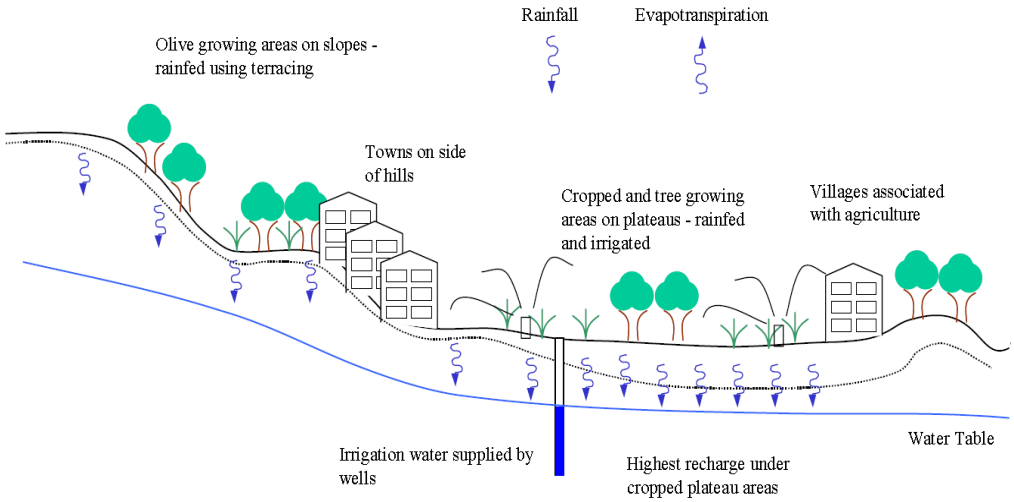

Figure 2.13: Rainfed agriculture predominates in the north and north-west of the West Bank suggesting development of soil moisture. (Hughes and Mansour, 2005)

2.4.2.2 Recharge from Wadi Losses

Rainfall events in the West Bank can be of high intensity and storms with rainfall intensity of 10 to 15 mm hour^{-1} can take place. These intense rainfall events lead to rapid development of runoff to wadis where water is recharged into the groundwater system either directly or via the superficial deposits.

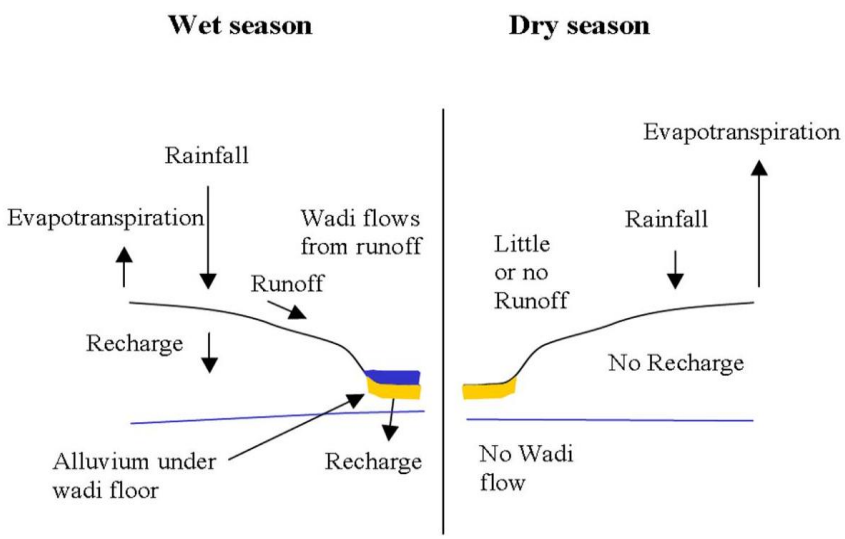

Figure 2.14: Indirect recharge from wadis predominates in the south and east of the West Bank. (Hughes and Mansour, 2005)

2.4.2.3 Urban Recharge

Leakage from pressurized water mains and from breaks in sewers can become a potential recharge source. In addition, the runoff resulting from impermeable surfaces is collected and routed via storm drains to wadis and recharged. Foul sewers also empty into wadis offering an additional source of urban recharge.

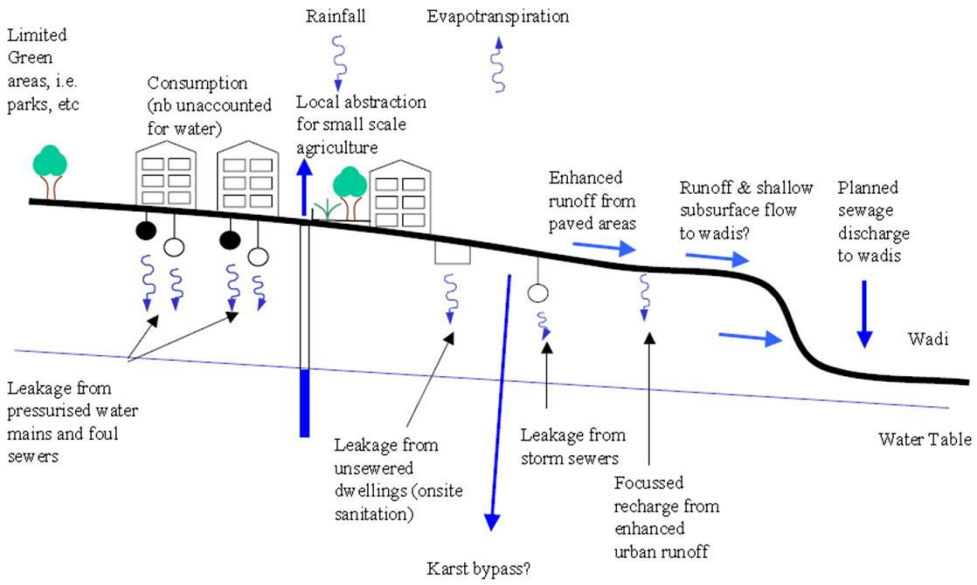

Figure 2.15: Complex interaction of processes in urban areas. (Source: Hughes and Mansour, 2005)

2.4.2.4 Irrigation Losses:

Most field crops in the West Bank are rainfed while vegetables such as tomatoes, cucumber, aubergine, and courgette are irrigated. Greenhouses are found in Tulkarm, Jenin and Jericho areas that are used to cultivate vegetables and fruits. Water stored in the soil is used to cultivate rainfed crops such as olive trees and grapes. Irrigation accounts for 83 MCM yr^{-1} or about 70% of the water withdrawn from the groundwater aquifers for Palestinian use (Nazer *et al*., 2010).

Two methods of irrigation exist in the West Bank: the traditional method and the modern method. The traditional method includes forming water channels, basins, and flooding whereas the modern methods include sprinkler and drip systems (ARIJ, 1998).

The traditional method is considered less sufficient and the water losses are higher, therefore providing another potential source of recharge.

Recharge may be quantified using several methods: direct measurements, water balance methods, Darcian approach, tracer techniques, and empirical methods. In this research, monthly soil moisture balance approach will be used to estimate rainfall recharge mechanism in which the monthly precipitation and actual evapotranspiration are inputs to soil moisture.

Recharge rates for the three aquifer basins of the West Bank have been estimated between 800 MCM yr^{-1} and 836 MCM yr^{-1} according to the Israeli Hydrological Service (1997) and Guttman (1995) respectively. It has been calculated based on water balance theory, where spring discharges and groundwater abstractions are equated to recharge (SUSMAQ, 2001). They are estimated using two equations: Goldschmidt formula which is an empirical formula considering only rainfall and the other is the Tahal/Guttman model applied to the Eastern Aquifer Basin which is also based on rainfall but with varied rainfall coefficient depending on rainfall intensity.

Hughes and Mansour (2005) state that the nature of the three aquifers, the climatic variations over the West Bank, local springs, flows to wadis, and irrigation and urban processes variance make the process of estimating recharge on the regional scale a difficult one. These measurement approaches are considered point estimates of recharge and their implementation over the whole West Bank is costly. In addition, a lack of ground field data exists and political constraints are imposed preventing easy access to land.

Other recharge estimates have been produced from three groundwater models: Bachmat (1995) for the Western Aquifer Basin, Guttman and Zukerman (1995) for the Eastern Aquifer Basin, and Camp Dresser Morganti (CDM) in 1998 for the Eastern Aquifer Basin (Hughes *et al*., 2008; SUSMAQ, 2001). The three models share a similar method of having grid cells and estimating recharge of each cell using a different rainfall coefficient depending on the intensity of the rain. Table 2.4 summarizes previous recharge studies taken on aquifer scale.

Table 2.4: Recharge estimates for aquifer basins of the Mountain Aquifer (MCM yr^{-1})

Aquifer Basin	Source	Year	Annual Recharge	Assumptions
Eastern Aquifer Basin	CDM	1977	140	Recharge Coefficients (recharge is a percentage of rainfall): • 0% over thick chalk • 10% where rainfall <250mm • 20% rainfall between 250-450mm • 30% rainfall between 450-700mm • Accounted for wadis and water mains as 8.2 (16% of flow) and 12.4 MCM yr^{-1} (30-40% of water delivered), respectively
	CDM	1998	197	
	Guttman	1998	125	
	Ba'ba'	1996	129	• Rc= 0.2327avP -32.52 • Recharge equals springs discharge plus changes in groundwater storage
	EXACT		173	
	Article 40, Oslo Agreement	1995	172	
	Guttman and Zukerman	1995	118.5	• Recharge is estimated by assuming it is equal to a percentage of mean rainfall where areas of highest rainfall were set with high recharge coefficients. • Ri= Cd(year)*Rs
	Tahal/ Guttman	1998	460	• Rc= 0.8(avP-360) Rainfall >650mm • Rc= 0.534(avP-216) Rainfall 300-650mm • Rc= 0.8(avP-360) Rainfall <300mm
Northeastern Aquifer Basin	EXACT	-	145	
	Article 40, Oslo Agreement	1995	145	
Western Aquifer Basin	Bachmat	1995	330-332	Rainfall coefficients are based on historical water balance of Goldschmidt and Jacob (1958)

	Goldschmidt and Jacobs	1955	317.5	• Used catchment scale water balance • Rc= 0.86(avP-360) • Assuming there are only two stream springs outlets discharges • Their baseflow is derived from replenishment of catchment • Gauged data accurately reflects base flow • Measured period from 1943-1954 was typical of long term aquifer conditions • Abstraction from boreholes and other springs discharges are negligible • 4% of rainfall storms is assumed as runoff
	MNIWC	1961 - 1990	366	
	EXACT		366	
	Article 40, Oslo Agreement	1995	362	

Sources: SUSMAQ, (2001) Palestine Conceptual Recharge Report, p. 16-20
Rc= Recharge (mm), avP= long term average annual rainfall, Ri= Recharge in each model cell, Cd= factor relating recharge in a given year to the calculated steady state recharge, Rs= steady state recharge

Other estimates have been carried out at a catchment scale such as:

- The Israeli Hydrological Service: Jordan and Litani Rivers Catchments
- Rofe and Raffety (1963): Jerusalem and Hebron Aquifers
- Wolfer (1998): Wadi el Qilt Basin

Previous approaches disregard other hydrological parameters such as the geology at the surface, rainfall distribution over the West Bank, actual evapotranspiration, soil thickness, topography of the land where runoff is highly generated in steep slopes during heavy rainstorms creating therefore, intense recharge from wadi floors, and land use/ land cover (Hughes and Mansour, 2005). Thus, such estimates have resulted in inaccurate estimations of recharge and its distribution where such measurements may be more than the actual natural recharge (SUSMAQ, 2001).

Therefore, to determine the actual recharge distribution over the Mountain Aquifer within the West Bank, spatial and temporal distribution of recharge inputs are required. These layers include monthly evapotranspiration derived from the Moderate Resolution Imaging Spectroradiometer (MODIS) by the application of Surface Energy Balance Algorithm for Land (SEBAL) (Chapter 7); monthly precipitation derived from Tropical Rainfall Measuring Mission (TRMM) (Chapter 8), and assumed runoff values (Chapter 8) manipulated in a Geographic Information System (GIS) map (Figure 2.16).

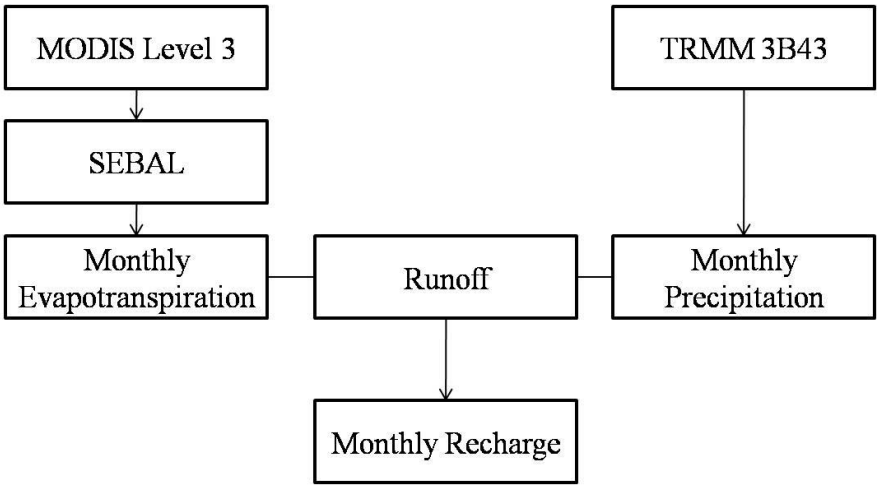

Figure 2.16: Recharge Model for monthly rates estimation

Recharge is a critical input to estimating and quantifying the total water availability of the West Bank aquifers. Evapotranspiration (ET) estimates are the most important hydrological variable concerning water availability as it determines the water loss from evaporative surfaces, soil storage, and precipitation (Oke, 1997). Short-term point measurements of potential evapotranspiration in key stations are the only data available. Therefore, a major part of this research will be dedicated to estimating the regional evapotranspiration using satellite images and remote sensing.

2.5 Relief, Drainage, and Geomorphology

2.5.1 Relief

The West Bank is a mountainous area where hills extent from north to south with elevation ranging from 453 m below sea level in the Dead Sea to 1011 m in Tell Asur in the southern part (Figure 2.17).

The West Bank can be divided into four major geomorphologic parts: Nablus Mountains, Jerusalem Mountains, Ramallah Mountains, Hebron Mountains, and the Jordan Valley. The drainage and valley systems originate from the mountain range and extend eastwards and westwards.

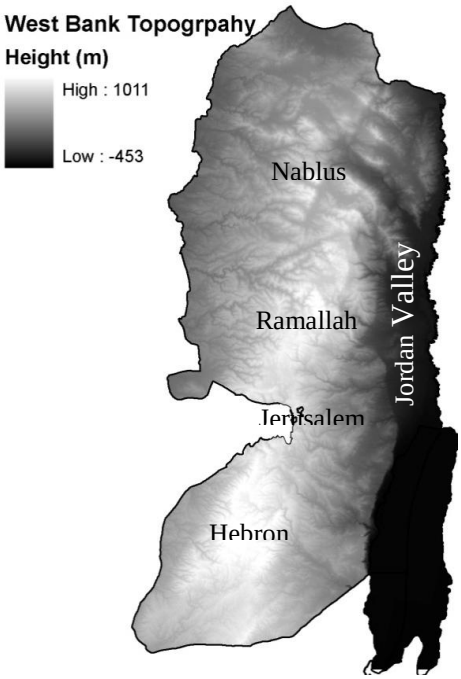

Figure 2.17: Digital Elevation Model (DEM) of the West Bank derived from ASTER

The Nablus Mountains extend from Marj Ben Amer in the north to Jerusalem Mountains in the south. The water divide separating the western and the eastern basins in Palestine coincides with the summits of these two mountains. The elevations of these mountains range, on average, between 750 m and 800 m above the sea level. The highest land surface appears at Mount ‘Ebal with an elevation of 918 m above sea level.

Jerusalem Mountains are composed of three main groups, the eastern slopes’ (ranges between 100 and 250 m above sea level), central mountain crests (ranges between 750 and 880 m above sea level), and western slops (ranging from 250 to 300 m above sea level). The eastern slopes are located between the Jordan Valley and the central mountains. They lie to the south of the Nablus Mountains and are separated from them by Wadi Deir Ballout. The watershed line passes through the summits of these mountains; the highest point is located between Deir Jarir and Silwad.

Ramallah Mountains can be divided into three parts: the eastern slopes, mountain crests and western slopes (elevation ranging between 250 –500 m above sea level). Mountain crests from the watershed line separate the eastern and western slopes. Elevation ranges on average between 750 and 800 m above sea level. The highest point in Ramallah district is 1022 m above sea level at Tel A'sour and the lowest elevation is 24 m below sea level at the southeast corner of the district.

The Hebron Mountains form the southern rim of the West Bank Mountains. They are located south of Jerusalem and extend to Negev. On average they are 850 m above sea level near Kherbit Khellan to the north of Hebron City, the highest elevation of approximately 1011 m above sea level is found in Halhul area. Sharp slopes, called the Eastern Slopes, where elevation drops from 1011 to 100 m above sea level, characterize the eastern part of the district. Most of the Palestinian built up areas in the district are located at elevations between 600 and 1000 m above sea level. Despite the numerous valleys among these mountains on both eastern and western sides, they are relatively more bare than other mountain areas in the West Bank. This is basically due to the closeness of the Hebron Mountains to the Negev Desert in the south to the Negev Desert in the south and to the Dead Sea in the east, where arid conditions prevail.

The Jordan Valley is part of a long and deep depression of the Earth's crust, widely known as the Jordan Rift, which forms the eastern boundary of Palestine. The Jordan Valley has its own uniqueness with a semi-tropical climate characterized by hot summer and warm winters. This region would be desert-like without access to water (ARIJ, 1994).

2.5.2 Surface Water Runoff

Previous studies have suggested that surface water runoff plays a minor role in the recharge of the West Bank aquifers. Goldschmidt and Jacob (1958) adopt a value of 4% of rainfall as runoff. Similar figures are adopted in Rofe and Raffety (1963), while higher values of runoff are considered by CDM (1998) where the total Eastern Aquifer Basin wadi flow is up to 50 MCM (million cubic meters). Another study by Husary *et al.*, (1995) looked at rainfall-runoff relationships for Hadera catchment (shared

catchment in the Northwest of the West Bank) and concluded that runoff in normal years average 3% of rainfall, but in abnormally wet 1991/1992 winter runoff represented 16% of rainfall. Data from several Israeli gauging stations have been used to calculate runoff but as a percentage of precipitation, giving values of between 0.1 and 4.7% of precipitation. Although these data do not give a direct indication of wadi bed infiltration, the low values of runoff suggest that infiltration from this source is likely to be small. A study in Southern Israel which is considered more arid than the West Bank, have suggested that 50% of stream flow infiltrates over the aquifer (Shentis *et al*., 1999; Meirovich *et al*., 1998). As a result, runoff events occur only during high-intensity rainfall events, where excess water is drained to valley floors creating wadi flows. The low precipitation and high evapotranspiration are the reasons behind the uncommon high runoff and stream flow. Despite this, few streams flow westwards towards the Mediterranean and eastwards towards the Jordan River. They flow only for days each year as they are associated with intense runoffs and discharges.

A limited amount of data for stream flow is available and more recent data are confined to a couple of wadis draining towards the River Jordan. Tables 2.5 and 2.6 indicate the flow of gauged wadis in the year 2006 (PWA database).

Table 2.5: Eastwards and westwards wadis runoff (2006)

Wadi Name	Runoff (MCM)
Wadi Al-Malih	1.0
Wadi Al-Nowa'ameh	1.0-2.0
Wadi Al-Fara	3.5-11.0
Wadi Al-Ahmar	1.0-2.0
Wadi Al-Ouja	2.0-3.0
Wadi Al-Qilt	3.0-11.0
Wadi Zimar	8.7
Wadi Al-Teen	8.1
Wadi Qana	12.8
Wadi Sarida	22.8
Wadi Dalb	16.4
Wadi Al-Nar	4.9
Wadi Al-Muqata'a	3.6
Wadi Abu Nar	8.3
Wadi Mas	11.7

Table 2.6: Runoff Data from 1996-1997. (SUSMAQ, 2001)

Station Name	Area of catchment (km^2)	Precipitation ($mm\ yr^{-1}$)	Runoff as % of Precipitation	Runoff ($MCM\ yr^{-1}$)
Qana	240	665	1.9	3.06
Shilo	357	586	2.1	2.94
Natuf	251	495	0.2	0.21
Ayyalon	135	471	4.7	5.37
Soreq	78	505	1.5	1.87
Harel	13	530	0.1	0.12
Haela	423	536	0.4	0.52
Adorayim	207	305	0.7	0.54
Shiqma	38	311	0.9	0.69

As wadis (illustrated in Figure 2.18) are considered an indirect groundwater recharge contributor to the aquifer basins, they are also considered a runoff collector. Flows may accumulate over less permeable wadi bed deposits, but then the water is recharged once it flows towards more permeable sediment. This is further illustrated in Chapter 8 of recharge modelling.

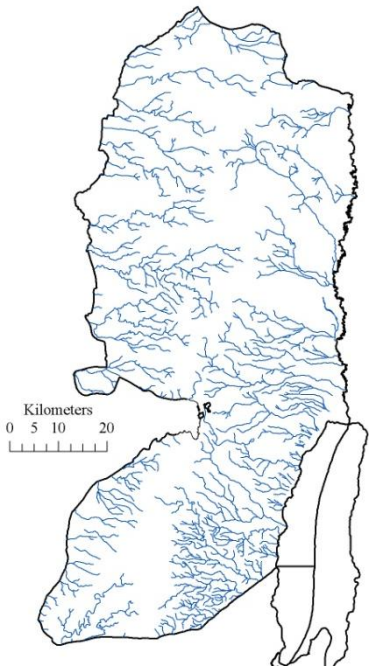

Figure 2.18: Wadis of the West Bank taken from Israeli maps (PWA database)

2.6 Unsaturated Zone

The unsaturated zone is the soil layer transporting water into the aquifers. It determines the amount of water to become recharge as it may not be capable of transporting all infiltrated water from upper soil layer to the water table and some may re-emerge as springs. Its thickness determines the time recharge takes to get to the water tables (Hughes and Mansour, 2005). For instance, if the unsaturated zone is hundreds of meters thick, as in the Eastern Aquifer Basin, then the time of recharge to the water tables will be significantly delayed. Furthermore, the karstic nature and zone layering of the unsaturated zone determine if water can move vertically or laterally. Lateral movement results localised springs which intercept infiltration and prevent direct recharge to the water tables. Also, the karstic nature determines the timescale water takes to be recharged.

2.7 Geology

Runoff and recharge are both determined by the nature of rocks where runoff occurs over the less permeable layers as in Yatta and Abu Dis.

The hydrogeology may be summarised by four types (Hughes and Mansour, 2005):

i. Highly transmissive allowing recharge to water table such as Lower Beit Kahil, Hebron, and Jerusalem.
ii. Moderately transmissive allowing limited recharge such as Upper Beit Kahil.
iii. Relatively impermeable layer causing high runoff such as Yatta and Abu Dis.
iv. Perched systems producing localised springs such as Kobar and Soreq.

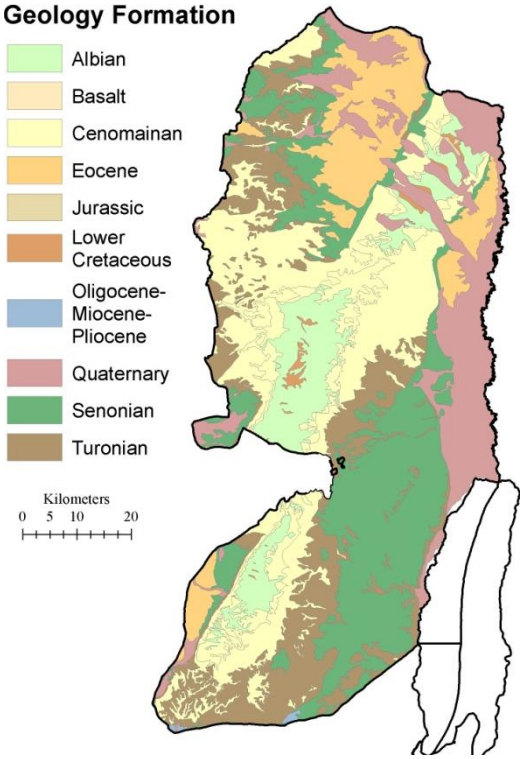

Figure 2.19: Geological Map of the West Bank (PWA database based on Israeli maps)

The principal formations that allow for wadi losses are the Hebron, Upper Bethlehem, and Jerusalem formations in the upper aquifer and Kesalon for the lower aquifer.

2.8 Soil

The different soil types of the study area are presented in Table 2.7. The predominant soil type found in the central and western parts of the West Bank are the Terra Rosa (41%) and Brown Rendzina, and Pale Rendzina (26%) (ARIJ, 1998). They are found in rocky areas where 30-50% of the area is bare rock.

Table 2.7: Main Soil Types in the West Bank

Soil Type	Total Area (ha)	Thickness	Proportion of Rock Outcrop (%)	Crops Grown
Terra Rosa, Brown Rendzina, and Pale Rendzina	235210	Soils in pockets and cracks may be deep	30-50	Field crops (wheat barley), vineyards, olives and fruit trees in valley sides
Brown Rendzinaz and Pale Rendzinas	145698		30-50	Field crops (wheat barley), vineyards, olives and fruit trees in valley sides
Brown Lithosols and Loessial Arid Brown Soils	48391		50-60	Field crops or grazing
Brown Lithosols and Loessial Serozams	24485	Rock outcrops "many"		Winter crops
Bare rocks and desert lithosols	19573	Very shallow		Grazing

Source: Hughes and Mansour (2005)

This combination of bare rock and soils has impacts on recharge where soil moisture is restrained and runoff is increased compared to areas with more evenly distributed soil over the surface. The eastern slopes consists four types of soil: brown lithosols and Loesoils Arid Brown soils, Brown lithosoils and Leosoils Serozems, Regosols, and Bare Rocks and Desert lithosols (Hughes and Mansour, 2005).

2.9 Vegetation and Land Use

The predominant land use in the West Bank is agriculture and olive plantation. Their outcome is modification of the hill slopes through terracing, hence, decreasing runoff and enhancing recharge. Figure 2.20 illustrates some of the main land uses of the West Bank. Vegetation varies by seasonality as most of the cultivated areas are rain fed and

only 6% is irrigated (ARIJ, 1998). A relation between rainfall, biomass volume, and developed soil moisture varies from north to south and south east. Therefore, the majority of agriculture is found in the northern part of the West Bank.

The Palestinian Land Research Centre, within the land system classification study, presented estimations for the agricultural and urban areas at the first level of CORINE land cover system. The estimations were as follows: cultivated hills (46%), uncultivated hills (34%), arable plains (12%) and the rest are made of other minor forms of land use. These data are approximate and depending on the general use of the land unit in each land system. The West Bank is classified into four zones as follows (Dudeen, 2004):

- The Central Highlands: These include the area from Jenin to Hebron. Out of the total cultivated area, 95% is rain-fed 60% under olives, grapes, almonds, and fruit trees, and 35% under field crops, mainly winter cereals and grain legumes. The remaining 5% of the cultivated land is irrigated and used mainly for vegetables.
- The Semi-coastal zone: This is a narrow strip comprising parts of the Jenin and Tulkarm districts. Less than half of the cultivated area depends on rain only. More than half is irrigated or receives some supplementary irrigation water. The rainfed crops are cereals and grain legumes, however, fruit trees are also grown under rainfed conditions. Irrigated crops include a wide variety of vegetables, potatoes, citrus, and other fruit trees.
- The Eastern Slopes zone: This is zone transitional between the Central High-land and the desert areas of the Jordan Valley. Agricultural production is of marginal importance and is limited to rainfed cereals such as wheat and barley. Olives are cultivated as well. Average annual rainfall is 250-300 mm. Some parts of the zone are used for spring grazing.
- The Jordan Valley zone: Jordan Valley is a narrow strip between the Eastern Slopes and the River Jordan. This zone is the most important irrigated area in the West Bank. The availability of both springs and ground water makes this area most suitable for off-season vegetables and for semi-tropical tree plantations, including bananas and citrus. All strains and varieties of dates palm trees are still in existence. Citrus orchards with special taste and early ripping season are remarkable in the Jordan Valley.

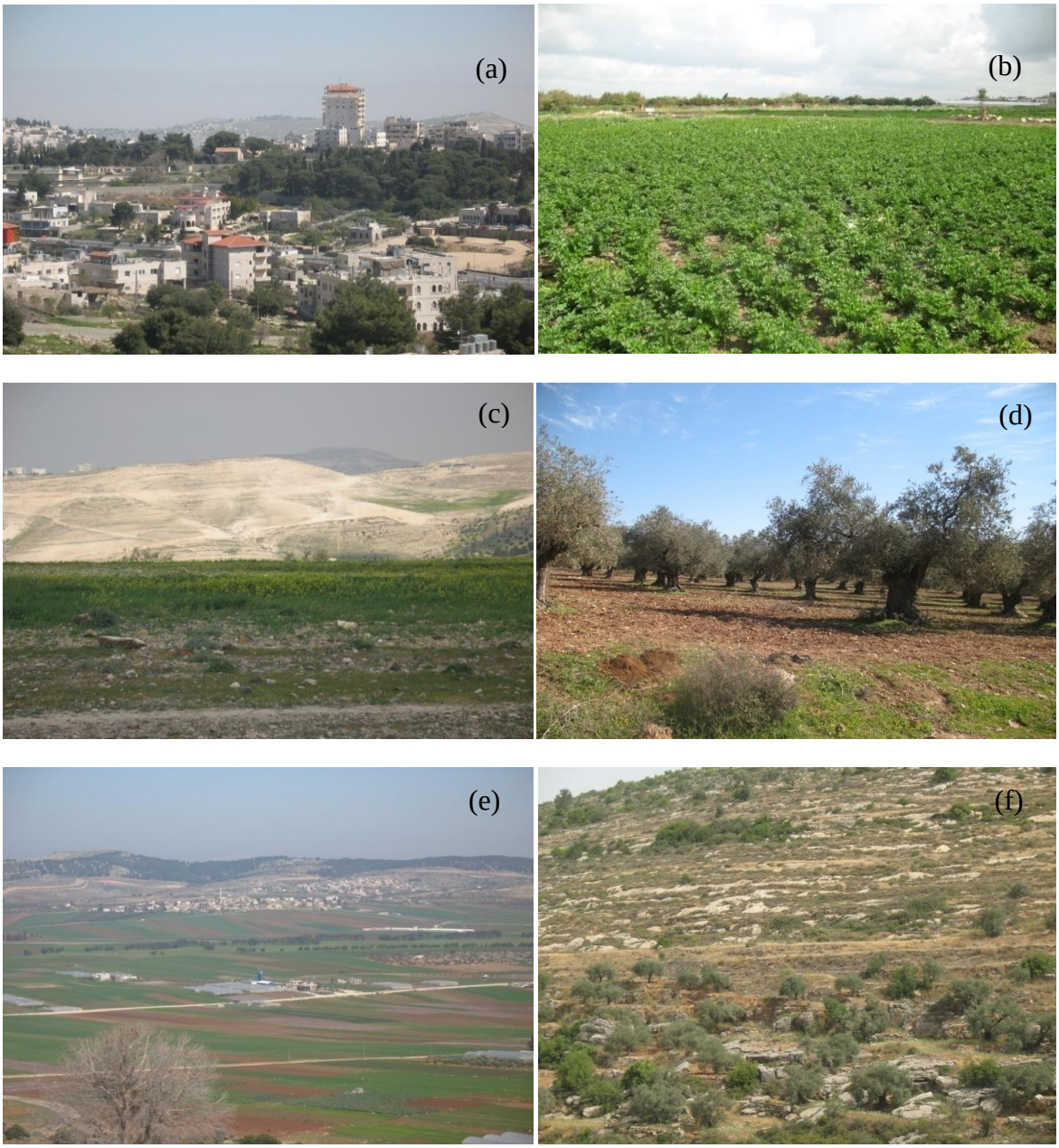

Figure 2.20: (a) urban area, (b) irrigated agriculture, (c) the arid Jordan Valley Mountains, (d) olive trees plantations (e) rainfed agriculture, , and (f) semi natural area. Source: MOP (2008)

2.10 Conclusion

This chapter provides a description of the West Bank area and variables related to its climate, geomorphology, and groundwater recharge. A limited amount of short-term climatic data is available for the stations at Jenin, Tulkarm, Ramallah, Jericho, and Hebron. Long-term daily values of rainfall and temperature are available only for Jerusalem station. The lack of ground measurements will constrain the determination of recharge distribution and its temporal variance based on the conventional methods. Therefore, a regional scale model that covers the West Bank Mountain Aquifer System, to determine the recharge distribution is needed.

One of the most important contributions of this research is introducing a new approach to the hydrological research domain in the West Bank that has been constrained by the scarcity of data at the scale of the Mountain Aquifer. The thesis will now move on to introduce a method of estimating land, hydrological, and atmospherical variables from remote sensing data which places less reliance on ground observations. Chapter three will introduce the satellite data sets employed to estimate recharge rates and mapping model over the study area in addition to the GIS data of geology, soil types, and wadis. Also, a detailed description of images calibration, processing, and geo-referencing is also provided.

Chapter Three

Data Sources and Methodology: Previous and Current Study

3.1 Introduction

The purpose of this chapter is to present and provide a detailed description of the satellite sensors from which some hydrological parameters such as evapotranspiration and precipitation are derived. In conjunction with available field measurements, a descriptive methodology is presented to calculate and map recharge.

Remote sensing, with its advantages of spatial, spectral, and temporal availability of data covering large and inaccessible areas within short time, has become a very valuable tool in exploring, evaluating, and managing vital groundwater resources (Chowdhury *et al*., 2003). The hydrogeological interpretation of satellite data is becoming a valuable survey tool in areas where little or inaccurate information exists (Engman and Gurney, 1991). It provides rapid and useful information about factors controlling the occurrence and movement of surface and groundwater water as well as land use/land cover, drainage, and geomorphology (Bobba *et al*., 1992; Meijerink, 2000). Shallow groundwater can also be inferred by soil moisture measurements and by changes in vegetation types and pattern (Nefedov and Popova, 1972). In arid regions, vegetation characteristics may indicate groundwater depth and quality. Groundwater recharge and discharge areas in drainage basins can be detected from soils, vegetation, and shallow/perched groundwater (Todd, 1980). Furthermore, differences in surface temperature measured by remote sensing have also been used to measure evapotranspiration and identify near-surface groundwater (Bastiannssen *et al*., 1998a, b; Mayers and Moore, 1972; Heilman and Moore, 1981; van de Griend *et al*., 1985).

Integrated solutions of regional water and energy balance equations using satellite measurements complemented by minimum ground data have also been derived by several authors (e.g. Bastiannssen *et al*., 1998a, b; Su *et al*., 1999; Bastiannssen, 2000; Lyon *et al*., 2003). Literature reviews of remote sensing applications in groundwater hydrology are presented in, for example Farnsworth *et al*. (1984), Waters *et al*. (1990),

Engman and Gurney (1991), and Meijerink (2000). These reviews indicate that remote sensing has been widely used as a tool, mostly to complement standard geophysical techniques. Meijerink (2000) recognizes the value of remote sensing in groundwater recharge-based studies and suggests that it can add to the conventional assessment and modelling techniques. Hence, remotely sensed data is becoming one of the main sources for providing information on land and water related subjects. These data, being digital in nature, can be efficiently interpreted and analyzed using various kinds of software packages (e.g. ArcGIS, ENVI, and ERDAS IMAGINE). It is then easy to feed such information into a Geographic Information System (GIS) environment for integration with other types of data to conduct further analysis (Faust *et al*., 1991; Hinton, 1996). The following sections present the remotely sensed data sets used and their properties for recharge modelling.

3.2 Satellite Data Sets

Groundwater recharge computations and mapping (Figure 3.1) is undertaken by the use of the observations extracted from a wide range of global remote sensing data sets.

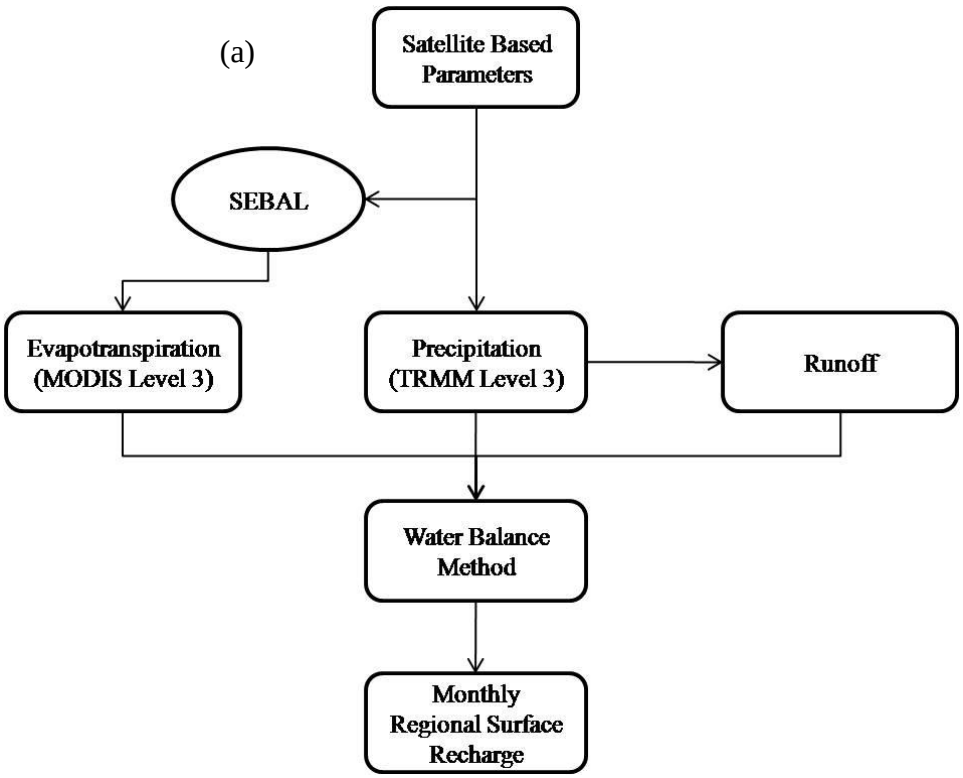

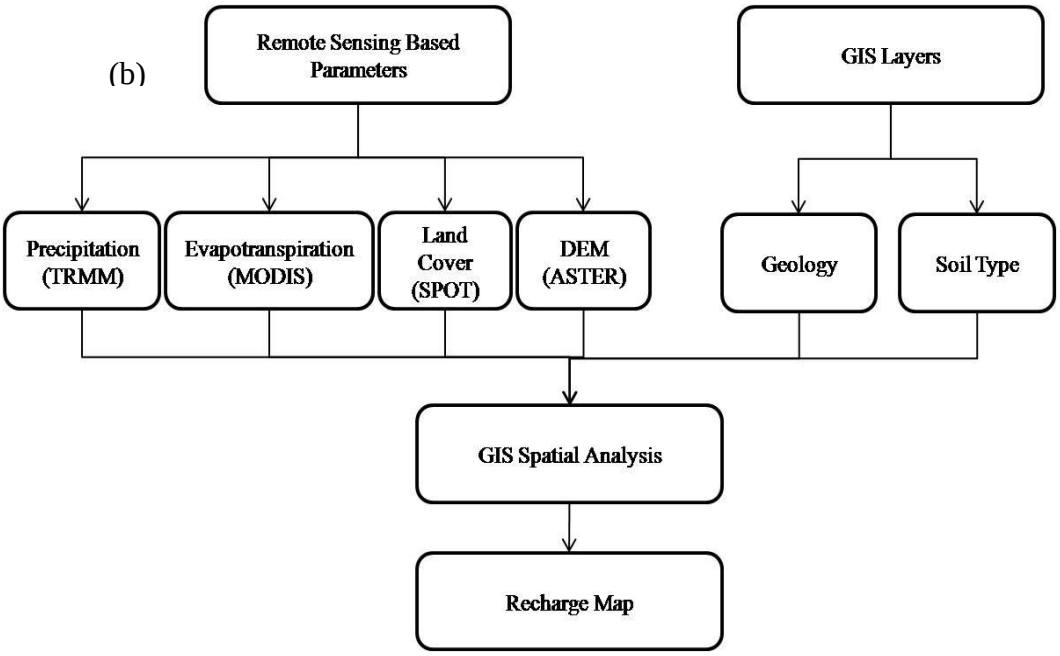

Figure 3.1: Methodology flowchart for: (a) calculating and (b) mapping actual recharge

Five types of remote sensing datasets are collected and processed over the study period to enable the extraction of actual spatial and temporal distribution of recharge inputs. These include: (1) SPOT-2 and SPOT-5 data at 20 m and 10 m spatial resolution providing data on land cover classification and change (Chapter 6) using its visible, red, and infrared sensors; (2) Landsat and (3) MODIS providing red and near infrared, surface reflectance and surface temperature and emissivity to estimate the temporal evapotranspiration maps (Chapters 4 and 7) that are validated by results derived from empirical equations such as Penman-Monteith, Thornthwaite, and pan measurements (Chapter 5); (4) ASTER Global Digital Elevation Model (GDEM) visible image data, available at 30 m spatial resolution used to extract digital elevation and drainage of the West Bank area to enable groundwater recharge computations; and (5) TRMM data that provides global (50°N- 50°S) data on rainfall and precipitation using microwave and visible-infrared sensors with a 0.25° × 0.25° footprint (Chapter 8). These products are radiometrically and geometrically calibrated and are applicable for use in GIS-based hydrological models. Table 3.1 displays the general characteristics of the multispectral datasets in this research. Collection and pre-processing of data is further explained in the subsequent sections.

Table 3.1: General characteristics of satellite data sets

Data Source	Spatial Resolution	Spectral Range (μm)			
		Visible	Near Infrared	Infrared	Thermal Infrared
SPOT-2	10 m for panchromatic and 20 m for multispectral	Band1 (0.5-0.59) Band2 (0.61-0.68)	Band3 (0.78-0.89)		
SPOT-5	5 m for panchromatic and 10 m for multispectral	Band1 (0.5-0.59) Band2 (0.61-0.68)	Band3 (0.78-0.89)		Band4: SWIR (1.58-1.75)
MODIS Level 1B	250 m for bands 1-2 500 m for bands 3-7 1000 m for bands 8-36	Band1 (0.620-0.670) Band3 (0.459-0.479) Band4 (0.545-0.565) Band8 (0.405-0.420) Band9 (0.438-0.448) Band10 (0.438-0.493) Band11 (0.526-0.536) Band12 (0.546-0.556) Band13(0.662-0.672) Band14 (0.673-0.683)	Band2 (0.841-0.876) Band5 (1.230-1.250) Band15 (0.743-0.753) Band16 (0.862-0.877) Band17 (0.890-0.920) Band18 (0.931-0.941) Band19 (0.915-0.965)	Band6 (1.628-1.652) Band7 (2.105-2.155) Band26 (1.36-1.39)	Band20 (3.66-3.84) Band21 (3.92-3.98) Band22 (3.92-3.98) Band23 (4.02-4.08) Band24 (4.43-4.49) Band25 (4.48-4.54) Band31 (10.78-11.28) Band32 (11.77-12.27)
Landsat TM (4 and 5)	30 m for bands 1-5 and 7 120 m for band6	Band1 (0.45-0.52) Band2 (0.52-0.6) Band3 (0.63-0.69)	Band4 (0.76-0.9) Band5 (1.55-1.75)	Band7 (2.08-2.35)	Band6 (10.40-12.50)

Source: http://daac.gsfc.nasa.gov; http://www.spotimage.com; http://landsat.usgs.gov/;

SWIR=Shortwave infrared

3.3 SPOT Data

SPOT (Satellite Pour l'Observation de la Terre) is a high-resolution, optical imaging Earth observation satellite system that is run by SPOT Image based in Toulouse, France. It is initiated by the CNES (Centre National d'Etudes Spatiales- the French space agency) in the 1970s and is developed in association with SSTC (Belgian Scientific, Technical and Cultural Services) and the Swedish National Space Board (SNSB). Two SPOT images are employed for land cover change detection to study its impact on recharge (Chapter 8). The first image is a SPOT-2 image acquired with 20 m spatial resolution in January 1994, and the second is a SPOT-5 and is acquired with a 10 m spatial resolution in May 2004 simulated from a 5 m resolution in multi-spectral mode and 2.5 m in panchromatic.

The HRV (High Resolution Visible) SPOT-2 image has three bands sensor resolution: two visible bands, the green (0.5-0.59 µm) and the red (0.61-0.68 µm) and one near infrared band (0.79-0.89 µm). While the HRG (High Resolution Geometric) SPOT-5 image has four bands sensor resolution: two visible bands and near infra-red as in SPOT-2 in addition to the infrared band (1.58-1.75 µm). Table 3.2 below summarizes the principal characteristics of the two SPOT images.

Table 3.2: General characteristics of SPOT satellite data used

Data Set	Acquisition Date	Spatial Resolution	Spectral Range (µm)		
			Visible	NIR	IR
SPOT-2	19 January 1994	20 m	Band 1 (0.5-0.59) Band 2 (0.61-0.68)	Band 3 (0.79-0.89)	
SPOT-5	16 May 2004	10 m	Band 1 (0.5-0.59) Band 2 (0.61-0.68)	Band 3 (0.79-0.89)	Band 4 (1.58-1.75)

NIR= near infra-red, IR= infra-red

Both satellite images are recorded, processed, and stored with 11-bit quantification by SPOT Image. Radiometric calibrations and geometric corrections are applied using 1:50,000 Israeli topographic maps, and georeferenced to the Palestinian National Grid Projection (PalGrid).

SPOT images are used in order to take advantage of the high spatial resolution for the available dates in the study area as they provided more spatial details and longer time series than the other available data sets available free of charge such as MODIS (which was launched in 1999).

3.4 MODIS Data

The Moderate Resolution Imaging Spectroradiometer (MODIS) is a key instrument operating on both Terra (EOS AM) and Aqua (EOS PM) spacecraft. The Terra satellite transmits data from all 36 MODIS bands to the ground, while Aqua only transmits bands 20 through 36. The Terra space craft was launched in December 1999. Its orbit around the Earth is timed so that it passes from north to south across the equator in the morning, while Aqua passes south to north over the equator in the afternoon. Terra MODIS and Aqua MODIS have a viewing swath width of 2330 km and view the entire surface of Earth every 1 to 2 days, acquiring data in 36 spectral bands, or groups of wavelengths (see Table 3.1). Level 1B data consists of three products files and one on-board calibrator (OBC) product file:

- **MODIS Level 1B 250M Earth View Data Product:** contains calibrated Earth View observations for MODIS bands 1 and 2, at 250 m resolution;
- **MODIS Level 1B 500M Earth View Data Product:** contains calibrated Earth View observations from MODIS bands 3 through 7, at 500 m resolution. In addition, data from MODIS bands 1 and 2 are each aggregated to appear at the 500 m resolution; and
- **MODIS Level 1B 1KM Earth View Data Product:** contains calibrated Earth View observations from MODIS bands 8 through 36, at 1 km resolution in scientific units. It also contains calibrated data from MODIS bands 1 through 7, each aggregated to appear at the 1 km resolution.

3.4.1 MODIS Level 3 (8-day) Products

The high level cloud free MODIS Land products distributed from LP DAAC are produced at various temporal resolutions, based on the instruments' orbital cycle. These time steps are possible in the generation of MODIS Land products: daily, 8-day, 16-day, monthly, quarterly, and yearly. Details of all MODIS products may be found using the

link (https://lpdaac.usgs.gov/lpdaac/products/modis_products_table). In this research, the Surface Reflectance 8-Day level 3 (L3) Global 250 m (MYD09Q1) and Land Surface Temperature and Emissivity 8-Day L3 Global 1 km (MYD11A2), version 5, are chosen. Daily and 8-day temporal resolutions are the only two available temporal resolutions available for the surface reflectance bands products, therefore, the 8-day products are used due to time limit for this research. While for the land surface temperature and emissivity, 5-min, daily, 8-day, and monthly are available. For temporal resolution consistency the 8-day product has been chosen given the fact that it consists of the highest spatial resolution of the four products as shown in Table 3.3.

Table 3.3: Reflectance and land surface temperature and emissivity MODIS products

MODIS Product	Short name	Resolution (m)	Temporal Granularity
Surface Reflectance Bands 1-7	MOD09A1	500 m	8 Day
Surface Reflectance Bands 1-7	MOD09CMG	5600 m	Daily
Surface Reflectance Bands 1-7	MOD09GA	500/1000 m	Daily
Surface Reflectance Bands 1-2	MOD09GQ	250 m	Daily
Surface Reflectance Bands 1-2	MOD09Q1	250 m	8 Day
Land Surface Temperature & Emissivity	MYD11 L2	1000 m	5-min
Land Surface Temperature & Emissivity	MOD11A1	1000 m	Daily
Land Surface Temperature & Emissivity	MOD11A2	1000 m	8 Day
Land Surface Temperature & Emissivity	MOD11B1	6000 m	Daily
Land Surface Temperature & Emissivity	MYD11C1	5600 m	Daily
Land Surface Temperature & Emissivity	MYD11C2	5600 m	8-Day
Land Surface Temperature & Emissivity	MYD11C3	5600 m	Monthly

Source: (https://lpdaac.usgs.gov/lpdaac/products/modis_products_table)

It is to be noted that level 1B (L1B) is a swath (scene) of MODIS data geolocated to latitude and longitude centres of 1 km resolution pixels. A level 2 (L2) product is a geophysical product that remains in latitude and longitude orientation; it has not been temporally or spatially manipulated. A level 3 (L3) product is a geophysical product that has been temporally and or spatially manipulated, and is usually in a gridded map

projection format referred to as tiles. Each tile is a piece, e.g., about 1113 km by 1113 km in 1200 rows by 1200 columns, of a map projection.

Data and products have been downloaded using the Warehouse Inventory Search Tool (WIST) where data sets are chosen based on the geographical area of interest and time range as shown in Figure 3.2 below.

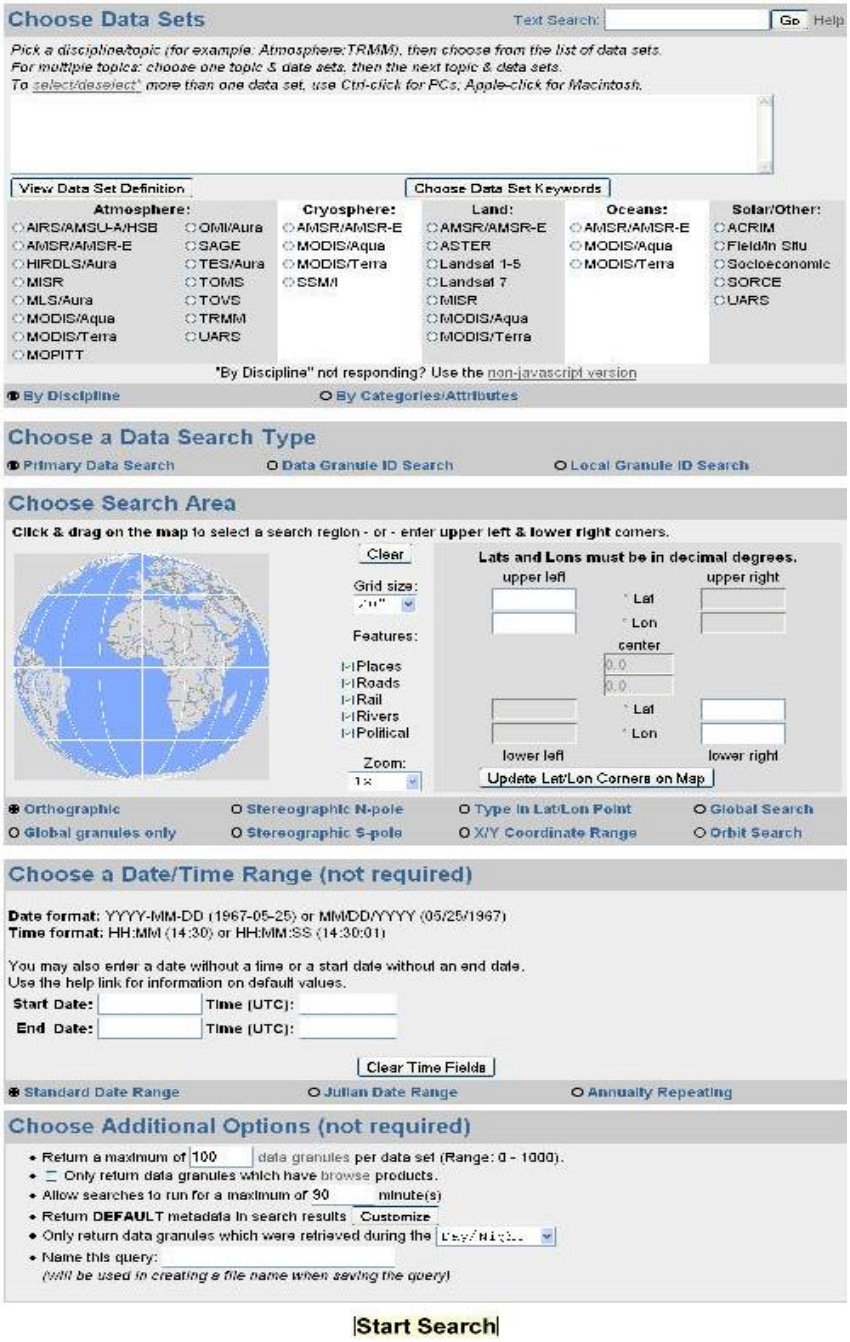

Figure 3.2: NASA Warehouse Inventory Search Tool (WIST)

3.5 Landsat TM5 Data

Thematic Mapper (TM) data, the sensor on board the Landsat TM5 satellite, is one of the most used for environmental studies. TM comprises seven bands, six of them in the visible and near infrared, and only one band located in the thermal infrared region (Table 3.1). Band 1 (with central wavelength of 0.49 µm) in TM1 is used for coastal water studies, TM2 (0.56 µm) is used for crops identification and vegetation stage studies, TM3 and TM4 (0.66 and 0.83 µm, respectively) are used to calculate vegetation indexes, as the Normalized Difference Vegetation Index (NDVI), TM5 and TM7 (1.65 and 2.22 µm, respectively) can be used for clouds, ice, snow and geological formations discrimination, and finally band TM6 (with an effective wavelength of 11.457 µm) is used for Land Surface Temperature (LST) retrieval.

3.5.1 Processing Landsat TM5 Data

The USGS Global Visualization Viewer (http://glovis.usgs.gov/) managed by the Center for Earth Resources Observation and Science (EROS) constitutes the main browser for ordering Landsat TM5 data. For this research, a single cloud free Landsat TM5 scene is used to validate SEBAL results obtained from MODIS images (Figure 3.3 and Table 3.4).

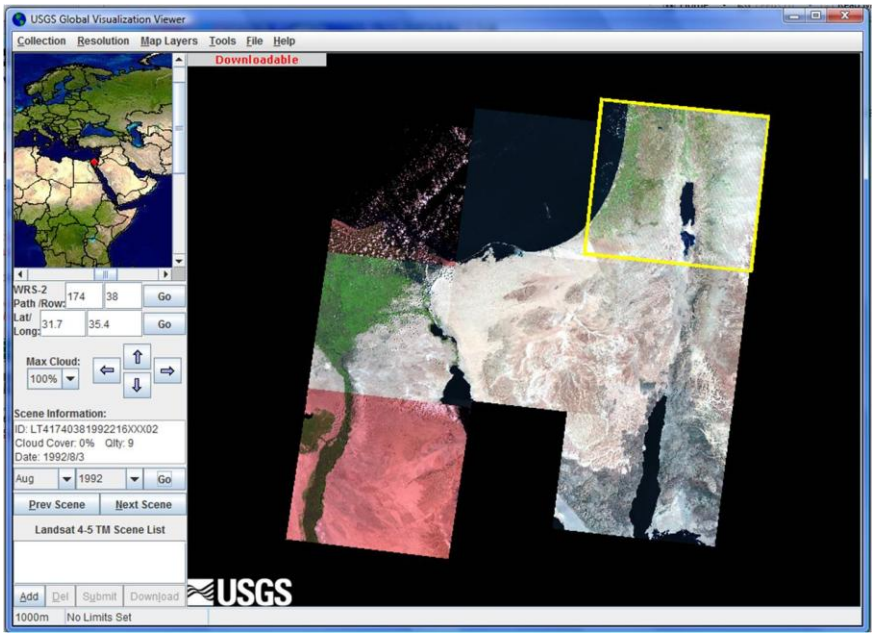

Figure 3.3: USGS Global Visualization Viewer (GLOVIS)

Table 3.4: Landsat TM5 image used

Parameter	Landsat TM5
Date of image acquisition	26/08/2003
% Cloud cover	0%
Path	174
Row	38
Central coordinates	Lat 31.742°N; Long 35.388°W

3.6 ASTER GDEM Data

The Advanced Spaceborne Thermal Emission and Reflection Radiometer (ASTER) Global Digital Elevation Model (GDEM) is developed jointly by the Ministry of Economy, Trade, and Industry (METI) of Japan and the United States National Aeronautics and Space Administration (NASA). The ASTER GDEM is contributed by METI and NASA to the Global Earth Observation System of Systems (GEOSS) and is available at no charge to users via electronic download from the Earth Remote Sensing Data Analysis Center (ERSDAC) of Japan and NASA's Land Processes Distributed Active Archive Center (LP DAAC).

The ASTER instrument is built by METI and launched onboard NASA's Terra spacecraft in December 1999. It has an along-track stereoscopic capability using its near infrared spectral band and its nadir-viewing and backward-viewing telescopes to acquire stereo image data with a base-to-height ratio of 0.6. The spatial resolution is 15 m in the horizontal plane. One nadir-looking ASTER visible and near-infrared (VNIR) scene consists of 4100 samples by 4200 lines, corresponding to about 60 km × 60 km ground area.

The methodology used to produce the ASTER GDEM involved automated processing of the entire 1.5-million-scene ASTER archive, including stereo-correlation to produce 1,264,118 individual scene-based ASTER DEMs. Cloud masking is applied to remove cloudy pixels, stacking all cloud-screened DEMs, removing residual values and outliers, averaging selected data to create final pixel values, and then correcting residual anomalies before partitioning the data into 1° × 1° tiles. It took approximately one year to complete production of the beta version of the ASTER GDEM using a fully automated approach. Version 1 differs only slightly from the beta version, with the most

significant difference being that elevation anomalies caused by residual clouds have been replaced with -9999 values for those anomalous values detected on the Eurasian continent north of 60° north latitude. ASTER GDEM tiles are available from LP DAAC website or from the Earth Remote Sensing Data Analysis Center (ERSDAC) (http://www.gdem.aster.ersdac.or.jp/search.jsp) by either selecting tiles directly, or by polygon, shapefile, or coordinates as shown in Figure 3.4.

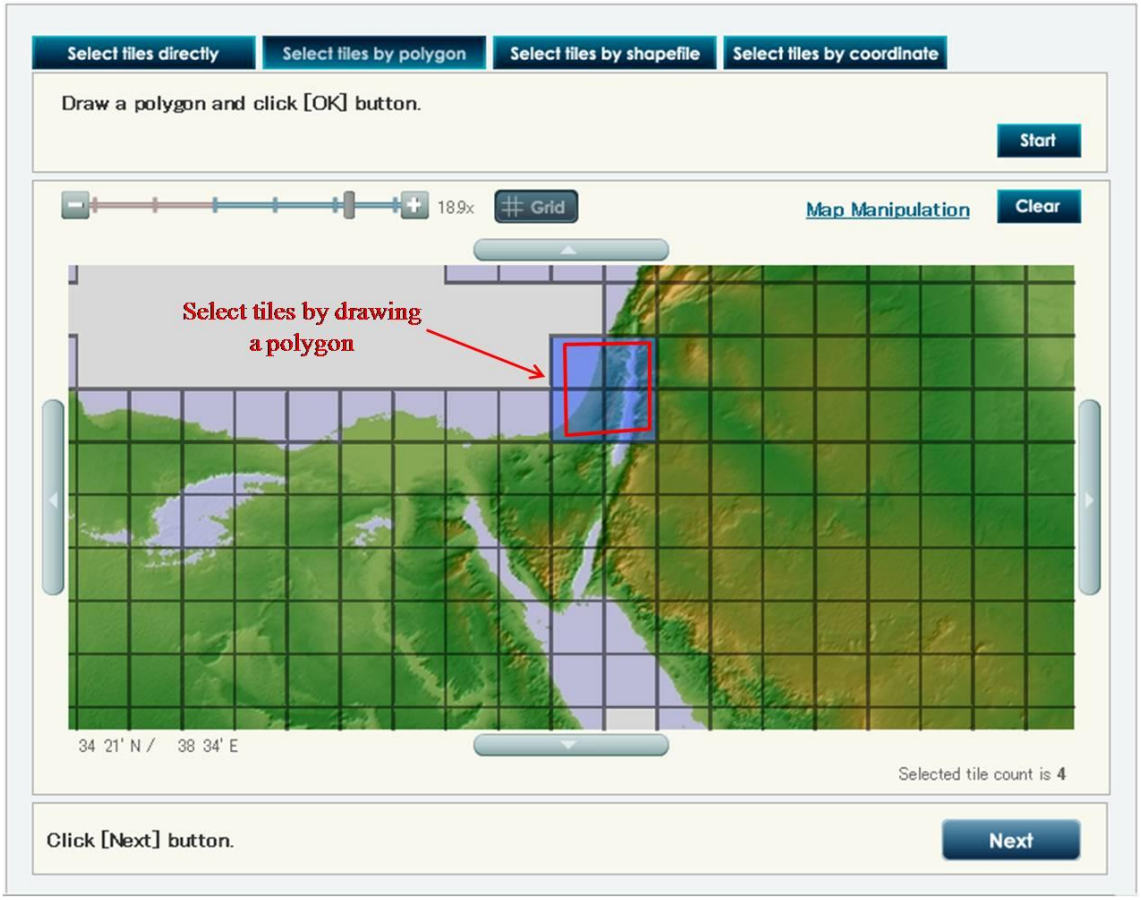

Figure 3.4: ASTER GDEM tile selection

3.6.1 ASTER GDEM Characteristics

The ASTER GDEM covers land surfaces between 83°N and 83°S and comprises of 22,600 1° × 1° tiles. Tiles that contain at least 0.01% land area are included. The ASTER GDEM is in GeoTIFF format with geographical lat/long coordinates and a 1 arc-second (approximately 30 m) grid at no charge. Table 3.5 summarizes the basic characteristics of the ASTER GDEM. Pre-production estimated accuracies for this

global product were 20 m at 95 % confidence for vertical data and 30 m at 95 % confidence for horizontal data.

Table 3.5: ASTER GDEM Characteristics

Tile Size	3601×3601 (1°-by-1°)
Posting interval	1 arc-second
Geographic coordinates	Geographic latitude and longitude
DEM output format	GeoTIFF, signed 16 bits, and 1m/DN Referenced to the WGS84/EGM96 geoid
Special DN values	-9999 for void pixels, and 0 for sea water body
Coverage	North 83° to south 83°, 22,600 tiles for Version 1

Table 3.6 provides a comparison between ASTER GDEM and other available DEMs.

Table 3.6: Comparison of ASTER GDEM with other DEMs

	ASTER GDEM	SRTM[1]	GTOP[2]	10m mesh digital elevation data
Data Source	ASTER	Space shuttle radar	From organizations around the world that have DEM data	1:25,000 topographic map
Generation and distribution	METI/NASA	NASA/USGS	USGS	GSI
Release year	2009	2003	1996	2008
Data acquisition period	2000-ongoing	11 days (in 2000)		
Posting interval	30 m	90 m	1000 m	About 10 m
DEM accuracy (stdev.)	7-14 m	10 m	30 m	5 m
DEM coverage	83° N- 83°S	60° N- 56° S	Global	Japan only
Area of missing data	Areas with no ASTER data due to constant cloud cover (supplied by other DEM)	Topographically steep area (due to radar characteristics)	None	None

Other examples of available DEM: NED with a resolution of 30 m, covering the entire USA provided by USGS, CDED covering all Canada territories, and Alaska DEM covering all Alaska.
[1]SRTM: Shuttle Radar Topography Mission Data at 3 Arc-Seconds
[2]GTOP: Global 30 Arc-Second Elevation Data Set
Source: http://www.ersdac.or.jp/GDEM/E/2.html

3.6.2 Geo-referencing ASTER GDEM

The raw ASTER GDEM tiles are downloaded from the ERSDAC website; 4 tiles are selected based on the spatial extent of the West Bank. ASTER GDEM tiles are provided in GeoTIFF format that are geometrically corrected to the WGS84/EGM96 geoid and are directly readable using ArcGIS software. However, image geo-referencing to the local Palestinian Grid map coordinates is necessary in order to integrate with other available raster and vector files. This has been done using ArcGIS/Info where local projection has been imported directly to the image and then saved. The four projected images have been mosaiced using ArcGIS/Info mosaic tool as shown in Figure 3.5.

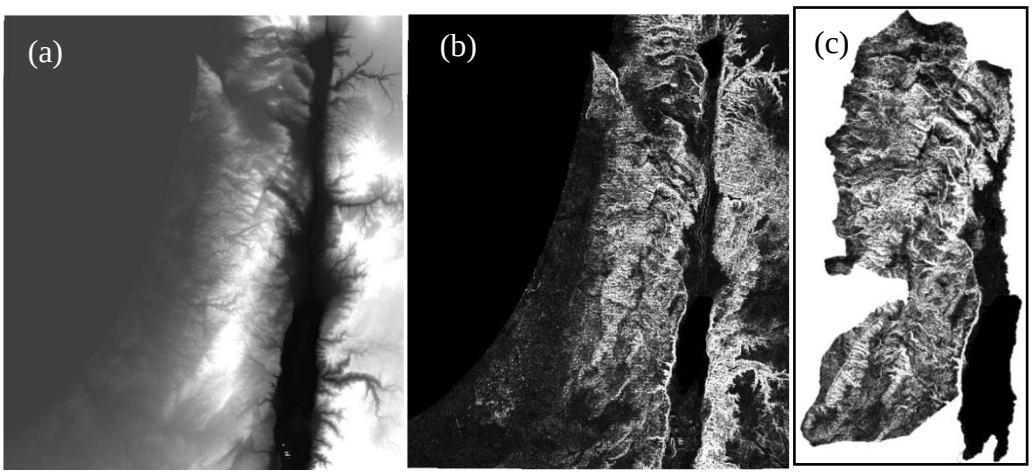

Figure 3.5: (a) Mosaic of 4 ASTER GDEM granules, (b) Slope map, (c) study area clipped out

3.6.3 Slope Map Generation

The ESRI ArcInfo software is used for digital elevation model generation and spatial modelling. Its Spatial Analyst-Surface Analysis-Slope tool is employed to automatically derive a slope map of the study area. Figure 3.5 (b) and (c) shows the end product of the slope map and the clipped area. Slope map is used as an input for recharge mapping modelling.

Initial studies done by NASA and METI in cooperation with the U.S. Geological Survey (USGS), ERSDAC, and other collaborators, to validate and characterize the ASTER GDEM confirm that pre-production accuracy estimates are generally achieved for most of the global land surface, although results vary and true accuracies do not

meet pre-production estimates for some areas. In addition, Version 1 of the ASTER GDEM does contain certain residual anomalies and artifacts that affect the accuracy of the product and may be impediments to effective utilization for certain applications. Consequently, METI and NASA acknowledge that Version 1 of the ASTER GDEM should be viewed as “experimental” or “research grade.” Nevertheless, ASTER GDEM represents an important contribution to the global earth observation community.

3.7 TRMM Data

The Tropical Rainfall Measuring Mission (TRMM) launched on November 27, 1997 as a joint project between the National Aeronautics and Space Administration (NASA) and the National Space Development Agency (NASDA) of Japan as part of the Earth Observing System (EOS). TRMM provides global (50° N- 50° S) data on rainfall where both active and passive microwave instruments are used at low inclination orbit of 35°. The primary TRMM instruments are the Precipitation Radar (PR), the first and only rain radar in space, and the TRMM Microwave Imager (TMI), a multi-channel passive microwave radiometer, which complements the PR by providing total hydrometeor (liquid and ice) content within precipitating systems. The Visible Infrared Scanner (VIRS) is used to provide the cloud context of the precipitation structures and is used as part of a transfer strategy to connect microwave precipitation information to infrared-based precipitation estimates from geosynchronous satellites. Estimates are provided at relatively fine scales 0.25°x 0.25°, and 3-hourly footprint until present. Table 3.7 lists the gridded TRMM data products from VIRS, TMI, and PR.

Table 3.7: TRMM gridded data products

Data Set	Description	Date Range
3A11: Monthly 5°×5° Oceanic Rainfall	Rain rate, conditional rain rate, rain frequency, and freezing height for a latitude band from 40° N to 40° S, from TMI	01-12-1997 to 01-10-2009
3A12: Monthly 0.5° x 0.5° mean 2A12, profile, and surface rainfall	0.5° x 0.5° gridded monthly product comprised of mean 2A12 data and calculated vertical hydrometeor profiles as well as mean surface rainfall	01-12-1997 to 01-10-2009
3A25: Monthly 5°x5° and 5°x5° Spaceborne Radar Rainfall	Total and conditional rain rate, radar reflectivity, path-integrated attenuation at 2, 4, 6, 10, 15 km for convective and stratiform rain; storm, freezing, and bright band heights, and snow-ice layer depth for a latitude band from 40° N to 40° S, from PR	01-12-1997 to 01-06-2009
3A26: Monthly 5° x 5° Surface Rain Total	Rain rate probability distribution at surface, 2 km, and 4 km for a latitude band from 40° N to 40° S, from PR	01-12-1997 to 01-06-2009
3A46: Monthly 1° x 1° SSM/I Rain	Global rain rate from SSM/I	01-01-1998 to 01-09-2009
3B31: Monthly 5° x 5° Combined Rainfall	Rain rate, cloud liquid water, rain water, cloud ice, grauples at 14 levels for a latitude band from 40° N to 40° S, from PR and TMI	01-12-1997 to 01-06-2009
3B42: 3-Hour 0.25° x 0.25° merged TRMM and other satellite estimates	Calibrated IR merged with TRMM and other satellite data	31-12-1997 to 31-05-2009
3B43: Monthly 0.25° x 0.25° merged TRMM and other sources estimates	Merged 3B-42 and rain gauge estimates	01-01-1998 to 01-06-2009
CSH: Monthly 0.5° x 0.5° Convective/Stratiform Heating	TRMM Monthly 0.5° x 0.5° Convective/Stratiform Heating	01-12-1997 to 01-06-2009
TRMM_3B42_daily.006	Daily TRMM and Others Rainfall Estimate (3B42 V6 derived)	31-12-1997 to 31-05-2009

Source: http://mirador.gsfc.nasa.gov/

Twelve monthly merged TRMM and other sources data (3B43.v6) at 0.25° × 0.25° are used for estimating monthly precipitation rate. The 3B43 algorithm combines four independent precipitation fields: (1) the monthly average unclipped TRMM Microwave Imager (TMI) estimate (intermediate product from Algorithm 3B42); (2) the monthly average Special Sensor Microwave/Imager (SSM/I) estimate (TRMM product 3A46); (3) the pentad-average adjusted merged-infrared (IR) estimate (TRMM product 3B42); and (4) the monthly accumulated Climate Assessment and Monitoring System (CAMS) or Global Precipitation Climatology Centre (GPCC) rain gauge analysis (TRMM product 3A45). All input data have a calendar month temporal resolution except the adjusted merged-IR data, which have a daily resolution. The data are stored in the Hierarchical Data Format (HDF), which includes both core and product specific metadata.

Several studies have employed TRMM data to estimate rainfall and precipitation, e.g. Huffman *et al*., 2008, Berg *et al*., 2006, Liu and Zipser 2005, Chen *et al*., 2006, Masunaga *et al*., 2006, Petersen *et al*., 2005, Lin *et al*., 2006, Yamamoto *et al*., 2006, Dai 2006, Tran *et al*., 2005, and Olson *et al*., 2006. A recent study was carried out in the Sinai Peninsula that used TRMM 3B42 (3 hour, 0.25°×0.25° footprint) to extract, identify, and verify precipitation events throughout the last ten years (Milewski *et al*., 2009). A correspondence of R^2= 0.92 is evaluated between precipitation derived and an eight rain gauge data set. TRMM sensor has the tendency to misidentify precipitation (Bauer *et al*., 2002) giving a false indication for light rainfall (<0.5 mm hr^{-1}) (Turk *et al*., 2003). Since TRMM measurements are acquired every three hours, short events starting and ending in between two consecutive TRMM acquisitions can go undetected (Milewski *et al*., 2009). Comparisons conducted by Chiu *et al*., (2006) of TRMM retrievals with rain gauge rates over New Mexico show high bias for satellite only algorithms. Merged satellite-gauge products such as the 3B43 are found to be better correlated with gauge data (Nair *et al*., 2009). Adeyewa and Nakamura (2003) have validated TRMM 3B43 and Precipitation Radar (PR) with the GPCC global precipitation over the major climatic regions of Africa. Significant seasonal and regional differences have been observed and a conclusion is drawn indicating that the best agreements are achieved with TRMM 3B43 data. Similar results are obtained by Nicholson *et al*., (2003) where a comparison is conducted over West Africa to evaluate

TRMM (3B43, PR, and TMI) rainfall products for the year 1998. TRMM 3B43 merged product has shown excellent agreement with gauge measurements on monthly to seasonally timescales. Chokngamwong and Chiu (2005) have compared TRMM level 3 rainfall products (TRMM 3B42 and 3B43 for V5 and V6) with gauge data from more than 100 rain gauges over Thailand. Their results indicate that 3B42- V6 data correlates best with the gauge data. Validation of TRMM merged rainfall products level 3 with gauge data have also been done over the Indian sub-continent by Narayanan *et al*., (2005). They have validated 3B42-V5 data with India Meteorological Department (IMD) rain gauge data. Their main finding is that the satellite algorithm does not pick up very high and very low daily average rainfalls. Rahman and Sengupta (2007) have compared the Global Precipitation Climate Project (GPCP) with 3B42-V5 and 3B42-V6 rainfall products with IMD daily rainfall for the monsoon season (June to September). Their results indicate that the spatial patterns of 3B42-V6 data shows closest agreement with observed patterns of IMD gauge data except over certain places like the Himalayan foothills and parts of east central India.

The 3B43 data set is accessed at no charge through the TRMM Online Visualization and Analysis System (TOVAS) that is created and supported by the Goddard Earth Sciences Data and Information Services Center (GES DISC). It provides a web-based resource for accessing several other data sets, performing basic subsetting, time- and space-averaging, and output of results in plots or ASCII text. The TOVAS URL is http://disc2.nascom.nasa.gov/Giovanni/tovas/.

3.7.1 Geo-Referencing TRMM

TRMM data are provided in HDF format and in order to view and read the image arrays, data are simply imported into MATLAB software. Data are then re-projected to the common local Palestinian grid before proceeding with the post-processing steps of analysis along with the ET derived maps and recharge inputs. The following steps are carried out to re-project TRMM data:

Step1: ASCII text files created along with the subset images are downloaded with the datasets. These files contain the selected time period, latitude and longitude for the selected area in addition to the latitude, longitude, and precipitation (mm hr^{-1}) for each

pixel. These data are modified for reprojection where latitudes and longitudes are converted to the false eastings and northings of the local Palestinian grid to allow automatic batch geo-referencing of the images.

It must be noted that the grid origin of TRMM images is at the southwest corner of the grid. Longitude indices begin at 180° W and end at 180° E. Latitude indices begin at the southern extreme and end at the northern extreme of the grid.

Step 2: using MATLAB commands, the TRMM raster is converted to a 8-bit, e.g. '*precipitation_jan=uint8(precipitation);*' where *precipitation_jan* is the **output** raster and *precipitation* is the **input** file. It is essential that the numbers in the MATLAB raster are integers in order to carry out the proceeding steps.

Step 3: the 8-bit output file is saved as 'tiff' file using the MATLAB command '*imwrite'*, e.g. *'imwrite(precipitation_jan,'precipitation_january','tiff'* where the second and first parts of the command are the **output** and **input** files. Note that the output name and format are string values and therefore should be written in quotations.

Step 4: in ERDAS, the TRMM output image is opened and a single band is exported as 'tiff' file. This may be done using the option *'save top layer as'* under the file command.

Step 5: open the output tiff file in ArcGIS/Info. Upload the ASCII text file and apply geo-referencing.

Step 6: the output geo-referenced file was exported with the attention given to output file format whether it is saved as an image or tiff, and the cell size as shown in Figure 3.6.

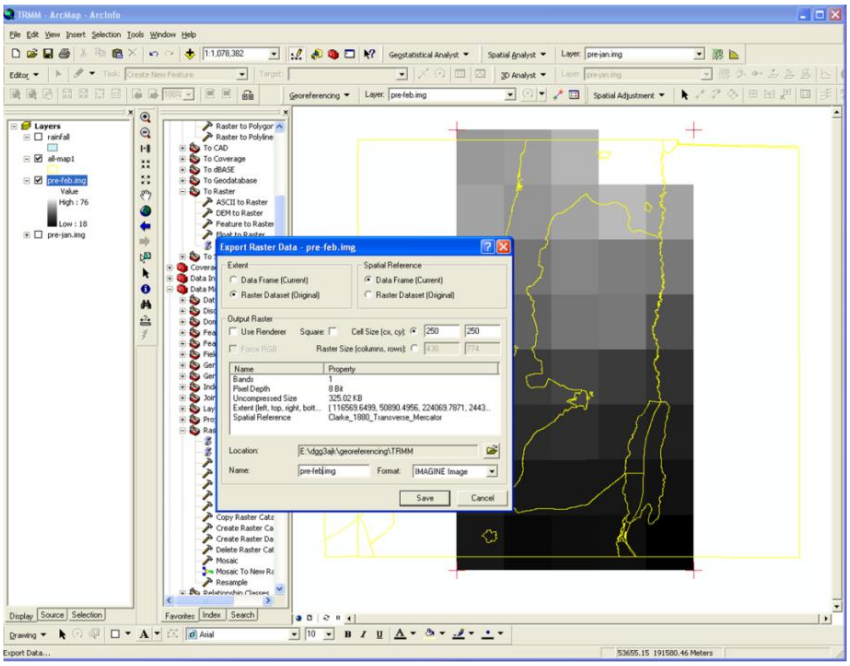

Figure 3.6: Exporting geo-referenced images using ArcGIS/Info

3.8 Methodological Framework

Estimating seasonal actual recharge for the West Bank includes several components. The first component includes the use of different satellite imageries to derive recharge parameters such as evapotranspiration and precipitation. A second component is using a GIS based model to map and identify the actual recharge areas where a combination of soil types, land cover, geology, slope, evapotranspiration, precipitation, and geology is used. The final component includes the water balance method to assign an estimate of actual recharge. The methodology adopted in the present study is presented schematically in Figure 3.1 and described in the following steps:

I. In the initial stage, field meteorological data including air temperature, humidity, and evaporation are collected as inputs for SEBAL model and validation. Spatial GIS data such as soil type and geology are collected from the Ministry of Agriculture to be used as inputs for recharge mapping along with the remotely sensed derived parameters such as precipitation, evapotranspiration, DEM, land cover, and drainage (Chapter 8). Moreover, a land cover survey covering parts of the study area for image classification (shown as the red dotted areas in Figure 3.7) is completed.

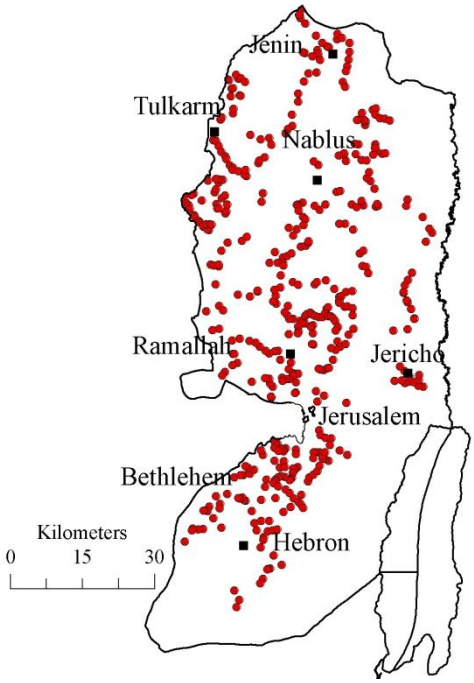

Figure 3.7: Sites covered for land cover detection

II. In the second stage, digital image processing of the satellite imagery are carried out for extraction of monthly data.

- SPOT-2 and SPOT-5 data are classified using supervised classification technique to derive land cover maps (Chapter 6). The original extent of the land cover in 1994 is compared with the changes that have occurred in 2004 to compute an overall change pattern and study its impact on recharge rates in a sensitivity analysis described in Chapter 8. SPOT images are selected for their high spatial resolution and availability from the Ministry of Planning.
- Raw MODIS Level 1B and Level 3 and Landsat TM5 images are downloaded and calibrated using calibration constants provided by the attached header files. These constants are applied to reflectance bands (bands 1 and 2 for MODIS Level 1B and 1-5 and 7 for Landsat TM5) and radiance bands (bands 31 and 32 for MODIS Level 1B and band 6 for Landsat TM5) as described in Chapter 4. Calibrated bands are employed to obtain brightness temperature at the top of the atmosphere that is converted to surface temperatures for SEBAL application and analysis.

MODIS Level 3 products include calibrated surface temperature and emissivity and reflectance bands.

The dependency of evapotranspiration rates on surface temperature makes satellites such as MODIS and Landsat TM5 with thermal bands well suited for ET mapping. Other satellite sensors such as Advanced Along-Track Scanning Radiometer (AATSR) or NOAA Advanced Very High Resolution Radiometer (AVHRR) can be considered suitable sources of land surface information and evapotranspiration derivation. All these products are radiometrically and geometrically calibrated and are applicable to the hydrological model proposed. However, the main reason for choosing MODIS is its daily temporal resolution. In addition, it has been selected along with Landsat TM5 for the ease of their application with SEBAL and the availability of algorithms for retrieving evapotranspiration parameters. MODIS has also been chosen for its constituency of narrower spectral bands at the visible and near infrared than AVHRR or NOAA which enhances the discrimination of vegetation properties. Also MODIS sensor has a higher radiometric resolution than any other high temporal resolution imagery where 16 bits of quantization is used for all its bands. On the other hand, Landsat TM5 is used as a source of MODIS validation on a single date for its high spatial resolution.

- Surface Energy Balance Algorithm for Land (SEBAL) is applied to produce monthly evapotranspiration maps. The SEBAL model calculates ET (or the latent heat flux, λE) for each image pixel from the energy balance equation:

$$\lambda E = Rn - G - H \ (Wm^{-2}) \qquad (3.1)$$

where Rn is the net radiation (W m^{-2}), G the soil heat flux (W m^{-2}) and H is the sensible heat flux (W m^{-2}). Instantaneous net radiation (Rn) values in the applied SEBAL method are derived from incoming global radiation and spatially variable reflectances and emittance of radiation.

Other operational algorithms that have produced evaporation maps on local, regional, or national scales are: the North American land data assimilation systems (NLDAS) (Cosgrove *et al*., 2003), the land information systems (LIS) (Peters Lidard *et al*., 2004), the atmosphere–land exchange inverse (ALEXI) (Anderson *et al*., 1997; Norman *et al*., 2003), the disaggregated ALEXI model (DisALEXI) (Norman *et al*., 2003), the surface energy balance system (SEBS) (Han and Yang, 2004; Jia *et al*., 2003; Su, 2002), the surface energy balance algorithm for land (SEBAL) (Bastiaanssen *et al*., 1998 a&b), mapping evapotranspiration at high spatial resolution with internalized calibration (METRIC) (Allen *et al*., 2007 a&b), as well as algorithms without distinct acronym (Jiang and Islam, 2001; Ma *et al*., 2004; Ma *et al*., 2006; Schuttemeyer *et al*., 2007).

SEBAL and METRIC calculate the energy balance using extreme thermal and vegetation conditions within an image using a ‘‘cold’’ and ‘‘hot’’ pixel. These procedures index sensible heat flux from the land surface (one of the major energy balance components) to satellite measured surface temperatures at specific surface boundary conditions. The main difference between SEBAL and METRIC is that the latter makes use of the reference evapotranspiration (ET) calculated using high-quality ground measurements from weather stations (Allen *et al*., 1998) while the former can be applied without using ground measurements. Since many areas of the world have no adequate ground measurements there is a need for algorithms such as SEBAL, while METRIC allows assimilation of ground measurements which can improve the quality of the evaporation maps.

SEBAL has been selected to estimate evaporation distributions in the West Bank for the following reasons:

(1) SEBAL consists of physically-based image analysis algorithms using standard satellites imagery and requires a minimum of ancillary

meteorological information from surface measurements or atmospheric models;

(2) SEBAL deals with a large number of environmental variables and does not assume variables to be constant over space as do many other methods. For example, some methods assume all variables besides surface and air temperatures to be spatially constant (Jackson *et al*., 1996; Seguin and Itier, 1983);

(3) In SEBAL the need for atmospheric correction of shortwave and thermal information in images is reduced (Tasumi, 2003), since SEBAL evaporation estimates depend only on radiometric temperature differences in the scene rather than on the absolute value of the surface temperature. This greatly enhances the applicability of SEBAL since the measurements needed for atmospheric corrections are often not available (Allen *et al*., 2007a); and

(4) SEBAL is not only used with Landsat TM5 images at spatial scales of 30 m (and 120 m for thermal bands) but also with other medium and low spatial resolution data sets such as AVHRR and MODIS images at spatial scales of 250–1000 m (Bastiaanssen *et al*., 2002b; Hafeez *et al*., 2006; Hong *et al*., 2005).

- Monthly precipitation is derived from the Tropical Rainfall Measuring Mission (TRMM) and runoff is estimated as a percentage of these precipitation values in January and February. TRMM estimates are validated with monthly rain gauge measurements in six stations located in six different geographic regions and different precipitation regimes.
- ASTER GDEM was processed to derive a digital elevation model and slope map of the study area.

III. In the third stage, all the above themes are brought into ArcGIS/Info for further processing and analysis. Two folds of exercises are carried out: the first is calculating recharge using the water balance method. In this exercise, temporal remote sensing data including the 12 precipitation TRMM data, 12 derived

actual evapotranspiration, 2 runoff data are used to calculate monthly recharge for the year 2004. The second exercise is mapping its actual areas using the previously mentioned remote sensing datasets in addition to the other GIS data inputs such as land cover, slope, geology, drainage density, and soil type. It is to note that fractures, joints, and faults are not considered in recharge mapping exercise as data is unavailable. GIS spatial analysis technique is used to integrate the multiple layers of the above information determining area of high and low recharge.

IV. The fourth stage involved the validation of recharge results through the comparison of literature data and maps. Also, an analysis studying the impact of land cover change on recharge has been carried out.

3.9 Field Research

The derived remote sensing data should be accompanied and verified by ground truth data and observations about the areas of research. Such data may be either derived from maps such as soil maps or from other remotely sensed data such as aerial photographs. Data may also be obtained from field observations on land use or water tables and abstractions. Other data may include field measurements of temperature, rainfall, and evapotranspiration. These data were used in the research to aid in the analysis and interpretation of the satellite imagery and verify the information extracted from them.

In this research, the field work included two parts: the first was collecting monthly meteorological data such as rainfall, air temperature, wind speed, and humidity from relevant institutions. The second part is surveying some of the West Bank areas for land cover classification where the land use maps available are not suitable for this research as they are based on office work with minor field validation. Therefore, a new land cover map of specific interests to this study is derived from SPOT images acquired in 1994 and 2004 as described in Chapter 6. The sites covered in this field search are shown in Figure 3.7.

Field work span extended to three months. Data collection was carried out in two weeks and the rest was spent on land cover investigation. Each governorate was surveyed within two days where a Global Positioning System (GPS) was used to locate the land

cover type scanned. A total of 1014 pictures were taken covering the eleven governorates. Restrictions on movement was the main cause for the lengthy field research where roads were blocked, access denied into governorates, or military forces imposed curfews and blockades. If such constrains were absent, surveying the main land cover types in each governorate would take one day only.

On related issue, not all the required and necessary field measurements were carried out to support the satellite images interpretation and validation. Various land, vegetation, and atmospheric parameters needed to be measured in field in order to either apply the energy and water balance approaches or validate measurement results from remote sensing imagery. Other temporal and quantitative measurements parameters such as net radiation, soil moisture, wind speed, air and surface temperature were not available due to limited access of movement and the presence of physical barriers imposed by the Israeli military forces. Moreover, in situ measurements of solar radiation, air and surface temperatures, relative humidity, and wind speed during satellite overpass were also not available which added more constraints to the application of the energy balance approach and calculating sensible heat flux.

3.10 Summary

The increasing usefulness and number of satellite sensors that are becoming available is providing unprecedented opportunities for new applications in various scientific disciplines. The utilization of these images is also presenting challenges for the scientific community as these large temporal satellite data sets often come in varying formats, are usually uncalibrated, and are not geo-referenced.

This chapter highlights some of these data sets and their processing methods. Further descriptions of these sensors and the algorithms used are provided in the following chapters, where the actual results obtained are also presented. Chapter four presents the detailed calculations and equations of SEBAL model used to derive evapotranspiration rates.

Chapter Four

Regional Scale Evapotranspiration Modelling using Remote Sensing and SEBAL Processing

4.1 Introduction

Evapotranspiration (ET) is probably the most crucial factor for assessing and understanding the water balance cycle. Its accurate determination reduces the uncertainties in the water balance of a basin providing water managers with information on water resources being consumed; a critical factor especially in arid regions where water is scarce and expensive. A large literature on potential and reference ET is available and various methods have been developed for the calculation of evapotranspiration from water surfaces such as scintillometers and Soil Water Atmosphere Plant (SWAP) model (Droogers, 2000). Nonetheless, these models are limited in relation to scale, cost, time, and the need for field work. Therefore, remote sensing is becoming another option for calculating the actual evapotranspiration based on the equilibrium between the radiation and the energy balance at the surface of the Earth where information on vegetation cover is minimal and often provided by satellite information. Although remote sensing cannot measure the surface flux directly, it can make indirect estimates based on temperature and land cover data derived from remote sesning through the application of algorithms and schemes. The energy balance approach determines the average rate of evapotranspiration over a selected time period, where the rate of energy input and output by various modes and changes in heat storage are determined.

Since the beginning of the 1990's, the most popular remote sensing algorithms in the retrieval of ET are based on surface energy balance, such as the SEBAL (Surface Energy Balance Algorithm for Land) (Bastiaanssen *et al*. 1998b) and SEBS (Surface Energy balance System) (Su, 2002; Han and Yang, 2004; Jia *et al*., 2003), both developed in the Netherlands. Operational algorithms that have produced evaporation maps on local, regional, or national scales are: the North American land data assimilation systems (NLDAS) (Cosgrove *et al*., 2003), the land information systems

(LIS) (Peters Lidard *et al*., 2004), the atmosphere–land exchange inverse (ALEXI) (Anderson *et al*., 1997; Norman *et al*., 2003), the disaggregated ALEXI model (DisALEXI) (Norman *et al*., 2003), mapping evapotranspiration at high spatial resolution with internalized calibration (METRIC) (Allen *et al*., 2007a,b), as well as algorithms without distinct acronym (Jiang and Islam, 2001; Ma *et al*., 2005, 2006; Schu¨ttemeyer *et al*., 2007).

The Surface Energy Algorithm for Land (SEBAL) developed by Bastiannssen *et al*., (1998a), modified by Tasumi *et al*., (2003), is one of the remote sensing-based land surface algorithms developed to assess the energy and moisture fluxes and enables the calculation of the actual evapotranspiration during the time of satellite over pass (Mekonnen, 2005; Chmin *et al*., 2000). SEBAL uses the surface temperature, hemispherical surface reflectance, and Normalized Difference Vegetation Index (NDVI), to infer surface fluxes. It has been applied in a number of projects and studies and validated with large field experiments in Spain, Italy, Turkey, Pakistan, India, Sri Lanka, Niger, and China (Bastiaanssen *et al*., 1998 a&b; Bastiaanssen and Bos, 1999) and proved to be applicable with good results. One of the advantages of SEBAL is that it requires minimal data for calculating the pixel-based actual evapotranspiration (Mekonnen, 2005) and covers large areas (Bashir *et al*., 2008). It calculates both the instantaneous and 24-hour integrated surface heat fluxes. The data required is the visible, near infrared, and thermal infrared bands of satellite images along with ancillary meteorological data such as temperature and wind speed (Figure 4.1). Satellite radiances are converted into land surface characteristics such as surface albedo, leaf area index (LAI), and surface temperature. There are no data required on land use, soil type, or hydrological conditions to apply SEBAL.

In this research, SEBAL has been applied to two MODIS products: the first is MODIS Level 1B single day product and the second is MODIS Level 3 with a temporal granularity of 8 days. MODIS Level 3 (8-day) products are aggregated into monthly estimates and validated with the monthly aggregated single day MODIS Level 1B. Also SEBAL is applied to one Landsat TM5 acquired in August 2003 to validate MODIS sensor results of the same date.

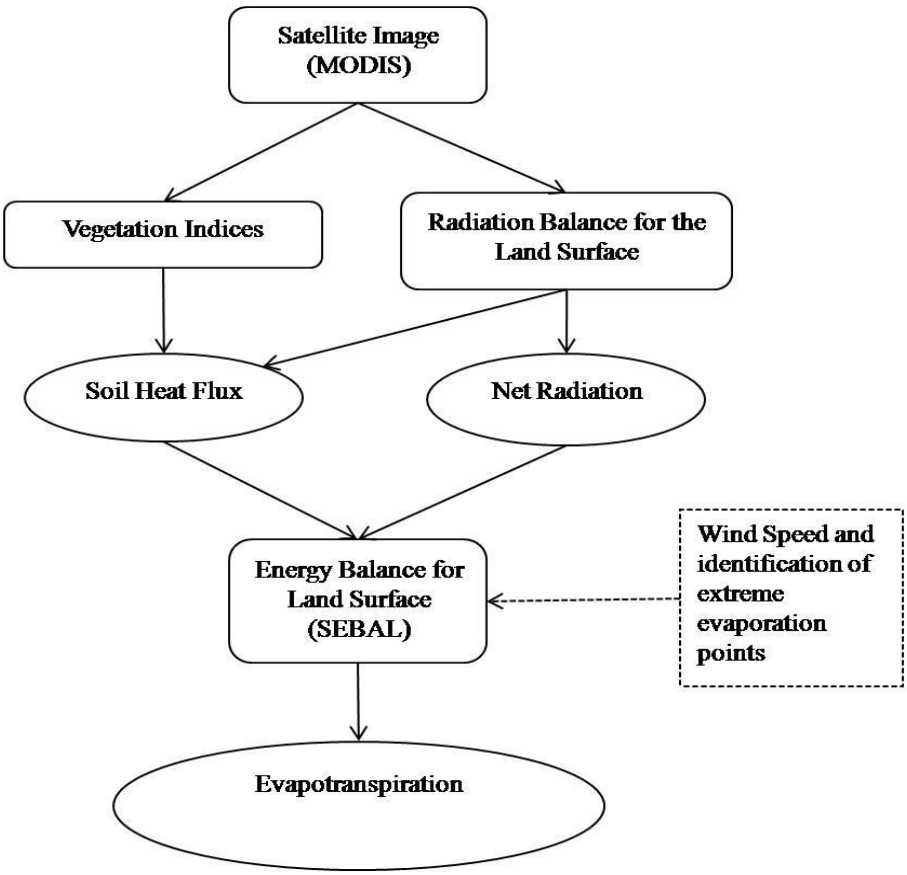

Figure 4.1: Schematic of the general computational process for determining evapotranspiration using SEBAL (Modified after Morse *et al*., 2000)

4.2 Steps and Equations in SEBAL Algorithm

SEBAL is an image-processing model comprised of more than 25 computational steps that calculates actual evapotranspiration as a residual term of surface energy balance at the time of satellite overpass (Figure 4.2).

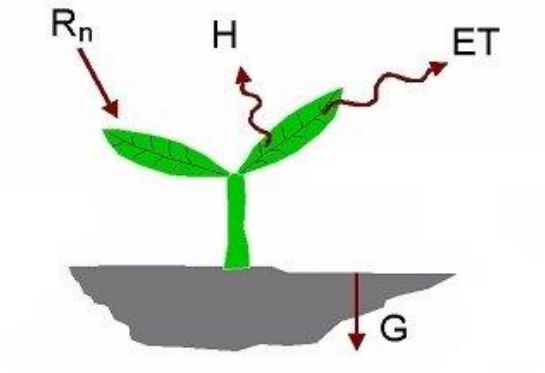

Figure 4.2: The main equation of SEBAL where ET is the latent energy of evaporation, Rn is the net radiation flux, G is the soil heat flux, and H is the sensible heat flux

$$ET = Rn - H - Go \tag{4.1}$$

where ET is the latent heat flux (evapotranspiration) associated with evaporation of water from soil and water from vegetation, Rn is the net radiation absorbed at the land surface, H is the sensible heat flux to warm or cool the atmosphere, and Go is the soil heat flux to warm or cool the soil, all expressed in (Wm^{-2}).

4.2.1 Net Radiation (Rn)

The net radiation is the amount of radiation left after all the outgoing radiations are subtracted from the incoming radiations. It is equal to the sum of the net shortwave as a function of the surface albedo and longwave radiation computed from the difference between incoming and outgoing longwave radiation.

$$Rn = K\downarrow (1 - \alpha) + (L\downarrow - L\uparrow) \tag{4.2}$$

where K↓ is short wave radiation (0.3-3μm) reaching the Earth surface, α is broad band surface albedo, and L↓ and L↑ are incoming and outgoing long wave radiation (3.0-100μm), respectively.

4.2.1.1 Instantaneous Short Wave Radiation (K↓)

The short wave radiation reaching the earth's surface under cloud free conditions is calculated by:

$$K\downarrow = \tau K\downarrow^{toa} \quad (4.3)$$

where τ is atmospheric transmissivity and K↓toa is the extraterrestrial solar radiation (Wm^{-2}). The extraterrestrial solar radiation on instantaneous time scale is calculated as:

$$K\downarrow^{toa} = GscEo(\sin\delta \sin\varphi + \cos\delta \cos\varphi \cos\omega) \quad (4.4)$$

where Gsc is the solar constant (1367 Wm^{-2}), Eo is the eccentricity correction factor, δ is solar declination, φ is latitude and ω is the hour angle (in radians). The derivation of these parameters, except for latitude which can be obtained from the images, is given in Table 4.1.

Registrations within spectral band of reflected radiation at the top of atmosphere (TOA) by operational Earth observation satellites are usually acquired from a single direction, therefore, corrections for atmospheric interference are based on detailed information on the state of the atmosphere such as temperature, humidity, and wind velocity at different altitudes extracted from the radiosoundings. Since the data are not available, the hemispherical surface reflectance, surface albedo (α), may be obtained from the broadband directional planetary reflectance (r_p) calculated as (Chen and Ohring, 1985):

$$\alpha = \frac{r_p - r_a}{\tau^2} \quad (4.5)$$

where r_p is the planetary reflectance, r_a is the fractional path radiance, and τ^2 is the two way transmittance for broad band solar radiation. Surface albedo of the darkest pixel such as deep seas, is assumed to equal zero. Therefore, if α=0, it follows from Equation 4.5 that r_a is equal to r_p of a deep sea or any other dark target.

Fractional path radiance (r_a) ranges between 0.025-0.04 and the error in estimating surface albedo from (r_p) is 0.04.

Tasumi (2003) have shown that for a known surface elevation (z), the one way transmission (τ) may be estimated using the following:

$$\tau = 0.75 + 2\times10^{-5} z \quad (4.6)$$

Assuming that the average elevation of the West Bank is 500 m, the two way transmittance (τ^2) is approximately, 0.5776.

Table 4.1 Determination of intermediate radiation balance parameters

Parameter	Symbol	Unit	Equation
1.	$K\uparrow^{toa}$	$Wm^{-2}\ sr^{-1}\ \mu m^{-1}$	$K\uparrow^{toa} = c12 + (c13 - c12)/255*DN$
2.	δ	Rad	$\delta = 0.409*\sin(0.0172*JD - 1.39)$
3.	$\omega_{(x)}$	Rad	$\omega_{(x)} = \pi\{t_{(x)} - 12\}/12$
4.	$t_{(x)}$	Decimal hours	$t_{(x)} = t + min/60 + lon12/\pi$
5.	ø	Rad	$Cos ø = \sin(\delta)/\{lat_{(y)}\} + \cos(\delta)\cos\{lat_{(y)}\}\cos\{\omega_{(x)}\}$
6.	d_s	AU	$d_s = 1 + 0.0167 \sin(2\pi (JD - 93.5))/365$
7.	Eo	Dimensionless	Average/Actual d_s
8.	$K_{\downarrow}toa$	Wm^{-2}	$K_{\downarrow}^{toa} = K\uparrow^{toa} Cos(ø)/d_2$ (varies with characteristics of radiometer)
9.	$K_{\downarrow}$	Wm^{-2}	$K_{\downarrow} = G_{SC} *\cos\theta*d_r*\tau$
10.	r_p	Dimensionless	$r_p = \pi K_{\downarrow}^{toa}/ K_{\downarrow}^{toa}$
11.	r_a	Dimensionless	$r_a = 0.025 - 0.04$
12.	$L_{\downarrow}$	Wm^{-2}	$L_{\downarrow} = \varepsilon_a*\sigma T_a^4$
13.	ε_o	Dimensionless	$\varepsilon_o = 1.009 + 0.047 \ln NDVI$
14.	$L\uparrow$	Wm^{-2}	$L\uparrow = \varepsilon_o*\sigma T_s^4$
15.	Rn	Wm^{-2}	$Rn = K_{\downarrow} (1-\alpha) + (L_{\downarrow} + L\uparrow)$

where

ci = Parameter number	
d_s = Earth-sun distance	Ta = air temperature
d_r = inverse Earth-sun distance	Ts = surface temperature
σ = Stefan-Boltzmann constant	t = local time
ø = sun zenith angle	δ = solar declination
JD = Julian day	$\omega_{(x)}$ = solar hour angle
r_a = atmospheric reflectance	$t_{(x)}$ = decimal hours
ε_o = surface emissivity	θ = solar zenith angle
ε_a = atmospheric emissivity	Eo = eccentricity factor
r_p = planetary reflectance	Lat/lon = latitude/longitude

Sources: Tasumi (2003); Bastiannssen *et al*., (1998); Iqbal (1983); Opoku-duah, (2007)

4.2.1.2 Instantaneous Incoming Long Wave Radiation (L↓)

The incoming long wave radiation is the downward thermal radiation flux from the atmosphere. It is calculated using the Stefan-Boltzmann equation:

$$L\downarrow = \varepsilon_a \sigma Ta^4 \qquad (4.7)$$

where ε_a is atmospheric emissivity (dimensionless), σ is Stefan-Boltzmann constant (5.67×10^{-8} $Wm^{-2}K^{-4}$), and Ta is the air temperature (K). ε_a is calculated based on the equation developed by Bastiannssen (1995):

$$\varepsilon_a = 0.85\ (-ln\tau) \tag{4.8}$$

4.2.1.3 Instantaneous Outgoing Long Wave Radiation (L↑)

The outgoing long wave radiation is the upward thermal radiation leaving the surface. It is calculated using Stefan-Boltzmann equation:

$$L\uparrow = \varepsilon_o \sigma Ts^4 \tag{4.9}$$

where ε_o is the surface emissivity, σ is Stefan-Boltzmann constant ($5.67\times10^{-8}Wm^{-2}K^{-4}$), and Ts is the surface temperature (K) which calculated from radiance of thermal bands using Plank's equation.

4.2.1.4 Surface Emissivity (ε_o)

Emissivity is the ratio of the energy radiated by an object at a given temperature to the energy radiated by a black body at the same temperature. Since the thermal radiation of the surface is observed in the thermal bands of satellite data, one can compute the surface temperature if the emissivity of the land surface is estimated. In SEBAL, surface emissivity is estimated using NDVI and an empirically-driven (van de Griend & Owe, 1993) method:

$$\varepsilon_o = 1.009 + 0.047\ ln(NDVI) \tag{4.10}$$

where NDVI >0; otherwise, emissivity is assumed to be zero (e.g. water). Equation 4.10 is restricted to measurements conducted in the range of NDVI=0.16-0.74. NDVI is calculated as a ratio of the difference in reflectance for the near infrared band (NIR) and the red band (R) to their sum as (Goetz, 1997):

$$NDVI = \frac{rNIR - rR}{rNIR + rR} \tag{4.11}$$

NDVI is calculated based on reflectance (r), instead of the brightness (DN) values of the original bands.

4.2.2 Soil Heat Flux (Go)

The soil heat flux is the rate of heat storage in the soil as a result of the temperature gradient between the soil surface and the underlying soil layers. The temperature gradient varies with the fractional vegetation cover and the leaf area index (LAI), as light interception from and shadow formation on the bare soil determine relative heating of the bare soil surface. Go can be measured using Equation 4.12 if the soil's thermal conductivity is known (see Figure 4.3):

$$Go = \lambda s \frac{\Delta T_S}{\Delta Z} \tag{4.12}$$

where λs is thermal conductivity of soil, ΔTs is temperature difference between T_o and T_1, and Δz is the depth difference between z_o and z_1.

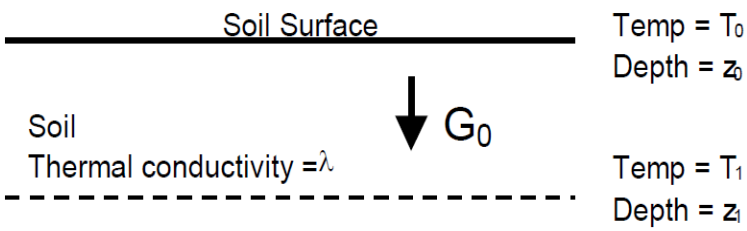

Figure 4.3: Soil Heat Flux (Morse *et al*., 2000)

Since there is a lack of spatial information about the soil's thermal conductivity, the empirical equation developed by Bastiaanssen (1995) has been applied. It calculates soil heat flux as a function of Rn, NDVI, broad band albedo, and surface temperature:

$$Go = Rn\left(\frac{Ts-273}{\alpha}\right)[0.0032(1.1\alpha)+0.0062(1.1\alpha)^2](1 - 0.978\ NDVI^4) \tag{4.13}$$

where Rn is net radiation (Wm^{-2}), Ts is surface temperature (°K), α is broad band surface albedo, and NDVI is as defined in Equation (4.11).

4.2.3 Sensible Heat Flux (H)

Sensible heat flux is the rate at which energy loss from soil through convection and diffusion process as a result of temperature difference between the surface and the lowermost overlaying atmosphere. It is estimated from surface temperature, surface roughness, and measured wind speed.

$$H = \frac{\rho_a c_p \Delta T}{r_{ah}} \tag{4.14}$$

where ρ_a is density of air ($Kg.m^{-3}$), Cp is air specific heat 1004 ($J.Kg^{-1}.K^{-1}$), ΔT is the difference between surface and air temperature (°K), and r_{ah} is the aerodynamic resistance for heat transport ($s.m^{-1}$), determined by wind speed, surface roughness, displacement height, and thermal instability of the atmosphere (Figure 4.4).

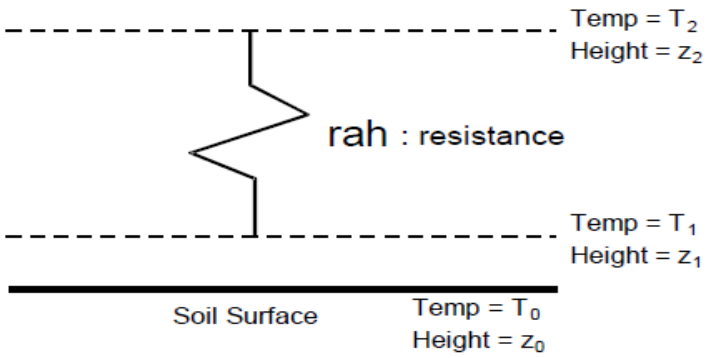

Figure 4.4: Aerodynamic heat transfer (Morse *et al*., 2000)

$$r_a = \frac{1}{ku^*} ln \frac{z_{ref} d}{z_{ah}} \psi_h \tag{4.15}$$

and

$$u^* = \frac{ku_{blend}}{\left[ln\left(\frac{z_{blend} - d}{z_{om}}\right)\right] - \psi_m} \tag{4.16}$$

where u* is friction velocity, k is Von Karman's constant (0.41), u_{blend} is wind speed at blending height, z_{blend} is blending height, z_{oh} is roughness length for heat transport, z_{om}

is roughness length for momentum transport, d is displacement height and ψ_h and ψ_m are stability correction factors for heat and momentum transport, respectively.

The temperature difference ΔT is predicted in order to estimate H from equation (4.17):

$$\Delta T = \frac{H r_{ah}}{\rho_a C_p} \tag{4.17}$$

In this equation H and ΔT are both unknown but are directly related to one another as well as to the value of r_{ah}. Therefore, ΔT is calculated at two extremes, the wettest and driest pixels, by assuming values for H at these reference pixels. The wettest pixel is the pixel where H~0, i.e. all the available energy (Rn-Go) is converted λET or ΔT becomes zero. The driest pixel is the where λET~0, so that H= Rn-Go or ΔT is maximum. The wettest pixels (coldest pixels) are selected in a well watered agricultural field i.e., at pixels with high NDVI but with low temperature, while the driest pixels (pixels with highest estimated temperature) are selected at pixels with high temperature but with low NDVI and albedo. Water bodies should be avoided during the selection of either pixels due to the problem of lag in stored heat (Go) into the body that may not be available at the same instant as Rn or H. Once the wettest and the driest pixels have been selected, temperatures are noted from surface temperature image as T_{cold} and T_{hot} and locations of the pixels are also noted.

Values of Rn_{hot}, Go_{hot}, and rah_{hot} are recorded at the place where T_{hot} is located from the net radiation map, soil heat flux map, and aerodynamic resistance map, respectively. As the latent heat flux is assumed to be equal to zero at the hottest pixel, the sensible heat flux therefore is equal to the net available energy:

$$H_{hot} = Rn_{hot} - Go_{hot} \tag{4.18}$$

ΔT is then calculated from the following equation (4.17) as follows:

$$\Delta T_{hot} = \frac{H_{hot} \times r_{ah} hot}{\rho_a \times 1004} \tag{4.19}$$

Values of T_{cold}, T_{hot}, and ΔT_{hot} are known and may be used to apply the following equation:

$$T_{hot}-T_{cold}=\Delta T=a+bTs \tag{4.20}$$

By making this linear relationship between Ts and ΔT, a and b may be calculated from slope and intercept as shown in Figure 4.5 below:

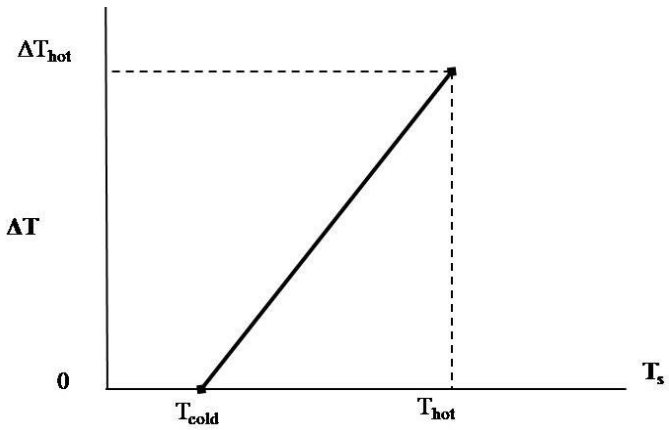

Figure 4.5: Concept of temperature difference between surface and air in SEBAL

After solving for a and b the sensible heat flux, H, for the whole image is calculated iteratively until convergence in the successive value is found.

Finally, the latent heat flux (λET) is computed for each pixel as a residual term of the surface energy balance. An equivalent amount of instantaneous ET is also calculated by dividing the latent heat flux by the latent heat of vaporization (λ).

4.3 Evapotranspiration Up-Scaling

4.3.1 Evaporative Fraction

The evaporative fraction Λ, which is the ratio of latent heat flux over available energy, is one of the methods for using remote sensing data to evaluate land surface fluxes such as evapotranspiration. It is calculated using equation (4.21):

$$\Lambda = \frac{\lambda AE}{\lambda AE+H} = \frac{\lambda AE}{R_n-G_o} \tag{4.21}$$

Although the sensible and the latent heat fluxes are fluctuating during daytime, it is assumed that the evaporative fraction behaves steady during the day time (Bastiaanssen *et al*., 1996; Shuttleworth *et al*., 1989). Then the instantaneous and the integrated daily evaporative fraction remains the same:

$$\Lambda_{ins} = \Lambda_{day} \tag{4.22}$$

4.3.2 Daily Net Radiation

Net radiation is aggregated as daily net radiation ($R_{n\text{-}day}$) based on Bastiannssen *et al*., (1996) approach:

$$R_{n\text{-}day} = (1\text{-}1.1\alpha)K\downarrow_{day} - 110\tau_{day} \tag{4.23}$$

where τ_{day} is daily atmospheric transmissivity for radiation calculated using Angstrom formula as follows:

$$\tau_{day} = 0.25 + 0.5\,\frac{n}{N} \tag{4.24}$$

where n is the actual duration of sunshine and N is maximum possible sunshine or daylight hour.

Daily incoming short wave radiation ($K\downarrow_{day}$) is also calculated using the following:

$$K\downarrow_{day} = 11.5741\tau_{day}K^{toa}{}_{\downarrow\text{-}day} \tag{4.25}$$

where $K\downarrow_{day}$ is the daily incoming shortwave radiation at the top of atmosphere calculated as:

$$K^{toa}{}_{\downarrow\text{-}day} = \frac{24}{\pi}G_{SC}E_o sin\delta sin\varphi\left[\frac{\pi}{180}\omega_s - tan\omega_s\right] \tag{4.26}$$

Or

$$K^{toa}{}_{\downarrow\text{-}day} = \frac{24}{\pi}G_{SC}E_o cos\delta cos\varphi\left[sin\omega_s - \frac{\pi}{180}\omega_s - cos\omega_s\right] \tag{4.27}$$

where ω_s is the sun set or rise hour angle. The remaining parameters definitions are given in Equation (4.4).

4.3.3 Daily Actual Evapotranspiration (ETa-day)

The daily actual evapotranspiration is calculated based on the combination of equations (4.20) and (4.21) as follows (Bastiannssen *et al*., 1996):

$$AE_{day} = \frac{\Lambda R_{n\ day}}{28.588} \tag{4.28}$$

where Rn-day is the daily net radiation in Wm^{-2}.

4.3.4 Monthly Actual Evapotranspiration

Actual daily evapotranspiration could be aggregated into monthly values using the daily rate reference crop evapotranspiration (ET_{ref}) and the daily actual evapotranspiration as expressed in Equation 4.31. Recalling that reference evapotranspiration is the rate of evapotranspiration from hypothetical reference crop with assumed height crop of 0.12 m, a fixed surface resistance of 70 sec m^{-1}, and an albedo of 0.23, resembling the evapotranspiration from an extensive surface of green grass of uniform height, actively growing, well-watered, and completely shading the ground (Allen *et al*., 1998).

The daily reference evapotranspiration may be calculated using either Priestly-Taylor (1972) equation with α=1.26 as applied by Mekonnen and Bastiaanssen, (2000), Mekonnen (2005), and Parodi (2002):

$$PE_{ref\text{-}day} = 1.26[(1\text{-}0.23)K\downarrow_{day} + L_{net\text{-}day}] \tag{4.29}$$

where $K\downarrow_{day}$ is incoming daily shortwave radiation determined using Equation (4.23) and $L_{net\text{-}day}$ is daily net long wave radiation determined based on the empirical relation described by de Bruin (1987). The coefficient α=1.26 was developed for humid regions, which may not be applicable for dry areas. The ASCE (1990) has developed a range of constants: 1.32, 1.56, and 1.74 for dry vegetated, sparsely-vegetated, and arid environment, respectively.

Daily reference evapotranspiration may also be calculated using FAO Penman-Monteith equation (see Chapter 5):

$$ET_{ref} = \frac{0.408\Delta(Rn-Go)+\frac{\gamma 900}{T+273}u2(es-ea)}{\Delta+\gamma(1+0.34u2)} \quad (4.30)$$

where ET_{ref} is reference crop evapotranspiration (mm day^{-1}), Rn is net radiation at the crop surface (MJ m^{-2} day^{-1}), Go is soil heat flux density (MJ m^{-2} day^{-1}), T is mean daily temperature at 2 m height (°C), u^2 is wind speed at 2 m height (m s^{-1}), e_s is saturation vapour pressure (KPa), e_a is actual vapour pressure (KPa), e_s-e_a is saturation vapour pressure deficit (KPa), Δ is slope of vapour pressure curve (KPa °C^{-1}), and γ is the psychrometric constant (KPa °C^{-1}).

The monthly actual evapotranspiration is then determined based on the assumption that the daily relative evapotranspiration at date of image acquisition remains the same for the whole period of the month:

$$ET_{a-mon} = (AE_{-day}/PE_{ref-day}) \times PE_{ref-mon} \quad (4.31)$$

where $ET_{ref-day}$ and $ET_{ref-mon}$ are daily and monthly reference evapotranspiration, respectively, and ET_{a-day} and ET_{a-mon} are actual daily and monthly evapotranspiration.

4.4 MODIS and Landsat Calibration and Atmospheric Correction

Reflectance and radiance values are corrected to calculate temperature brightness and vegetation indices as inputs to SEBAL algorithm (Figure 4.6). Reflectance is used instead of radiances for two reasons: first, the cosine effect of different solar zenith angles due to time difference between data acquisition is removed, and second, reflectance compensates for different values of the exoatmospheric or planetary solar irradiances arising from spectral band differences.

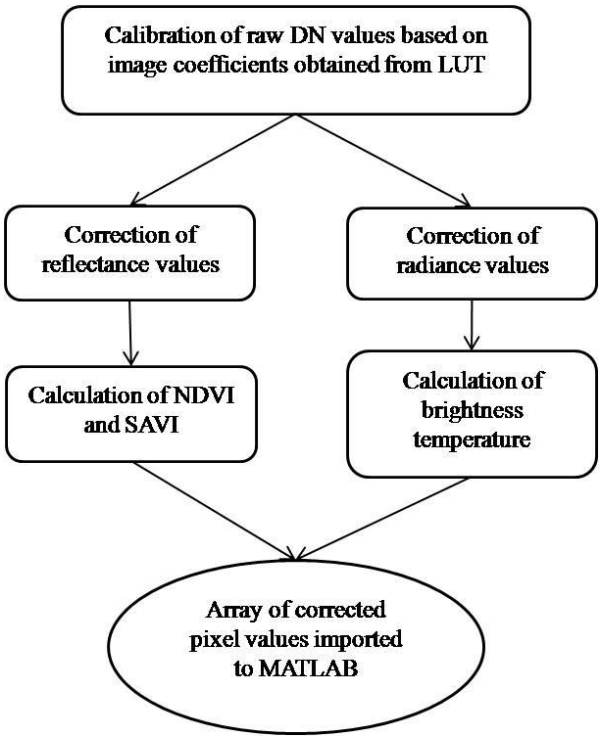

Figure 4.6: Correction of MODIS and Landsat TM5 DN values for SEBAL processing using MATLAB

4.4.1 Calibration for Reflective Solar Bands

4.4.1.1 Reflective Solar Bands for MODIS Level 1B, Bands 1 and 2

The MODIS Level 1B generates two calibrated data products for the Reflective Solar Bands (RSB): the reflectance and the Earth-exiting radiance (MODIS User Guide, 2003). Writing these two products in floating-point format to the Level 1B Earth view product files would make the file sizes excessively large. Instead, the Level 1B writes a 16-bit scaled integer representation of the calibrated digital signals measured by the MODIS, from which the reflectance and radiances can be calculated from two pairs of scale and offset terms written as attributes to the reflective band datasets. These two pairs are derived from the calibration parameters that are input to Level 1B as look up tables. Level 1B corrects the raw digital signals measured at the reflective band detectors, DN, for all known instrumental effects, to produce corrected digital signals, dn*. Level 1B then adjusts the values of dn* for the effects of variations in calibration parameters from detector to detector within each band so that one pair of calibration

terms applies to every detector in each band. The values of dn* adjusted in this way, called dn**, are scaled to the 16-bit representation in the RSB science datasets.

The values of dn** over the dynamic range of [D_{min}, D_{max}] are scaled to a range of [0, 32767] and placed into an integer variable. The values of D_{max} and D_{min} are input to Level 1B through look up tables, and are indexed by band only. Figure 4.7 shows the relationship between dn** and the scaled integer values, SI. Note that dn** is a 32-bit floating point number. It is scaled to an integer in the range of 0 to 32767, which utilizes 15 bits of a 16-bit integer variable.

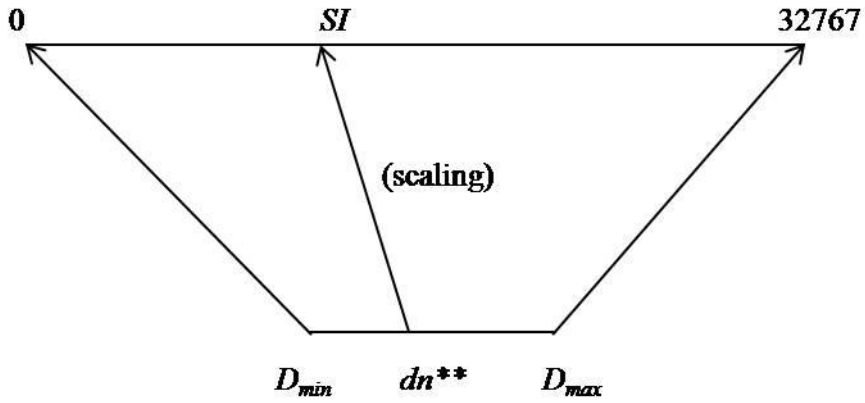

Figure 4.7: Relationship between dn** and scaled integers (SI) (MODIS User Guide, 2003)

The relationship between dn** and SI is given by the equation:

$$dn^{**} = corrected_counts_scale\ (SI - corrected_counts_offset) \tag{4.32}$$

$$corrected_counts_scale = (D_{max} - D_{min}) / 32767 \tag{4.33a}$$

$$corrected_counts_offset = -(32767\ D_{min})/(D_{max} - D_{min}) \tag{4.33b}$$

The values of corrected_counts_scale and corrected_counts_offset are computed inside Level 1B and are written as attributes to the science datasets. Thus, dn** is easily recovered from SI values by reading the attributes and applying Equations 4.33 a, and b.

The images calibration constants are retrieved from imagery product files and used to calibrate the data following the procedures described previously (MODIS User Guide, 2003). Table 4.2 summarizes MODIS Level 1B images reflection calibration scales.

Table 4.2: MODIS Level 1B reflectance calibration scales

Date of Image Acquisition	Reflectance Scales	
	Band 1 (λ=0.620-0.670µm)	Band 2 (λ=0.841-0.876µm)
26082003	5.35025E-05	3.36372E-05
19012004	5.03985E-05	3.17282E-05
24022004	5.09277E-05	3.20684E-05
16032004	5.14467E-05	3.23995E-05
14042004	5.22583E-05	3.29165E-05
13052004	5.29899E-05	3.33833E-05
13062004	5.34760E-05	3.36960E-05
15072004	5.35106E-05	3.37245E-05
16082004	5.30504E-05	3.34411E-05
9092004	5.24475E-05	3.30660E-05
16102004	5.13180E-05	3.23613E-05
21112004	5.03465E-05	3.17558E-05
19122004	4.99069E-05	3.14841E-05

4.4.1.2 Reflective Solar Bands for Landsat TM5, Bands 3 and 4

The calibrated data during Level 1 (L1) product generation, pixel values (Q) from Level 0, (L0), raw unprocessed image data are converted to absolute radiance values 32-bit floating-point calculations (Chander and Markham, 2003). The absolute radiance values are then scaled to eight-bit values representing calibrated digital numbers (Q_{cal}) before output to the public. Conversion from calibrated digital numbers (Q_{cal}) in L1 products back to at-sensor spectral radiance (Lλ) requires knowledge of the original rescaling factors; therefore the following equation is used for the conversion of L1 products:

$$L\lambda=\left(\frac{Lmax\lambda-Lmin\lambda}{Qcal\ max}\right)Q_{cal}+L_{min\lambda} \tag{4.34}$$

Where Lλ is the spectral radiance at the sensor's aperture in (W m^{-2} sr µm), Q_{cal} is the quantized calibrated pixel value in DNs, Q_{calmin} is the minimum quantized calibrated

pixel value (DN=0) corresponding to $L_{min\lambda}$, Q_{calmax} is the maximum quantized calibrated pixel value (DN=255) corresponding to $L_{max\lambda}$, $L_{min\lambda}$ is the spectral radiance that is scaled to Q_{calmin} in W m^{-2} sr μm, and $L_{max\lambda}$ is the spectral radiance that is scaled to Q_{calmax} in W m^{-2} sr μm. The above equation may be written as

$$L\lambda = Grescale \times Q_{cal} + L_{min\lambda} \tag{4.35}$$

Table 4.3 provides band-specific $L_{max\lambda}$ and $L_{min\lambda}$ parameters and the corresponding Grescale and $L_{min\lambda}$ values used. It should be noted that products generated before May 5, 2003 and converted to radiance using older L_{mins} and L_{maxs} will not provide the same radiances as those processed since May 5, 2003 and converted to radiance with the new L_{mins} and L_{maxs} (Chander and Markham, 2003).

Table 4.3: Landsat TM5 post-calibration (Chander and Markham, 2003)

Spectral Radiances, $L_{min\lambda}$ and $L_{max\lambda}$						
	From March 1, 1984 to May 4, 2003			After May 5, 2003		
Band	$L_{min\lambda}$	$L_{max\lambda}$	Grescale	$L_{min\lambda}$	$L_{max\lambda}$	Grescale
1	-1.52	152.1	0.602431	-1.52	193	0.762824
2	-2.84	296.81	1.175100	-2.84	365	1.442510
3	-1.17	204.3	0.805765	-1.17	264	1.039880
4	-1.51	206.2	0.814549	-1.51	221	0.872588
5	-0.37	27.19	0.108078	-0.37	30.2	0.119882
6	1.2378	15.303	0.055158	1.2378	15.303	0.055158
7	-0.15	14.38	0.056980	-0.15	16.5	0.065294

The spectral radiance as calculated above is converted then to planetary reflectance. The combined surface and atmospheric reflectance of the earth is computed according to:

$$Pp = \frac{\pi \times L\lambda \times d2}{ESUN\lambda \times cos\Theta s} \tag{4.36}$$

Where Pρ is planetary reflectance (unitless), Lλ is the spectral radiance at the sensor's aperture, d is the earth-sun distance in astronomical units, ESUNλ is the mean solar exoatmospheric irradiances, and Θs is the solar zenith angle in degrees. Table 4.4 gives the solar exoatmospheric spectral irradiances (ESUNλ) for Landsat TM5.

Table 4.4: Solar exoatmospheric spectral irradiances (Chander and Markham, 2003)

Band	ESUN ($W.m^{-2}.\mu m^{-1}$) Landsat TM5
1	1957
2	1826
3	1554
4	1036
5	215
7	80.67

The reflectance calculations depend on the earth-sun distance (d) which varies by each image and may be read from the images attributes.

4.4.1.3 MODIS Level 3 Surface Reflectance (MOD09Q1)

MODIS surface reflectance (MOD09Q1) provides MODIS band 1-2 surface reflectance at 250 m resolution in an 8-day gridded level 3 product in the Sinusoidal projection. Each MOD09Q1 pixel contains the best possible gridded level 2 observation during an 8-day period as selected on the basis of high observation coverage, low view angle, the absence of clouds or cloud shadow, and aerosol loading. Version-6 MODIS/Terra Surface Reflectance products are validated and accuracy has been assessed over a widely distributed set of locations and time periods via several ground-truth and validation efforts. Table 4.5 provides scale factors for MOD09Q1.

Table 4.5: Science Data sets for MOD09Q1 (MOD09 User's Guide, 2008)

Science Data Sets (HDF Layers (3))	Units	Bit Type	Fill Value	Valid Range	Scale Factor
250 m Surface Reflectance Band 1 (620-670 nm)	Reflectance	16-bit signed integer	-28672	-100-16000	0.0001
250 m Surface Reflectance Band 2 (841-876 nm)	Reflectance	16-bit signed integer	-28672	-100-16000	0.0001
250 m Surface Reflectance Quality	Bit Field	16-bit unsigned integer	65535	0-32767	NA

4.4.2 Calibration for Radiance Values

4.4.2.1 Thermal Emissive Bands for MODIS Level 1B, Bands 31 and 32

The Level 1B data also generate radiances in 32-bit floating-point format for each thermal emissive band measurement. It scales these radiances to an integer representation to the Earth View 1 km Emissive science datasets. The values of radiance, L, over the dynamic range of [L_{min}, L_{max}] are scaled to a range of [0, 32767] and placed into an integer variable. The values of L_{max} and L_{min} are input to Level 1B through look up tables and are indexed by band only. Figure 4.8 shows the relationship between L and the scaled integer values, SI. Values of radiance that lie outside the range of [L_{min}, L_{max}] are set to L_{min} or L_{max} as appropriate.

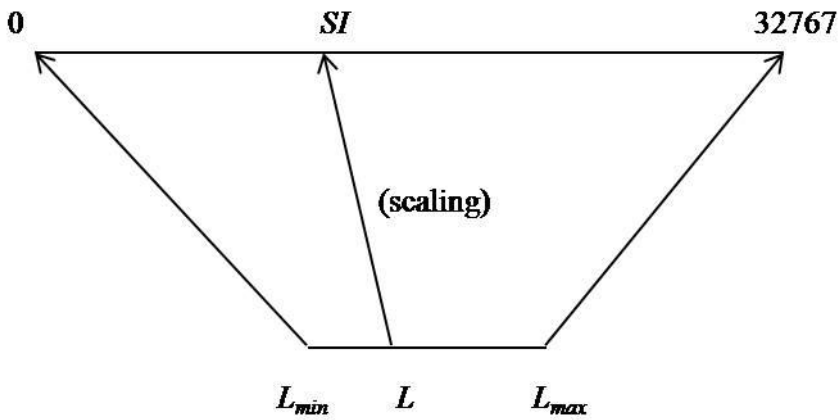

Figure 4.8: Relationship between Thermal Emissive Band Radiance (L) and its scaled integer representation. (MODIS User Guide)

In the Level 1B product scaled integer SDS (which is a 16-bit unsigned integer data type), the least significant 15 bits are used for the valid range of the scaled value of L. The most significant bit of the 16-bit integer is reserved to indicate invalid data. Thus, the dynamic range of valid data in integer representation is [0, 32767] and any value greater than 32767 represents invalid (or unusable) data. The relation between L and SI is given by an equation of the form:

$$L = \text{radiance_scales} \, (SI - \text{radiance_offsets}) \tag{4.37}$$

$$\text{radiance_scales} = (L_{max} - L_{min}) / 32767 \tag{4.38a}$$

$$\text{radiance_offsets} = -(32767 \, L_{min})/(L_{max} - L_{min}) \tag{4.38b}$$

The values of radiance_scales and radiance_offsets are computed inside Level 1B and written as attributes to the science data sets. Thus, radiance may be simply recovered from SI by reading these two attributes and applying Equations 4.38, a, and b.

The scale and offset coefficients for emissive bands (Band 31 & 32) are extracted using NASA's specialised HDF Explorer Toolbox. The coefficients for each MODIS scene used in this research are given in Table 4.6.

Table 4.6: MODIS radiance calibration scales

Date of Image Acquisition	Radiance Scales				Radiance Offsets	
	Band1	Band2	Band31	Band32	Band31	Band32
26082003	0.0267811	0.0104012	0.000840022	0.000729698	1577.34	1658.22
19012004	0.0266174	0.010352	0.000840022	0.000729698	1577.34	1658.22
24022004	0.0265897	0.010343	0.000840022	0.000729698	1577.34	1658.22
16032004	0.0265735	0.010338	0.000840022	0.000729698	1577.34	1658.22
14042004	0.0265512	0.010331	0.000840022	0.000729698	1577.34	1658.22
13052004	0.0265289	0.010324	0.000840022	0.000729698	1577.34	1658.22
13062004	0.0265049	0.010317	0.000840022	0.000729698	1577.34	1658.22
15072004	0.0264803	0.010310	0.000840022	0.000729698	1577.34	1658.22
16082004	0.0264556	0.010302	0.000840022	0.000729698	1577.34	1658.22
09092004	0.0264372	0.010296	0.000840022	0.000729698	1577.34	1658.22
16102004	0.0264087	0.010288	0.000840022	0.000729698	1577.34	1658.22
21112004	0.0263809	0.010279	0.000840022	0.000729698	1577.34	1658.22
19122004	0.0263594	0.010273	0.000840022	0.000729698	1577.34	1658.22

4.4.2.2 Thermal Emissive Band for Landsat TM5, Band 6

The thermal band, Band 6, is calibrated using the internal calibrator where it is converted from spectral radiance to effective at-satellite temperature (Chander and Markham, 2003). The effective at-satellite temperature of the imaged earth surface assumes unity emissivity where the conversion formula is presented in Equation 4.39 and Table 4.7 (Chander and Markham, 2003).

$$T = \frac{K2}{ln\left(\frac{K1}{L\lambda}\right)+1} \tag{4.39}$$

Where T is the effective at-satellite temperature in Kelvin, K2 is the calibration constant 2 in Kelvin, K1 is the calibration constant 1 in $W.m^{-2}.sr.\mu m$, and $L\lambda$ is the spectral radiance at the sensor's aperture.

Table 4.7: Landsat TM5 thermal band calibration constants (Chander and Markham, 2003)

	K1	K2
Landsat TM5	607.76	1260.56

4.4.2.3 MODIS Level 3 Land Surface Temperature and Emissivity (MOD11A2)

The level 3 MODIS global Land Surface Temperature (LST) and Emissivity 8-day data are composed from the daily 1 km LST product (MYD11A1) and stored on a 1 km Sinusoidal grid as the average values of clear-sky LSTs during an 8-day period. MYD11A2 is comprised of daytime and night-time LSTs, quality assessment, observation times, view angles, bits of clear sky days and nights, and emissivities estimated in Bands 31 and 32 from land cover types. Scale factors and offsets are presented in Table 4.8.

Table 4.8: The science data set in the MOD11A2 (MODIS LST Users' Guide, 2009)

Name	Bit Type	Fill Value	Valid Range	Scale Factor	Add offset
Band 31 emissivity	8-bit signed integer	0	1-255	0.002	0.49
Band 32 emissivity	8-bit signed integer	0	1-255	0.002	0.49

4.4.3 Atmospheric Correction

The use of MODIS data for land products algorithms such as albedo, vegetation indices or LAI (Leaf Area Index) requires that the top of the atmosphere signal be converted to surface reflectance. Several atmospheric corrections algorithms from which the surface reflectance are calculated for MODIS channels 1 to 7: 0.648 µm, 0.858 µm, 0.470 µm, 0.555 µm, 1.240 µm, 1.640 µm, and 2.13 µm. The algorithms corrects for the effects of gaseous and aerosol scattering and absorption as well as adjacency effects caused by variation of land cover, Bidirectional Reflectance Distribution Function (BRDF) and

atmosphere coupling effects, and contamination by cirrus (Vermote and Vermeulen, 1999). The correction has been achieved by means of look-up tables which provide the transmittances and path radiances for a variety of sun-sensor geometry's and aerosol loadings. Cai *et al.*, (2005) have described similar split window methods which use MODIS Band 31 (10.78 – 11.28µm) and Band 32 (11.78 – 12.27µm), firstly to correct for atmospheric defects and secondly to derive land surface temperature (LST).

4.5 Procedural Steps in SEBAL Processing

SEBAL has been processed using a number of programs such as ERDAS Imagine (Morse *et al*., 2000; Bastiannssen *et al*., 1998; Chemin, 2003; French *et al*., 2005), C language (Mekonnen, 2005), and MATLAB (Brata *et al*., 2006). MATLAB has been chosen for this research for its least complicated procedural algorithms and computational efficiency related to SEBAL's iterative steps for calculating the sensible heat flux. MATLAB, meaning "**mat**rix **lab**oratory", is a numerical computing environment and programming language maintained by The MathWorks (http://www.mathworks.com). It allows easy matrix manipulation, plotting of functions and data, implementation of algorithms, creation of user interfaces, and interfacing with programs in other languages. MATLAB is created by Prof. Cleve B. Moler, Professor of Computer Science (a specialist in numerical analysis) at the University of New Mexico, USA. One of the disadvantages in MATLAB is the loss of pixel geographical coordinates, which prevents verification of specific targets and validation of results. This problem is overcome by the conversion of MATLAB outputs into data formats such as TIFF and then georeferencing them using ArcGIS program.

4.5.1 MODIS Level 1B and Level 3 and Landsat TM5

The procedural steps of MODIS Level 1B single day product and Landsat are described as follows:

- **Step 1: Calibration of Image DN values**

Reflectance and radiance corrections and calculating brightness temperature for MODIS Level 1B and Landsat TM5 data sets are performed using ERDAS Imagine spatial models, the Model-Maker Toolbox (Figure 4.9). MODIS Level 3 is fully calibrated but

scale factors as shown in Tables 4.5 and 4.8 are applied. NDVI modeling is also applied using ERDAS because it is easier to handle denominator zeros of the NDVI equation as the sum of red and near infrared may sum up to zero in some vegetated areas. Intermediate functions are defined using ERDAS to exclude the zeros as the denominator after the input image is identified.

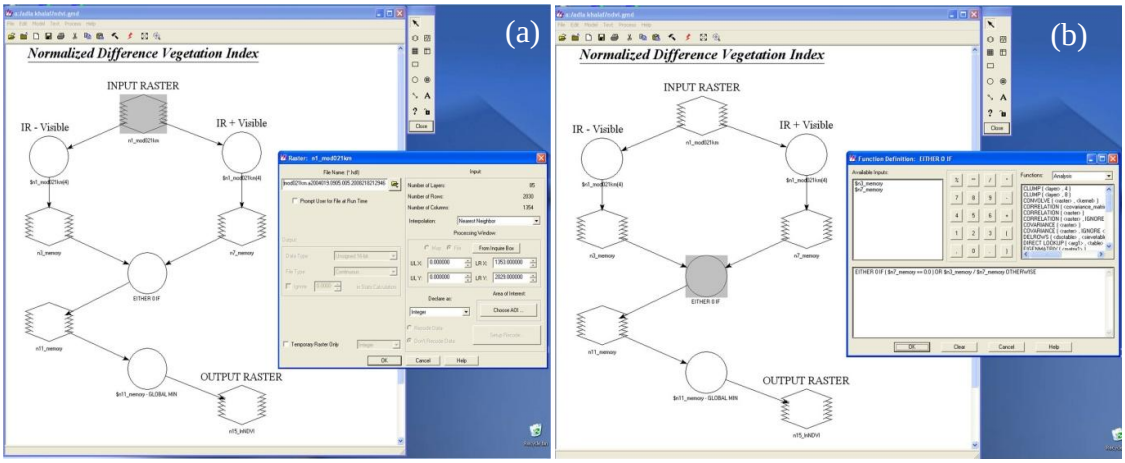

Figure 4.9: ERDAS Imagine defining (a) input raster image and (b) function excluding zeros as denominator in the NDVI algorithm. The left side of both figures represents the NDVI model while the right side defines the input image and the function definition.

Thus, after the raw data calibration, the output arrays are then imported into MATLAB for further SEBAL computations.

It is worth mentioning that the input and output variables may be stored as single or double precision floating-point. The single and double precision floating-point refers to computer memory storage as 32 and 64 bits, respectively. Choosing the size determines the number of significant digits the value might contain, e.g. the single precision float (simply float) is generally guaranteed to offer six significant digits, while the double precision float (simply double) can offer at least 10 significant digits (Lippmann *et al.*, 2005). The former is considered sufficient for SEBAL mathematical computations.

- **Step 2: Importing Data**

Three types of ERDAS Imagine files are imported into MATLAB: a) the corrected radiance DN values, (b) corrected reflectance DN values, and (c) two vegetation

indices, the NDVI and SAVI. It was important to make sure that the images have the same array size or else the mathematical functions won't run if arrays do not match.

- **Step 3: Re-writing SEBAL Code**

The SEBAL code is rewritten from two hardcopy sources previously used by Mekonnen (2005) and Opoku-duah (2007). The code is reorganized and verified in order to suit the West Bank area conditions. Earlier versions implemented using ERDAS Imagine modeler toolbox and FAO guidelines are both used as references for calculating ET and estimating related constants and atmospheric resistance.

It is worth noting that MODIS Level 3 (8-day) product includes surface temperature and emissivity within its data. Therefore, they are used directly with no mathematical function to derive them from reflectance and radiance bands.

- **Step 4: Creating MATLAB Functions and of SEBAL Code Analysis**

SEBAL mathematical functions are expressed as MATLAB functions using some of the programming skills (Figure 4.10). The SEBAL code is then entered into MATLAB and the code analyzer is utilized to identify problems in SEBAL formulation. Such problems include the use of real values of the natural logarithm function (log) and exclude the imagination numbers in arrays cells. Syntax and symbols are carefully used and observed in programming, such as the semi-colon terminator (;), mathematical functions (. *, . /), and comment modulus (%%), in order to run SEBAL without errors.

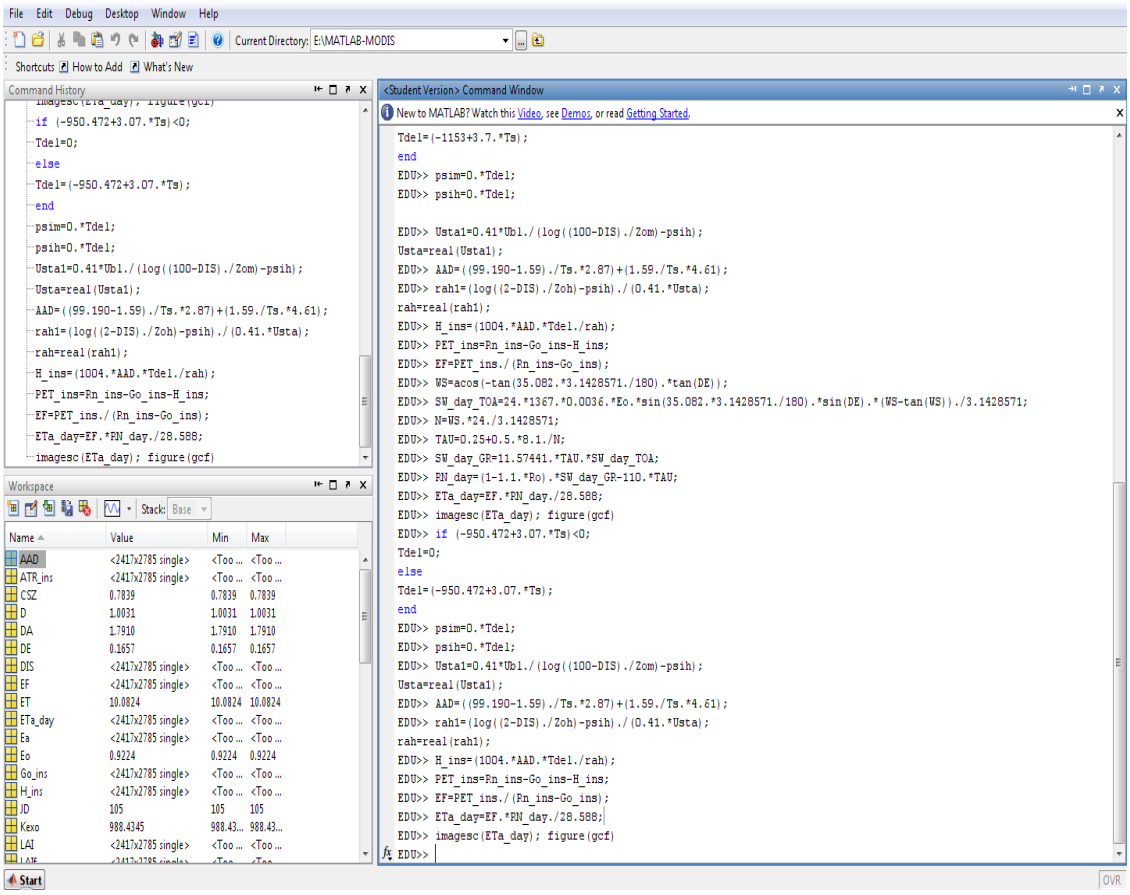

Figure 4.10: MATLAB interface

- **Step 5: Processing Decision-Making**

A couple of critical processing decisions are carefully thought of and taken to run-error-free SEBAL. Three of the most important ones are described as follows:

(1) Determination of prediction algorithms for surface roughness:

Surface roughness depends very much on leaf area index (LAI) which also has an inverse logarithmic relationship with vegetation index. The choice, therefore, exists for users to apply NDVI or a soil-adjusted vegetation index (SAVI). Note that SAVI is defined as (NIR-R)/ (NIR+R+L)(1+L), where NIR & R represent reflectance in the near infrared and visible bands, respectively and L = a soil-brightness dependent correction factor that compensates for the difference in soil background conditions; in this case L = 0.5, following Huete (1988). Morse *et al*. (2000) assume that SAVI accounts for soil reflectivity better than NDVI, which might lead to a more accurate determination of

surface roughness, therefore, SAVI is applied. However, further examination has revealed that there no significant difference between NDVI and SAVI (Opoku-Duah, 2007).

(2) Selection of ground-based weather data and development of prediction equations for surface to air temperature differences:

This is one of the most difficult approximations for SEBAL due to the scarcity of spatially distributed air temperature in the West Bank. Therefore, the mean of the seven field (point) measurements for each month is applied, using an empirical relationship developed by Bastiannssen *et al*., (1998a) for similar dry catchments.

(3) Selection of the driest and wettest indicator pixels as an aid for determining sensible heat flux.

A number of techniques have been developed (e.g. Morse *et al*., 2000) to avoid undue subjectivity of this process; the ERDAS-based trial-and-error is a popular method. In MATLAB, a 'for-else-end' loop function is developed to select pixels with the most extreme values.

- **Step 6: Running the Code**

Each function and MATLAB script of the SEBAL code (Appendix 3.1 and 3.2) is run in the command window. Repeating the same code for different images is done through copying and pasting and/or double clicking functions in Command History. Recalling and editing of previous statements is achieved from the Command Window by pressing the up-arrow key.

- **Step 7: Saving SEBAL Results**

Output files resulting from the run of each function is listed in the Workspace window. These files may be saved directly by clicking on the save icon. The functions script may be saved as M-file from the Command History. To save an image from the output results listed in the Workspace, are done by right clicking on the name of image and then choose image. After the image is displayed, it may be saved in any format the user wish. Displaying results may also be done using the 'display'.

- **Step 8: Geo-Referencing**

MODIS products have two sources of metadata: the embedded HDF metadata, and the external ECS metadata (Landsat has only an external metadata file). The HDF metadata contains valuable information including global attributes and data set-specific attributes pertaining to the granule. The ECS (generated by the EOSDIS Core System) .met file is the external metadata file in XML format, which is delivered to the user along with the MODIS product. It provides a subset of the HDF metadata. Some key features of certain MODIS metadata attributes include the rows and columns of the data and the projection parameters representing the latitude and longitude coordinates of the geographic tile corresponding to the data.

Most standard MODIS Land and Landsat products use the Sinusoidal grid tiling system. The tile coordinate system starts at (0,0) (horizontal tile number, vertical tile number) in the upper left corner and proceeds right (horizontal) and downward (vertical). Geo-referencing is carried out through the following steps:

- ***Step1:*** ASCII text files created along with the images are downloaded with the datasets. These files contain the latitudes, longitudes for each image. This data is modified for reprojection where latitudes and longitudes are converted to the false eastings and northings of the local Palestinian grid, which is based on the Transverse Mercator projection, to allow automatic batch geo-referencing of the images. Specifications of the Palestinian Projection System are shown in Table 4.9.

Table 4.9: Specifications of projection system used in Palestine

Projection	Transverse Mercator
Datum	D-Clarke 1880
Geographic coordinate system	GCS-Clarke 1880
Latitude of Origin	31.734096944 (31° 44′ 02.749″)
Central meridian	35.21208611 (35° 12′ 43.490″)
False Easting	170251.55499 m
False Northing	126867.90900 m
Scale Factor	1.0
Linear unit	meter

- ***Step 2:*** using MATLAB commands, the MODIS and Landsat output evapotranspiration rasters are converted to a 8-bit, e.g. '*ET_january=uint8(ET_jan);*' where *ET_january* is the **output** raster and *ET_jan* is the **input** file. It is essential that the numbers in the MATLAB raster are integers to continue in the proceeding steps.
- ***Step 3:*** the 8-bit output file is saved as 'tiff' file using the MATLAB command '*imwrite*', e.g. *'imwrite(ET_january,'ETa_january','tiff'* where the second and first parts of the command are the **output** and **input** files. Note that the output name and format are string values and therefore should be written in quotations.
- ***Step 4:*** in ERDAS, the *ETa-january* output image is opened and a single band is exported as 'tiff' file. This is be done using the option *'save top layer as'* under the file command.
- ***Step 5:*** the output tiff file is opened in ArcGIS/Info and the ASCII text file is uploaded and geo-referencing applied as illustrated in Figure 4.11.

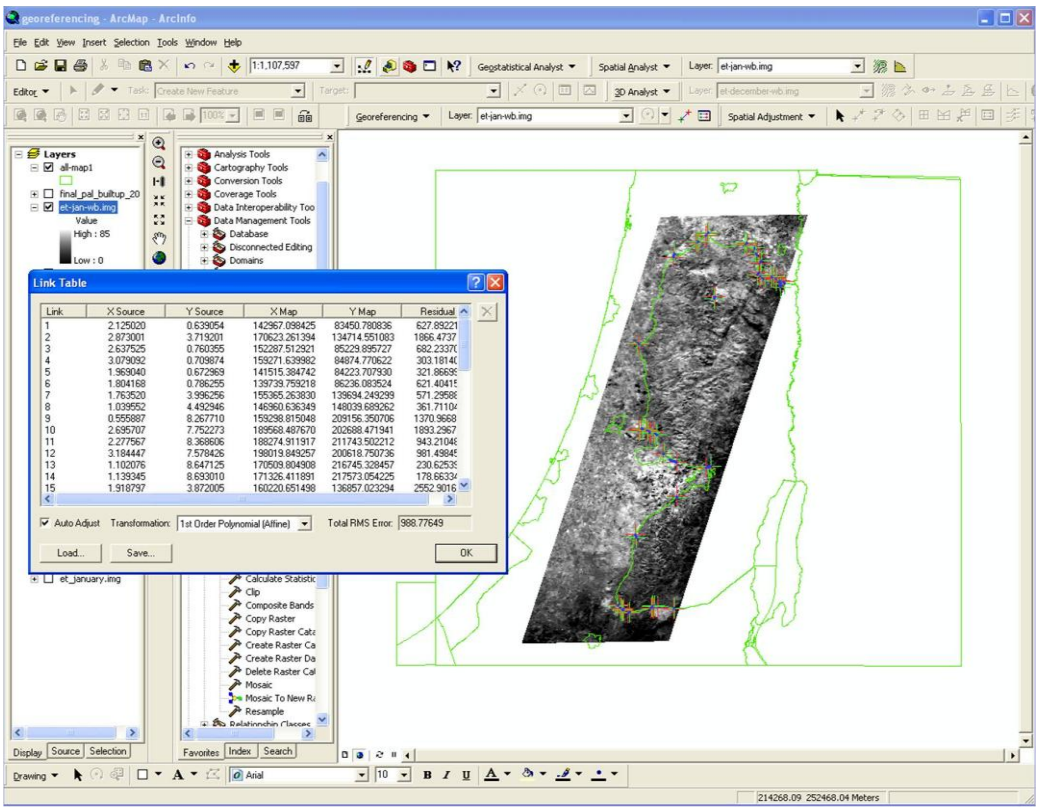

Figure 4.11: Geo-referencing ET MODIS Level 3 (8-day) product using ArcGIS/Info

- ***Step 6:*** the output geo-referenced file is exported.

- ***Step 7:*** for MODIS Level 3 (8-day) products, the same procedure has been applied to the other images covering the second half of the West Bank area. Geo-referenced images for each month are mosaiced using the ArcInfo mosaic tool.

Downloading images, modifying SEBAL algorithm, and applying the model was completed within couple of months. The main reason was that each MODIS image covered half of the research area so the number of MODIS images required to map ET was doubled. In other words, instead of employing 48 images covering the year span, 96 images were used instead. The final ET map was composed of two mosaiced images of each half. Otherwise, SEBAL application would much less time to modify and run.

4.6 Assumptions and Uncertainties Induced by of SEBAL Algorithm

There are four assumptions that SEBAL makes within the algorithm:

- The sensible heat flux range and the evaporative fraction are anchored by the "hot" pixel in the very dry terrain where latent heat flux reaches zero and the "cold" pixel in very moist terrain where sensible heat flux is zero.
- The vertical difference in air temperature (ΔT) is computed from inversion of the sensible heat flux at the anchor points which implies that neither the radiometric surface temperature nor the air temperature measurements are involved in the computations of ΔT.
- ΔT is assumed to be linearly related to radiometric surface temperature. The relation between the surface and air temperature and their gradient is significantly affected by the vegetative properties.
- The surface heat flux fractions such as the evaporative fraction and relative evapotranspiration, throughout the day are assumed constant.

SEBAL is comprised of computational steps some of which require decision-making by the user such as the selection of the dry and wet indicator pixels, determination of prediction algorithms for surface roughness, selection of ground-based weather data, and development of prediction equations for surface to air temperature differences.

These decisions are crucial and challenging in that they do not only influence accuracy of the SEBAL output but they also require a good theoretical knowledge about: (1) regional energy and radiation balance modelling; (2) the region's microclimate; (3) the local bio-physical environment, e.g. vegetation cover, soil physical conditions, etc.; (4) physics of the SEBAL algorithm; and (5) computing power, programming knowledge and allied resources. Though the above may not be limited to MATLAB processing, development of MATLAB and related skills is also a challenge.

4.7 Further Validation

Previous work with SEBAL has shown it to be an effective predictor of ET on crop fields during wet season (Bastiaanssen *et al*., 1998b; Bashir *et al*., (2008); Gao *et al*., (2008); Compaore *et al*., (2008); Kongo and Jewitt (2006); Mutiga *et al*., (2009); Ramos *et al*., (2009); Li *et al*., (2008); Kite and Droogers (2000); Timmermans and Meijerink (1999); Teixeira *et al*., (2009); Bastiaanssen and Chandrapala (2003); Bastiaanssen (2000); Zwart and Bastiaanssen (2007); Patel *et al*., (2006), Melesse and Nangia (2005)). SEBAL includes some uncertainties that should be eliminated or reduced if SEBAL is to become accurate. These uncertainties are in the form of: a) uncertainties created by extrapolating the ET predicted at the time of the satellite overpass to longer periods of time; b) uncertainties created by the need to refine SEBAL to account for slope, aspect, and elevation.

The application and accuracy of SEBAL is potentially limited by uncertainties created by extrapolating the ET predicted at the time of the satellite overpass to the entire day of the overpass, as well as to the period between overpasses. Further work is needed on SEBAL to test and refine the means for using SEBAL to extrapolate ET from an instantaneous observation to longer periods or from midday to the entire day.

As the instantaneous values of the actual evapotranspiration are not of interest to the water managers, but the daily 24-h is, it is important for water rights management to use SEBAL measurements based on monthly measurements which is why SEBAL has been applied on the twelve months period in this research to study the temporal variation of evapotranspiration.

4.8 Conclusion

Although remote sensing techniques cannot measure actual evapotranspiration directly, it can provide an indirect estimate over large spatial and temporal scales. The Surface Energy Balance Algorithm for Land (SEBAL) procedure allows the estimation of evapotranspiration at a regional scale using a small amount of ground based inputs and satellite-based visible, near infrared, and thermal data to estimate surface albedo, surface temperature, atmospheric and surface emissivity, soil heat flux, surface roughness, net radiation, air temperature gradients, sensible heat flux, latent heat flux, evaporative fraction, and photosynthetically active radiation. Both the instantaneous and the 24-hour integrated surface heat fluxes may be retrieved. SEBAL is thought to be the most promising algorithm that is widely applied in several countries due to its accurate estimation of actual evapotranspiration (Bastiaanssen *et al*., 1998b).

A description of the methodological approach for SEBAL algorithm for calculating ET at the West Bank scale is introduced in this chapter. A stepwise procedure of how surface energy and water fluxes may be derived using MATLAB processing addresses the major assumptions used in the prediction equations. The performance of SEBAL is enhanced by the integration of local meteorological measurements such as air temperature, wind speed, and net radiation (Mekonnen, 2005; Bastiannssen *et al.* 1998b). A full discussion of SEBAL application in the West Bank area and its results are discussed in Chapter 7. Chapter 5 presents a detailed procedure of some empirical equations such as Penman-Monteith and Thornthwaite methods to calculate evapotranspiration from meteorological data. In addition to pan measurements, SEBAL estimates are validated with the calculated rates.

Chapter Five

Local Scale Evapotranspiration Modelling

5.1 Introduction

This chapter presents results from some of the local scale evapotranspiration models which are used to validate the satellite derived regional evapotranspiration estimates (Chapter 8). Monthly meteorological measurements are applied to calculate potential evapotranspiration using the Penman-Monteith and Thornthwaite methods that are later validated to the Class-A pan measurements. Actual evapotranspiration is then calculated by applying the soil moisture deficit method (SMD) to validate SEBAL estimates (Chapter 7). Field measurements of actual evapotranspiration are missing in the West Bank area which makes the SMD and SEBAL validations to real estimates not possible.

In the West Bank, as in other dry areas, evaporation is considered the largest output flux in the water-mass balance, where in some cases it may account for more than 95% of the total annual water budget at a catchment scale (Maneta *et al*., 2008). It affects soil moisture, and therefore, the amount of precipitation available for runoff and aquifer recharge.

Evapotranspiration is composed of two aspects: firstly, direct transfer of water from open surface water and soil (evaporation); and secondly, the water transpired from plants and vegetation (transpiration). Evaporation is the process where liquid water is converted to water vapour through the energy supplied by solar radiation and the ambient temperature of the air (Allen *et al*., 1998). The water vapour is removed as the difference between water vapour pressure at the evaporating surface and air pressure increases. And as evaporation proceeds and the surrounding air become saturated, evaporation slows down and might cease at the time when it is unable to take up any more moisture. The replacement of saturated air by drier air enables evaporation to continue. Thus, the rate of evapotranspiration depends on the climatic conditions such as wind speed, the surface and air temperatures, vapour and atmospheric pressures, surface roughness, and latent heat. In vegetated areas, the degree of shading of the crop

canopy and the amount of water available at the evaporating surface affect evaporation and therefore evaporation is influenced by the soil moisture of that area. Frequent rain, irrigation, and water transported upwards in a soil from shallow water tables are additional factors that influence evaporation process. Evaporation can be directly measured using the 'evapotron' instrument or indirectly using the water budget method (difference in storage of a water body measured at two known times).

Transpiration is the vaporization of liquid water in plant tissues and its removal to the atmosphere. As plants draw their supply from the soil, the rate of transpiration is governed by the stomata in the leaves which act like valves to regulate the passage of water through the pores according to the light prevalence. Pores close in darkness and therefore transpiration ceases at night. When there is shortage in water soil, the stomata regulate the pores and reduce transpiration. As a result transpiration, like direct evaporation, is dependent on the meteorological factors including energy supply, vapour pressure gradient, and wind. It is also influenced by soil moisture and the capacity of plants to transpire that is affected by the environmental aspects, cultivation practices, crop characteristics and development, and type of plants.

FAO (1998) has proposed an estimation for calculating actual evapotranspiration by first estimating the reference evapotranspiration (ETo) and then applying a corresponding crop coefficient. Reference evapotranspiration is defined in Allen *et al*. (1998) as the rate of evapotranspiration from a hypothetical crop with an assumed crop height (0.12 m), a fixed canopy resistance (70 s m^{-1}), and albedo equal to 0.23. The assumption resembles evapotranspiration from an extensive surface of green grass cover of uniform height, actively growing, completely shading the ground and not short of water. Numerous equations have been developed to estimate ETo which most require several weather parameters. Evaporation Class-A pans are widely used because of the simplicity of its technique, low cost, and ease of application in determining crop water requirements for irrigation (Trajkovic, 2009). Evapotranspiration may also be estimated empirically using the soil water balance but because recharge is a missing parameter, the soil water balance cannot be applied to estimate evapotranspiration. Lysimeters are measuring devices used to measure the amount of actual evapotranspiration released by plants and trees. They are considered expensive and difficult to construct and their

operation and maintenance require special care. Evapotranspiration may also be estimated using the energy balance which is the concept behind the Surface Energy Balance Algorithm for Land (SEBAL) method described in Chapter 4.

In this research, SEBAL is applied and estimates are validated with actual evapotranspiration derived from the soil moisture deficit using the empirical equations of Penman- Monteith, Thornthwaite, and field pan evaporation.

The framework for estimating potential and actual evapotranspiration is summarized in Figure 5.1 and described in the following sections.

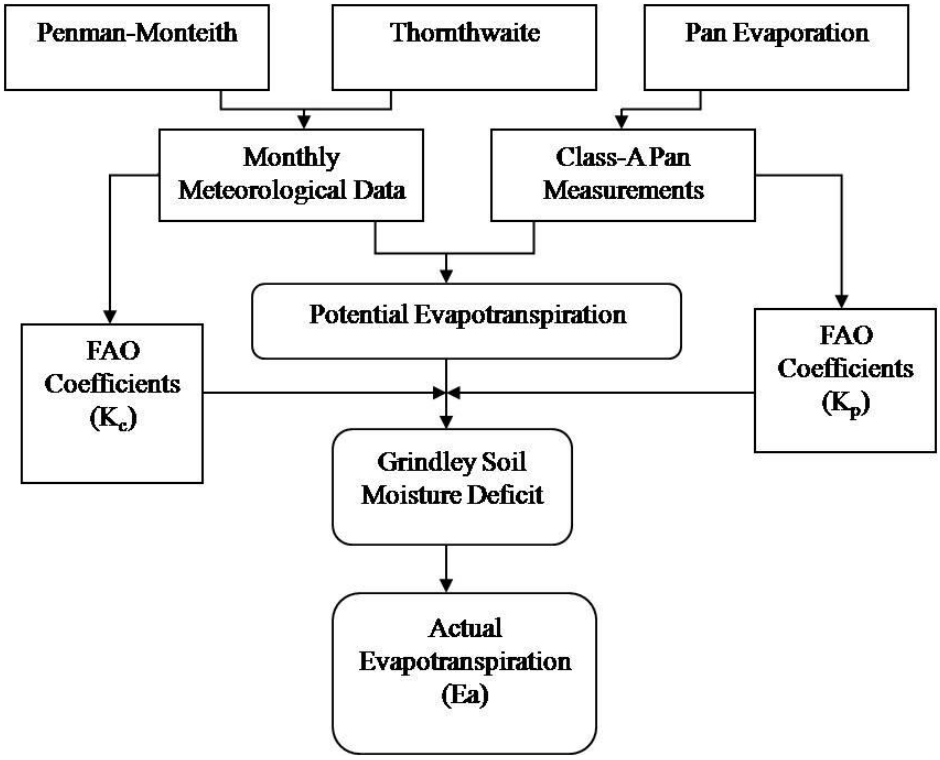

Figure 5.1: A schematic model for local scale evapotranspiration estimation

5.2 Local Scale Evapotranspiration Methods

Evapotranspiration may be computed from weather data where empirical equations have been developed for such estimations. The FAO Penman-Monteith method is one of the recommended methods for the definition and computation of evapotranspiration (FAO, 1998).

5.2.1 Penman-Monteith Equation

The FAO Penman-Monteith offers the best results with minimum possible errors in relation to a living grass reference crop when compared to other common methods such as the Blaney-Criddle, radiation, and pan evaporation (Allen *et al*., 1998). It is based on Penman (1948) method that combines the energy balance with the mass transfer method. Air temperature, radiation, humidity, and wind speed are the input data. The Penman-Monteith equation is described by the following:

$$\lambda ET = \frac{\Delta(Rn - G) + \rho_a\, c_p\, (\frac{e_s - e_a)}{ra}}{\Delta + \gamma\left(1 + \frac{r_s}{r_a}\right)} \tag{5.1}$$

where Rn is the net radiation, G is the soil heat flux, (e_s - e_a) represents the vapour pressure deficit of the air, ρ_a is the mean air density at constant pressure, c_p is the specific heat of the air, Δ represents the slope of the saturation vapour pressure temperature relationship, γ is the psychrometric constant, and r_s and r_a are the (bulk) surface and aerodynamic resistances.

The transfer of heat and water vapour from the evaporating surface into the air above the canopy is determined by the aerodynamic resistance as follows:

$$r_a = \frac{ln\left[\frac{z_d - d}{z_{om}}\right] ln\left[\frac{z_h - d}{z_{oh}}\right]}{k^2 u_z} \tag{5.2}$$

where r_a is the aerodynamic resistance, z_d the height of wind measurements (m), z_h the height of humidity measurements (m), d is the zero plane displacement height (m), z_{om} is the roughness length governing momentum transfer (m), z_{oh} is the roughness length governing transfer of heat and vapour (m), k is the von Karman constant (k= 0.41), and u_z is the wind speed (m s^{-1}) at height z (m). The equation is restricted to neutral stability conditions, i.e. where temperature, atmospheric pressure, and wind velocity are distributed in nearly adiabatic conditions where there is no heat transfer. Therefore, the application of this equation requires the use of correction factors for stability, but if ET is estimated for well watered surfaces, heat exchange is considered small and correction

factors are not required. Aerodynamic resistance for a grass reference surface may be reduced to:

$$r_a = 208/u_2 \tag{5.3}$$

where u_2 is the wind speed at 2 m assuming d=2/3 h, z_{oh}=0.1z_{om}, and a constant crop height of 0.12 m.

Surface resistance of dense full cover vegetation is defined as follows (FAO, 1998):

$$r_s = \frac{r_1}{LAI_{active}} \tag{5.4}$$

where r_s is the bulk surface resistance (s m^{-1}), r_1 is the bulk stomatal resistance of the well-illuminated leaf (s m^{-1}), and LAI is the sunlit leaf area index [m^2 (leaf area) m^{-2} soil surface)]. Considering the fact that in general only half of dense grass contributes to the surface, LAI is equal to 24h where h is the crop height assuming to equal to 0.12 m, and the stomatal resistance r_1 of a single leaf equal to 100 s m^{-1}, Equation 5.4 may then be simplified to:

$$r_s = 70 \text{ s } m^{-1} \tag{5.5}$$

Figure 5.2 below describes the characteristics of the hypothetical reference crop method.

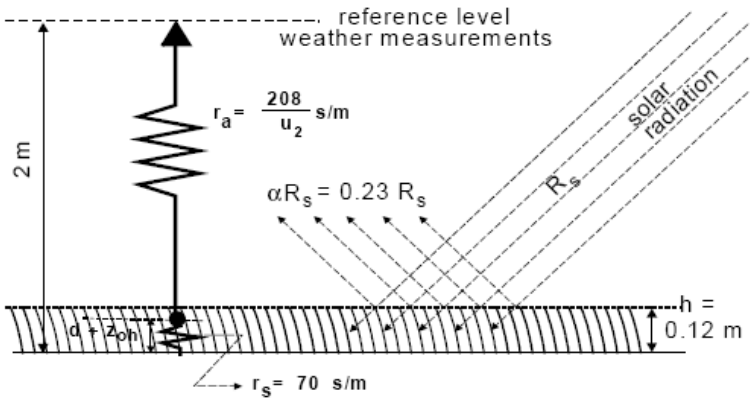

Figure 5.2: Characteristics of the hypothetical reference crop (FAO, 1998)

From the Equations 5.2, 5.3, and 5.5, the Penman-Monteith equation may be written as follows:

$$PE = \frac{0.408\Delta(Rn-G_o)+\gamma\frac{900}{T_a+273.16}u_2(e_s-e_a)}{\Delta+\gamma(1+0.34u_2)} \quad (5.6)$$

where PE is the reference evapotranspiration (mm day^{-1}), Rn is the net radiation at the crop surface (MJ m^{-2} day^{-1}), G is the soil heat flux density (MJ m^{-2} day^{-1}), Ta the mean daily air temperature (°C) at 2 m height, u_2 is the wind speed (m s^{-1}) at 2 m height, e_s is the saturation vapour pressure (kPa), e_a is the actual vapour pressure (kPa), e_s-e_a is the saturation vapour pressure (kPa), Δ is the slope vapour pressure curve (kPa °C), and γ is the psychrometric constant (kPa °C) (Tables 2.1 and 2.2). The equation uses climatological data and to ensure the integrity of the computations, the weather measurements should be made at 2 m above the green grass, shading the ground, and not short of water.

5.2.1.1 Model Inputs and Calculation Procedures

5.2.1.1.1 Mean Saturation Vapour Pressure (e_s)

Saturation vapour pressure is related to air temperature; therefore it can be calculated using this meteorological element based on the following equation:

$$e°(Ta) = 0.6108exp\left[\frac{17.27T_a}{T_a+237.3}\right] \quad (5.7)$$

where e°(Ta) is the saturation vapour pressure (kPa) at the air temperature Ta. But do to the non-linearity of the equation, the mean saturation vapour pressure for a day, week, decade, or a month should be computed as the mean between the saturation vapour pressure at the mean daily maximum and minimum air temperature as follows:

$$es = \frac{e°(T_{max})+e°(T_{min})}{2} \quad (5.8)$$

5.2.1.1.2 *Slope of Saturation Vapour Pressure Curve (Δ)*

The slope of the relationship between saturation vapour pressure and temperature, Δ, is a requirement for the calculation of evapotranspiration. It is given by the following formula (FAO, 1998):

$$\Delta = \frac{4098\left[0.6108exp\left(\frac{17.27T_a}{T_a+237.3}\right)\right]}{(T_a+237.3)^2} \tag{5.9}$$

where *Ta* is the mean air temperature in Celsius degrees.

5.2.1.1.3 *Actual Vapour Pressure (e_a)*

The actual vapour pressure, e_a, is the saturation vapour pressure at dew-point temperature that is defined as the temperature to which the air needs to be cooled to make the air saturated. It may be derived from either dew-point temperature, the psychrometric data (dry and wet bulb temperatures), and/or relative humidity data (FAO, 1998). One of the equations by which actual vapour pressure may be estimated is by:

$$e_a = \frac{RH_{mean}\left[\frac{e^\circ(RH_{max})+e^\circ(RH_{min})}{2}\right]}{100} \tag{5.10}$$

where RH_{mean} is the mean relative humidity defined as the average between maximum relative humidity, RH_{max}, and the minimum relative humidity, RH_{min}.

5.2.1.1.4 *Vapour Pressure Deficit (es-ea)*

The vapour pressure deficit is the difference between the saturation (e_s) and actual vapour pressure (e_a) for a given period of time. Mean saturation vapour pressure is computed from Equation 5.8 and e_a is computed using Equation 5.10.

5.2.1.1.5 *Soil Heat Flux (G)*

The soil heat flux, G, is the energy that is utilized in heating the soil. G is positive when the soil is warming and negative when the soil is cooling. Although soil heat flux is

considered a small value compared to net radiation (Rn) especially when the surface is covered by vegetation and calculation time is 24 hours or longer, the amount of energy gained or lost by the soil in this process should theoretically be subtracted or added to Rn when estimating evapotranspiration. Several models have been introduced to calculate soil heat flux, but a simple formula is presented below for monthly calculations based on the idea that the soil temperature follows air temperature (FAO, 1998):

$$G_{month,i} = 0.07(T_{month,i+1} - T_{month,i-1}) \quad (5.11)$$

Or, if $T_{month,i+1}$ is unknown:

$$G_{month,i} = 0.14(T_{month,i} - T_{month,i-1}) \quad (5.11a)$$

where $T_{month,i}$ is the mean air temperature of month i, $T_{month,i-1}$ is the mean air temperature of previous month, and $T_{month,i+1}$ is the mean air temperature of next month, all in degrees Celsius.

5.2.1.1.6 Net Radiation (Rn)

The net radiation is the difference between the incoming and the outgoing radiation of both short and long wavelengths. It is the balance between energy absorbed, reflected, and emitted by the earth's surface or the difference between incoming net shortwave (Rns) and the net outgoing longwave (Rnl) radiation. It is normally positive during the daytime and negative during the nighttimes.

$$Rn = Rns - Rnl \quad (5.12)$$

where Rns (MJ m^{-2} day^{-1}) may be expressed by the following equation:

$$Rns = (1-\alpha)Rs \quad (5.12a)$$

where α is the albedo or canopy reflection coefficient, which is 0.23 for the hypothetical grass reference crop, and Rs is the incoming solar radiation expressed by the below equation:

$$Rs = (a_s + b_s\, n/N)Ra \quad (5.12b)$$

where Rs is the solar or shortwave radiation (MJ m^{-2} day^{-1}), n is the actual duration of sunshine (hour), N is the maximum possible duration of sunshine or daylight hours (hour), n/N is the relative sunshine duration, Ra is the extraterrestrial radiation (MJ m^{-2} day^{-1}), as is the regression constant, and a_s+b_s is the fraction of extraterrestrial radiation reaching the earth on clear days. Where no actual solar radiation data is available and no calibration has been carried out for improved a_s and b_s parameters, the values a_s=0.25 and b_s=0.5 are recommended.

The extraterrestrial radiation for daily periods, Ra, can be estimated from the solar constant, the solar declination and the time of the year by (FAO, 1998):

$$Ra = \frac{24(60)}{\pi} G_{sc} d_r [\omega_s \sin(\varphi) \sin(\delta) + \cos(\varphi) \cos(\delta) \sin(\omega_s)] \quad (5.12c)$$

where Gsc is the solar constant= 0.0820 (MJm^{-2} min^{-1}), d_r is the inverse relative distance Earth-Sun, ω_s is the sunset hour angle (rad), φ is the latitude (rad), and δ is the solar declination (rad). The conversion from decimal degrees to radians is given by:

$$Radians = \pi/180 \text{ (decimal degrees)} \quad (5.12d)$$

The inverse relative distance Earth-Sun, d_r, the solar declination, δ, and the sunset hour angle, ω_s, are given by the following equations:

$$d_r = 1 + 0.33\cos(2\pi/365\ J) \quad (5.12e)$$

$$\delta = 0.409\sin(2\pi/365\ J - 1.39) \quad (5.12f)$$

$$\omega_s = \arccos[-\tan(\varphi)\tan(\delta)] \quad (5.12g)$$

where J is the number of the day in the year between 1 (1 January) and 365 or 366 (31 December). Values for J for all days of the year and an equation for estimating J are given in (Appendix 2.3).

The rate of longwave energy emission, Rnl, is proportional to the absolute temperature of the surface raised to the fourth power. The relation is expressed quantitatively by the Stefan-Boltzmann law. The net energy flux leaving the earth's surface is less than that emitted and given by the Stefan-Boltzmann law due to the absorption and downward

radiation from the sky. The net longwave radiation, Rnl, may be expressed by the following formula (FAO, 1998):

$$Rnl=\sigma\left[\frac{T_{max}K^4+T_{min}K^4}{2}\right]\left(0.34-0.14\sqrt{e_a}\right)\left(1.35\frac{R_s}{R_{so}}-0.35\right) \qquad (5.12h)$$

where Rnl is the net outgoing longwave radiation (MJm^{-2} day^{-1}), σ is the Stefan-Boltzmann constant (4.903×10^{-9} MJK^{-4} m^{-2} day^{-1}), T_{max}, K is the maximum absolute temperature during the 24-hour period, T_{min},K is the minimum absolute temperature during the 24-hour period, e_a is the actual vapour pressure (kPa), Rs/Rso is the relative shortwave radiation (limited to $\leq$1.0), Rs is the measured solar radiation (MJ m^{-2} day^{-1}) calculated from Equation 5.12b, and Rso is the calculated clear sky radiation (MJ m^{-2} day^{-1}). The clear sky solar radiation, Rso, when calibrated values for a_s and b_s are not available, it may written as:

$$Rso = (0.75 + 2\times10^{-5}z)Ra \qquad (5.12i)$$

where z is the station elevation above sea level in meters.

5.2.2 Thornthwaite Method

Thornthwaite (1948) has tried to establish a relationship between monthly precipitation/evaporation (P/E) and temperature (T) for the summer months in arid parts of the USA. The formula has been further modified by Crowe in 1971 to P/E=9P/(T-10). The Thornthwaite-Crowe simple formula is used to provide rough estimates of evapotranspiration in months of growing seasons in moderate climates. It may be usefully used when only precipitation and temperature data are available despite that its validity is still questionable (Shaw, 1983).

Further work on the above formula has resulted in an equation that is based on temperature with an adjustment being made for the number of daylight hours. The Thornthwaite model which estimates PE calculated on a monthly basis is given by:

$$PE = 16Nm(10Tm/I)a \qquad (5.13)$$

where m is the months 1, 2, 3, ...12, Nm is the monthly adjustment factor related to hours of daylight obtained from (Appendix 11.1.2 p273- Shaw, 1983) and dividing it by 12, Tm is the monthly mean temperature °C, I is the heat index for the year, given by:

$$I = \sum im = \sum(Tm/5)1.5 \qquad for\ m = 1, ...12 \qquad (5.13a)$$

and

$$a = 6.7\times10^{-7}I3 - 7.7\times10^{-5}I2 + 1.8\times10^{-2}I + 0.49 \qquad (5.13b)$$

5.2.3 Grindley's Soil Moisture Deficit Model

Water loss from a catchment area does not always proceed at a potential rate since this process is dependent on a continuous supply of water. When vegetation is no longer able to abstract water from the soil, actual evaporation (Ea) becomes less than potential (PE), thus the relation between Ea and PE depends upon the soil moisture content (Shaw, 1983). The Grindley (1970) soil moisture accounting method is examined as a combined approach with the Thornthwaite, Penman-Monteith, and pan evaporation methods. The Grindley's method has been credited for its capability to accurately model both Ea and soil moisture (Burt and Shahgedanova, 1998).

5.3 Crop Evapotranspiration (PEc)

Crop evapotranspiration may be estimated directly from cropped surface using the mass transfer and/or the energy balance methods. It may also be derived from soil water balance determined from cropped fields or from lysimeters. Another method that may be applied is the Penman-Monteith equation by adjusting the albedo and the aerodynamic and canopy surface resistances to the growing characteristics of the crop. But several challenges are present for accurate derivation: the albedo and aerodynamic and canopy resistances are difficult to estimate as they vary continually during the growing season, change of climate conditions, crop development, and the soil wetness (FAO, 1998).

For small cropping areas, the crop coefficient (Kc) approach may be used with acceptable accuracies. While for complex vegetated areas, other approaches are used.

In the crop coefficient approach, the crop evapotranspiration, PEc, is calculated by multiplying the reference crop evapotranspiration, PE, by a crop coefficient, Kc:

$$PEc = Kc \times PE \tag{5.14}$$

The reference crop evapotranspiration is defined using the FAO Penman-Monteith equation. Kc values range between 0.3-0.8 for several single-tree-species woodlands (Snyder *et al*., 1989; Rogers *et al*., 1983; FAO, 1998) while they are larger than 1 in close spacing of plants and taller canopy heights and roughness of full grown agricultural crops. The Kc values shown in Figure 5.3 below are typical values expected for average Kc under a standard climatic condition which is defined as a sub-humid climate with average daytime minimum relative humidity (RH_{min}) ≈ 45% and having calm to moderate wind speeds averaging 2 ms^{-1} (FAO, 1998).

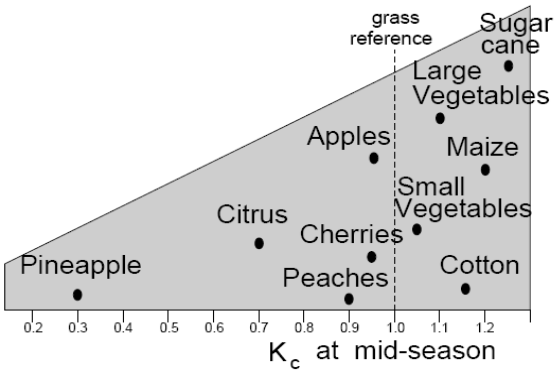

Figure 5.3: Typical Kc values by time for different types of full grown crops (FAO, 1998)

Alternative approaches include cross-validation of PE with local evaporation measurements such as pan evaporation, and the application of soil moisture deficit models.

5.4 Results and Discussion

5.4.1 Monthly Penman-Monteith

Table 5.1 presents PE estimates derived by Penman-Monteith method (equation 5.6) for year 2004 calculated for Jenin (north), Ramallah (central), and Hebron station (south).

Table 5.1: PE values for Jenin, Ramallah, and Hebron stations for the year 2004 derived by Penman-Monteith equation (mm month^{-1})

Month	Jenin	Ramallah	Hebron
January	41.0	36.9	33.4
February	47.1	48.5	37.2
March	82.0	101.8	77.2
April	114	125.7	106.5
May	145	161.5	144.9
June	147.9	163.4	177.5
July	174.8	183.6	202.8
August	171.4	163.1	174.5
September	135.4	148.6	135.6
October	109.9	119.2	101.8
November	62.5	71.1	68.4
December	39.4	54.7	50.1

Field observations of net radiation are not available and therefore are derived from air temperature differences, along with wind speed and air humidity data. Detailed calculations of the Penman equation applied to the three stations are presented statistically in Appendix 2.4-2.7.

To validate Penman-Monteith method, estimates are compared to the monthly records of Class A pan measurements for the three stations. Epan values are calculated using the pan coefficients (Kp) from look-up table derived by FAO (1998) where Jenin is given a Kp= 0.65, Ramallah Kp =0.60, and Hebron Kp =0.60.

Kp is derived in terms of evaporation pan type (Class-A pan), local wind speed, relative humidity, and land cover type in the pan area. Results from a linear regression model between Epan and Penman-Monteith PE for the three stations are shown in Figure 5.4.

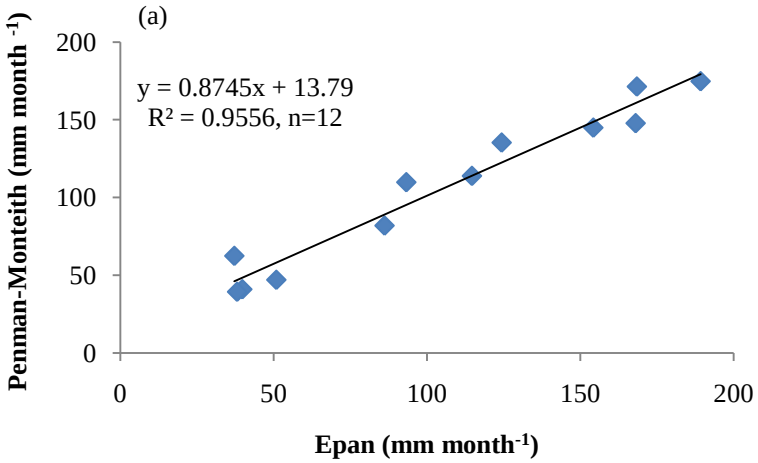

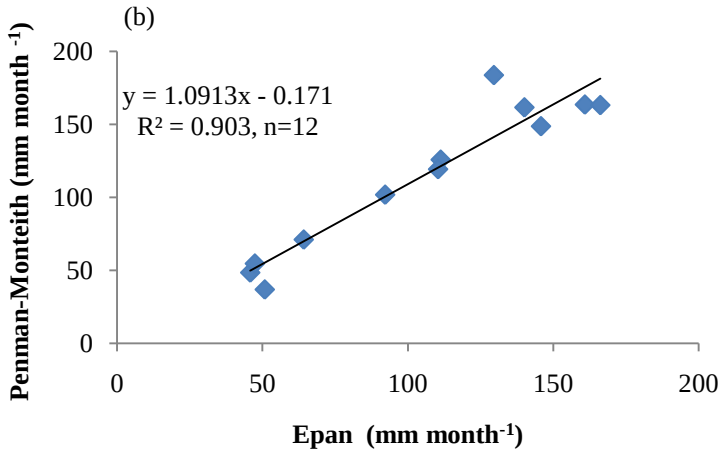

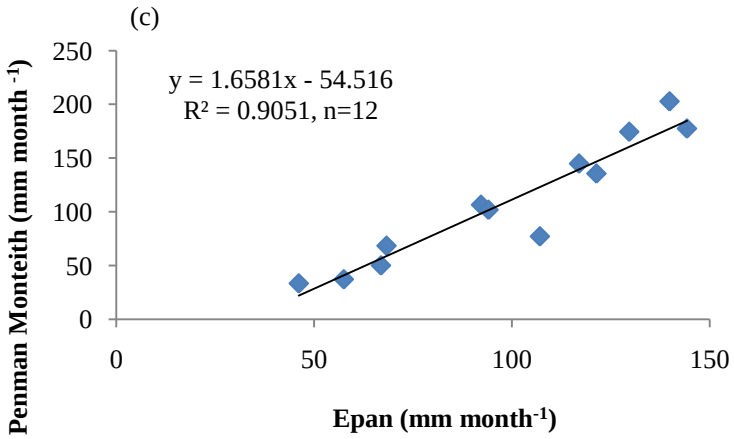

Figure 5.4: Linear regression between Epan and Penman-Monteith PE in: (a) Jenin, (b) Ramallah, and (c) Hebron

Results show that for the three stations, both estimates are in good agreement where the correlation for Jenin, Ramallah, and Hebron are R^2=0.9556, R^2=0.903, and R^2=0.9051, respectively. It may be noticed that Penman-Monteith are underestimated compared to Epan measurements in Jenin, overestimated in Hebron, and almost equal in Ramallah station. This is probably due to the fact that Jenin is a densely vegetated area, and vegetation in general does not radiate as perfectly as other bodies, such as bare soil found in Hebron. Penman-Monteith computations rely on temperature measurements and since dense vegetation areas experience cooler temperatures, the measured temperature by the instruments could be underestimated. Discrepancies may also be due to the estimated monthly Pan evaporation where some daily measurements are incomplete and therefore, inaccurate monthly estimates as seen from Figure (b) where the month of July has a Penman-Monteith PE of 183.6 and an Epan measurement of 129.6 mm $month^{-1}$. Moreover, the Penman- Monteith method is considered a temperature method and requires local calibration in order to achieve satisfactory results.

Such results are important for two main reasons: first the monthly, and therefore the daily, estimations of actual evapotranspiration of the Penman-Monteith method estimations, may be used with reasonable accuracy, and second it may be used as comparative and validation results for other empirical models.

FAO (1998) has recommended that further Kp increase adjustments of 5-10% should be applied in cases where evaporation pans are sited in non-agricultural environments such as grass surface, or where the pan is enclosed by tall crops; environment would differ significantly from the FAO look-up tables. Such adjustments are applied to Ramallah station as shown in Table 5.2.

Table 5.2: Relationship between 5, 8, and 10% adjustments of monthly Epan compared to Penman-Monteith estimates for Ramallah station

Month	Penman-Monteith	EPan	Kp=0.05	Kp=0.08	Kp=0.1
January	33.4	50.8	53.3	54.9	55.9
February	37.2	45.8	48.1	49.5	50.4
March	77.2	92.2	96.8	99.6	101.4
April	106.5	111.3	116.9	120.2	122.4
May	144.9	140.1	147.1	151.3	154.1
June	177.5	160.9	168.9	173.8	177.0
July	202.8	129.6	136.1	140.0	142.6
August	174.5	166.2	174.5	179.5	182.8
September	135.6	145.8	153.1	157.5	160.4
October	101.8	110.4	115.9	119.2	121.4
November	68.4	64.2	67.4	69.3	70.6
December	50.1	47.4	49.8	51.2	52.1

The results show that the 5% adjustment is more reflective of the accurate evapotranspiration in Ramallah station where overestimation of the dry summer values increases with the other adjustments. Such overestimating measurements of the pan may due to several reasons; first, improper installations of the pan where it should be installed inside a short green cropped area with a square size of at least 15×15 m, and second it should be installed at a distance at least 10 m from the green cropped edges in the general upwind direction (FAO, 1998). Other causes such as deterioration and repainting may also lead to such imprecise measurements and results.

Another method to estimate evapotranspiration from a cropped surface is the crop coefficient approach. It directly measures evapotranspiration rate by the mass transfer or the energy balance method. It can also be derived from meteorological and crop data by means of the Penman-Monteith equation.

The crop evapotranspiration, PEc, is calculated by multiplying the reference crop evapotranspiration, PE, by a crop coefficient, Kc:

$$PEc = Kc \times PEo \tag{5.15}$$

Weather conditions are incorporated into the PE estimates; therefore, Kc varies predominantly with the specific crop characteristics and only to a limited extent with climate (FAO, 1998). This enables the transfer of standard values for Kc between locations and climates. This is why Kc approach has been globally accepted and is considered a useful method.

The crop coefficient integrates the effect of characteristics that distinguish a typical field crop from the grass reference, which has a constant appearance and a complete ground cover. Consequently, different crops will have difference Kc coefficients. The changing characteristics of the crop over the growing season also affect the Kc coefficient. Finally, as evaporation is an integrated part of crop evapotranspiration, conditions affecting soil evaporation will also have an effect on Kc.

However, the FAO (1998) has recommended that the empirical crop coefficient of single crops can only be extended to land cover classes of the majority of the land cover within a cell equals this crop type or a crop type with comparable evaporative characteristics. As olive trees are the dominant crops in Jenin and Ramallah and Grapes in Hebron, crop coefficients of 0.7 and 0.85 are assigned for these stations, respectively. Figure 5.4 shows the correlation between Epan and PEc.

Correlations for Jenin and Hebron remained fixed as in the Penman-Monteith versus Epan measurements as indicated by Figure 5.4, while for Ramallah it has dropped from R^2=0.903 to R^2=0.8486. This could be attributed to the heterogeneity of Ramallah station where different vegetation crops exist in the same area.

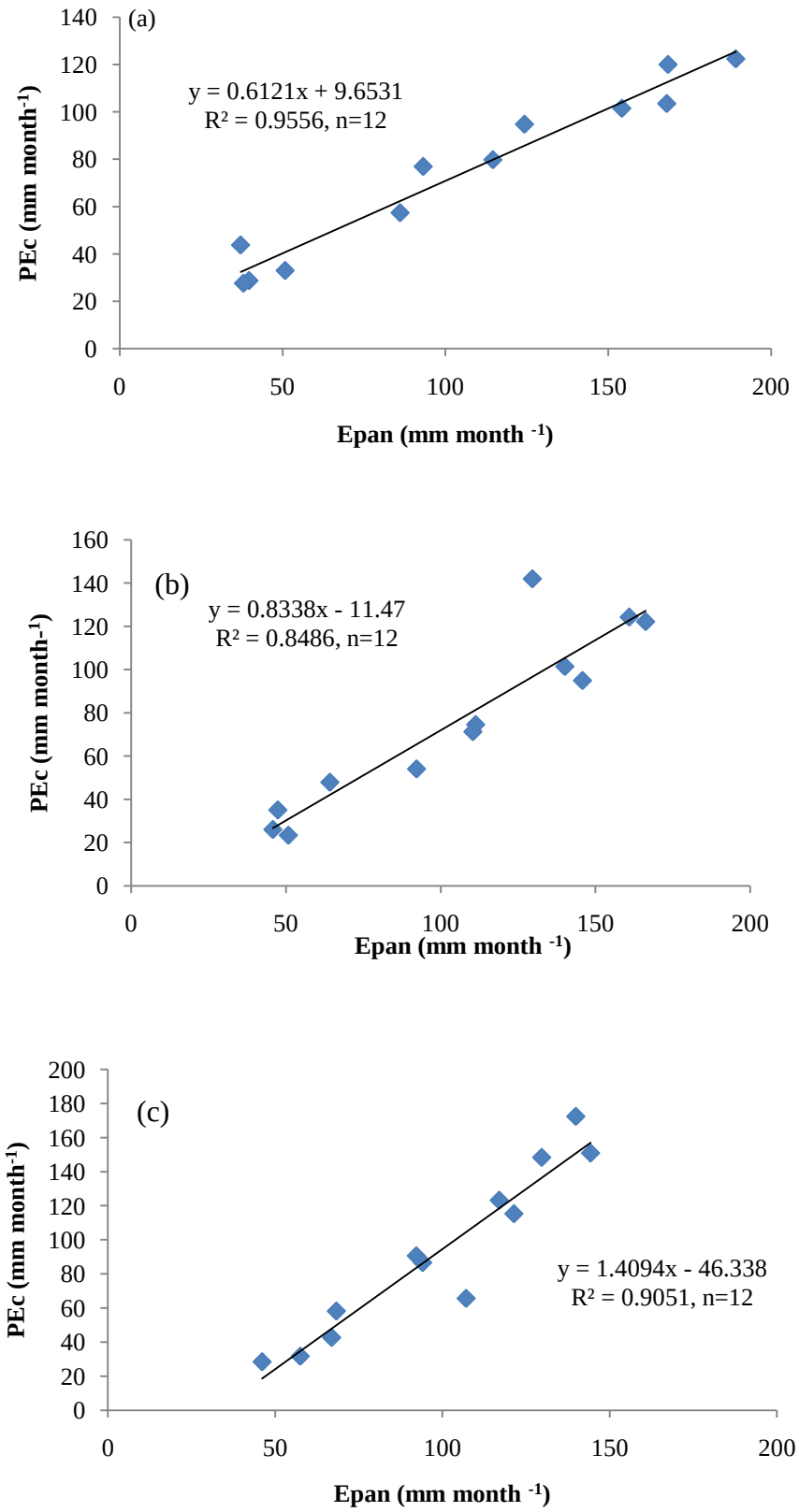

Figure 5.5: Predicted monthly crop evapotranspiration against Epan measurements for (a) Jenin, (b) Ramallah, and (c) Hebron

It is significant to note how Kc adjustment factors improves PE predictions but fails to overcome the complexities of the mixed natural vegetations. The Kc factors assumes unlimited soil water supply which is not the case in the West Bank. They are designed to estimate evapotranspiration for single crop stands which makes it difficult to apply for complex crops areas, and the environmental conditions such as height, canopy resistance, and vegetation soil albedo are hard to satisfy in the natural catchments of the area. Therefore, the Penman-Monteith-Kc adjustments are successfully applied to humid than to arid or semi-arid catchments (FAO, 1998; Shaw, 1994; Allen *et al*., 1992).

5.4.2 Thornthwaite Method

Monthly potential evapotranspiration (PE) values using the Thornthwaite formulas are calculated using the monthly mean temperature for year 2004. The stages in computations are shown in Table 5.3. Regression between Epan and Thornthwaite results are shown in Figure 5.6.

Table 5.3: Thornthwaite calculations and it relationship with Pan measurements for Jenin station

Month	Tm	Nm	i	Thornthwaite PE	Epan
January	11.7	0.85	3.58	19.31	39.7
February	12.7	0.92	4.05	24.91	50.8
March	16.5	0.99	5.99	47.80	86.1
April	18.9	1.08	7.35	70.00	114.6
May	22.1	1.15	9.29	104.67	154.2
June	24.7	1.19	10.98	137.90	168.0
July	27.9	1.18	13.18	178.17	189.2
August	27.3	1.11	12.76	160.85	168.4
September	26.1	1.03	11.93	135.39	124.4
October	24.5	0.95	10.85	108.37	93.2
November	17.2	0.87	6.38	45.78	37.1
December	11.7	0.83	3.58	18.84	38.0
		I=	99.9157		

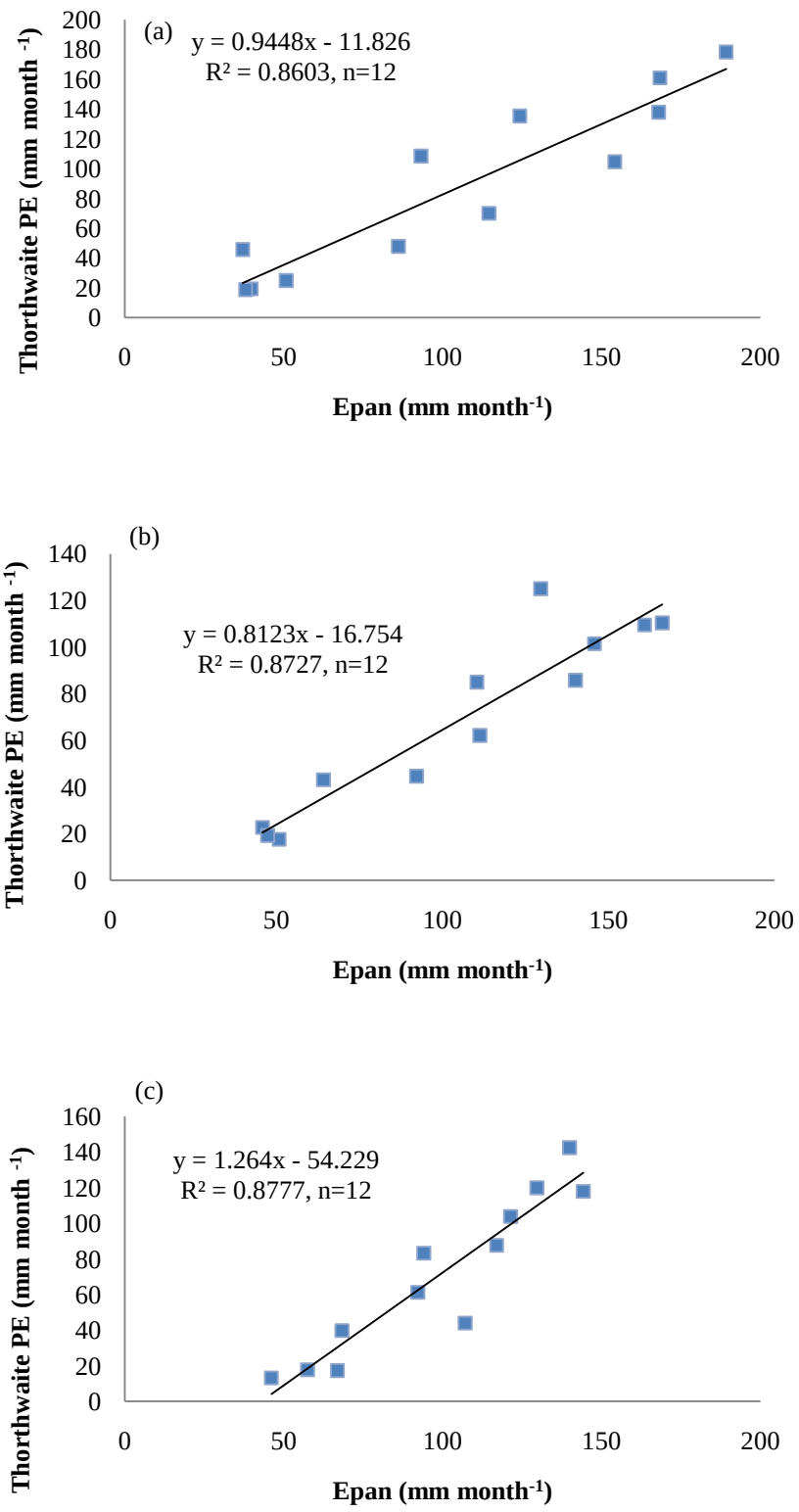

Figure 5.6: Relationship between Pan Evaporation and Thornthwaite model results in: (a) Jenin, (b) Ramallah, and (c) Hebron

The correlation between Thornthwaite's model results pan measurements are R^2=0.8603, R^2=0.8727, and R^2= 0.8777 for Jenin, Ramallah, and Hebron, respectively. Fits among pan measurements and Thornthwaite are seen to be less than those with Penman-Monteith. This may be due to the fact that; first, Thornthwaite is only based on mean temperatures disregarding humidity and vegetation and second, Thornthwaite is only considered valid in climates similar to that area where it is developed and that is the Eastern USA (Shaw, 1994).

5.4.3 Soil Moisture Deficit

Grindley's (1970) soil moisture method (SMD) is considered one of the most appropriate ways of estimating local actual evapotranspiration, Ea, and water balance. It is used to validate actual evapotranspiration estimates by other models. It involves information on rainfall and PE data (Burt and Shahgedanova, 1998; Shaw, 1994, Karongo and Sharma, 1997). The Grindley model relates potential evapotranspiration with soil moisture deficit and root constant. The root constant is described by Penman (1948) as a characteristic of vegetation and it determines how fast a crop's evapotranspiration falls below the prevailing potential evapotranspiration. Three PE approaches are examined, the Penman-Monteith, Thornthwaite and Pan measurements methods.

For catchment areas, water does not always proceed at the potential rate; it depends on the continuous supply of soil water. The Grindley method tracks vegetation soil moisture abstraction and its relationship with potential and actual water losses. It may be feasible to evaluate drought occurrence as well as soil field capacity, i.e Ea<PE when vegetation is unable to abstract water from the soil, and Ea=PE when the soil is at field capacity (Shaw, 1994). Table 5.4 highlight this point and presents further details about Ea calculations.

Aggregated PE results derived from Penman-Monteith, Thornthwaite methods, Pan evaporation, and monthly rainfall for the year 2004 are the data input for applying the model. The following example has been applied to Jenin area using Penman-Monteith estimates and it shows the detailed procedure of SMD as described in Shaw (1994).

Table 5.4: Calculation of soil moisture deficit (SMD) and Ea for Jenin (2004)

Month	Rainfall (P)	Potential Penman-Monteith Evaporation (PE)	P -PE	Potential Soil Moisture Deficit (PSMD)	SMD at 75mm Root Constant (RC75)	Actual Evapotran spiration
	1	**2**	**3**	**4**	**5**	**6**
October				**125**	**125**	
November	86.2	64.62	21.59	103.42	101	64.62
December	43.9	39.45	4.46	98.96	98	39.45
January	175.9	41.05	134.85	0.00	0	41.05
February	94.6	52.16	42.44	0.00	0	52.16
March	8.1	81.98	-73.88	73.88	74	81.98
April	15.1	117.76	-102.66	176.55	115	56.10
May	1.0	144.99	-143.99	320.53	125	11.00
June	0.0	152.80	-152.80	473.33	125	0.00
July	0.0	174.84	-174.84	648.17	125	0.00
August	0.0	171.43	-171.43	819.60	125	0.00
September	0.0	139.92	-139.92	959.52	125	0.00
October	0.0	109.89	-109.89	1069.40	125	0.00

*until potential SMD reaches 125 mm, actual ET= potential ET

Step1: Column 1 represents the mean monthly rainfall; Column 2 (PE) is calculated using Penman-Monteith equation.

Step2: Column 3 is then calculated as the difference between monthly rainfall and Penman-Monteith PE (Column1 – Column2).

Step3: Potential soil moisture deficit (PSMD) is defined as the moisture deficit that would result if the potential evaporation is always fulfilled. It is the aggregate of the difference between P and PE considered as a deficit and is assumed to apply to the riparian lands or above field capacity (Shaw, 1983; 1994). The actual soil moisture deficit (ASMD) follows the PSMD until it reaches the vegetation zone maximum of 75 mm. Given that the month of October is the beginning of winter season, the soil deficit is at its highest, i.e. 125 mm. PSMD of next month is calculated by subtracting the difference

between rainfall and PE of that month from the PSMD of previous month. For example, PSMD of November equals 125- 21.59 = 103.42 mm.

***Step4**:* Based on the assumption that the main vegetation class for Jenin (as well as for Ramallah and Hebron) is mainly grass and vegetation, the root constant value assumed is 75 mm. The actual soil moisture deficits, Column 5, are reconstructed from published look-up tables (UK Meteorological Office Hydrological Memorandum No. 38) and reproduced by Shaw (1983) in her hydrology textbook as Appendix 11.3.1 p. 280. The soil moisture deficit for PSMD values greater than 300 mm is assumed constant and equal to 125 mm.

***Step5**:* The actual evapotranspiration, Ea, (Column 6) for a particular month is then calculated as the change in soil moisture deficit plus the rainfall. For example, Ea for February is calculated as: *Ea = SMD April- SMD March + April Rainfall = 56.1 mm*. Actual evapotranspiration is equal to the potential where the soil moisture deficit is zero. Also January and February are the two months of excess water where potential soil moisture deficit of previous month is less than (P-PE) of that month. For example, PSMD for December is 98.96 mm and (P-PE) for January= 134.85 mm, so excess water going to recharge equals 35.9 mm.

Actual evapotranspiration results of Penman-Monteith, Thornthwaite, pan evaporation applying the soil moisture deficit are illustrated in Figure 5.7.

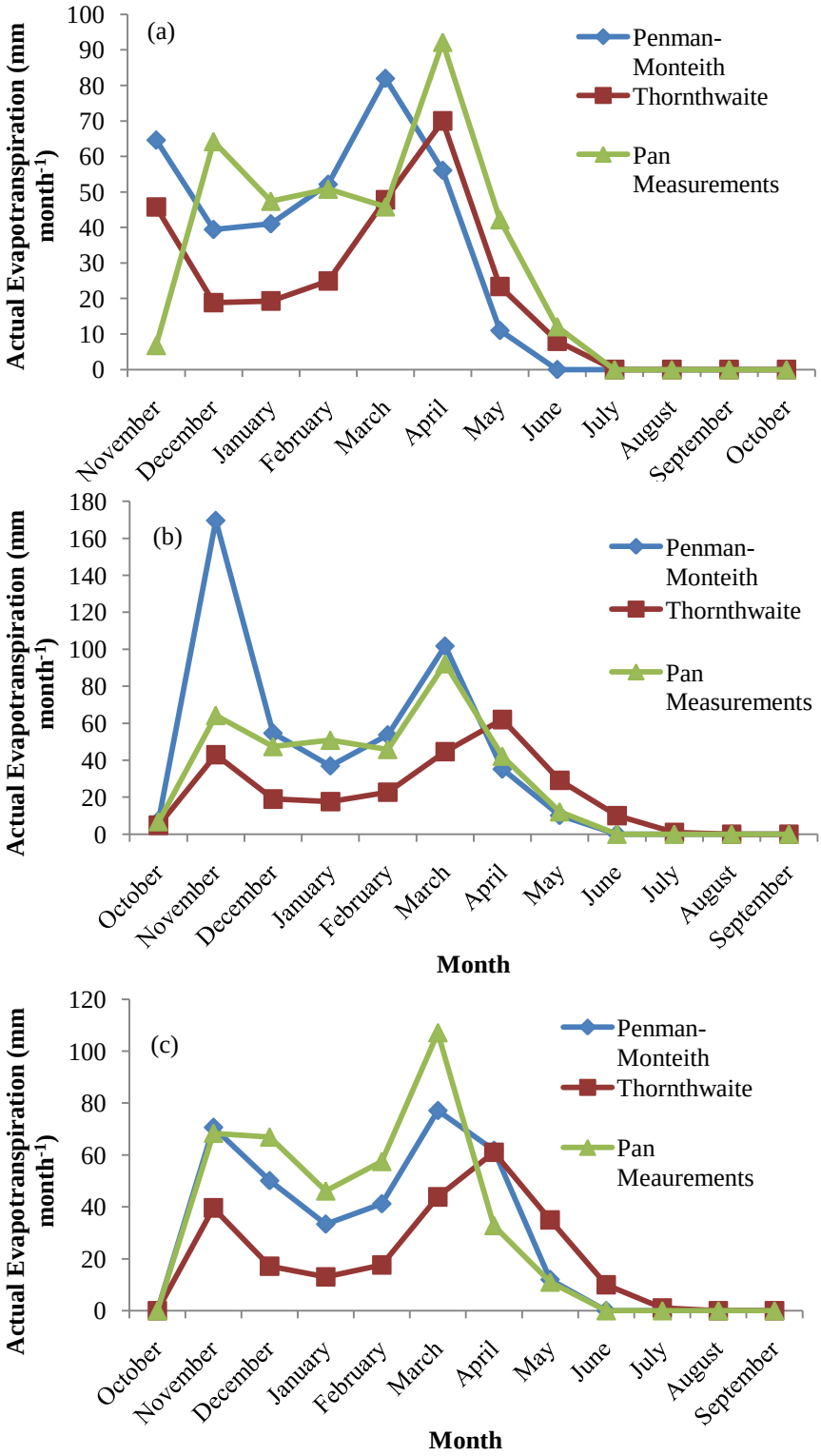

Figure 5.7: Actual Evapotranspiration of Penman-Monteith, Thornthwaite, and pan measurements based on the Grindley soil moisture deficit integrated method for (a) Jenin, (b) Ramallah, and (c) Hebron

Actual evapotranspiration is at its highest at the end of the winter season reaching zero in the summer months. During the spring when potential evapotranspiration exceeds rainfall, the soil moisture deficit begins in the surface soil and moves further downwards into the lower layers until the summer months. And when rainfall totals begin to exceed potential evapotranspiration in the autumn starting from October-November, the soil moisture stores are gradually replenished from top soil layers downwards until they all reach field capacity again in winter. Figure 5.7 shows variations in the monthly Ea estimates. Pan measurements are almost higher than the other two methods estimates in the three stations, while Thornthwaite is the lowest. This may be due to the difference in PE inputs for the each method and the uncertainties in measurements obtained from the field as explained in Chapter 2. Results accuracy is dependent on the field measurements and on a more accurate estimation of proportions of vegetation types and consequently the derivation of root constant. Penman-Monteith gives acceptable monthly estimates but estimates can be very sensitive to errors in determining its variables.

5.5 Summary

This chapter has demonstrated how potential evapotranspiration are determined on a local scale for Jenin, Ramallah, and Hebron using Penman-Monteith, Thornthwaite and pan measurements. The Penman-Monteith method is considered a preferred model for evaporation estimations due to its better predictive power whilst the Thornthwaite approach is considered a less data-intensive approach. Potential evapotranspiration using Penman-Monteith and Thornthwaite methods is determined from meteorological data while it is obtained from the evaporation loss from a water surface through Pan-A class evaporation measurements. The main input parameters are mean monthly rainfall, temperature, wind speed, humidity, and daily radiation. Potential evapotranspiration is later applied to Grindley's soil moisture deficit method to obtain actual evapotranspiration.

To evaluate the accuracy of Penman-Monteith and Thornthwaite outputs, potential evapotranspiration results are compared to the local Class-A pan evaporation records over the same year. Pan measurements exaggerated estimated values therefore there has been a need to apply the FAO pan coefficients (Kp). Kp values of 0.6 and 0.65 are

applied for Ramallah and Hebron and Jenin based on relative humidity, wind speed and distance of pan from green crops. Comparison results show that for the three stations, both methods produce good agreement with pan measurements where the correlation for Jenin, Ramallah, and Hebron are R^2= 0.9556, R^2= 0.903, and R^2= 0.9051, respectively. However, it is noticed that Penman-Monteith underestimates evapotranspiration in Jenin, overestimates it in Hebron, and almost is equal in Ramallah. This could be due to the dense vegetation in Jenin that does not radiate as perfectly as other bodies such as bare soil or shrubs.

To obtain actual estimates, monthly potential values from Thornthwaite, Penman-Monteith, and pan measurements are incorporated into Grindley's (1970) soil moisture balance model. The Grindley model relates potential evapotranspiration with soil moisture deficit and root constant. Its application is considered instructive in many ways: first, it shows how vegetation water uptake is contributing to the actual evapotranspiration, second, it is an indicator of soil moisture deficits, and thirdly, it signifies information for water resources management. However, assuming a root constant in estimating actual evapotranspiration throughout the growing period, ignoring the type of soil and growth stages, could have errors in the case of annual crop where crop stages vary with time. Grindley models result a distinctive actual evapotranspiration peaks at the end of the winter season and zero values in the summer months. This is attributed to the fact that water content in the topsoil drops and the soil surface starts to dry out. In the absence of water supply to the soil surface, evapotranspiration decreases rapidly and ceases almost completely at the beginning of dry season. Recharge takes place mainly in January and February months as indicated by the soil moisture deficit calculations where potential soil moisture deficit is less than the difference between rainfall and evapotranspiration. The three approaches have produced similar results but with some variations in certain months. These variations are explained by the different inputs of each model and data used. The results are considered inconclusive as require further research as field data of actual evapotranspiration is lacking. Nevertheless, the integrated three methods with Grindley's approach can be used as a useful approach for estimating actual evapotranspiration especially in the West Bank that is considered a data-stress area.

The final parameter derived from satellite imagery to be integrated within the recharge model is land cover classification. Classification methods and results are presented in Chapter Six and the impact of their changes in 1994 and 2004 is evaluated in Chapter 8.

Chapter Six

Land Cover Classification

6.1 Introduction

In this study, land cover classification is used to extract land cover types that are of interest to the recharge process. There are other applications for image classification such as estimating water use by irrigated crops by classifying areas of different crops and then assigning consumptive use values for each crop. In addition, groundwater uptake by trees can be quantified by trees species classification and measurement of evapotranspiration of each type.

Several land cover/land use mapping exercises have been undertaken in the West Bank using visual interpretation of different satellite images. They have been classified on several levels of categories such as the CORINE (Coordination of Information on the Environment) land cover initiative led by the European Environment Agency. These data provide a general observation of land cover/land use changes, and useful information for fieldwork. However, they are not suitable for the current study and its purposes for several reasons. First, some of the available land cover data have been extracted and delineated by polygons using visual interpretation based on image texture and features colours of the satellite images. Such methodology is considered biased as it relies on the interpreter's skills and visual judgements of the area and not on the spectral value of the training sites. Second, for some of these data, the source and methodology are unknown such as the 1994 land cover classification brought from the Land Research Centre. Classification is not supplemented by any details of methodology; therefore, its reliability is uncertain. Third, there is a huge lack of a national GIS database updated by relevant organizations such as the Ministry of Agriculture or the Ministry of Public Works and Housing. As a result, no agricultural maps or basemaps can be provided for validation of the classified data.

To study the impact of land cover changes on recharge, image classification of the two SPOT images acquired in 1994 and 2004 are carried out. Monthly vegetation densities,

e.g. the Normalized Difference Vegetation Index (NDVI) are used to study the seasonal growth of vegetation and the presence of groundwater. Areas with denser vegetation may indicate areas of higher rainfall and occurrence of recharge.

6.2 Change Detection

Different land cover change detection algorithms are used in remote sensing. Image differencing, image rationing, image regression, and change vector analysis are some of the widely used algorithms. Each has its own merits and no single approach is considered optimal or applicable to all cases. For instance, image differencing is a common change detection approach for forested and agricultural areas (Singh, 1989; Fung, 1990). Image rationing mitigates the effects of topology like shadowing and illumination (Berberoglu and Akin, 2009). Regression methods reduce the adverse effects from divergence in atmospheric conditions and/or sun angles (Coppin and Bauer, 1996), and the change vector analysis detects changes present in the input of multispectral data (Berberoglu and Akin, 2009).

The large variety of change detection techniques within the literature produces various results due to the characteristics of the remotely sensed data, physical environment, and image processing methods. The West Bank as part of the Mediterranean environment limits the capability of some of the above-mentioned remote sensing techniques (Berberoglu and Akin, 2009). This is due to: (a) the high temporal variability of the spectral properties of major land covers causes large class spectral variability; (b) scene complexity due to varied spatial frequency of the landscape; (c) the similar reflectance properties of major land covers makes spectral separation difficult. For instance, soil can have similar reflectance properties to urban areas and similar near-infrared reflectance to a crop canopy. As a result, monitoring land cover change in the West Bank becomes a difficult task.

In this study, change detection has been carried out through the comparative analysis of the spectral classifications for 1994 and 2004. SPOT data of both dates are independently classified using the maximum likelihood classifier and then compared. Spectral classification is performed using SPOT-5 HRG (High Resolution Geometric) image while SPOT-2 HRV (High Resolution Visible) image classification uses the

spectral information in addition to the information supplied by the texture of the image. Texture analysis has been used to introduce spatial information for the different object classes into classification. Several authors have demonstrated that structural and spectral information can lead to significant improvements in classification accuracy especially for built up areas, green houses, and bare soil (Aguera *et al*., 2008; Puissant *et al*., 2005; Gong and Howarth, 1990). The output image generated by texture analysis is then used as an additional band together with the other multispectral bands in image classification.

Several studies propose change detection techniques for monitoring land use change based on changes in the Normalized Difference Vegetation Index (NDVI). NDVI is defined as the normalized difference between near infrared and visible reflectance. It is the measurement of the photosynthesis capacity of vegetation that is linearly related to the absorbed fraction of photosynthetically active radiation (Torres-Vera *et al*., 2009). NDVI is derived from the two SPOT images in addition to twelve MODIS Level 1B images for the year 2004. NDVI is regarded as an effective method to enhance the difference among spectral features and suppress topographic and shade effects. Therefore, the difference or ratio of NDVI between two dates has a potential to detect land cover change more effectively (Lu *et al*., 2005; Berberoglu and Akin, 2009; Mas, 1999).

6.3 Image Classification

Classification algorithms attempt to reduce the information contained in multi-band spectral reflectance imagery to a single thematic map by assigning each multi-band pixel to one of a limited number of classes. The thematic class to which a pixel is assigned is generally determined by some measures of similarity of the spectral reflectance of that pixel to the characteristic spectral reflectance of a particular class. This similarity is based on the evaluation of proximity to the region of the spectral feature associated with that land cover class (Torres-Vera *et al*., 2009).

The overall objective of the SPOT images classification is to categorize all pixels into land cover classes to be used as input for recharge estimation. The spectral patterns present within the data for each pixel are used as the numerical basis for categorization, i.e. the different features manifest different combinations of digital numbers (DN) based

on their inherent spectral reflectance and emittance properties. Historically, the spectral approaches have formed the backbone of the multispectral classification. However, with the current wide-scale availability of high-resolution data, there has been an increase use of spatially oriented procedures. Multispectral classification may be performed using a variety of algorithms, among which is supervised classification.

In the supervised classification, identification and location of the West Bank land cover types, such as urban, agriculture, or wetland, are known *a priori* through fieldwork that has been carried out and through personal experience. In other words, pixel categorization process is supervised by specifying, to the computer algorithm, numerical descriptors that represent homogenous examples of the various known land cover types present in the scene. These areas are known or referred to as training sites because the spectral characteristics of these known areas are used to train the classification algorithm for land cover mapping of the remainder of the image. Statistical parameters such as means, standard deviations, covariance matrices, and correlation matrices are calculated for each training site. Every pixel within and outside these training sites is then evaluated and assigned to the class of which it has the highest likelihood of being a member. This is often referred to as a hard classification because a pixel is assigned to only one class, for instance forest, even though the sensor system records radiant flux from a mixture of biophysical materials, for example, 10% bare soil, 20% shrubs, and 70% forest.

The general steps followed to extract land cover information are summarized in Figure 6.1 and described in detail as follows:

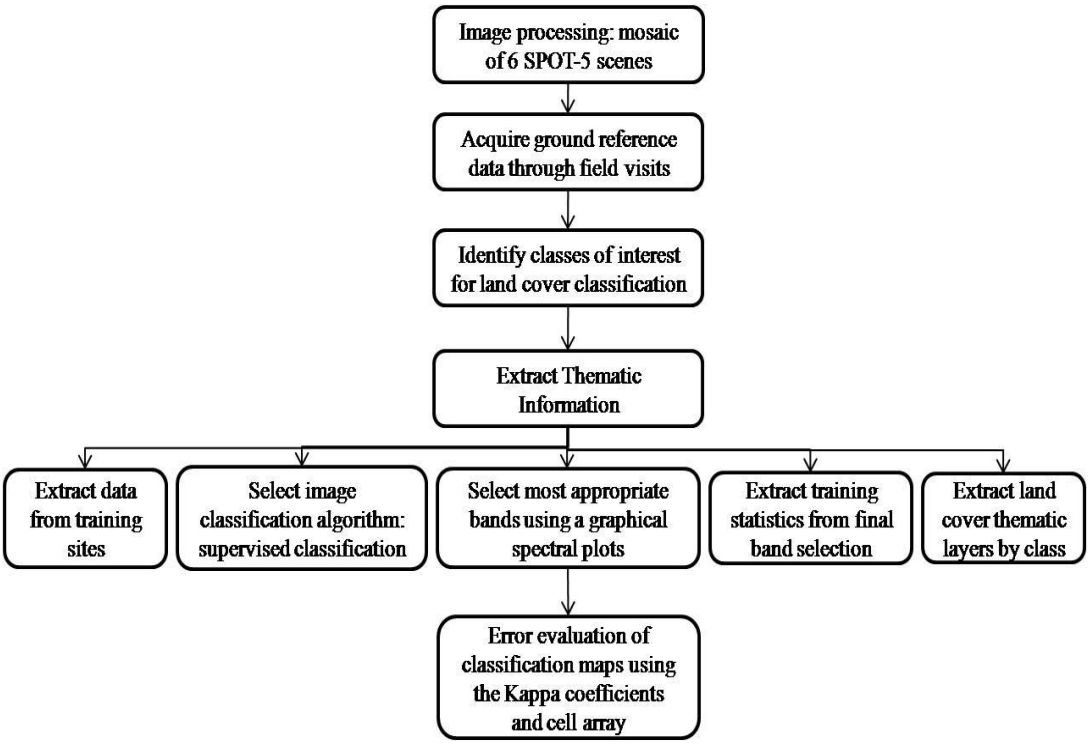

Figure 6.1: General steps used to extract land cover maps from digital remote sensing data

Step 1: Image Processing of SPOT-5 HRG

SPOT images are bought with radiometric and geometric corrections already done by SPOT Image as explained in Chapter 2. However, SPOT-5 HRG is provided in scenes. Six scenes cover the West Bank area that had to be mosaiced to perform classification (Figure 6.2). Mosaicing the scenes did not affect classification or altered the DN of the image, but merged the scenes into one regional image.

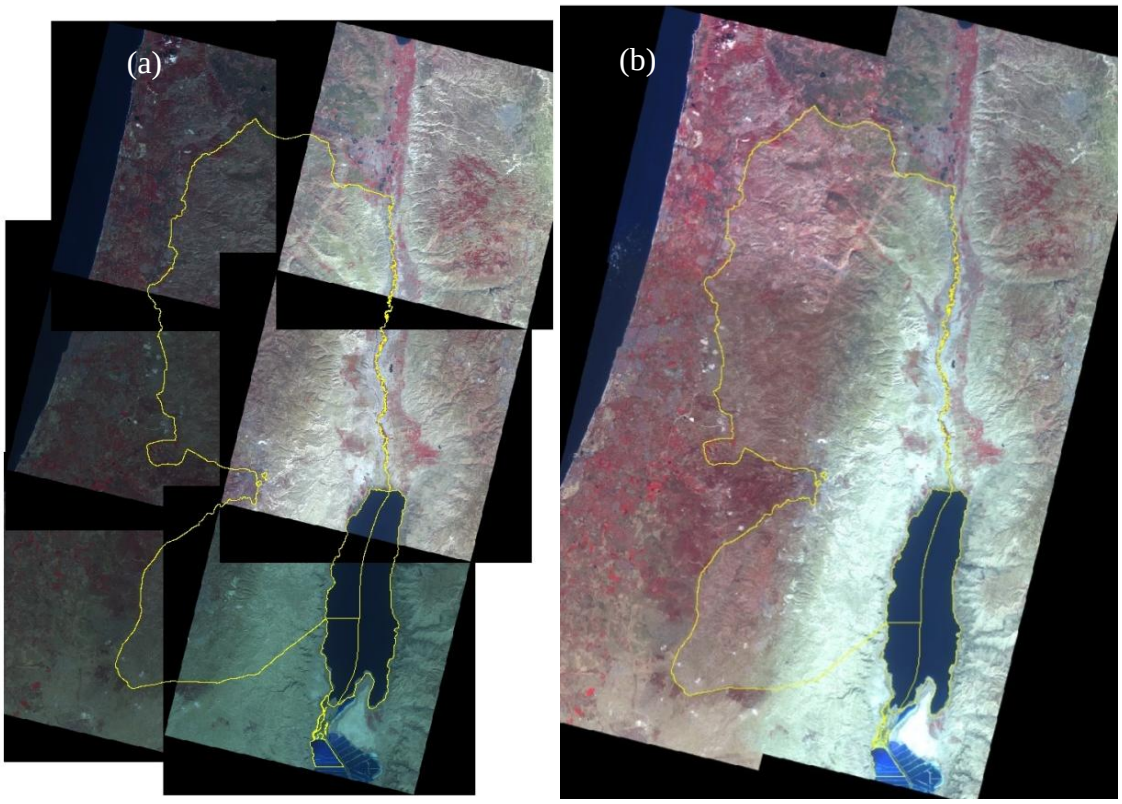

Figure 6.2: (a) SPOT-5 scenes (b) mosaiced SPOT-5 using ERDAS Imagine 9.2

Classification is then carried out on governorate scale (Figure 6.4). During classification, it became apparent that different land covers of the West Bank area have similar spectral bands on the graphical plot such as the urban areas and bare soil. This has led to enormous misclassification of the area as shown in Figure 6.3. Therefore, it has been decided to perform classification on smaller scale, i.e. governorate scale (district scale).

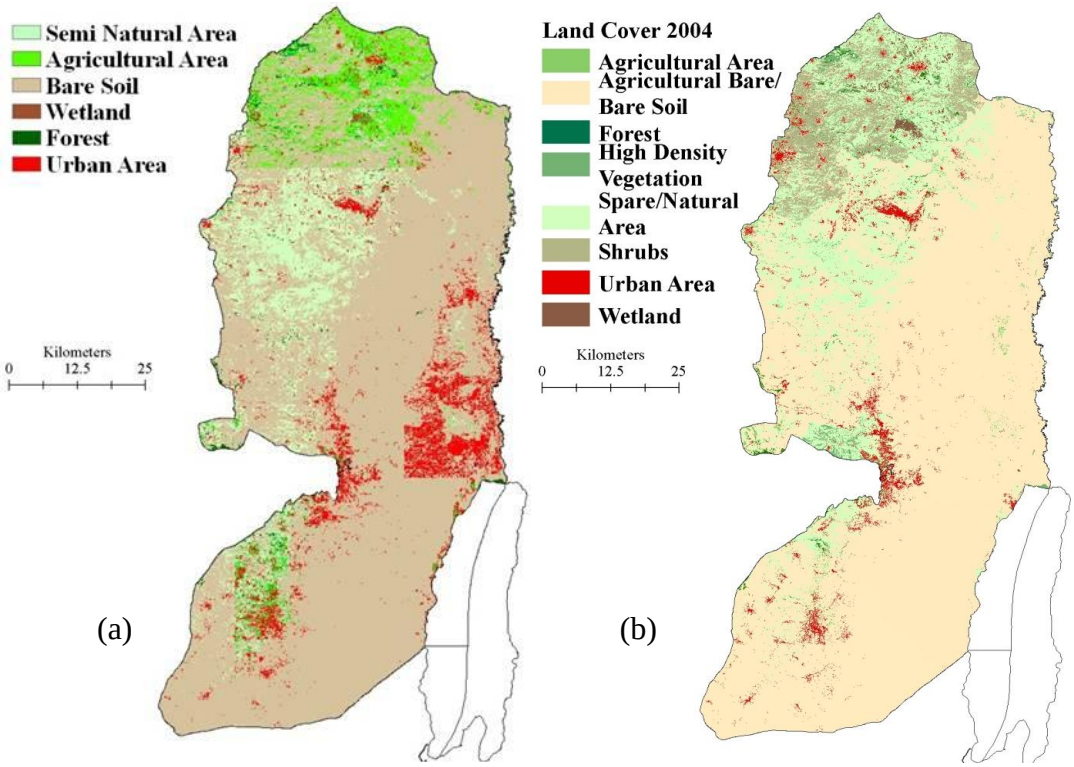

Figure 6.3: (a) Classification on regional basis and (b) classification on governorate scale

Step 2: Identifying Representative Training Samples

Information and pictures of different land covers in the West Bank have been collected to define the spectral signatures of these classes and evaluate classifications. After sites are visited in the field, training samples representing land cover classes of interest are selected according to the classification scheme adopted. The training sites are obtained from relatively homogenous environments through on-screen selection and digitizing of training data.

Step 3: Identify Land Cover Classes

All classes of interest are carefully selected and defined to classify the images into land cover information. It is worth noting that there is a fundamental difference between information classes and spectral classes. The information classes are those that human beings define, while the spectral classes are those that are inherent in the remote sensor data and must be identified and then labelled by the analyst (Jensen, 1996). For

example, in a remotely sensed image of an urban area there is likely to be a single-family residential housing. A relatively high spatial resolution, 20×20 m, remote sensor such as the SPOT-2 HRV image might be able to record a few pixels of vegetation and a few pure pixels of asphalt road or shrubs. However, it is more likely that in this residential area the pixel brightness values will be a function of the reflectance from mixtures of vegetation and concrete. Therefore, the mixture class is renamed as a single family, e.g. residential. This is done only when there has been a good association between the mixture class and the single-family residential housing.

Step 4: Categorizing Training Samples

Spectral separability of training samples within each feature class is evaluated. A second spectral separability including each two-feature classes is evaluated to ensure that each pixel is categorized into the land cover it most closely resembles and that no overlapping of pixel classification is taking place. In addition, histograms are examined and an overall evaluation of all feature classes is performed using contingency matrices and divergence.

Step 5: Supervised Classification

Supervised classification is found to be more appropriate and less sensitive to radiometric variations when dealing with two scenes captured at different dates (Mas, 1999). A one-level classification scheme with eight initial classes is introduced in the supervised classification. They are selected according to the needs of recharge estimations and its hydrological mechanism. The eight classes are: (1) urban, (2) forest, (3) high-density vegetation, (4) agriculture, (5) sparse/natural vegetation, (6) shrubs/natural grassland, (7) wetland vegetation, and (8) bare soil and vegetation bare. The resulting classes are examined both spectrally and spatially with ground information from Google earth and field photos and they corresponded to the following land covers:

(1) Urban: Areas of high residential and residential, commercial, industrial, roads, and large houses.
(2) Forest: includes broad-leaf, coniferous, and mixed forests.

(3) High density vegetation: non-forest areas, healthy crops, vegetation with large leaves areas, and olive groves.
(4) Agriculture: includes rainfed and irrigated agricultural areas, permanent crops, vineyards, and pastures.
(5) Sparse/ natural vegetation: small leaf vegetation areas.
(6) Shrubs/ natural grass land: shrubs and grass areas.
(7) Wetland vegetation: includes inland marshes and seasonally water logged areas.
(8) Bare soil and vegetation bare: areas without vegetation cover, abandoned cropland, and sandy soil.

The characteristic signatures from these classes are then used as input to a maximum likelihood classification process, which allocates pixels to the class to which they have the highest probability of belonging. The supervised classification is performed using the maximum likelihood algorithm in the ERDAS Imagine software. The classes selected are utilized in the classification process of both the SPOT-2 HRV and SPOT-5 HRG images, to facilitate the comparison in the multi-temporal image suite.

The maximum likelihood decision rule assigns each pixel having pattern measurements or features to the most probable class. It assumes that the training data statistics for each class in each band are normally distributed, that is, the Gaussian where both the variance and covariance of the category spectral response patterns are quantitatively evaluated. Given these parameters, the statistical probability of a given pixel value being a member of a certain land cover class is computed. Several studies have successfully used this classification method, e.g. Gong *et al*., (2003), Green *et al*., (1998), Gao (1999), Lee *et al*., (2003), Wang *et al*., (2004), Puissant *et al*., (2005) and Aguera *et al*., (2008).

Classification is applied on governorate scale (Figure 6.4) as described in ***step 1*** where each governorate is classified separately. This is done to avoid the similarity of pixel signature values of different classes in different areas and the influence of image mosaicing.

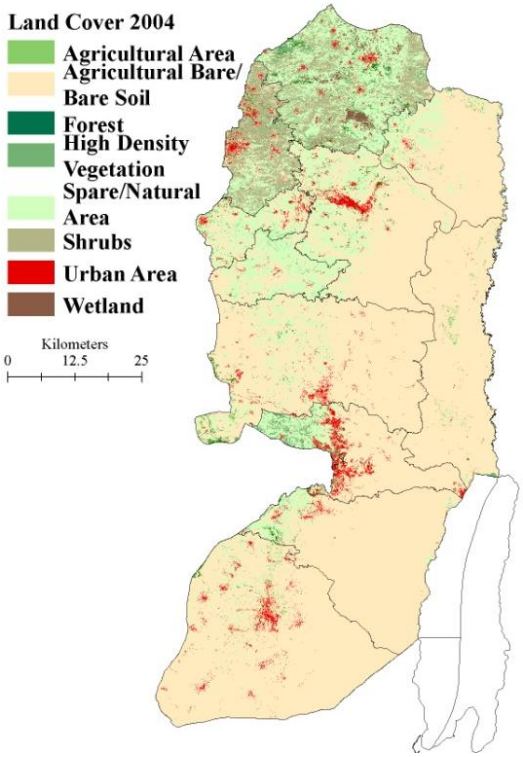

Figure 6.4: Classification on governorate scale

Step 6: Classification Accuracy Assessment

A quantitative evaluation of classification accuracy is done through choosing a set of pixels on the classified image and then comparing them to the actual image and ground truth data through blending tool in ERDAS Imagine software.

To perform quantitative classification accuracy assessment, it is necessary to compare two sources of information: first, the remote sensing derived classification data and second, what is called reference test information. The relationship between these two sets of information is summarized in a CellArray. The CellArray is a list of class values for the pixels in the classified image and the corresponding reference image (Leica Geosystems, 2003) where the class values for the reference are based on ground truth data and the Cell Array data is retrieved from the image file.

From the CellArray assessment, two reports are derived: the error matrix comparing reference points to classified points, and the accuracy report. The error matrix is a square array of numbers laid out in rows and columns that express the number of

sample units assigned to a particular category relative to the actual category as verified in the field. The columns usually represent the reference data, while the rows indicate the classification generated from the remotely sensed data. It is considered an effective way to represent accuracy because accuracy of each category is clearly described.

Once accuracy data are collected and summarized in the error matrices, they are subjected to detailed interpretation and further statistical analysis. The Kappa coefficient is used to express the proportionate reduction in error generated by the classification compared with the error of a random classification (Leica Geosystems, 2003). It is a discrete multivariate technique that is used in accuracy assessments (Jensen, 1996). Kappa analysis yields a *K*hat statistics (an estimation of Kappa) which measures the difference between actual agreement in the error matrix (i.e., the agreement between the remotely sensed classification and the reference data), and the chance agreement between the reference data and a random classifier (Lillesand *et al*., 2008). Consequently, *K*hat, is defined as:

$$\textit{K}\text{hat} = \frac{\text{observed accuracy- chance agreement}}{1 - \text{Chance agreement}} \qquad (6.1)$$

Such a statistic serves as an indicator of the extent to which the percentage correct values of an error matrix are due to true agreement versus the chance agreement. As the true agreement or the observed agreement approaches 1 and chance agreement approaches 0, *K*hat approaches 1 which is considered the ideal case. In actual classification, usually *K*hat ranges between 0 and 1. For instance, a *K*hat value of 0.67 indicates that the observed classification is 67 percent better than the one resulting from chance. A *K*hat of 0 indicates that a given classification is no better than random classification or assignment of pixels while if *K*hat takes negative values, then it is an indication of very poor classification.

The *K*hat statistic is computed as:

$$\textit{K}\text{hat} = \frac{\text{N} \sum_{i=1}^{r} xii - \sum_{i=1}^{r} (xi+ . x + i)}{\text{N2} - \sum_{i=1}^{r} (xi+ . x + i)} \qquad (6.2)$$

where

r = number of rows in the error matrix

x*ii* = number of observations in row *i* and column *I* (on the major diagonal)

x*i*+ = total of observations in row *I* (shown as marginal total to right of the matrix)

x +*I* = total observations in column *I* (shown as marginal total at bottom of the matrix

N = total number of observations included in matrix

It is worth mentioning that there are two other error measurements derived from the error matrix. The first is the omission error or the producer's error. It indicates the probability of a reference pixel being correctly classified and is estimated by dividing the total number of correct pixels in a category by the total number of pixels of that category (pixels in a column) (Congalton, 1991). The other is called the commission error or user's error and it indicates the probability that a pixel is classified on the map/image actually represent that category on the ground. It is estimated by dividing the total number of correct pixels in a category by the total number of pixels that were classified in that category (pixels in a column) (Congalton, 1991). The k*hat* incorporates the off-diagonal elements as a product of the row and column marginal.

A post processing filtering may be applied on the two SPOT classifications in order to reduce the shadow class. It allows a reclassification of the central pixel of a size window, taking into account the highest frequency of the neighbouring classes. Even though this process allows a reduction of shadow effects, it tends to be biased of the outcome-classified results because they are always in favour of large, compact, and regularly shaped classes (Shaban and Dikshit, 2001; Mas, 1999).

6.3.1 SPOT-2 HRV Classification

The insufficient spatial resolution of SPOT-2 HRV (20 m) satellite sensor, spatial complexity and spectrally mixed classes, can cause classification inaccuracies. For

SPOT-2 HRV image, different land cover types have shown similar spectral response and therefore classes have been difficult to separate. For instance, concrete flat roofs reflect the same signature as bare rocks or bare soil. It has been suggested that improvement to classification can be achieved if the spatial properties of classes can be incorporated into the classification criteria (Lee and Philpot, 1991; Shaban and Dikshit, 2001). There are two distinct types of analysis, which utilize spatial information from an image: region-based and window-based (Gong and Howarth, 1990; Shaban and Dikshit, 2001). The region-based classification involves two steps: image segmentation and image labelling. This type of classification method is particularly useful in classifying images with homogeneous structures. This allows a small number of regions to be extracted during the segmentation process and therefore, making the region labelling easier. Nevertheless, this method requires considerable computation when used with images having heterogeneous structures such as that of the West Bank. The window-based approach for incorporating spatial information in a classification can be broadly divided into three groups as suggested by Gong and Howarth (1989). These three groups are: pre-classification approach, post-classification procedures, and contextual classifiers. The contextual classifiers involve using complex parametric models with assumptions that are rarely valid for remote sensed data (Shaban and Dikshit, 2001; Mas, 1999). Therefore, these classifiers may not perform optimally.

Two kinds of approaches exist for pre-classification procedures to tackle the problem of reduced class separability. The first consists of applying mathematical transformations to the original data to remove the excess spectral detail that is considered as noise. This approach is not implemented here as it attempts to solve the problem of higher spectral confusion by eliminating part of the information that is present in the SPOT-2 HRV image. The second method uses the texture measures. It offers the advantage of fully exploiting the potential of medium high spatial resolution imagery to achieve a more detailed land cover classification (Lee and Philpot, 1991; Shaban and Dikshit, 2001).

As SPOT-2 HRV contains elements that are not spatially homogeneous and mixed pixels, it is thought that taking into account only the spectral properties is not enough to map land cover for this medium high resolution image because of the identical spectral reflectance values that correspond to very different objects. At the same time, taking

into account only the geometric criteria also could cause problems in classification because of the similar geometric shape that can refer to different objects. As a result, it is concluded that the extraction of spatial information and incorporate it to the spectral properties is a sufficient approach to classify the image.

Figure 6.5 shows a few samples of the spatial patterns seen from SPOT-2 HRV multi-spectral imagery. Non-built-up areas such as forests and agricultural fields are homogeneous and spectrally separable (Figures 6.5 a&b), while the urban and bare soils have interclass spectral confusion (Figure 6.5, c).

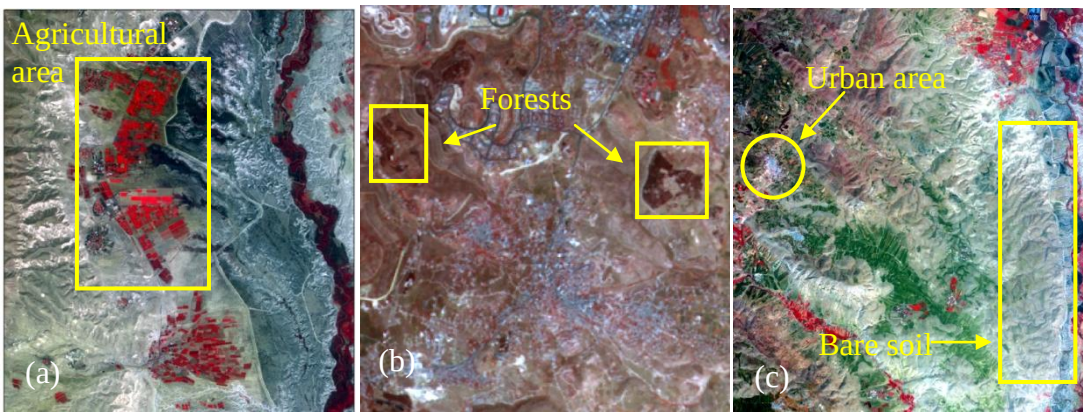

Figure 6.5: Homogeneity and spectral similarity of land covers: (a) agriculture homogeneity, (b) forests homogeneity, (c) spectral overlapping of urban and bare soil

Texture is the visual effect caused by spatial variation in tonal quantity over relatively small areas (Aguera *et al*., 2008). Texture analysis provides a way to incorporate both the spectral as well as the spatial distribution of image grey values, contrary to the simple statistical approach that uses mean or standard deviation, which does not take into account fully the grey value distribution. Literature indicates that the majority of methods using texture information have supported the idea that texture analysis may resolve the spectral confusion between land cover classes especially between urban and bare areas. It could result in an increase in the rate of correct classification (Puissant *et al*., 2005; Marceau *et al*., 1990; Gong *et al*., 1992; Gong and Howarth, 1990; Shaban and Dikshit, 2001).

The main approach used in texture analysis is a statistical approach based on the grey level co-occurrence matrix method (Haralick and Shunmugan, 1973) which describes

the grey value relationships in the neighbourhood of the pixel. This method involves two steps to generate spatial features: the first is where the spatial information from a digital image is extracted by co-occurrence matrix calculated on a pixel neighbourhood defined by a moving window of a given size. Such a matrix contains frequencies of any combination of grey levels occurring between pixel pairs separated by a specific distance and angular relationship within the window (Marceau and Howarth, 1992). The second step is to compute statistics from the gray level co-occurrence matrix to describe the spatial information according to the relative position of the matrix elements. Some of these commonly used spatial measures are the angular second moment, contrast, inverse difference moment, skewness, entropy, and correlation (Marceau and Howarth, 1992). In this research, one texture statistic is involved in the final classification, the MEAN texture feature, obtained from the original image that is defined as the average grey level in the small neighbourhood.

The procedure involves transforming the spectral image, using ENVI 4.2, into a texture unit image by assigning each pixel a texture unit number according to the relative magnitude of the grey level of this pixel to those of its eight nearest neighbours. The output image generated by the texture analysis is then used as an additional band to the multispectral bands. The four bands are then classed by the supervised classification resulting in a spectral/textural classification.

The co-occurrence matrix values are calculated with an inter-pixel distance of 1 and with a window size of 3×3. The 3×3 window size is chosen as it allows the discrimination between two thematic groups, the built-up class and shadow on one hand, and the other classes on the other hand (Puissant *et al*., 2005; Zhang, 1999). The window size cannot be bigger than the size of the object to be identified which are the urban areas and individual scattered houses. Also, if the window size is larger, then bare and urban or any other two land cover types may overlap and contribute less to the separation of classes, thus causing incorrect spatial information.

The classification results from the 3×3 moving window and combination of mean texture channel with the spectral have greatly improved the results from the original SPOT-2 HRV multi-spectral imagery as shown in Figure 6.6. The overall classification

accuracy and Kappa coefficients have considerably improved (Table 6.6). For example, in Jenin area the overall accuracy has increased from 65% to 94.9% and the Kappa coefficient from 0.4332 to 0.9278, and in Ramallah area the overall accuracy increased from 61.27% to 96.21% and the Kappa coefficient from 0.3924 to 0.9451.

6.3.2 SPOT-5 HRG Classification

The fine spatial resolution of SPOT-5 HRG (2.5 m) results in an increase in the number of pure pixels and a decrease in the number of mixed pixels, which as a result, should increase the classification accuracy (Shaban and Dikshit, 2001; Toll, 1984). On the other hand, this fine spatial resolution results in larger number of detectable sub-class elements, which implies a high spectral variance of classes within-class corresponding to land cover units. This may cause a decrease in spectral separability and results in a higher number of classes. To avoid such problem by a certain extent and to lower the frequency enhancement of the image to be in similar enhancement as with SPOT-2 HRV (20 m-resolution), a spatial filtering (convolution) is applied using a 3×3 pixel-majority filter. Convolution includes weighted sum of the input pixels within the 3×3 window where the weights are the values of the filter assigned to every pixel of the window itself (Figure 6.6).

1/9	1/9	1/9
1/9	1/9	1/9
1/9	1/9	1/9

(a) Kernel DN

67	67	72
70	68	71
72	71	72

(b) Original Image DNs

	70	

(c) Convolved image

Convolution:1/9(67)+1/9(67)+1/9(72)+1/9(70)+1/9(68)+1/9(71)+1/9(72)+1/9(71)+1/9(72)=630/9=70

Figure 6.6: Concept of convolution: shown is a 3×3-pixel kernel with all coefficients equal to 1/9. The central pixel in the convolved image contains the average of DNs within the kernel (Lillesand *et al*., 2008)

SPOT-5 HRG image has shown a high variability in the reflectance of bare and urban areas. Therefore, in some scenes, urban and bare soil classes are divided into more than one sub-class with more homogeneous spectral signatures in the RGB combination bands. In spite of such problems, the level of spectral variability of SPOT-5 HRG is sufficient to apply the automatic multispectral classification procedure.

6.4 Change Detection

6.4.1 Results

Land cover change over the ten years period is a response to the economic, social, and political forces. Information about the any change in land cover and/or land use is essential for proper planning and management of resources. In this study, the two single-date images classified individually are compared on a pixel by pixels basis. Post-classification comparison results suggest that the principal land cover changes observed in the study area between 1994 and 2004 are the urban and agricultural areas presented in Table 6.1 and Figures 6.7 and 6.8 below.

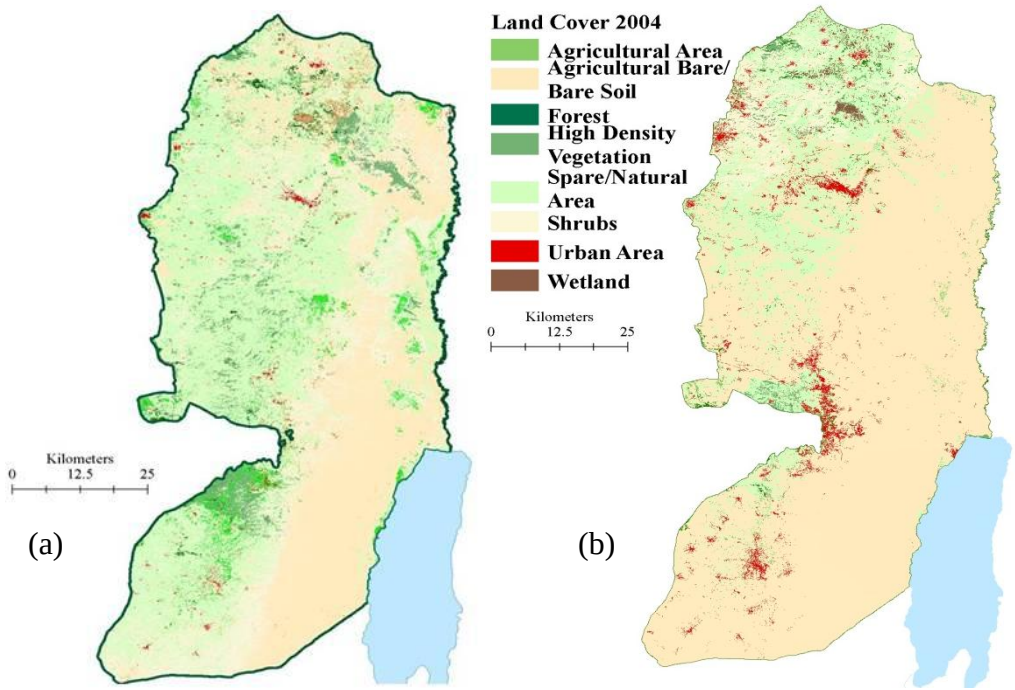

Figure 6.7: Land cover of the West Bank obtained from supervised classification of multispectral SPOT images collected in (a) 1994 and (b) 2004

Table 6.1: Land cover classification results

Land Cover	1994 Area (km^2)	2004 Area (km^2)	Percentage
Urban areas	42.3	148.8	258%
Forest	34.64	24.9	-28%
High Density Vegetation	254.6	62.6	-75%
Permanent/Winter Agriculture	131.5	30.95	-76%
Sparse/Natural Vegetation	2273.2	1039.5	-54%
Shrubs/Natural Grass Land	975.5	303.9	-69%
Bare Soil and Agriculture Bare	1898.7	4015.6	111%
Wetland Vegetation	42.27	28.1	-33%

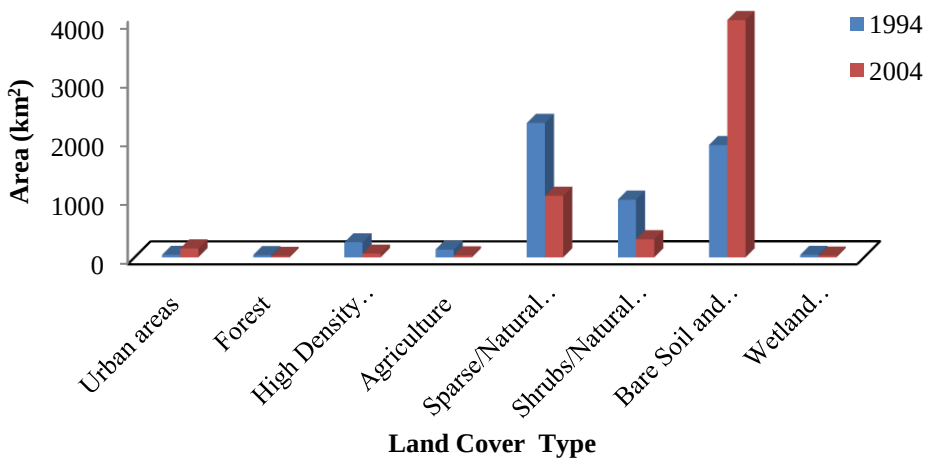

Figure 6.8: Land cover change

Figures 6.8 and 6.9 show the spatial distribution of changes in all land cover classes between the two dates on the West Bank and governorate basis. It is shown that the extent area of built up land during 1994 is 42.3 km^2 and has increased to 148 km^2 (258%) by 2004. During the same period, the areal extent of high-density vegetation is 254.6 km^2 in 1994 and has decreased to 62.6 km^2 (75%) by 2004. Over the same period, agricultural area has decreased by 76%, and forest by 28%. The decrease of agricultural areas is partially due to the difference of date of capture of the two SPOT images (January, 1994 and May 2004). As mentioned in Chapter 2, agriculture in the West Bank is rainfed agriculture and by the month of May, the agriculture season is over.

Therefore, image signals of the same agricultural area differ by seasonality and vegetation.

The most obvious change is that urban areas have significantly increased in size while the vegetation cover has decreased. Formerly vegetated areas whether cropped, natural, or forest, have changed to either urban or bare soil. However, the decrease in permanent/winter agricultural land may be attributed to the fact that May is the end of the winter-season cropping and not to change in land cover type. In addition, the decrease in shrubs and grass areas is expected as the temperature starts to rise in spring months and such plantations start to dry up. A more detailed analysis is carried out in the following section as the seasonal NDVIs extracted from MODIS images are studied.

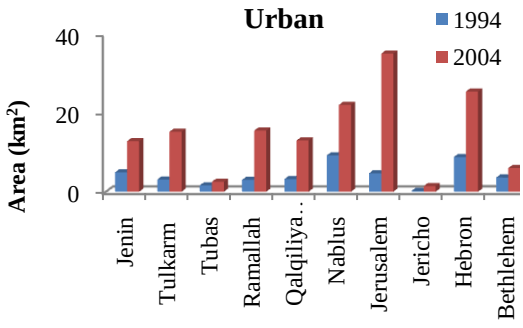

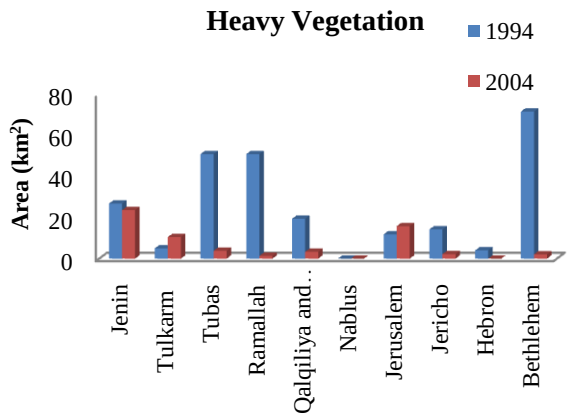

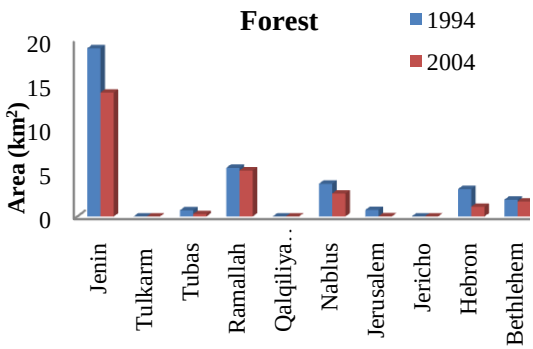

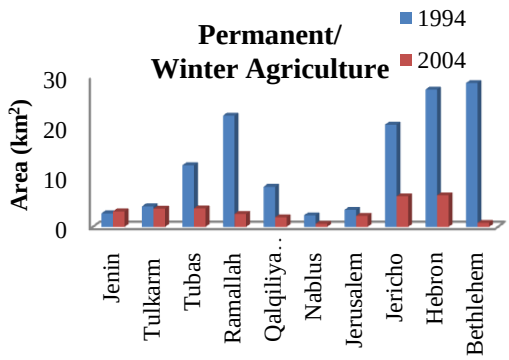

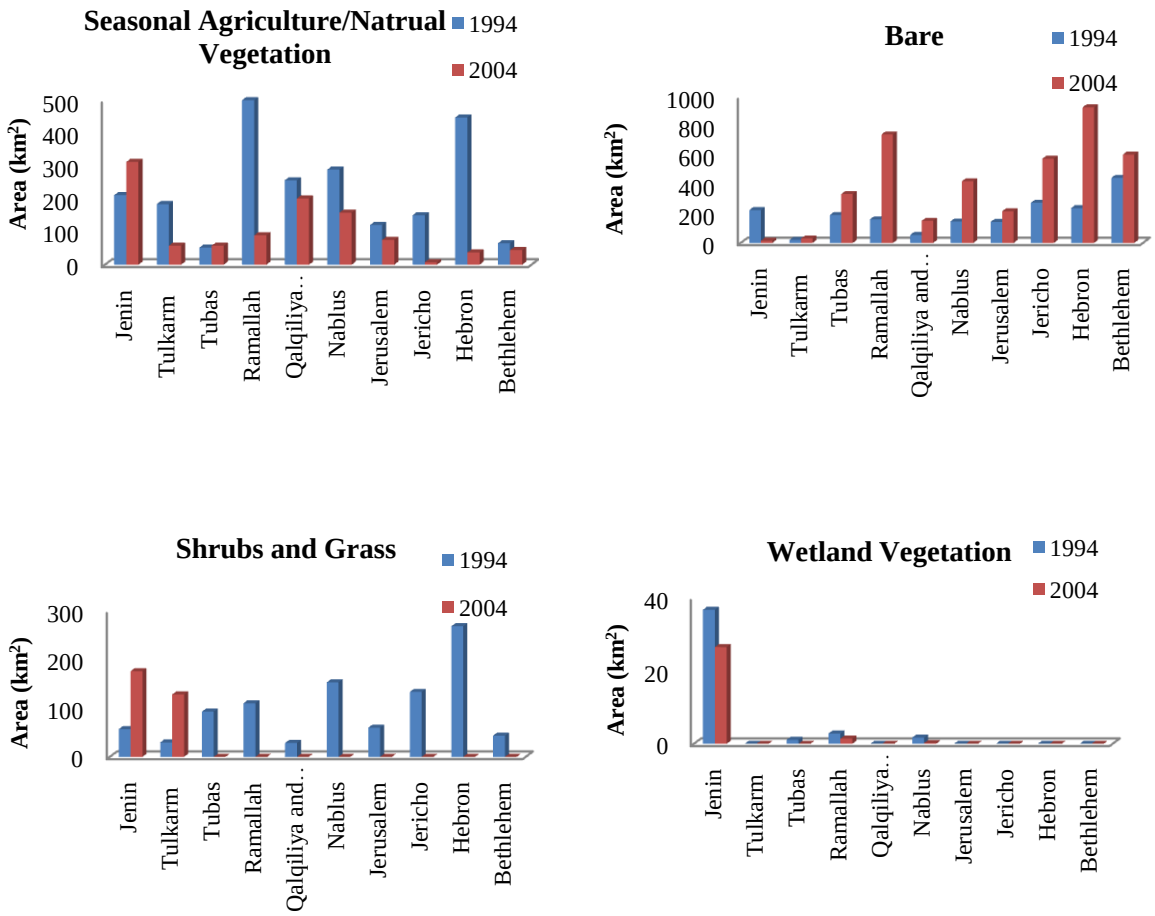

Figure 6.9: Land cover change by governorate

Vegetation has shown an overall decrease; however, in Jerusalem it has increased, as new parks, vegetation along main roads, and within low-density residential areas. At the same time, agriculture and forests areas have declined in Jerusalem. This is due to the Israeli settlement expansion on the expense of natural vegetated areas. Building Israeli settlements and the bypass roads leading to such settlements on areas designated as nature reserves or forests have resulted in the declining of these areas. It is estimated that Israel is responsible for the destruction of 82% of the forested areas in the West Bank and Gaza Strip (ARIJ, 2006). Figure 6.10 below demonstrates a clear example of the Abu Ghnaim Mountain turned into by the Israeli administration into Har Homa settlement south of Jerusalem.

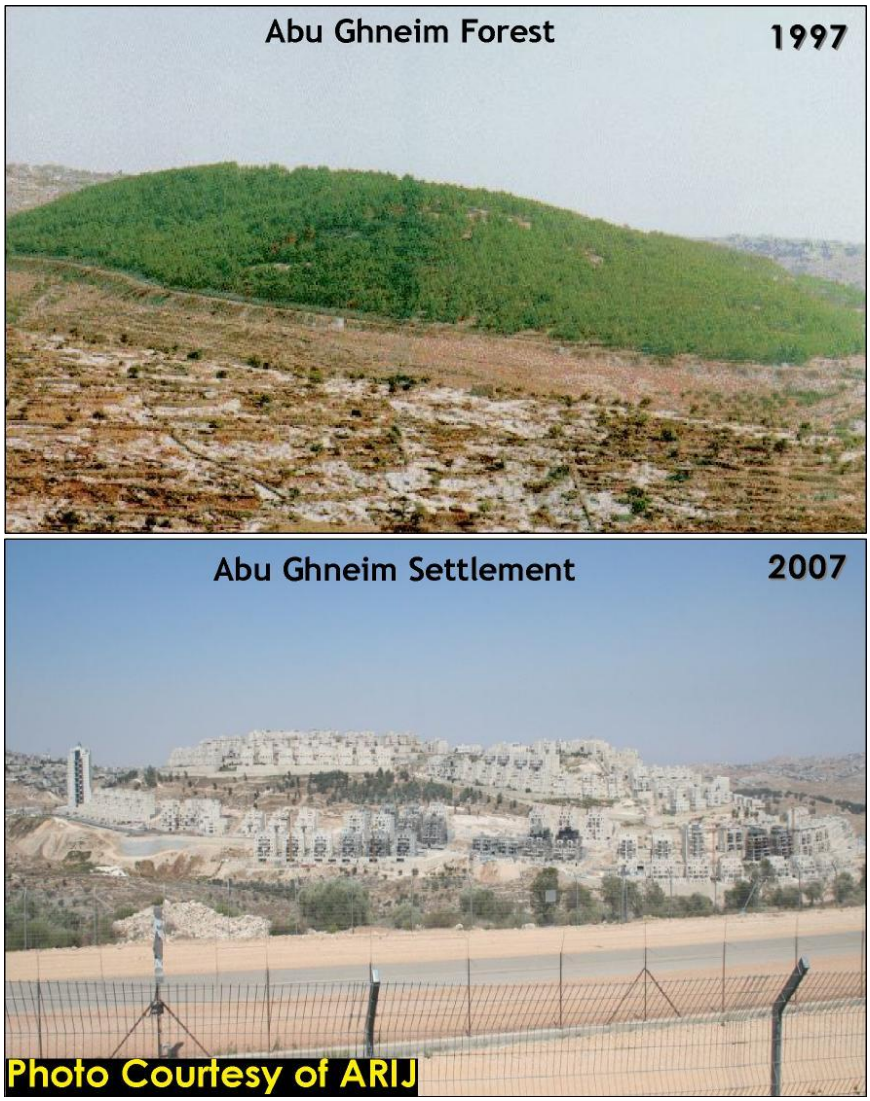

Figure 6.10: Har Homa settlement (Abu Ghneim Forest) between 1997 and 2007

6.4.2 Normalized Difference Vegetation Index (NDVI)

The Normalized Difference Vegetation Index (NDVI) is one of the most widely used vegetation indices derived from satellite data for monitoring the location and distribution of vegetation changes. It is used in this research for modelling evapotranspiration using surface energy balance methods (see Chapter 4). Past studies have demonstrated its potential use to study the vegetation dynamics (Townshend and Justice, 1986; Verhoef *et al*., 1996). It is estimated by the division of the difference between the near infrared and visible wavelength observations and the sum of these measurements.

The green normalized difference vegetation index (GNDVI) is thought to be a more reliable indicator of crop conditions than other vegetation indices (Lillesand *et al*., 2008). The GNDVI is identical in form to the NDVI except that the green band is substituted for the red band. Similarly, the wide dynamic range vegetation index (WDRVI) has shown to have improved sensitivity. Such indices are applicable when the biophysical parameters reach moderate to high levels. The purpose of using the NDVI is to detect the changes in vegetation and not to precisely calculate the biomass vegetation.

6.4.2.1 SPOT Images NDVI

NDVI is calculated for both dates, 1994 and 2004, using the two SPOT images, SPOT-2 HRV and SPOT-5 HRG, while the seasonal variation has been studied using a twelve 250 m MODIS images over the year 2004. Accuracy assessment and validation has been conducted using the 16-day composite data provided by the United States Department of Agriculture http://www.pecad.fas.usda.gov/cropexplorer/modis_ndvi/index.cfm). Vegetation cover change is illustrated in Figures 6.11.

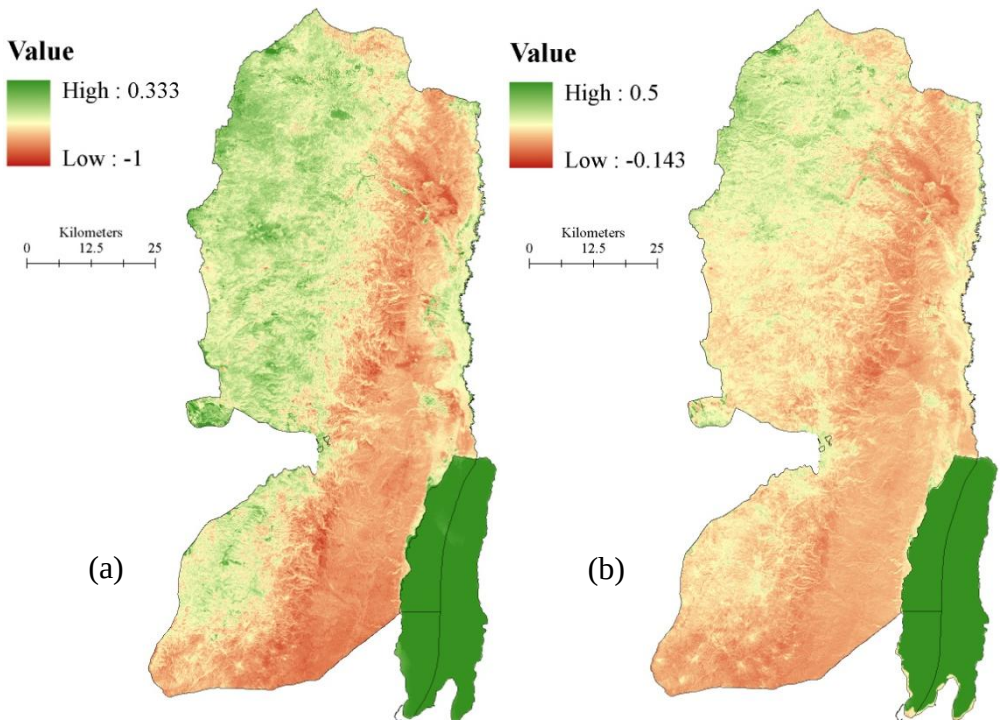

Figure 6.11: SPOT NDVI variation over the a ten years period based on SPOT images data (a) 1994 and (b) 2004

The NDVI values for vegetation range from a low of -1 to a high of +0.333 for SPOT-2 HRV image (1994) and from a low of -0.1429 to a high of +0.5 for SPOT-5 HRG (2004). Non-vegetated surfaces have NDVI values of less than zero and the highest NDVI values represent the maximum vegetation at that day. It is noticed that the NDVI is higher in the north and west of the West Bank than the south and east. Such indication could be of interest in understanding the hydrology of the area. The value of the NDVI indicates the absence or presence of groundwater assuming that vegetation response to presence of water in the soil. Areas with denser vegetation, i.e. higher NDVI, may indicate areas with higher rainfall and presence of groundwater by deep roots, which is the case in the north and west of the area. Also, the presence of vegetation affects the soil moisture budgets and therefore recharge and the uptake of groundwater by the deep roots. Therefore, in order to study the state of development of plants and trees through the seasons and within the season and determine their water consumption, it is necessary to study the vegetation index through seasonal sequential images.

The decrease in NDVI in year 2004 compared to year 1994 is also reflected in the NDVI maps. This decrease could be attributed to other factors than change in land cover vegetation. Such factors include climatological conditions and date of imagery. Table 6.2 and Figure 6.12 are examined to interpret and evaluate the output NDVI results.

Table 6.2: Climatic variables for 1994 and 2004

Average	1994	2004
NDVI (high)	0.5	0.333
Rainfall (mm year^{-1})	650	472
Temperature (°C)	18.5	20.3
Pan Evaporation (mm year^{-1})	1831	2002
Relative Humidity (%)	62	55

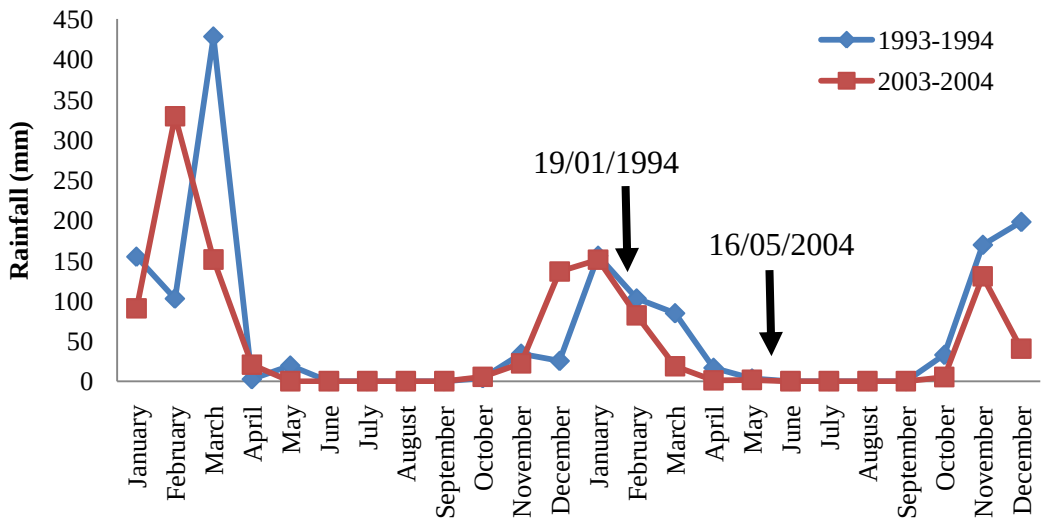

Figure 6.12: Rainfall graph for Jerusalem (1993-1994 and 2003-2004)

The rainfall graph (Figure 6.12) shows that the 1994 image is captured in the middle of a wet season while the 2004 image is captured at the beginning of a dry season. Daily rainfall data show that there is 254 mm of rainfall during the week previous to the capture of the 1994 image, but for the 2004, no rainfall is recorded for the whole month of May. Moreover, temperature and evaporation are higher in corresponding months of 2004 and 1994 as shown in Table 6.2. Such conditions indicate that there are significant differences in soil moisture and vegetation phenology between both dates. Therefore, a large amount of variation of spectral responses and NDVI values are attributed to these differences. In addition, it may be noted that a number of factors can influence NDVI observations that are unrelated to vegetation conditions. Among these factors are the variability in incident solar radiation, radiometric response characteristics of the sensor, atmospheric effects, and off nadir viewing effects.

Since the two images are acquired under different climatic conditions, it also means having different amounts of haze and dust in the atmosphere. These differences could have masked real changes or made similar land cover appears to have changed. This problem may be overcome by applying the atmospheric correction developed by Chavez (1996) known as the Cosine (t) (COST) model. The COST model uses the cosine of the solar zenith angle which is considered a good approximation of the atmospheric transmittance. It incorporates all of the elements of the Dark Object

Subtraction model that is used for haze removal plus a procedure for estimating the effects of absorption by atmospheric gases. It requires no additional parameters over the Dark Object Subtraction model and estimates these additional elements based on the cosine of the solar zenith angle (90º - solar elevation) (Berberoglu and Akin, 2009). Nevertheless, this method could not be applied to the SPOT images, as the solar zenith angle is unknown; it is applied on MODIS images when applying SEBAL method described in Chapter 4.

6.4.2.2 MODIS Images NDVI

Monthly MODIS Level 1B product (1 km resolution) (MOD021KM) of 2004 are downloaded from the NASA Earth Observing System data gateway (http://daac.gsfc.nasa.gov/data/) (Table 6.3).

Table 6.3: Characteristics of Terra-MODIS data used

Date of Image Acquisition	Satellite Overpass (UTC)	Orbit	Central Coordinates	
			Latitude	Longitude
19/01/2004	09:05:00-09:10:00	21742	28° 08’ 58’’	25° 01’ 12’’
24/02/2004	08:40:00-08:45:00	22266	28° 11’ 33’’	31° 16’ 17’’
16/03/2004	08:55:00-09:00:00	22572	39° 52’ 24’’	29° 58’ 08’’
14/04/2004	08:25:00-08:30:00	22994	35° 04’ 55’’	36° 20’ 33’’
13/05/2004	07:55:00-08:00:00	23416	32° 35’ 04’’	43° 17’ 18’’
13/06/2004	08:50:00-08:55:00	23868	34° 01’ 26’’	29° 46’ 58’’
15/07/2004	08:50:00-08:55:00	24334	33° 35’ 34’’	29° 38’ 25’’
16/08/2004	08:50:00-08:55:00	24800	32° 37’ 37’’	29° 22’ 56’’
09/09/2004	08:00:00-08:05:00	25149	34° 09’ 23’’	42° 08’ 23’’
16/10/2004	08:20:00-08:25:00	25688	27° 50’ 17’’	35° 48’ 23’’
21/11/2004	07:55:00-08:00:00	26212	27° 11’ 19’’	41° 58’ 08’’
19/12/2004	08:20:00-08:25:00	26620	27° 54’ 34’’	35° 54’ 35’’

MODIS Images are geocorrected and re-projected to the Palestine Grid (PalGrid) using ENVI v. 4.2. The aggregated reflective solar bands, band 1 (620-670 nm) and band 2 (841-876 nm) with a 250 m resolution, are used for the automated NDVI (Figure 6.13) calculations provided by ENVI.

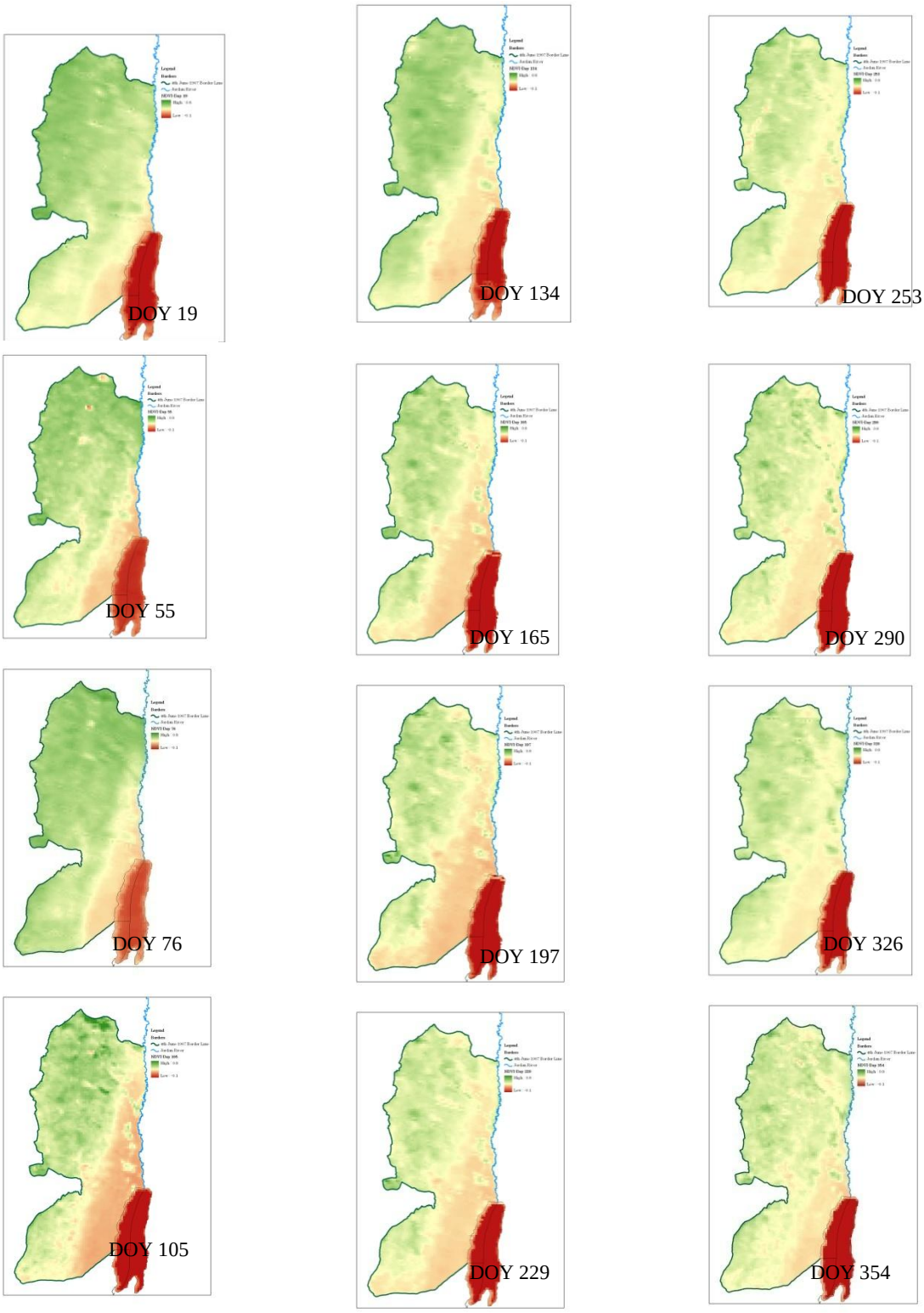

Figure 6.13: Seasonal and spatial variation of NDVI over the West Bank area for the year 2004 (DOY: day of year)

The monthly variations of NDVI are in coherence with the SPOT-NDVIs but with fewer details due to the lower resolution. They resemble vegetation and rainfall intensities pattern which shows a peak from December until February indicating a higher soil moisture and therefore, higher recharge. Minimum NDVI occurs during the summer season until November (Table 6.4).

Table 6.4: Monthly range of NDVI for 2004

Date	NDVI Range
DOY 19- January	-0.35 – 0.61
DOY 55- February	-0.30 – 0.66
DOY 76- March	-0.24 – 0.75
DOY 105- April	-0.47 – 0.68
DOY 134- May	-0.31 – 0.44
DOY 165- June	-0.50 – 0.51
DOY 197- July	-0.26 – 0.59
DOY 229- August	-0.37 – 0.56
DOY 253- September	-0.37 – 0.46
DOY 290- October	-0.29 – 0.44
DOY 326- November	-0.37 – 0.48
DOY 354- December	-0.38 – 0.57

6.5 Accuracy Assessment

To assess the reliability of the results, an error matrix is produced. As defined in section 6.3 (step 6), the error matrix is a square array of numbers laid out in rows and columns that expresses the number of sample units assigned to a particular category relative to the actual as verified by the user (Jensen, 1996; Congalton, 1991; Lillesand *et al*., 2008). The error matrix summarizes the relation between the remote sensing derived classification map and the reference information where columns represent the reference data rows indicate the classification generated. Using the ERDAS IMAGINE Accuracy Assessment utility, reference random test pixels in the study area are located which are not used in the training of the classification algorithm to eliminate to the possibility of bias of training samples chosen in classification. These pixels chosen are referenced on the ground and used to assess the accuracy of classes in the remote sensing classification map.

Congalton (1991) suggested a minimum of 50 samples for each land cover class or 250 reference pixels in the error matrix to be collected to assess the accuracy of the

classification. In this classification accuracy, 256 pixels are used. After the test reference information has been collected from the randomly located sites, it is compared on a pixel-by-pixel basis with the information present in the remote sensing derived classification map. An error report containing the error matrix and accuracy report summarizing the agreement and disagreement are produced. The Kappa coefficients are then calculated for each governorate scene of both SPOT imageries. The computation of Kappa and the overall accuracies for three scenes are summarized in Table 6.5.

Table 6.5: Comparison of classification accuracy

Governorate	SPOT-2 HRV (spectral)		SPOT-2 HRV (spectral/textural)		SPOT-5 HRG (spectral)	
	Kappa (K*hat*)	Overall Accuracy	Kappa (K*hat*)	Overall Accuracy	Kappa (K*hat*)	Overall Accuracy
Jenin	0.4332	65.00%	0.9278	94.92%	0.9283	94.86%
Ramallah	0.3924	61.27%	0.9451	96.21%	0.8727	96.09%
Bethlehem	0.4269	64.35%	0.9523	96.48%	0.7176	93.36%

The initial spectral classification carried out with SPOT-2 HRV image has low Kappa coefficients due to image misclassification that has resulted from the similarity of spectral signatures of different classes. Significant improvement to accuracy has resulted when the textural analysis is integrated within the classification procedure. As seen from the above table, Kappa coefficients have risen from 0.4332 to 0.9278, from 0.3924 to 0.9451, and from 0.4269 to 0.9523 for Jenin, Ramallah, and Bethlehem, respectively. Even though the overall accuracy incorporates only the major diagonal and excludes the omission (producer's) error and the commission (user's) error, it is still considered an indicator of classification improvement between the two approaches. The results of the Kappa analysis for spectral classification of SPOT-5 HRG images show high values. This indicates that the spectral information is enough to carry out to map land cover classification.

There are two factors to consider in relation to the Kappa analysis. First, the reference data used were the same data used to train the classifier. This may have caused an overestimation of classification accuracy as the two training and testing procedures are carried on the same data. Second, the samples collected for each land cover class are not evenly distributed, i.e. one class may have over 50 pixels while others may have 8 or 10 only. Therefore, the random selection needed to be stratified, in other words, a

minimum number of samples should have been selected for each class. Finally, accuracy assessment must be designed to reflect the intended use of classification. Therefore, if an agricultural pixel is misclassified as sparse/natural vegetation, the error might be of little significance in the study of the hydrological process taking place during recharge.

6.6 Classification Validation

To further validate results of classification maps, findings are compared to the manually delineated land use available by the Palestinian Ministry of Planning. Land use classes are manually determined using the same two SPOT images but with further validation using the high resolution panchromatic IKONOS image (1 m) of 2005.

Table 6.6: Manually delineated land use versus spectral land cover classification

Land use/land cover type	Land Use (km^2)		Land Cover (km^2)	
	1994	2004	1994	2004
Urban areas	489.0	600.0	42.3	148.8
Forest	65.0	60.0	25.0	25.0
Arable land/high density vegetation	456.6	342.4	254.6	62.6
Permanent/winter agriculture	905.6	872.5	131.5	31.0
Sparse/ natural vegetation	949.0	928.0	227.3.2	1039.5
Shrubs/ natural grass	1746.0	1623.0	975.5	303.9
Bare soil and agriculture bare	1033.8	1221.4	1898.7	4015.6
Wetland	7.3	0.6	42.3	28.1

Results of the two methods of classification are seen to vary considerably. For example, the urban area is found to equal 489 km^2 in 1994 increasing to 600 km^2 using the manual delineation while the spectral classification used in this study results an area of 42.3 km^2 and 148.8 km^2 in 1994 and 2004, respectively. Discrepancies in outcomes are due to several reasons. First, during the manual delineation of land use classes, polygons are inaccurately delineated where lines are drawn out of class borders as illustrated in Figure 6.14.

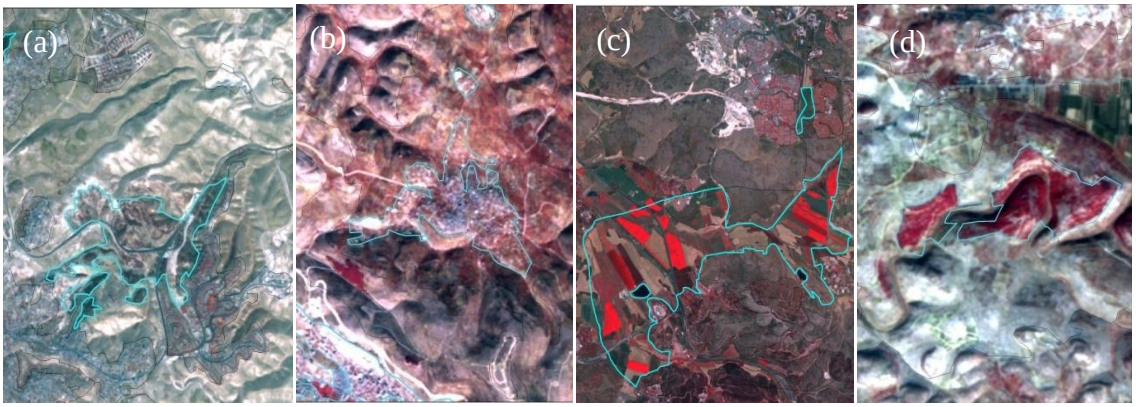

Figure 6.14: Manual land cover classification: (a) natural vegetation, (b) urban, (c) agricultural, (d) forest

Second, mixed pixels are treated as homogeneous areas of same class. For instance, sparse vegetation or agricultural areas with an urban cluster are classified as urban area, forests and natural vegetation are classified as one class, and bare vegetation and agricultural lands are grouped as cropped areas. This has caused overestimation of land use classes areas as shown in Table 6.6. Finally, using the SPOT-2 HRV medium spatial resolution, pixels classification using manual delineation has been difficult to determine and define to which class they belong to, therefore, inaccuracy is thought to be higher than the spectral classification.

6.7 Conclusion

This chapter presents a methodology and results of classifying two single date SPOT images acquired in 1994 and 2004. The purpose of land cover classification is to incorporate it as an input to the recharge model to obtain a spatial distribution estimate of recharge rates. It is also to be used to perform a sensitivity analysis to understand the impact of land cover change on recharge estimation and distribution over the study area.

Supervised classification using the maximum likelihood classifier is used to derive land cover classes and detect changes. It is performed on governorates basis to avoid the overlapping in the spectral signatures between the different classes over the regional area. SPOT-5 HRG image has been suitable for applying the classification procedures using the multi-spectral bands. The spatial resolution of SPOT-5 HRG is sufficient to capture the characteristics of each class, and the spectral range of the sensor is able to

distinguish each class from the other types of land cover change. On the other hand, using SPOT-2 HRV image, land covers have exhibited similar spectral characteristics making separation in feature space by simple per-pixel classifiers difficult, leading to inaccurate classification. Therefore, texture analysis is considered a potential solution for the classification of land cover in the West Bank region although it did not significantly improve the quality of classification for SPOT-5 HRG.

To quantify changes between the two single date classifications, a post classification comparison is carried out where the classified images are simply compared on a pixel-by-pixel basis. Comparison indicates that natural vegetation has been removed and replaced by non-evaporating and non-transpiring surface such as asphalt and concrete during the urban development that took place during this period. This alteration will result in the redistribution of the incoming solar radiation, and stimulate the urban-rural contrast in surface radiance and air temperature. In addition, results show that there is an increase in bare soil by 111% and a decrease in high-density vegetation and winter agriculture by 75%. Forests decreased by 28% and wetlands by 33%.

Accuracy assessment is performed using the error matrix and the Kappa coefficients. The initial spectral classification carried out with SPOT-2 HRV image has resulted low Kappa coefficients due to image misclassification because of the similarity of spectral signatures of the different classes. Accuracy is significantly improved when the textural analysis is integrated within the classification procedure as seen from the Kappa coefficients where they increased from 0.4332 to 0.9278, 0.3924 to 0.9451, and from 0.4269 to 0.9523 for Jenin, Ramallah, and Bethlehem, respectively. The results of the Kappa analysis for spectral classification of SPOT-5 HRG image show high values. This indicates that the spectral information has been enough to carry out spectral land cover classification.

Chapter Seven

Spatial and Temporal Distribution of Evapotranspiration

7.1 Introduction

The traditional estimation of evapotranspiration (ET) relies on the meteorological and ground data available from nearby weather stations, restricting its application to small areas. Extrapolation of point data especially in heterogeneous land surfaces and soil characteristics beyond the measuring area would be inaccurate because of the dynamic and regional variability of ET. Even at local scale, ET information may not always be available, because very few weather stations measure it or do not satisfy the requirements for computing a reference ET (FAO 1997, 1998). In this context, satellite data and remote sensing techniques offer an alternative for ET estimation over large areas by complementing locally observed measurements and numerical simulations of ET. Remote sensing has shown to be a reliable approach since some of the main constraints on suitable and available data is overcome by providing a precise spatial representation. Another important advantage of using remote sensing is that it provides detailed and independent ET estimations on a pixel-by-pixel basis. Quantification from spectral satellite data requires determination of the surface energy balance components such as surface albedo, normalized difference vegetation index (NDVI), surface temperature (Ts), and energy balance parameters (Bastiannssen *et al*., 1998 a&b; Chemin, 2003; Mekonnen, 2005; Brata et al., 2006) with the support of field observations, physical and statistical/semi-empirical methods or the Penman–Monteith equation.

This chapter discusses the monthly spatial estimations of evapotranspiration (ET) over the West Bank area in 2004 derived on a pixel by pixel basis from the 1 km resolution MODIS Level 1B and Level 3 (8-day products) data by employing the Surface Energy Balance Algorithm for Land (SEBAL). ET estimates derived from MODIS are validated by comparing results with those derived from Landsat TM5 acquired on the same cloud free day (August 26th, 2003). Landsat TM5 is used as a validation tool for

its detailed coverage and higher spatial resolution. Results are then used as inputs for groundwater recharge estimation (Chapter 8).

This chapter includes three parts: part one presents the results derived from the energy balance model and estimates the monthly evapotranspiration over 2004. Part two compares ET mapping accuracy of MODIS and Landsat TM5 data and validates them to field pan evaporation measurements and results using Penman-Monteith and Thornthwaite equations (Chapter 5). The final part discusses the results.

An illustrative presentation of the methodology used is given in the following flow chart (Figure 7.1).

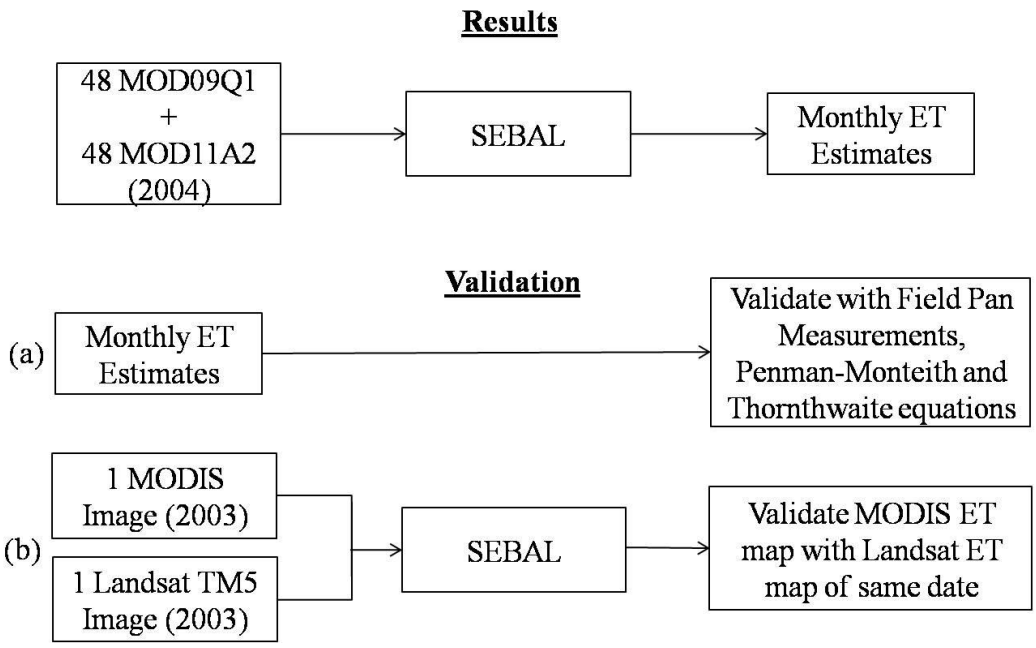

Figure 7.1: Study concept

7.2 SEBAL Monthly Evapotranspiration

In order to use the outcome of ET maps on a routine basis and to generate seasonal ET maps for predicting recharge to the groundwater aquifers, monthly ET maps are to be created as inputs for such models. This section is devoted to investigate the ability to estimate the mean monthly evapotranspiration for the West Bank area using MODIS Terra reflectance (MOD09Q1), land surface temperature (LST) and emissivity data (MOD11A2) over an 8-day period collected over the year 2004. The decision for

choosing which MODIS tiles product is based on two factors: (1) the spatial resolution and (2) the frequency of acquisition. MOD09Q1 and MOD11A2 comprise the highest resolution among MODIS products and the time required to obtain detailed ET maps requires less time than the daily products with the same spatial resolution MOD09GA and MOD11A1 as shown in Chapter 3, Table 3.3).

(a) MODIS Surface Reflectance (MOD09Q1)

MODIS Terra provides bands 1 and 2 at 250 m resolution in an 8-day gridded level-3 product. Each pixel contains the best possible observation as selected on the basis of high observation coverage, low view angle, and absence of clouds or cloud shadows and aerosol loading. Table 7.1 provides the science data sets for MOD09Q1.

Table 7.1: MODIS 8-day reflectance products

Data Set (HDF Layers)	Bit Type	Fill Value	Valid Range	Scale Factor
250m Surface Reflectance Band 1 (620-670nm)	16-bit signed integer	-28672	-100-16000	0.0001
250m Surface Reflectance Band 2 (841-876nm)	16-bit signed integer	-28672	-100-16000	0.0001

MODIS surface reflectance product, MOD09Q1, provides an estimate of the surface spectral reflectance as it would be measured at ground level in the absence of atmospheric scattering or absorption. The bands are corrected for the effects of gaseous and aerosol scattering and absorption as well as adjacency effects caused by variation of land cover, Bidirectional Reflectance Distribution Function and atmosphere coupling effects, and contamination by thin cirrus. Version-5 MODIS/Terra surface reflectance products are validated and assessed over a widely distributed set of locations and time periods via several ground-truth measurements. Atmospheric correction is conducted through the use of MOD04: aerosols, MOD05: water vapour, MOD07: ozone, MOD35: cloud mask, and ancillary data sets, e.g. Digital Elevation Model and Atmospheric Pressure, as inputs to an atmospheric correction algorithm for each spectral band.

(b) Land Surface Temperature and Emissivity (MOD11A2)

MODIS land surface temperature (LST) and emissivity are composed from the daily 1 km LST product (MOD11A1) and stored on a 1 km sinusoidal grid as the average values of clear sky LSTs during an 8-day period. It comprises daytime and night-time LSTs and emissivities estimated in Bands 31 and 32 from land cover types. Validation and assessment have been applied over a widely distributed set of location via ground truth measurements.

Table 7.2: MODIS 8-day land surface temperature and emissivity products

Data Set (HDF)	Units	Bit Type	Valid Range	Multiply by Scale Factor
LST_Day_1km: 8-Day daytime 1km grid land surface temperature	Kelvin	16-bit unsigned integer	7500-65535	0.02
Emis_31: Band 31 Emissivity	None	8-bit unsigned integer	1-255	0.002 (+0.49)
Emis_32: Band 32 Emissivity	None	8-bit unsigned integer	1-255	0.002 (+0.49)

Comparison done in the University of California between land surface temperature (LST) and in situ values in 47 clear sky cases indicate that the accuracy of the MODIS LST products is better than 1 K in most cases (39 out of 47) and the root of mean squares of differences is less than 0.7 K for all 47 cases or 0.5 K for all but 8 cases (www.lpdaac.usgs.gov). Slightly larger errors may occur at large viewing angles and in semi-arid regions for the daily 1 km products, and larger errors in some arid regions for these products generated by the split-window algorithm, due to larger uncertainties in classification-based surface emissivities, and for the 5 km (MOD11B1) product generated by the day/night algorithm, due to the strong influence from the incorporated split-window algorithm. The error in cloud-contaminated land surface temperatures (LSTs) may be very large (4-11 K or even larger). It is very difficult for the MODIS cloud-mask to discriminate all of the pixels affected by clouds from clear-sky pixels, particularly near cloud edges and/or with sub-pixel clouds. The LST pixels severely contaminated by clouds are removed from Collection 5 Level-3 MODIS LST products using empirical constraints on temporal variations in clear-sky LSTs (MODIS Land Team, 2008).

7.3 SEBAL Model Results

7.3.1 Monthly ET Results

Monthly ET estimates are obtained in this study through the following steps:

Step 1: MODIS Level 3 product geographical coverage splits the West Bank into two areas as shown in Figure 7.2.

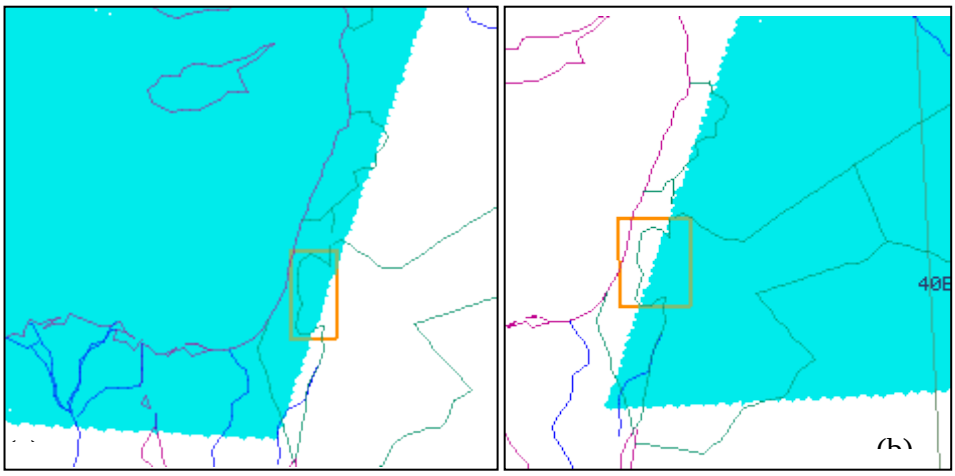

Figure 7.2: MODIS geographical coverage of the West Bank area extracted from MODIS website. The orange box includes the extent of West Bank borders

After SEBAL is applied and ET map are produced, monthly results of both areas are mosaiced into one image covering the whole West Bank.

Step 2: HDF tiles are stored as 'single precision' offering six significant digits necessary for SEBAL mathematical calculations.

Step 3: SEBAL algorithm is applied as described in Chapter 4.

Step 4: Monthly ET maps are attained by summing up the corresponding days of each month. The ET results per 8-day image are presented in Figure 7.3:

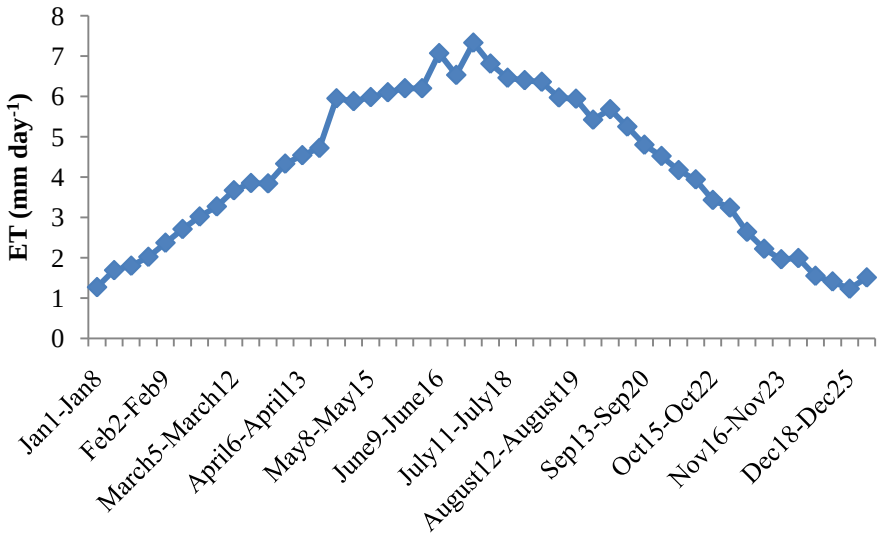

Figure 7.3: Evapotranspiration cycle over the year 2004 using MODIS 8-day reflectance and land surface temperature and emissivity products

From the graph above, it is noticed that the peak of SEBAL ET cycle occurs in the period between June 25-July 2 starting the summer season with an average ET of 7.12 mm day^{-1} and the lowest in December 18- 25 at the beginning of winter season with an average ET of 1.24 mm day^{-1}.

7.3.2 Net Radiation (Rn)

Radiation is a critical input variable in the energy balance equation and the most sensitive variable in ET estimates (Zhang *et al*., 2001; Gao *et al*., 2008). Therefore, the accuracy of estimating ET is to some extent determined by the accuracy of the retrieved instantaneous and daily net radiation especially for various slopes and azimuths of terrain. In many cases, the daily net radiation is obtained from meteorological stations or calculated based on simplification of the terrain assuming a uniform slope and azimuth. This may lead to gross errors when applied to rough terrain (Fu, 1998; Allen *et al*., 2007). For example, if the solar declination angle is very small, especially during winter seasons, the north facing surfaces in middle or high latitude region, such as the West Bank Mountains, receive relatively smaller net radiation compared to the south facing surfaces. If the terrain is more complex, some areas might not receive any direct radiation, because of the high obstacles surrounding them. Therefore, it is essential to

accurately retrieve the net instantaneous and daily net radiation when estimating ET. The daily net radiation distribution for 2004 is shown in Figure 7.4.

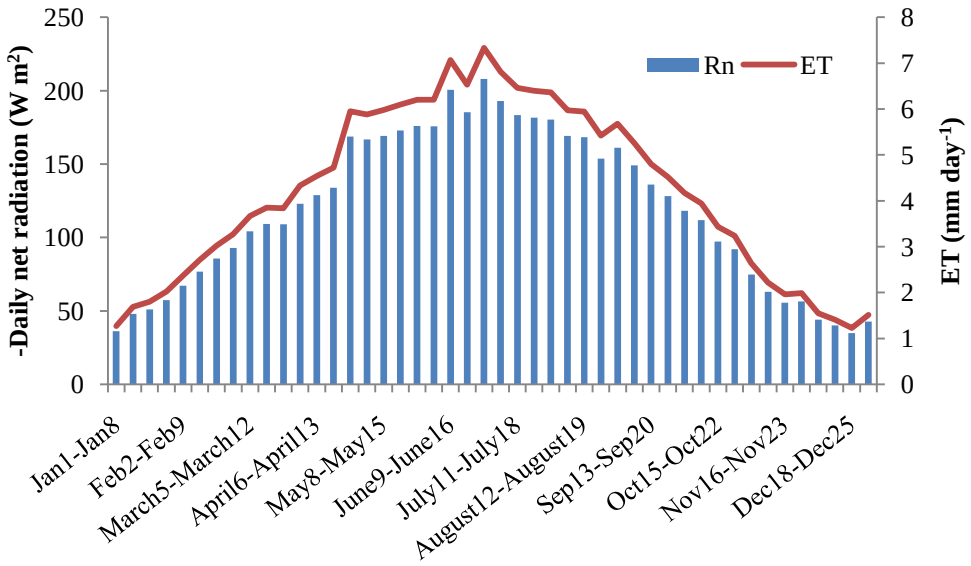

Figure 7.4: Distribution of daily net radiation (Rn) and daily ET derived from MODIS 8-day products

The week of June25-July2 has the highest net radiation and December 18-25 is the week with lowest net radiation. Net radiation and ET has a direct relation with a ratio equal to the evaporative fraction (EF).

Evaporative fraction is defined as the ratio of latent heat flux over the sum of the latent and sensible heat fluxes (see Equation 4.21). It is one of the parameters used to define the soil moisture conditions. For instance, an evaporative fraction of 100 percent reveals that the soil moisture is the constraint on actual evapotranspiration, while an evaporative fraction of 50 percent indicates a severe reduction of potential evapotranspiration (Kite and Droogers, 2000). One of MODIS Level 3 disadvantages is the inability to detect EF variations over time and assuming a constant fraction of 100% which means that the soil is well supplied with water all year contrary to the actual status.

7.3.3 Soil Heat Flux (Go)

Soil heat flux (Go) is commonly assumed to be negligible in remote sensing studies (Jacobsen and Hansen, 1999; Seguin and Itier, 1983). Since its measurement depends

on soil moisture and the amount of vegetation cover, this approximation is considered appropriate because ground-based measurements of the soil heat flux cannot be extrapolated to large areas. However, when extrapolating near-midday estimates of the energy balance components, the values of Go are not always negligible (Jacobsen & Hansen, 1999) and a significant amount of energy may be conducted into the soil (Kustas *et al*., 1990).

From Equation 4.13, it is noticed that Go should be proportional to net radiation (Rn). Most literature describes this ratio to be a function of leaf area index (LAI) or NDVI (Clothier *et al*., 1986; Choudhury, 1989). The main factors controlling the G0/Rn ratio are plant physiological parameters, such as biomass, leaf area index and percentage vegetation cover (Kustas and Daughtry 1990). Go/Rn over bare soil ranges from 0.20 ± 0.50 depending on the soil moisture (Idso *et al*., 1975), and from 0.05 ± 0.30 for surfaces with varying amounts of vegetation cover (Clothier *et al.*, 1986, Kustas and Daughtry, 1990). The magnitude of Go/Rn at midday is essentially a function of the amount of vegetation cover (Jacobsen and Hansen, 1999).

Because plant physiological parameters controlling Go/Rn are related to spectral vegetation indices, a conceptual model of NDVI versus Go/Rn is regarded as a physically-based relation (El Mayaar and Chen, 2006; Bastiannssen *et al*., 1998a). Empirical studies show, however, that crop height, LAI and spectral vegetation indices, e.g. NDVI, often make a better fit to a linear expression when directly related to the Go/Rn ratio (Kustas *et al*., 1993; Kustas and Daughtry 1990; Choudhury *et al*., 1987). Figure 7.5 shows the observed relationship between NDVI (vegetation cover) and Go/Rn (soil heat flux-net radiation ratio) over the study area.

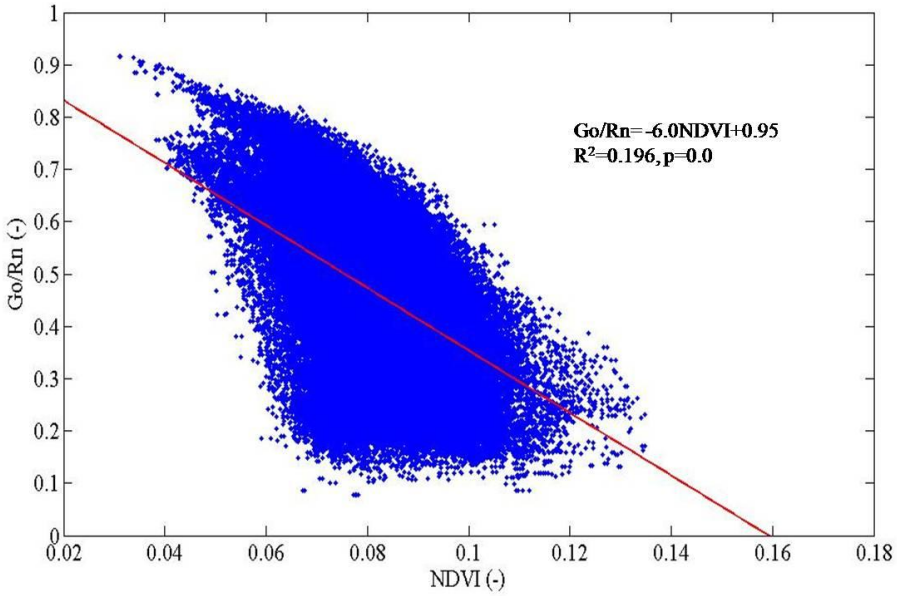

Figure 7.5: Relationship between NDVI and Go/Rn derived from MODIS Level 3 (n= 132000) products for the month of January 2004

Figure 7.5 illustrates the influence of the presence of vegetation on the transfer of soil heat flux and net radiation. There is a large degree of variance in the results presented by a wide scatter of points around the mean. This results in a low R2 value (0.196) which could be related to the variation of vegetation types and their ground cover. The negative relation is explained by the increased vegetation that disrupts the transfer of heat into the soil, therefore, decreasing surface soil temperature and soil heat flux (Go). As a result, the ratio of Go/Rn decreases as NDVI increases, i.e., the lower the Go/Rn ratio the higher the presence of vegetation. The variation in Go/Rn values is also explained by the presence of top soil moisture in the study area which is an important indicator of groundwater recharge. Soil moisture decreases as do soil heat capacity and soil heat flux as soil temperature decreases, therefore, the capacity for vegetation to withdraw water from the soil is less depressed. The ratio of Go/Rn tends to equal 1 when vegetation is completely absent (Bastiaanssen *et al.*, 1998a). This indicates that the derived relation is consistent with published data where vegetation and soil moisture are present in lower temperatures with less soil heat flux.

7.3.4 Relationship between NDVI and Surface Temperature (Ts)

The vegetation index shows an inverse linear relation with surface temperature (Ts) as illustrated in Figure 7.6. Previous studies have shown similar linear relation between percentage of vegetation cover and measured surface temperature e.g. Nemani and Running (1989), Carlson *et al*., (1990), Price (1990), and Kalluri and Townsend (1998). It suggests that vegetated areas are cooler than less-vegetated or non-vegetated areas. This is due to the fact that vegetation canopies with high LAI intercept the incident solar radiation, inhibiting the direct heating of the surface and modifying the energy fluxes at the surface due to the release of ET and consequently cooling it (Brata *et al*., 2006; Kalluri and Townsend, 1998; Price, 1990).

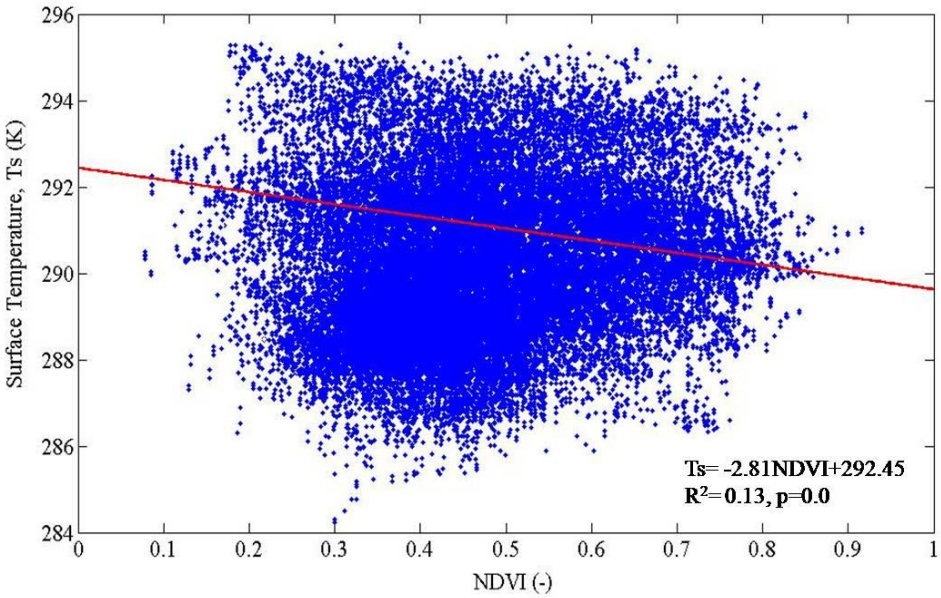

Figure 7.6: Regression model between NDVI and surface temperature (Ts) derived from MODIS (n=132000) January 2004

7.3.5 Relationship between ET and Surface Biophysical Variables

Several studies have analysed the relationship between ET and other biophysical parameters such as the NDVI and land surface temperature (Ts) from satellite sensors (Brata *et al*., 2006; Goetz, 1997, Di Bella *et al*., 2000). Vegetation indices have been widely used to study land cover, biomass and plant production (Franklin and Hiernaux 1991, Prince 1991, Sun and Zhu 1999). Since vegetation growth in arid and semi-arid

regions strongly depends on rainfall, most studies have so far been devoted to studying the response of land cover to rainfall in such areas (Srivastava *et al*., 1997, Yang *et al*., 1998, Milich and Weiss 2000, Sun *et al*., 2002). Others have involved the use of integrated NDVI based on its relationship with ET (Kerr *et al*., 1989, Lo *et al*., 1993, Srivastava *et al*., 1997, Di Bella *et al*., 2000). Srivastava *et al*., (1997) developed a relationship between integrated NDVI and plant transpiration, while Kerr *et al*., (1989) and Lo *et al*., (1993) estimated ET with NDVI data only. In the ET model developed by Di Bella *et al*., (2000), the effect of surface temperature is also considered with the surface temperature estimated from thermal infrared data. A relationship relating Ts, NDVI, and ET is developed for the Argentine Pampas as follows:

$$ET= -88.3439+1.77636Ts+286.406NDVI \quad (7.1)$$

where Ts is the land surface temperature (°C).

As seen from the above relation, ET is directly related to Ts, and NDVI similar to the case of the West Bank. The relationship between ET, Ts, and NDVI are shown to be positive (Figures 7.7 and 7.8). The derived relation is similar to those obtained by other authors such as Seguin *et al*., (1994) and Smith and Choudhury (1990). High vegetation densities indicate high water content, hence latent heat dominance.

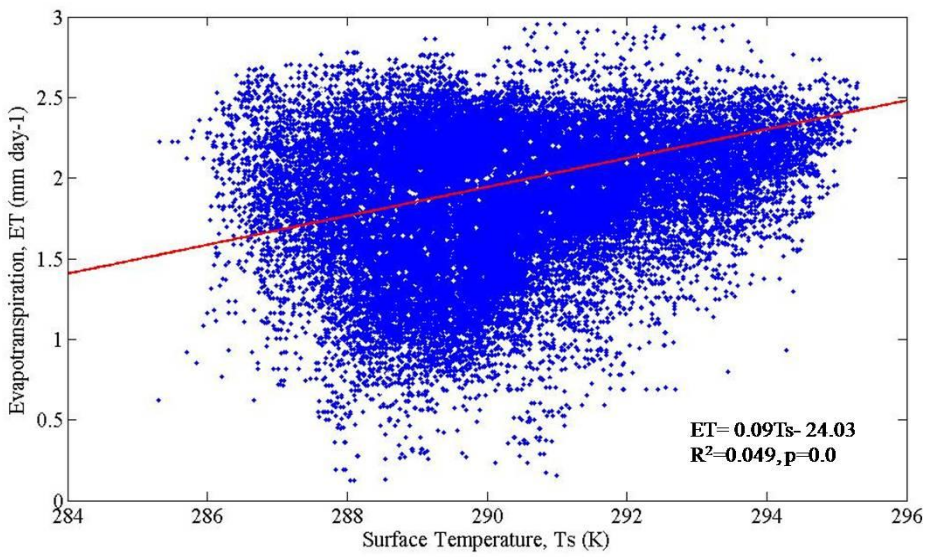

Figure 7.7: SEBAL ET and Ts relation over the West Bank area in January 2004 (n=132000)

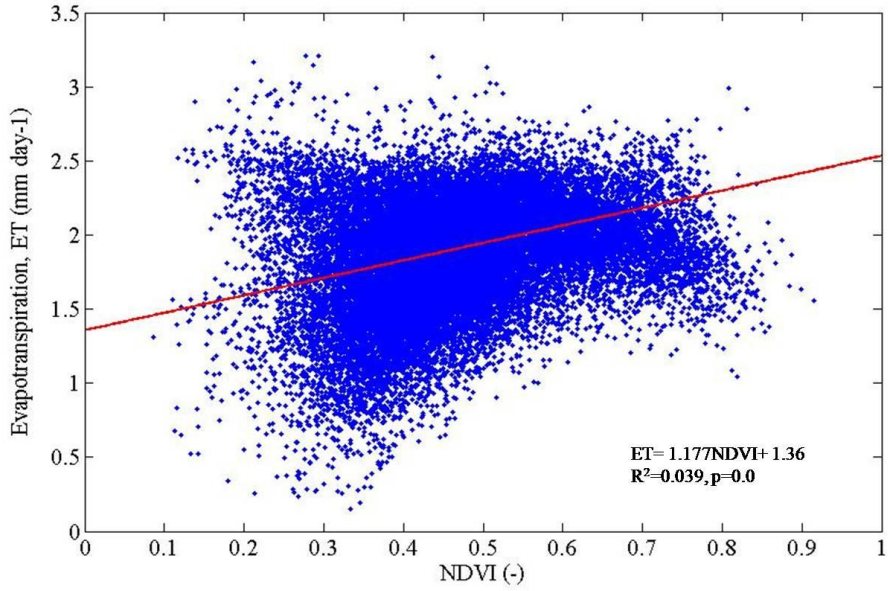

Figure 7.8: SEBAL ET and NDVI relation over January 2004

Examining the spatial patterns of ET and NDVI in Figure 7.9, it shows that the highest rates represent wetlands, forests, and irrigated areas. The highest vegetation cover and evapotranspiration rates are seen in the north and west of the area (dark green). Bare soil and natural vegetation have the lowest rates as seen in the east and south of the West Bank.

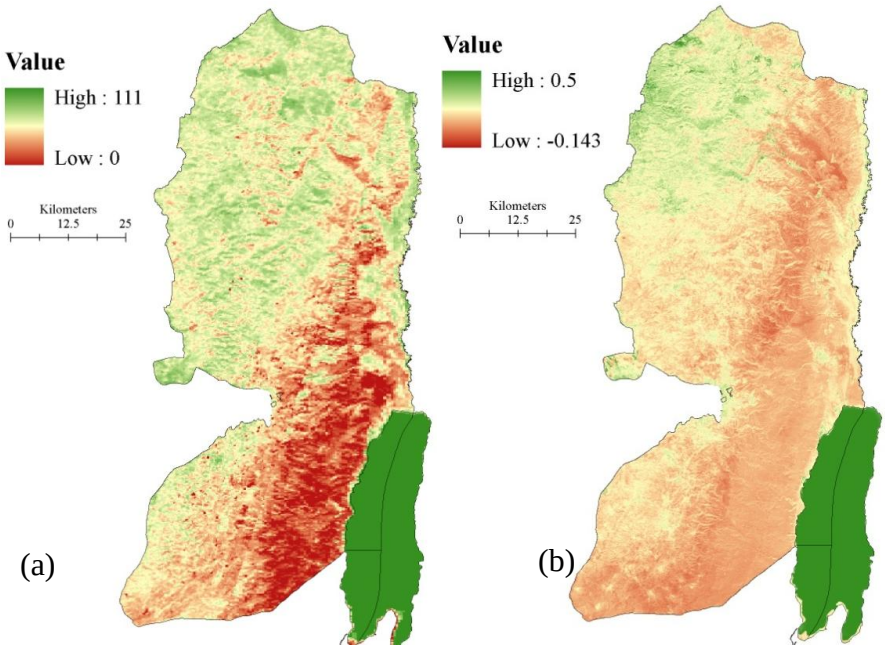

Figure 7.9: Relationship between (a) MODIS-derived ET and (b) SPOT-derived NDVI

7.4 SEBAL Model Validation

7.4.1 Validation to Ground Estimates

SEBAL validation is carried out on monthly basis by comparing estimates with field pan measurements, Penman-Monteith, and Thornthwaite calculations. Table 7.3 summarizes actual and potential estimates of the four methods for Jenin area and Figure 7.10 illustrates the numerical graphs for the three sites (Jenin, Ramallah, and Hebron). Actual ET estimates are derived through applying the soil moisture deficit (SMD) method (Chapter 5, Table 5.4).

Table 7.3: Comparison between conventional and SEBAL ET (mm month^{-1}) for Jenin *area*

Month	Potential Thornth-waite	Actual Thornth-waite	Potential Penman-Monteith	Actual Penman-Monteith	Potential Pan	Actual Pan	SEBAL
November	45.8	45.8	64.6	64.6	37.1	37.1	**69**
December	18.8	18.8	39.5	39.5	38.0	38.0	**52**
January	19.3	19.3	41.1	41.1	39.7	39.7	**47**
February	24.9	24.9	52.2	52.2	50.8	50.8	**87**
March	47.8	47.8	82.0	82.0	86.1	86.1	**116**
April	70.0	70.0	118.0	56.1	114.6	52.1	**155**
May	104.7	23.4	145.0	11.0	154.2	11.0	**184**
June	137.9	8.0	152.8	0.0	168.0	0.0	**203**
July	178.2	0.0	174.8	0.0	189.2	0.0	**210**
August	160.9	0.0	171.4	0.0	168.4	0.0	**190**
September	135.4	0.0	139.9	0.0	124.3	0.0	**143**
October	108.4	0.0	109.9	0.0	93.2	0.0	**114**

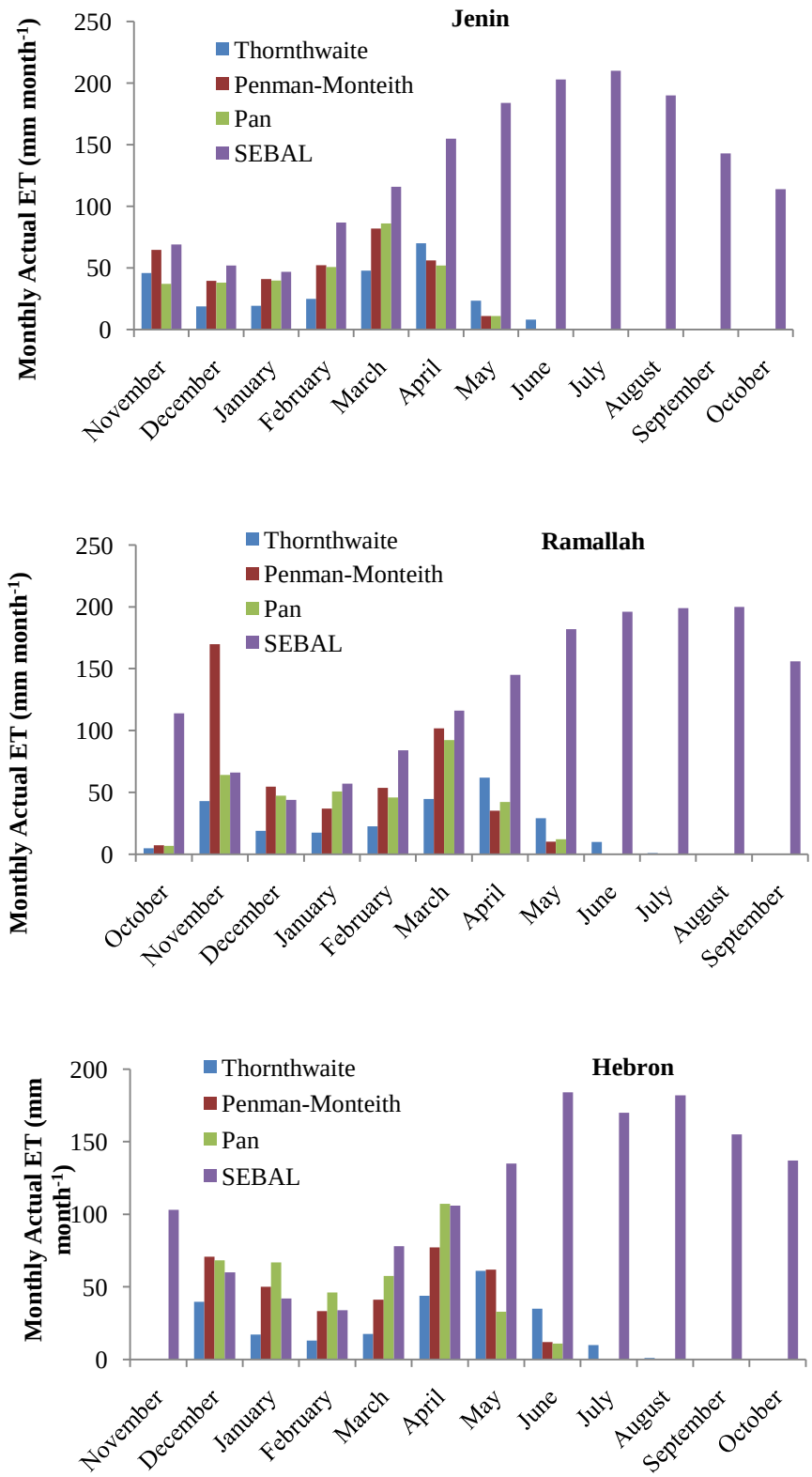

Figure 7.10: Monthly ET estimates derived from SEBAL, empirical equations, and field measurements

It is noticed that SEBAL estimates are found to exceed the potential rates derived from the other three methods. For instance, in the summer months, actual ET estimates are equal to zero using the SMD method while SEBAL estimates of the same period are of higher values equal or higher than the potential numbers derived by the three other methods. Evapotranspiration exists in small amounts in the dry season given that areas with trees and heavy vegetation are able to maintain evaporation rates even at the end of the dry season (Kurc and Small, 2004; van de Griend and Owe, 1993; Wythers *et al*., 1999). There could be some evapotranspiration occurring of water that has been condensed during the night which is almost an everyday phenomenon, thereby during the satellite overpass (all images are captured around 8:00 a.m.) evaporation may have been captured. Also, summer is the season for some agricultural crops such as grapes, irrigated agriculture, and some vegetation that could extract moisture from the soil profile during the dry season that is stored during the preceding wetter years. Yet evapotranspiration losses in the dry season decrease quickly to very low rates in the absence of precipitation, especially for bare soil and shallow rooted shrubs and grass. The total evapotranspiration from both the canopy and soil stays far below the total potential evapotranspiration because of the dry top soil. Capillary use could provide some additional moisture for ET, but for that to happen, a deep-rooted species should be present which might be the case in very small areas but not the bare soil and outcrop areas. Accordingly, it is evident that SEBAL is overestimating actual values and certain calibrations and refinements should be made in the approach in order to obtain results close to real values.

In winter months, estimates from November to February, actual SMD evapotranspiration estimates using the three methods are positively correlated with SEBAL numbers as shown in Figure 7.11 below:

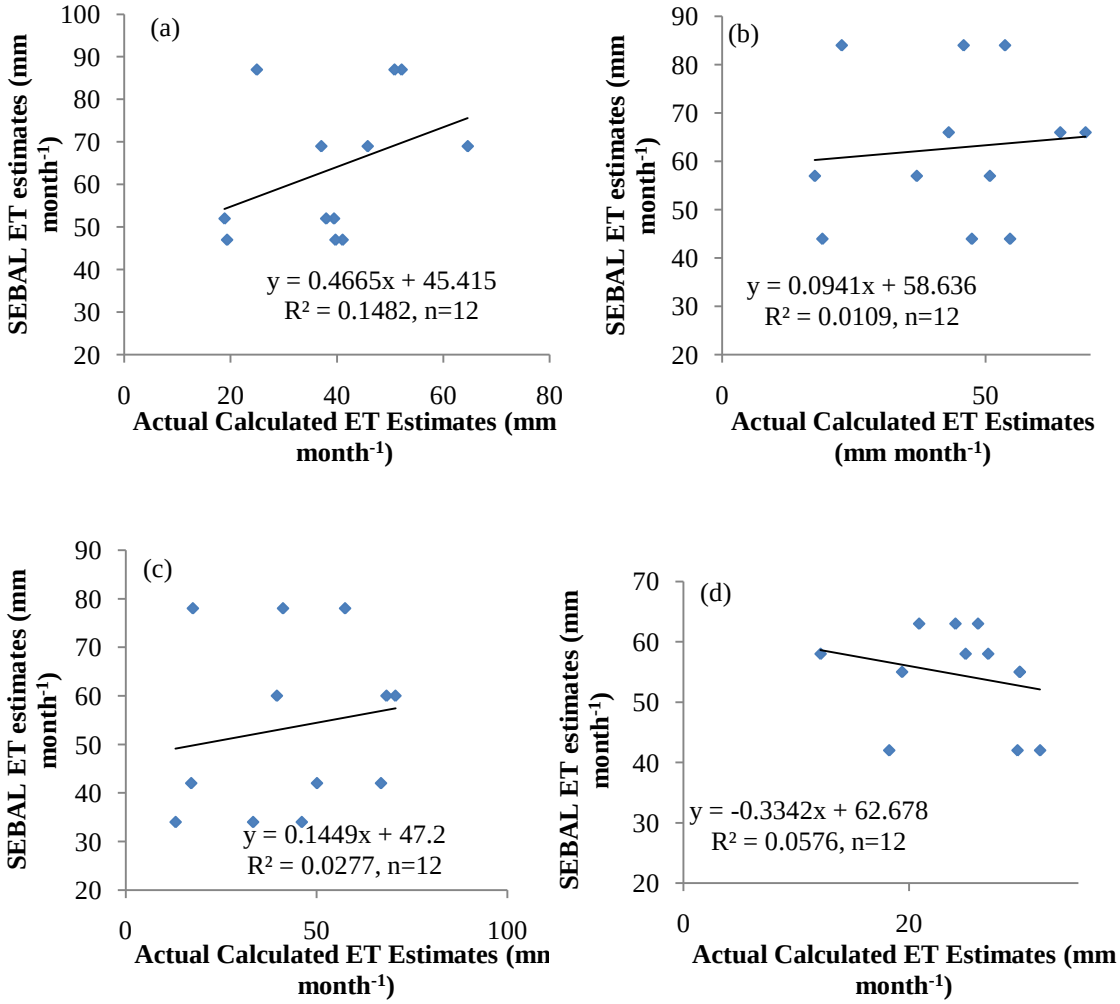

Figure 7.11: Correlation between evapotranspiration derived by SEBAL and the soil moisture deficit (SMD) in (a) Jenin (b) Ramallah, (c) Hebron, and (d) Jericho for the winter months (November to February)

The highest correlation exists in Jenin area where rainfed and irrigated agriculture is abundant. This indicates that SEBAL is less applicable in the semi-arid areas such as Hebron. The relation continued to be negative in the arid Jericho which indicates that SEBAL is not applicable to dry areas. This variation of applicability is attributed to two main factors. First, SEBAL uses the remotely sensed surface temperature as the primary boundary condition for providing estimates of fluxes. The latent heat flux is calculated based on the estimated total net radiation that uses surface albedo from satellite visible channels and vapour pressure using surface temperature from infrared channels (Kite

and Droogers, 2000, Granger, 1997). Since evapotranspiration consists of direct evaporation from vegetation surfaces and bare soil, it is then considered a function of soil moisture. However, SEBAL estimates are calculated based on the surface reflectance and emittance in different parts of the spectrum (Mohamed *et al*., 2004) disregarding the factor of water supply and moisture in the soil. Second, SEBAL produces instantaneous estimates and extrapolates these values into daily through the application of the evaporative fraction assuming that it is constant throughout the day (Bastiaanssen, 2000; Kimura *et al*., 2007), while it is well known that the evaporative fraction tends to be higher in the morning or evening and it is more stable at maximum evapotranspiration rate which takes place around midday on a clear day (Stewart *et al*., 1998; *Ramos et al*., 2009). Thus, using an evaporative fraction at the time of satellite overpass may not represent the cumulative heating, and hence the partitioning of available energy into sensible and latent turbulent heat flux during the day. Moreover, assuming that the evaporative fraction is constant over the 24 hours may lead to the assumption that a constant supply of water into the soil is provided, which is contrary to the actual situation. This is an additional error leading to high rates of evapotranspiration when applying SEBAL. In addition, surface temperature of MODIS Level 3 product exhibits similar values between vegetated (cold pixels) and arid areas (hot pixels) which leads to a zero temperature difference and therefore zero sensible heat flux and constant evaporative fraction equal to 1 (Equations 4.14 and 4.21). An evaporative fraction of 1 indicates that the West Bank is a wet surface and a constant supply of water exists. However in reality, during the spring time when potential evapotranspiration exceeds rainfall, soil moisture deficit begins in the surface layers of the soil and then moves further downwards into the lower layers until the summer months. When rainfall totals begin to exceed potential evapotranspiration in the autumn, the soil moisture stores are gradually replenished from top soil layers downwards until they all reach field capacity again in winter. Therefore, the evaporative fraction varies by season and evapotranspiration depends on the soil moisture content. This means that actual evapotranspiration should be at its lowest during the summer, contrary to SEBAL results.

It should be noted that sensor evaluation based on point data may not always be the most convenient method (El Maayar and Chen, 2006). First, for the point

measurements, the spatial resolution is limited by the degree to which weather data can be extrapolated that is affected, in the West Bank case, by its heterogeneity of the surrounding terrain and weather systems, while satellite approaches provide a regional overview. Second, SEBAL algorithm provides instantaneous estimates even though they may be integrated into a 24-hour period while point data provide real average daily measurements. Third, the three methods applied use regular climate data to estimate actual ET while SEBAL uses remotely derived data which could deviate from the actual. However, such comparison is seen to be indicative rather than qualitative. It can still provide a good way of comparing different sensors against other indicators in the absence of extensive field validation at the time of satellite overpass.

7.4.2 Validation Using Land Cover

Validation in previously published literature has been based on comparing crop coefficients that are equal to the evaporation rate predicted by SEBAL divided by the reference evapotranspiration from meteorological observations and evapotranspiration maps with land cover maps e.g. Bashir *et al*., (2008), Gao *et al,*. (2008), Compaore *et al.,* (2008), Kongo and Jewitt, (2006), Mutiga *et al.,* (2009), Ramos *et al..* (2009), Li *et al.,* (2008), Kite and Droogers, (2000), Timmermans and Meijerink (1999), Teixeira *et al.,* (2009) Bastiaanssen and Chandrapala (2003), Bastiaanssen (2000), Zwart and Bastiaanssen (2007), Patel *et al.,* (2006), Melesse and Nangia (2005). In some cases, actual crop coefficients could be lacking especially in areas of different vegetation types or stages of plants development therefore choosing the right coefficient could be difficult. Moreover, such comparison could be misleading for two reasons. First, the satellite image resolution used and the heterogeneity of the area where images of low resolution such as MODIS (1000 × 1000 m) have higher number of mixed pixels therefore pixels do not represent the actual ET of that area. Second, the misclassification of pixels into land cover classes could mislead the comparison between ET and land cover maps. Other methodologies of validation included comparing SEBAL estimates with the soil water balance residual which is ET, e.g. Bashir *et al.,* (2008). Also validation has taken place through comparing evapotranspiration maps of different sensors based on visual inspection in addition to histograms. Despite this fact, these studies have demonstrated that SEBAL tends to overestimate evapotranspiration

compared to field measurements or simulated data, even though study areas are specific field crops or local areas, yet, the results were considered acceptable with reasonable errors.

In this study, ET maps are validated by the land cover map produced using SPOT-5 HRG image for 2004. Such comparison took place because the meteorological infrastructure in the West Bank does not allow a thorough quantitative validation of SEBAL; hence other methods are employed such as the use of land cover map. Validation consists of studying the relation between ET and the surface biophysical variables such as the NDVI. Evaporation rates and land cover classes for each pixel are obtained with a GIS overlay analysis of land cover maps and the evaporation maps. However, this approach has not been an appropriate tool because the land cover extracted does not include a detailed crop types' classification, but rather whether the land is aggregated, urbanised, or bare (see Chapter 6, Table 6.2). Furthermore this method may be difficult to apply in heterogeneous landscapes (Compaore *et al*., 2008) such as the West Bank area. Finally, comparing land cover maps derived from SPOT images with a high spatial resolution of 20×20 m with the MODIS evaporation maps with coarse spatial resolution of 250×250 m may lead to inaccurate results where MODIS spatial resolution includes more mixed pixels than the SPOT imagery and its spatial scale is much larger than many spatial characteristics in the landscape of the West Bank. Nevertheless, MODIS based ET retrievals reflect the pattern related to the land cover classification as shown in Figure 7.12 below.

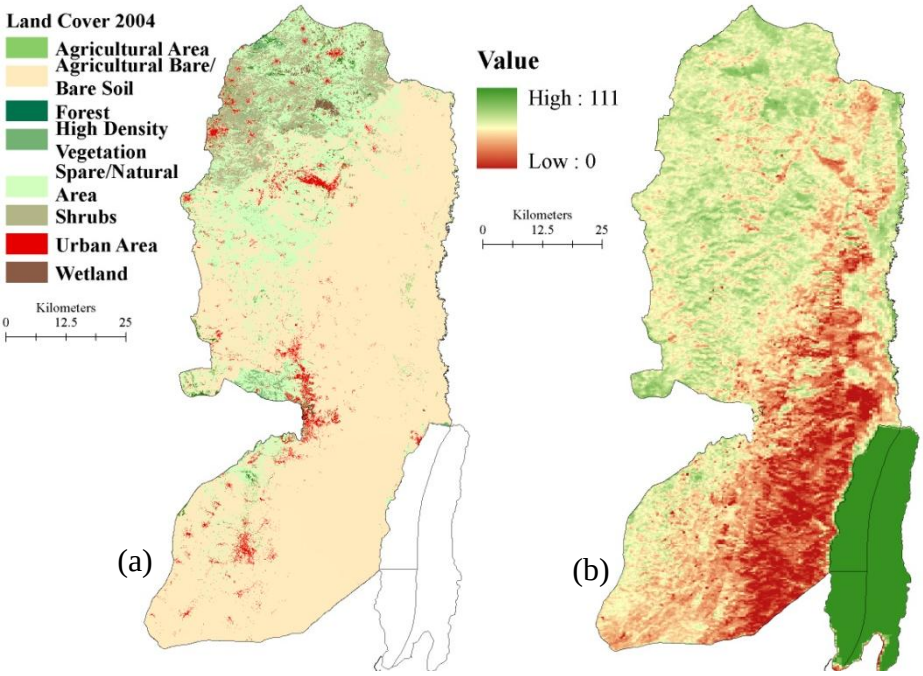

Figure 7.12: (a) Land cover classifications determined by supervised classification of SPOT imagery (May 2004) at 20 m resolution and (b) the aggregated product at MODIS 1 km of ET (May 2004)

The lack of spatial variability in the MODIS-based ET retrievals is evident in Figure 7.12. The higher values of ET correspond to the forests, wetlands, and vegetation in the North and western parts of the West Bank. These land cover types have lower surface temperature and sensible heat fluxes and so have higher ET values. Vegetation with a highly developed root system as in forests is often associated with high fractional vegetation cover which has much stronger transpiration than that of spare and moderate and/or low fractional vegetation cover areas. The lower ET estimates are noticed in the south and southeast areas of the West Bank. This is due to the predominantly sandy land and rocky bare hills existing and the high surface temperatures resulting in higher sensible heat fluxes.

7.5 Correlation of MODIS with Landsat Sensor

In order to check the performance for the MODIS sensor and its accuracy, ET is validated using Landsat TM5 of the same date. The comparison is based on the visual verification as well as the histograms of the two maps. Figure 7.13 shows SEBAL

spatial distribution over the West Bank in August 26th, 2003 using MODIS Level 1B and Landsat TM5.

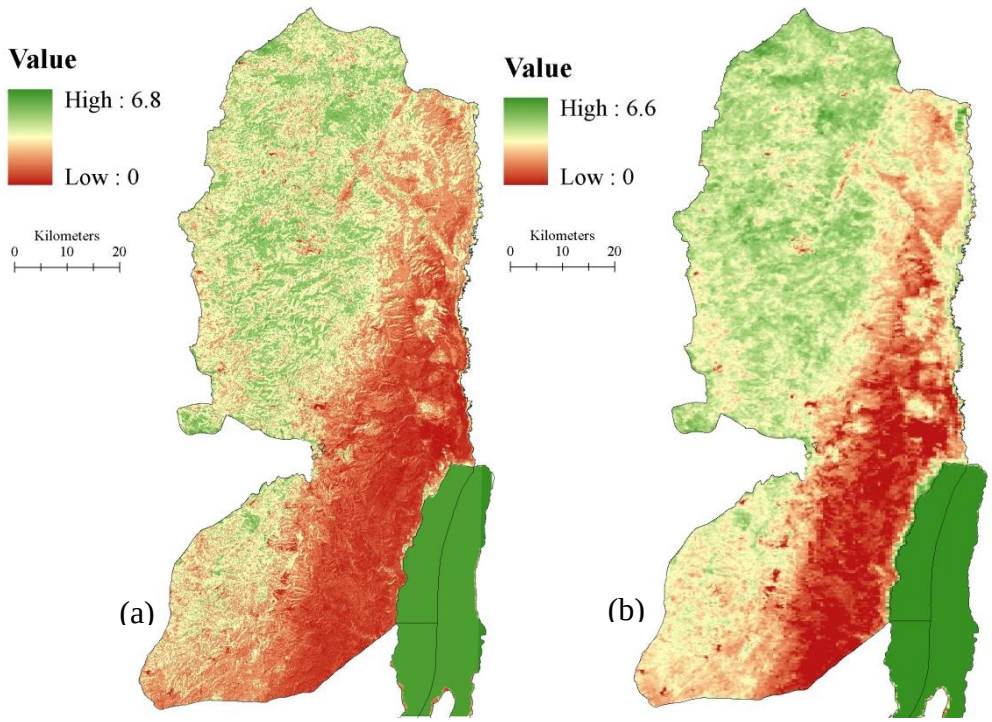

Figure 7.13: ET maps derived from (a) Landsat TM5 and (b) MODIS in August 26th, 2003

Results from both maps indicate that ET from the land surface varies similarly from place to place on both maps. Higher ET is associated with irrigated crops and forests in the western part of the area, while the low ET are observed from bare soil in the eastern and south-eastern parts, probably because of the higher soil moisture and groundwater tables in the western areas.

Some of the fine detail found on the Landsat TM5 map are not evident in the MODIS map. For example, forests and agricultural fields in the north and west of the area are more apparent on Landsat TM5 than on MODIS. The high spatial resolution of the Landsat TM5 ET map resulted in many homogeneous pixels having either high or low evaporation, while the low spatial resolution of the MODIS ET map results many mixed pixels consisting partially of high evaporation and partially of low evaporation areas. Yet despite the problem of mixed pixels, the Landsat TM5 and MODIS evaporation maps appear very alike.

Another way to compare the Landsat TM5 and MODIS ET maps is by the examination of the histogram (Figure 7.14).

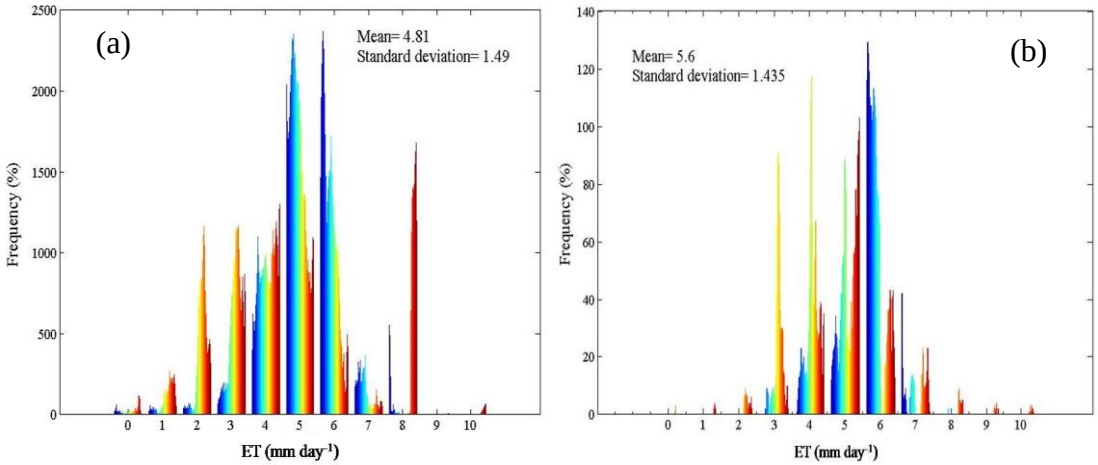

Figure 7.14: (a) Landsat TM5 and (b) MODIS maps of evaporation (August 26th, 2003)

The two histograms cover almost the same range of evaporation rates from around 2-7 mm day^{-1}. The mean evaporation rates for the Landsat TM5 and MODIS ET maps are 4.81 and 5.6 mm day^{-1}, respectively. Standard deviations are 1.49 mm day^{-1} and 1.44 mm day^{-1} for Landsat TM5 and MODIS images, respectively. Both histograms show a peak frequency of around 5.6 mm day^{-1}. The difference in SEBAL evaporation between the two ET maps is 0.8 mm day^{-1}, i.e., 16.6%. The Landsat TM5 histogram has some pixels of zero evaporation while the MODIS histogram starts with pixels of 2.2 mm day^{-1}. This could be attributed to the large mixed pixels of MODIS image where one MODIS pixel can contain many dry Landsat TM5 pixels plus moist ones which would result higher estimates.

To better illustrate the effect of pixel size, an area showing part of the Jordan Valley consisting of agricultural land, small reservoirs, and bare land is shown in Figure 7.15.

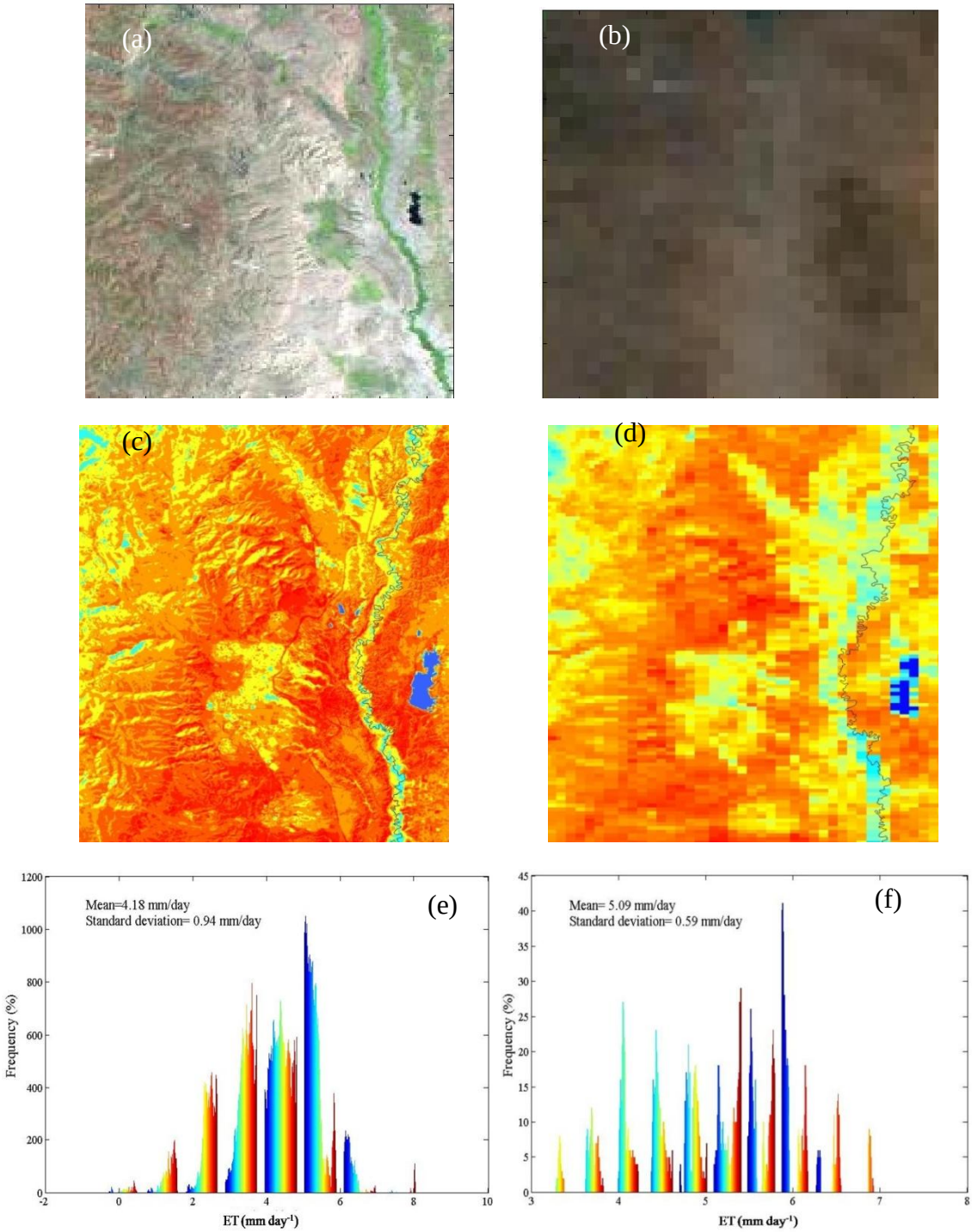

Figure 7.15: (a) Landsat, (b) MODIS, (c) Landsat ET map, (d) MODIS ET map, (e) Landsat TM5 histogram, and (f) MODIS histogram

The original Landsat TM5 image (Figure 7.15a) reveals more spatial details than the MODIS image; this difference becomes more apparent and stronger in the evaporation map (Figure 7.15c). The red colour represents high evaporation rates reaching 6.25 mm

day^{-1} in the Landsat TM5 image while in MODIS reaching 7 mm day^{-1}. The Landsat TM5 derived ET distribution has wider histogram distribution with some pixels having zero ET compared to the histogram from MODIS imagery. The ET map derived from Landsat TM5 image show a mean evaporation of 4.18 mm day^{-1} and a standard deviation of 0.94 mm day^{-1}, while MODIS shows a mean of 5.09 mm day^{-1} and a standard deviation of 0.59 mm day^{-1}. The peak values and frequencies also differ for both images. MODIS exhibit higher values than Landsat TM5 due to the larger pixel size. Yet the overall appearance of both evaporation maps is very similar and indicates that SEBAL derived from MODIS may be used as a mean for producing regional ET maps. This agreement between the Landsat TM5 and MODIS has been confirmed by other studies e.g. Hong *et al*., (2005), Opoku-duah *et al*., (2008), and Compaore *et al*., (2008) which indicates the potential of SEBAL with MODIS images under clear sky conditions. Other studies provide strong evidence that the SEBAL approach is a powerful tool for evaporation mapping (Bastiaanssen, 2005; Allen *et al*., 2007a,b; Bastiaanssen, 2000; Bastiaanssen *et al*., 2002).

7.5.1 Inter-Comparison of Ts, NDVI, and ET by MODIS and Landsat

To further illustrate the inter-comparison between the two sensors, Table 7.4 compares statistics of surface temperature (Ts), normalized difference vegetation index (NDVI), net radiation (Rn), and actual daily evapotranspiration (ETa) in the month of August.

Table 7.4: Variation of Ts, NDVI, Rn, and daily ET derived from MODIS and Landsat TM5 sensors

Variable	Landsat 5 26th August, 2003	MODIS 26th August, 2003
	Ts (K)	
Max	331.79	320.181
Min	284.699	303.365
Mean	314.587	311.769
SD.	4.764	0.802
	NDVI	
Max	0.630	0.416
Min	-0.138	-0.245
Mean	0.136	0.188
SD.	0.098	0.045
	ETa	
Max	6.8	6.6
Min	0.52	1.8
Mean	4.81	5.60
SD.	1.49	1.44
	Rn	
Max	253.407	229.093
Min	26.515	75.059
Mean	179.420	165.650
SD.	34.914	8.446

Surface temperature (Ts), NDVI, ET, and Rn derived from MODIS and Landsat TM5 sensors for the selected day in August are compared using maximum, minimum, mean, and standard deviation. In general, it is found to be a difference between MODIS and Landsat TM5 estimates. The average range of surface temperature measured by the MODIS sensor instrument is 312 K compared to 315 K by the Landsat TM5 sensor. Note that MODIS overpasses the study area at about 9:00 a.m. in the morning while Landsat TM5 does so at around 7:50 a.m. The standard deviation with Landsat TM5 is larger, which indicates that the difference between the mean values (~3K) is negligible and we might consider the two sensors to be not significantly different despite the differences in each sensor's characteristics, overpass time, atmospheric corrections, and spectral response function of the thermal infrared channels.

The retrieved mean NDVI values from MODIS and Landsat TM5 are much the same though the maximum NDVI from Landsat TM5 is higher than that from MODIS. With regard to ET values, the Landsat TM5 sensor measures a wider range on ET scale as shown in Figure 7.16, and each produces a different mean. The MODIS instrument

measures a mean regional ET value of approximately 5.6 mm day^{-1}, while Landsat TM5 measures 4.8 mm day^{-1}, which represents a difference of 0.8 mm day^{-1}, less than the standard deviation of either. Both sensors produce similar maxima and similar standard deviations. Landsat TM5 produces lower minima, one third lower than MODIS. These differences are due first to the difference in spatial resolution as explained earlier, and second, both images include the Dead Sea area, agricultural areas and forests lying outside the West Bank which highly affect the overall results.

Finally, Rn values considerably differ within each sensor in the maximum, minimum, mean, and standard deviation estimates. This may be due to several reasons among which are the technical factors such as the sensor characteristics, atmospheric correction, and the spectral response function of the thermal infrared channels (Brata *et al*., 2006; Goetz, 1997). The results are similar to those found in literature such as Batra *et al*., (2006), Huete *et al*., (2002), Opoku-duah *et al*., (2008), and Trishchenko *et al*., (2002).

MODIS measurements of Ts, Rn, and NDVI over the study area are in agreement with those of Landsat TM5 despite the difference in spatial resolution. The good agreement in this study confirm other studies (Hong *et al*., 2005; Compaore *et al*., 2008) and indicates the potential of MODIS images under clear sky conditions and high temporal resolution by which a continuous monitoring of key hydrological parameters such as ET, NDVI, and Ts over heterogeneous regional areas may be attainable. Yet MODIS needs to be validated using field observations to evaluate its accuracy and consistency with ground measurements.

7.6 Discussion

The relationship between visible and thermal infrared spectral radiances of areas with a sufficiently large hydrological contrast, dry and wet land surface types constitute the basis for the formulation of the SEBAL (Bastiaanssen *et al*., 1998a). It describes the latent heat flux (λE) as a function of:

$$\lambda T\ (ET) = Rn - G - H \qquad (7.2)$$

where λT is the latent heat (evapotranspiration), Rn is the net radiation, G is the soil heat flux, and H is the sensible heat all expressed in W m^{-2}.

The main parameter in the SEBAL algorithm is the evaporative fraction that is defined as the latent heat divided by the net available energy. The instantaneous evaporative fraction is considered similar to its 24-hour counterpart Shuttleworth *et al*., (1989) and the 24-hour net radiation can be computed as shown by Bastiaanssen *et al*. (1998) (Chapter 4, Equation 4.23). Knowing the instantaneous evaporative fraction and the 24-hour net radiation flux, and assuming the soil heat flux over a 24-hour period is negligible, the actual 24-hour evapotranspiration can be calculated as the evaporative fraction multiplied by the 24-hour net radiation flux.

SEBAL ET estimates when compared to Pan measurements, Penman-Monteith, and Thornthwaite equations are shown to be overestimating actual rates. This could be attributed to three factors:

I. *MODIS sensor:*

The terms in Equation 7.2 are constrained by remote sensing and depend upon the spatial and spectral resolutions of imagery used. Using visible near infrared (VNIR) to thermal infrared (TIR) detectors, constraints on three of the four terms are directly possible: sensible heat (H), net radiation (Rn) and soil heat flux (G). Sensible heat (H) is constrained by surface temperatures derived from TIR data, while both net radiation (Rn) and soil heat flux (G) fluxes are constrained by both VNIR reflectances and emitted TIR radiances. The remaining component, ET can be constrained indirectly by their residuals (French *et al*., 2005). The remote-sensing energy flux modelling is therefore determined by the sensor's ability to accurately determine the three flux terms from observed reflected and emitted radiances. Without sufficient accuracy, errors from estimates of H, Rn and G accumulate in ET flux estimates and could overwhelm results by 100s of W m^{-2} (Kustas and Norman, 1996; French *et al*., 2005). Hence, in this study, results accuracy is highly dependent on the MODIS sensor and its spatial and spectral resolution that are used to determine ET over the West Bank.

A study by Batra *et al*., (2006) compared ET and derived variables from MODIS, AVHRR, NOAA14, and NOAA16 sensors over the Southern Great Plains of the USA. The spatially distributed surface temperature, NDVI, and ET maps derived from MODIS are higher than the other three sensors. As ET derived from the four sensors is compared to ground measurements MODIS gave a root mean square error of 53 Wm^{-2}.

Referring to previous section, it is shown that when comparing Landsat TM5 ET results with that of MODIS of the same day of year 2003, the Landsat sensor produces lower values than MODIS. This is due to the difference in spatial and spectral resolution of Landsat TM5 thermal infrared channels and the dominance of mixed pixels in MODIS images. According to Woodcock and Strahler (1987), the adequate resolution to be used must be half the distance of the dominant land surface scale which in this case is smaller than the MODIS resolution. Spatial resolution is an important function of ET estimation as different land cover types are defined which have distinctly different heat flux properties, surface roughness, potential heat capacity, and spectral reflectance (French *et al*., 2005). In this case, MODIS images may not able to make these distinctions over bands with the 1 km resolution. Sufficient spectral resolution is also a requirement to accurately estimate the land surface temperature images, NDVI, and albedo. It is required that bands should be less sensitive to atmospheric water vapour content which is the case only with band 2 for the MODIS sensor (French *et al*., 2005, Kimura *et al*., 2007).

II. SEBAL methodology:

Despite SEBAL's ability to capture major characteristics of ET distribution at the regional scale, there are some uncertainties arising from assumptions and the operation of the model as it determines ET with the minimum amount of field data; this could make the user question its results (Doraiswamy *et al.*, 2008; Ramos *et al.*, 2009). These assumptions include:

- The presence of a dry pixel (zero evaporation) and a wet pixel (zero sensible heat) in the same image;
- The wind speed at the blending height (~100 m) is assumed constant over the whole area of study;

- The temperature difference ΔT is in a linear function with surface temperature Ts.

SEBAL is expected to deviate from true estimations on the regional basis as weathering conditions are not stable over the whole area. Meteorological measurements have shown how varied these conditions are and therefore, applying SEBAL with one averaged value for the whole area could lead to inaccurate results. For hill-slope surfaces, reflectance and emission differ in certainty by land height (Akbari *et al.*, 2007) and temperatures may deviate substantially from equivalent temperature for flat areas leading to inaccurate results; therefore, SEBAL results are considered unreliable for hilly areas (Akbari et al., 2007) such as the case of the West Bank topography.

Additional uncertainties in estimating ET using SEBAL are caused by the methodological procedures, uncertainties in input data, and uncertainties in the empirical coefficients. Some of these uncertainties include the incoming longwave radiation that is computed using field measurements of air temperature (Ta), outgoing short- and longwave terms that are estimated using remotely sensed surface temperature (Ts), albedo and emissivity, and surface albedo estimated using the linear model proposed by Valiente *et al*., (1995). The sensible heat flux is one of the main uncertainties in SEBAL model. Two pixels in the satellite image have to be selected: one completely wet for which H~0 and the temperature difference between surface temperature Ts and near surface air temperature Ta equals zero and a completely dry pixel where H=Rn. A study carried by Marx *et al*., (2008) in the Savannah region has shown that an uncertainty in H could reach up to 10% that is related to the surface temperature where the higher the surface temperature is the higher the uncertainty of H and therefore of ET. As SEBAL does not use near surface air temperatures because of its temperature normalization using wet and dry areas, the application of this approach may not work for the West Bank area due to the inability to fully distinguish wet and dry areas especially in summer months. *SEB*AL has also shown similar high deviations from field measurements when estimating sensible heat flux and underestimation of soil heat flux G, net radiation Rn, and overall evapotranspiration ET e.g. French *et al.*, (2005).

III. MODIS Level 3 (8-day) product:

Surface temperature differences are negligible in MODIS Level 3 (8-day) products, i.e. it assumes a low thermal emission and zero sensible heat flux. This leads to the assumption that the evaporative fraction equal to 1.0 within these products and that the West Bank area is a wet surface area. The evaporative fraction is expected to reach high values in the wet season but they do not reach 1.0 as MODIS images predict especially in the dry season. In the period from January to April, EF decreases as the rainy season ends while some events of rainfall do occur providing by thus sufficient water storage in the root zone. As atmospheric demand for water increases by the start of the summer season, actual evapotranspiration reaches to zero and so does EF. The challenge of the thermal infrared remote sensing is to correctly interpolate the surface energy balance of all other pixels between these two extremes.

Finally, cloud cover during fall, winter, and spring time decreases the intensity and affect of solar radiation. Therefore, in reality, solar radiation and net radiation is much less than estimates used with MODIS cloud free images.

7.7 SEBAL Calibration

Teixeira *et al.,* (2007, 2008 a&b, and 2009) have carried out a calibration procedure within certain irrigated crop fields. The calibration involved the ratio of evapotranspiration over reference evapotranspiration (ET/ETo) where the application of regression equations between field data and the satellite values of the same day of the year for the irrigated mango and natural vegetation is used. After the calibration is performed, successive interpolations are performed to retrieve the monthly and annual values of ET/ETo for the concerned years. After the interpolations, the annual and seasonal variations of ET are obtained for the fields within a 95% accuracy.

Timmermans *et al.,* (2007) have tried applying modifications to SEBAL inputs in order to reduce discrepancies with observations for bare soil and shrub classes in the Southern Great Plains in the Netherlands. Local calibrations are performed where empirical coefficients using measurements of NDVI, surface temperature, instantaneous and daytime averages surface albedo, soil heat flux, and net radiation measurements are

used. However, these adjustments modified the results for certain land covers and vegetation but increases the difference for others. For example, improvements to SEBAL inputs of surface roughness for momentum tended to increase errors in respect to observed fluxes. The study suggests that any internal calibration of SEBAL procedures, in particular the assumption of linearity between surface temperature and the aerodynamic temperature gradient used in defining the sensible heat fluxes, do not appear to be valid for heterogeneous landscapes.

A third calibration attempt has been done by Melesse and Nangia (2005) on flux estimation. Flux measurements from a flux tower station located in the study area is used to validate flux estimation and calibration is done on the Go equation as the SEBAL estimates overestimated the empirical. The average ratio of observed to predicted soil flux is used to modify the soil flux equation.

In addition to the above methods, additional calibration could be done on the H value that is considered the most complex to estimate and its value is associated with the greatest uncertainty. Scintillometers along with spatially dense meteorological measurements could be used to measure H and determine how it is related to temperature rates, wind speed, and water vapour deficit. The relation and measured H could then be used to calibrate estimates derived from SEBAL algorithm applied on satellite data. Also, a modified relation between NDVI and ET could be established where ET would equal 0 if NDVI is less than 0. This could be particularly true in arid and semi-arid areas where soil stressed surfaces exist and vegetation is absent starting from the summer months. Also, since soil moisture is a significant component of evapotranspiration, a relation between the two parameters could be integrated within the algorithm to sufficiently estimate ET based on water content in the soil and vegetation water consumption.

Although SEBAL has been tested and validated in a variety of wet environments like irrigated and agricultural areas, the algorithm need further calibration and validation for arid and semi-arid environments like the West Bank area. The model should be adapted to the arid conditions through redefining the ‘hot’ and ‘cold’ pixels to improve the prediction of ET in agricultural and bare areas. Yet still the main limitation for the

model calibration in the West Bank is the availability of weather data. Unfortunately, only monthly data is available which strongly constrains the calibration of SEBAL remote sensing model.

7.8 Conclusion

Water balance and irrigation management studies require accurate ET information. Ideally, ET information should have sufficient spatial detail at the aquifer level and cover large areas, such as entire river basins. Remote sensing energy balance models can produce ET estimates that meet these requirements. However, evapotranspiration cannot be measured directly from satellite imagery but rather it provides reasonably good estimates of evaporative fraction by the interpretation of radiometric surface temperature and vegetation indices from satellite sensors. With the use of maps of evaporative fraction and net radiation, it is possible to estimate ET from satellite imagery.

SEBAL model is based on the surface energy balance where net radiation flux density is considered the driving force for the processes as it heats up the air, evaporates water and heats up the soil. It uses surface temperature, Ts, hemispherical surface reflectance, r_o and Normalized Difference Vegetation Index (NDVI), as well as their interrelationships to infer surface fluxes for a wide spectrum of land types.

SEBAL has been applied to 48 MODIS Level 3 reflectance and 48 MODIS land surface temperature and emissivity images. ET maps show that the pixels in the west of the West Bank are of highest evaporation rates, which are in agreement with the abundant vegetation and water availability present in well developed soil. Lower rates are found in the eastern and south-eastern areas. Evaporation is lowest in the arid region of the Jordan Valley and Dead Sea area due to low rainfall (<100 mm year^{-1}), higher atmospheric pressure, and sand/stone surfaces.

Evapotranspiration estimated by SEBAL is validated with the actual rates derived by applying the soil moisture deficit method to three methods: Thornthwaite, Penman-Monteith, and Pan Evaporation. SEBAL estimates are found to be equal to the potential rates derived from the other three methods. While in winter months, estimates from

November to February, actual SMD evapotranspiration estimates using the three methods are positively correlated with SEBAL numbers as shown in Figure 7.11. The highest correlation exists in Jenin area (R^2= 0.148) where rainfed and irrigated agriculture is abundant indicating that SEBAL is more applicable in the humid and sub-humid areas. However, since these three methods give only point measurements and do not represent the actual conditions at a specific pixel, the relationship is only used as an indicator of relative change of evapotranspiration within the study area. Results show that SEBAL overestimates ET rates and may be considered inapplicable in the dry season. Overestimated ET outcomes are due to MODIS sensor characteristics, SEBAL assumptions, and MODIS Level 3 product. The main factor in MODIS product is its narrow range of surface temperature and low resolution, while the main factor in SEBAL methodology is not integrating the soil moisture within its algorithm and the computations of sensible heat flux.

Assessing consistency between MODIS and a higher resolution satellite sensor, a comparison with Landsat TM5 has been carried out. Maximum, minimum, mean, and standard deviation of different variables have been compared. The difference in estimates between the two sensors is mainly due to the difference in the spatial resolution of satellite data, vegetation heterogeneity, and scale-mismatch. The inter-comparison of spatially distributed ET and related variables (Ts, NDVI, and Rn) derived from MODIS and Landsat TM5 sensors shows that the obtained NDVI and ET values are similar while Ts and Rn are different as they are affected by the overpass times, spatial resolution, and number of infrared bands (Landsat has one thermal band- band 6, while MODIS has two- bands 31 and 32).

SEBAL method relies on empirical relationships which have been validated in many locations and it has shown to accurately estimate evapotranspiration over irrigated lands. However, the application of SEBAL for arid and semi-arid areas such as the West Bank have not been examined to make certain that the results are of good quality. Calibration to SEBAL in such areas could include applying local calibration to empirical coefficients in estimating heat fluxes and net radiation. In addition, integrating soil moisture content into the algorithm could improve SEBAL estimates as it is a significant component of ET particularly in arid and semi-arid areas.

Chapter Eight

Rainfall and Surface Recharge Mapping and Modelling

8.1 Introduction

Regional recharge models require distributed input data which classical measurements (that provide only point data obtained at weather stations, gauging stations, or boreholes) cannot fulfil. Hence, acquisition of distributed information is becoming one of the main goals in hydrological research. Data collection in the West Bank is considerably hampered by the limited accessibility, and weak observation infrastructure, hence it is unlikely that such a network of observing stations will be in place in the near future given the efforts and resources needed to construct and maintain such systems. A limited number of point measurements are available but groundwater models need spatial and temporal distributions of input and calibration data.

Recent developments in remote sensing have offered new sources for distributed spatial data for certain parameters including: evapotranspiration (Bastiaanssen *et al*., 1998 a& b), rainfall (Herman *et al*., 1997; Milewski *et al*., 2009), and soil moisture (Chabrillat *et al*., 2002; Leone and Escadafal, 2001; Shepherd and Walsh, 2002; Ben-Dor *et al*., 2004). Remote sensing offers data that can be translated into a deterministic distribution of input data on a cell-by-cell basis. Even if the absolute values are uncertain, relative data can still provide spatial information on key variables and lead to a better set of models.

This chapter aims to qualitatively estimate the recharge of water into the subsurface and to produce maps showing the spatial and temporal variability of actual recharge for 2004. Five types of remote sensing datasets are used, in addition to data on geology and soils to enable the extraction of realistic spatial and temporal distribution of recharge over the West Bank. These include: (1) Moderate Resolution Imaging Spectroradiometer (MODIS) with a resolution of 1 km (surface temperature and emissivity bands) and 250 m (reflectance bands); and (2) Landsat TM5 image with a resolution of 30 m used for comparing and validating MODIS evapotranspiration (ET);

(3) SPOT images with resolution of 20 m and 5 m used for extracting land cover; (4) monthly TRMM 3B43.V6 data that provides global data on rainfall using microwave and visible infrared sensors every three hours with a 0.25° × 0.25° footprint; and (5) ASTER Global Digital Elevation Model (GDEM) with 30 m grid resolution used to extract digital elevation to enable groundwater recharge mapping.

8.2 Surface Recharge Modelling

The recharge processes that occur in the West Bank are complex. The karstic nature of the aquifers, climatic variation from sub-humid to arid areas, local springs, flow to wadis, and urban and irrigation processes are difficult to quantify on a regional scale (Hughes and Mansour, 2005). However, recharge needs to be quantified regionally for water balance purposes and for use as an input to regional groundwater models.

The wetting thresholds (Lange *et al*., 2003) and the traditional soil moisture deficit (SMD) approach (Penman, 1948; Lloyd, 1980; Rushton, 1988) are two common approaches used in estimating recharge on local scale in the West Bank area (Hughes *et al*., 2008). Even though the soil moisture balance is an approach that is developed for humid climates conditions and has less reliability in arid and semi-arid climates. Lerner *et al*., (1990) argues that it could still be used if certain conditions are met when:

i. Whole year: $P + I > 500$
ii. Wet season: $ETp < 1.5(P + I)$
iii. Dry season: $ETp < 3(P + I)$

where P is precipitation (mm year^{-1}), I is irrigation (mm year^{-1}), and ETp is potential evaporation (mm year^{-1}). Other factors need to be met as Lerner *et al*., (1990) indicate: (a) soils are well developed and do not dry completely; (b) potential evapotranspiration and actual evapotranspiration are of similar sizes; and (c) widespread and relatively uniform precipitation. These conditions are only met in the Western and North-eastern Aquifer Basins (Hughes and Mansour, 2005; SUSMAQ, 2001). Nevertheless, the soil moisture deficit model is applied in this research over the whole study area to compare its calculations with SEBAL and to validate the remote sensing derived estimates with field observations (see Chapter 7).

On regional scale, a frequent approach is the apportionment of recharge in proportion to the amount of rainfall in a given month. Different empirical equations are proposed, e.g., Goldschmidt (1955), Goldschmidt and Jacobs (1958), Tahel (1988), Assaf *et al*., (1993), Guttman and Zuckerman (1995), Ba'ba' (1996), and Bachmat (1995) (see Table 2.4, p. 27). Surface recharge is estimated by multiplying annual rainfall by the proportion of rainfall falling in each month to form a set of monthly recharge estimates. Recharge is then clipped to the aquifer basins outcrop areas to form the aquifer's monthly recharge (SUSMAQ, 2003). This approach assumes a linear relationship between recharge and rainfall which is a false assumption in months with low precipitation where no significant recharge exists. Assuming a linear relationship between the two variables has resulted in small amounts of recharge outside the winter season which is incorrect. Moreover, this approach fails to account for other factors leading to significant localised inaccuracies in estimating recharge such as evapotranspiration, discharge, land use, soil moisture, or topography.

A model developed by the British Geological Survey and the Palestinian Water Authority calculates recharge at nodes held on grids where four types of calculations are used based on the climatology of the area. For instance, the soil moisture deficit is used at nodes lying in semi-humid areas and the wetting threshold method is used at nodes in arid areas. However, this model applies potential rather than actual evapotranspiration rates and it lacks the spatial distribution data of rainfall and evapotranspiration where point measurements are extrapolated.

To address these limitations, a remote sensing model is proposed where fundamental hydrological parameters such as evapotranspiration and precipitation are extracted on pixel basis to study the water balance process taking place on the study area scale.

8.2.1 Rainfall and Surface Recharge Modelling

Recharge modelling aims to quantitatively estimate the recharge of water into the subsurface media, and to produce a map showing the different zones of actual recharge. A simplified model of precipitation-recharge is employed. In principle, the model assumes that some of the precipitation returns to the atmosphere by evapotranspiration, some runs laterally on the ground surface through streams in the form of flood runoff,

and the remainder percolates through the soils and rock strata and becomes direct recharge to the groundwater aquifers. Other minor losses do exist such as subsurface flows and depression storage but are hard to measure; therefore, precipitation, evapotranspiration, and runoff are the major hydrological parameters to be used to calculate infiltration recharge. This section is concerned with estimating this direct surface recharge based on an applicable technique of water balance based on equation 8.1 and as illustrated in Figure 8.1.

$$\text{Recharge} = \text{Precipitation} - \text{Runoff} - \text{Actual Evapotranspiration} \qquad (8.1)$$

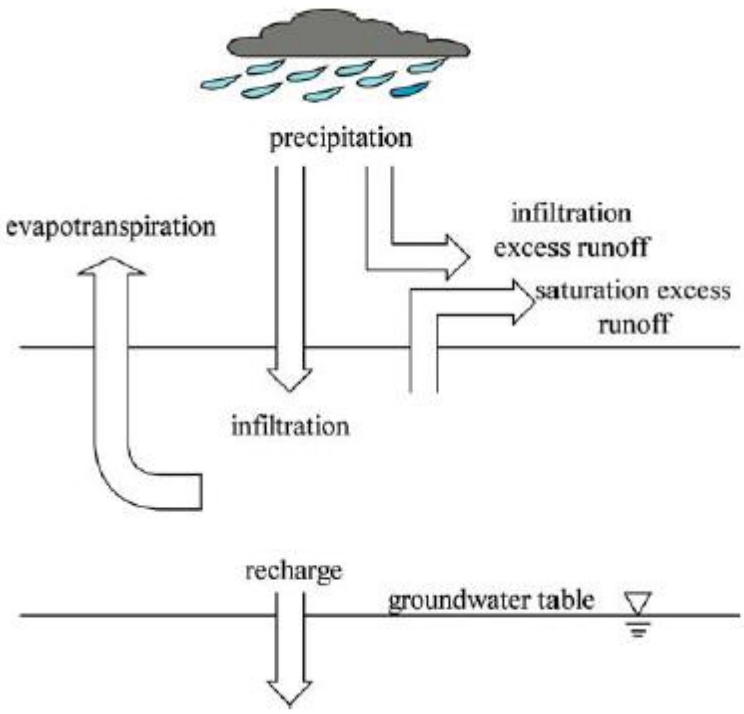

Figure 8.1: A schematic of the water budget. (Chen *et al*., 2005)

Evapotranspiration and precipitation are known parameters derived from satellite data; on the other hand, runoff is the parameter that is undefined and will be given an assumed value. Previous studies suggest a potential surface water runoff of 10 MCM yr^{-1} (million cubic meters per year). Goldschmidt and Jacob (1958) suggest a value of

4% of rainfall as runoff. A similar value, 2%, is suggested in a study by the Palestinian Hydrology Group and Newcastle University (Husary *et al*., 1995). Data from the Israeli Hydrological Service Yearbook for 1996 calculates runoff as a percentage of precipitation, giving values of between 0.1 and 4.7% for areas of the Western Aquifer Basin (SUSMAQ, 2001). Studies conducted under more arid conditions in Southern Israel suggest a 4% runoff (Shentis *et al*, 1999; Meirovich *et al*, 1998). Sabbah (2004) and Rofe and Raffety (1963, 1965) suggest that surface runoff in the West Bank is intermittent and most probably occurs when rainfall exceeds 50 mm in one day or 70 mm in two consecutive days. Higher runoff coefficients are considered by CDM (1998), 16% of rainfall in the Eastern Aquifer Basin based on literature reviews and discussions at the West Bank Water Department and Tahal. Similarly, Schneider (1965) adopts a value of 17% of rainfall as runoff.

Typically, there are sufficiently long dry periods between rain events for the soil to dry out and reduce the runoff potential of the next storm. However, runoff patterns in the West Bank area are unpredictable and it can fluctuate from zero flow in certain rain events to several million cubic meters per year in others. Exact numbers have not been reported and in order to make more accurate estimates of runoff, daily rainfall is required. In this research, predicting runoff from monthly precipitation is erroneous and invalid since daily rainfall intensities are unknown and they differ from one area to another and therefore one absolute runoff coefficient cannot be established. However, since wadi runoff lies in an order of up to 10 MCM yr^{-1} in strong and high-intensity rainfall winter seasons (SUSMAQ, 2003), then a 0.75 mm $month^{-1}$ (4.2 MCM $month^{-1}$) is used as a runoff value for the month of January and 0.4 mm (2.2 MCM yr^{-1}). The assumed percentages of runoff out of the total annual runoff, 41.5% and 22.4% for January and February, respectively, are assumed to equal the percentages of rainfall for each respective month to the total annual rainfall (e.g., rainfall percentage for January = 175.9/242 mm, therefore runoff percentage for January month equals 41.5%). Based on that, runoff is calculated. It is important to mention that some of the runoff flow will infiltrate into the ground as it reaches wadi depressions in Jordan Valley again and thus contribute to the groundwater flow; therefore, the numbers assumed remain uncertain.

8.2.2 Modelling and Mapping Recharge

Groundwater recharge mapping requires the integration of spatial information and criteria. Geographic Information Systems (GIS) are capable of managing such spatially distributed information providing the ability to integrate and manipulate multiple layers of information for such analysis (Krishnamurthy *et al*., 1996; Murthy 2000; Saraf and Choudhury 1998; Baker *et al*., 2001; Henry *et al*., 2008; Tabesh *et al*., 2009). However, only a limited number of studies have taken the approach of specifically mapping actual recharge zones, and as such there is no integrating of multi-criteria analysis using the rated aggregation method, associated with GIS techniques to derive the groundwater recharge map. Hence, this is a new approach adopted for mapping groundwater recharge zones (Chenini *et al*., 2010).

The National Remote Sensing Agency (NRSA, 1987) in India was the first to integrate information from remote sensing and the technology of the geographical information system (GIS) for delineating potential groundwater recharge zones (Yeh *et al*., 2009). GIS is used to manage, utilize, and classify the results of remote sensing, to explore sites, to combine the factors of groundwater recharge, and to provide appropriately weighted relationships (e.g. Chenini *et al*., 2009; Yeh *et al*., 2009; Krishnamurthy *et al*., 1996; Saraf and Choudhury 1998; Sener *et al*., 2005).

In this study, the actual recharge zones are set as a result of integrating five parameters derived from satellite imagery: precipitation, evapotranspiration, slope, land cover, and drainage density and two GIS thematic layers: geology and soil type as illustrated in Figure 8.2.

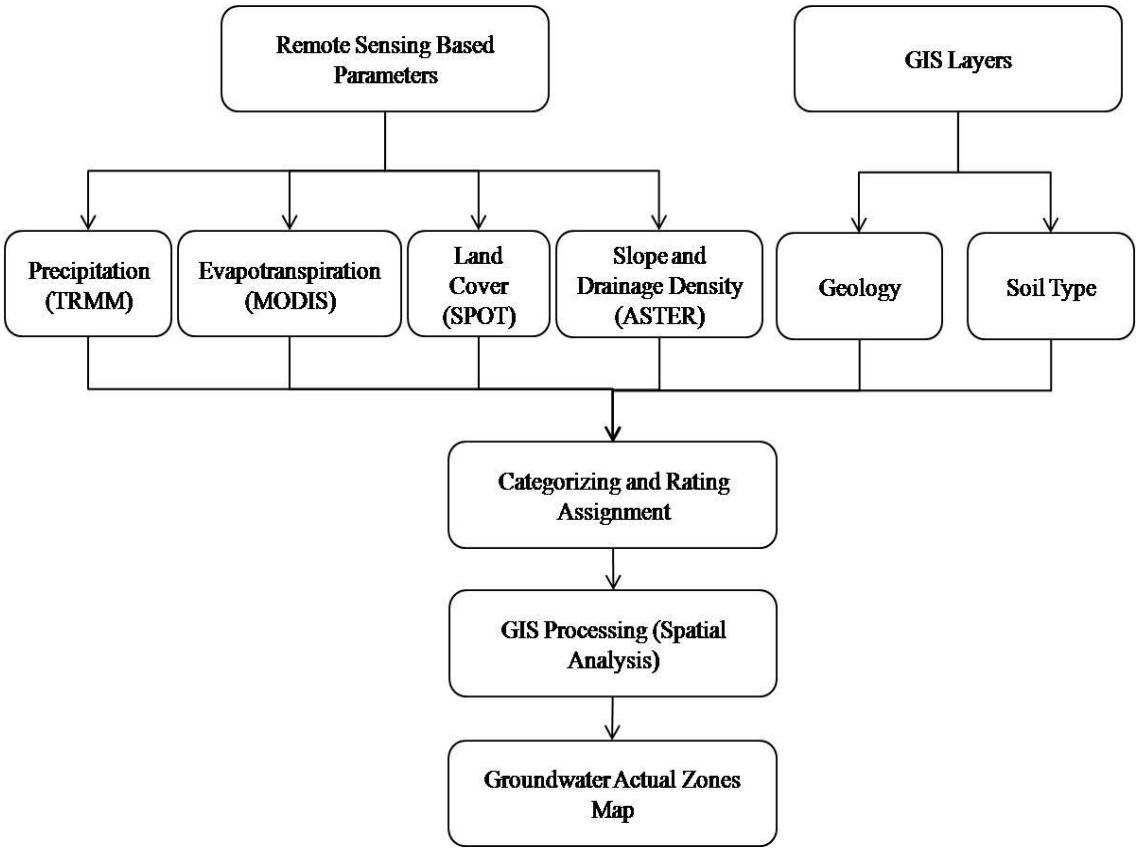

Figure 8.2: Methodology flowchart for actual groundwater zones mapping

To map recharge areas, all these thematic layers are integrated using ArcInfo software in a weighting system. The weighting system is a method for a combined analysis of multi-class maps. The weight represents the relative importance of each parameter classes vis-a-vis recharge. The weights of the different features of each parameter are assigned on a scale of 1 to 6 based on their relative importance for groundwater recharge. Based on the assigned weights, the qualitative evaluation of different features of a given parameter is performed as: very low (weight=6-11); low (weigh=12-18); intermediate low (weight=19-24); intermediate high (weight=25-30); high (weight=31-36); very high (37-42). In order to assign weights to the different features and relative importance of parameters, field research, questionnaires, and discussions are required among geologists and hydrologists. However, this step was not feasible and difficult to perform. Therefore, reference to literature and past studies was considered the source of differentiating the relative importance of each individual parameter and its features from the recharge viewpoint, e.g. Chowdhury and Jha (2010); Duraiswami *et al*., (2009);

Sener *et al*., (2005). Moreover, due to lack of sufficient information of these parameters interaction with recharge in the field, an equal weight is suggested. In other words, each parameter is assumed to have the same degree of influence on recharge as the other, and so, the equal interactivity. On that basis, the parameter classes influencing groundwater recharge, and their relative importance, have been compiled. Other factors such as the saturated zone depth, water table depth, well extraction, and discharge are of potential importance but are within the scope of deep recharge where as this study focuses on actual surface recharge.

The final step includes spatial analysis to demonstrate groundwater recharge zones of the research area where classes with higher values indicate the highest zone of recharge.

8.2.2.1 Precipitation

The network of rain gauges is not dense or evenly spaced in the West Bank as illustrated in Chapter 2 (Figure 2.2); thus, satellite observation of rainfall networks may be the best solution for adequate temporal and spatial coverage of rainfall. Accordingly, the Tropical Rainfall Measuring Mission (TRMM) is used to provide monthly precipitation data. The overall correspondence between the derived precipitations from the 3B43.V6 TRMM product and rain gauge data is evaluated for the study area. A correspondence of R^2=0.59 is observed between monthly precipitation extracted from the individual TRMM data in 2004 and rainfall measurements at six stations (Figure 8.3).

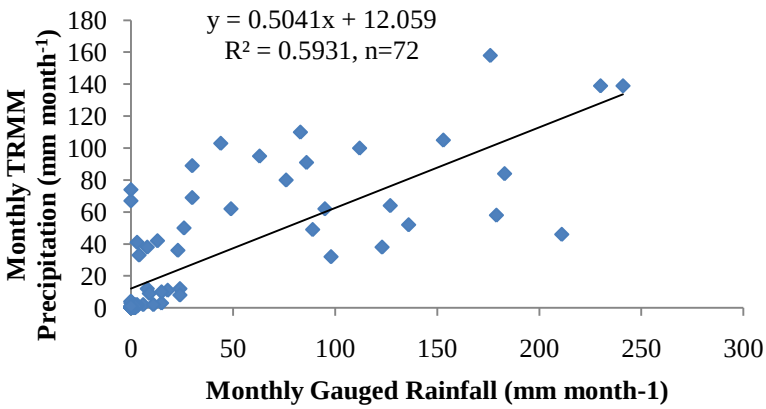

Figure 8.3: Relation between derived precipitation from monthly TRMM data sets and measured rainfall at six stations

Divergence of points from mean line could be attributed to the coarse spatial resolution of TRMM imagery (Figure 3.6) and uneven and insufficient distribution of rain gauge stations covering the study area (Figure 2.2). Implications are further discussed in section 8.5.2.

For each individual precipitation map, the weighting is set according to Table 8.1 (Sener *et al*., 2005):

Table 8.1: Weighing scheme for precipitation parameter

Value (mm month^{-1})	Weight
0-30	1
31-60	2
61-90	3
91-120	4
121-150	5
151-180	6

The weighting scheme in Table 8.1 is based on the highest precipitation values of the year which is the month of January. The same rating scheme is applied to all winter months.

8.2.2.2 Evapotranspiration

One of the main objectives of this research is to quantify evapotranspiration which has been accomplished through the application of the SEBAL algorithm (see Chapter 7). Evapotranspiration maps have shown variations over the West Bank reaching its maximum in the north and west. The evapotranspiration weighting is described in Table 8.2 according to the highest values of year.

Tale 8.2: Weighing scheme for evapotranspiration parameter

Value (mm month^{-1})	Weight
0-40	6
41-80	5
81-120	4
121-160	3
161-200	2
201-255	1

8.2.2.3 Geology

Geology controls recharge through the nature of rocks at outcrops and through the topography, slope, and nature of soil. Runoff generally is greatest over the less permeable deposits such as the calcareous serozems and loessial serozems formations underlying the Eastern Aquifer Basin. The existence of these formations combined with the limited soil coverage and arid climatic conditions results in high runoff to wadis, hence, indirect recharge.

In the study area, six types of geology, namely effusive rocks, alternating limestone, nodular limestone, basalt, sandstone, fluviatile deposits and gravels are found (Figure 2.19, p34). Effusive rocks, chalky marls, gypsum, and limestone are considered to be the least productive in term of water recharge. Gravels and sandstone are more coarsely grained than the other formations and has large hydraulic conductivities and therefore, most transmissive. Geology weighting (SUSMAQ, 2001, 2003; Aliewi *et al*., 2006; Hughes and Mansour, 2005) are described in Table 8.3 below.

Table 8.3: Weighing scheme for geology parameter

Formation	Weight
Basic effusive rocks Chalky marls, bituminous limestone and marls, locally gypsum, locally crystalline limestone Thick bedded limestone and dolomites	1
Alternating limestone, marls and cherts, coquina siliafied limestones, phosphorites Marls, clay, gypsum, and sulphur	2
Nodular limestone, clay sand marls with gypsum, thickened limestone	3
Basalts and middle flows	4
Argillaceous sandstone, sandy dolomite, sandy limestone Calcareous sandstone Fluviatile deposits, eolian sand, mantle rocks Sandstone, calcareous sandstone, conglomerates limestone	5
Fluviatile gravels	6

8.2.2.4 Soil Type

A summary of the main soil types is presented in Chapter Two (Table 2.7). The predominant soil types are Terra Rosa, Brown Rendzina, and Pale Rendzina (41% of the West Bank) and Brown Rendzina and Pale Rendzina (26%) (ARIJ, 2007) found in the central and western parts of the West Bank. These soils are described as being contained in pockets and cracks which may be deep (ARIJ, 2007) and therefore their distribution in the area creates a problem for defining soil thickness. This combination of soils with bare rock in the east and south has implications for recharge process where development of soil moisture may be inhibited and runoff increased in comparison with areas where soil is more evenly distributed over the surface as in the north and west of the West Bank.

A question may be asked: which is more important in terms of groundwater recharge, geology or soil? In terms of surface recharge, soil type is considered one of the important parameters in recharge calculations. However, in terms of deep recharge, geology is an important criterion. But in order to answer the question, further field research in the study area is required. Due to lack of such information, an assumption of equal influence on groundwater recharge is considered.

Different soil type classifications of the West Bank area exist. However, weight is determined based on literature reviews and analysis (Sener *et al*., 2005; Ravikovitch, 1960; Shapiro, 2005).

Table 8.4: Weighing scheme for soil type parameter

Type	Weight
Calcareous serozems, loessial serozems, brown lithosols and loessial serozems, and solonchaks	1
Grumusols	2
Alluvial and brown soils, dark brown soils, and loessial and brown soils	3
Brown randzinas, pale randzinas, and terra rosa, brown randzinas and pale rendzina	4
Regosols and sandy regosols	5
Bare rock and desert lithosols	6

8.2.2.5 Slope

Slope angle directly affects runoff but in this study it is considered equally weighted with the other parameters for recharge mapping. The implication of slope on recharge is that infiltration rate decreases with increased slope angle (Fox *et al*., 1997). Steep-sided slopes of the West Bank mountains result in enhanced runoff where water drains to the Jordan Valley floor and creates flow in the wadis. However, the relationship between the slope angle and infiltration rates remains unclear and no definite equation represents the relation (Fox *et al*., 1997). Several factors influence slope-infiltration relation such as surface storage, rainfall intensity, and the presence of rills. For example, surface storage capacity and mean ponding pressure head decreases with increasing slope angle, and infiltration rate therefore is to decrease. However, infiltration rate is observed to increase with increasing slope angle for a silty loam prone to surface crusting (Poesen, 1984). In a controlled field experiment, Luk *et al*., (1993) used a simulated rainfall to examine the influence of slope angle on infiltration in a loess soil that is prone to crusting and found out that for short duration infiltration increased with increasing slope angle, but for longer storms, infiltration decreased. Bradford and Huang found that infiltration rate increases with increased slope angle for 1 of 4 soils and stated that the relationship is probably soil-specific. Decreasing infiltration rate with increasing slope angle has been observed in the field in soils from different parts of the world (Nassif and Wilson, 1975; Djorovic, 1980; Sharama *et al*., 1983).

The influence of slope angle on infiltration rate remains undefined and further investigation is required to study the relationship. For the West Bank area, no field research has been done on the slope recharge relation; therefore, the study area is divided into six slope classes as shown in Table 8.5. The slope map is calculated with the help of ArcGIS/Info 9.2 package derived from ASTER GDEM data as described in Chapter 3 (section 3.6.2). The slope percentage in the area varies from 0 to 76%. Areas having 0 to 1% are assumed to be considered to be with the highest infiltration rate. Areas with slope percentage higher than 30% are considered the poorest due to the high slope and runoff (Sener *et al*., 2002; Chowdhury and Jha, 2010; Raymond *et al*., 2009).

Table 8.5: Weighing scheme for the slope parameter

Slope in percentage	Weight
0-1	6
1-3	5
3-5	4
5-10	3
10-30	2
>30	1

8.2.2.6 Land Cover

Land cover is a significant factor affecting the recharge process. Its classification is presented in chapter 6 (Table 6.2). Of the total study area 20% is agricultural and vegetation area, 0.5% is forests, 2.6% is urban, 0.5% is wetland, and 76% is bare soil, agricultural bare soil, and shrubs. Forest and agricultural lands are weighted highly as soils are developed and trees arrest water and reduce soil erosion. Moreover, since agriculture is carried out on more or less flat areas of potential infiltration is greater. Semi-natural areas and bare soils also have a high weight as they also aid infiltration. Built-up areas are surfaced areas having limited contribution to recharge; they do not have good coverage of drainage systems and therefore are given the lowest weight (Duraiswami *et al*., 2009; de Vries and Simmers, 2002; Sener *et al*., 2005; Raymond *et al*., 2009).

Table 8.6: Weighing scheme for land cover parameter

Land cover	Weight
Forest	6
Heavy vegetation	5
Agricultural area/ green houses	5
Wetland	4
Semi natural area	3
Bare soil/ shrubs	2
Urban area/water reservoir	1

8.2.2.7 Drainage Density

A large number of wadis exist in the West Bank, either flowing westwards towards the Mediterranean or eastward towards the River Jordan. Wadis only flow for a few days each year due to the nature of high-intensity rainfall and the associated flashy runoff. Transmission losses through the wadi beds enable runoff collected in the wadis to recharge the groundwater system. Wadi flows can also accumulate over less permeable deposits, and then flow is lost once the wadi bed passes over more permeable deposits with higher transmission losses. Wadis, therefore, have an important role in collecting runoff and promoting recharge.

The drainage density, expressed in terms of length of channels per unit area (km km^{-2}) indicates an expression of the closeness of spacing of channels, hillslope length, and nature of the topography. It thus provides a quantitative measure of the average length of stream channels within different portions of the whole basin. Drainage density indirectly indicates permeability and porosity due to its relationship with surface run-off (Krishnamurthy *et al*., 2000). Areas with high drainage density arrest excessive runoff and are given higher weights (Krishnamurthy *et al*. 1996; Chowdhury and Jha, 2010) as is expressed in Table 8.7 below.

Table 8.7: Weighting scheme for drainage parameter

Drainage $\times 10^{-4}$	Weight
0 - 3.7	1
3.7- 7.4	2
7.4- 11.1	3
11.1- 14.8	4
14.8- 18.5	5
18.5- 22.2	6

The step following categorizing and weighing of all features of the thematic layers is to produce a final map derived as a sum of the weights that have been assigned. Theoretically this final layer should have a maximum value of 42 (7 layers multiplied by highest weight which is equal to 6) and a minimum value of 7 due to existing polygon combinations. The final integrated layer is classed as either very high, high, high intermediate, low intermediate, low, and very low based in the weight ranges obtained as shown in Table 8.8.

Table 8.8: Recharge mapping weighing values

Value	Weight
42-37	Very high
36-31	High
30-25	Intermediate high
24-19	Intermediate low
18-12	Low
11-7	Very low

The integration of all above-mentioned factors in the GIS is an approach to estimate and assess areas of recharge.

8.3 Surface Recharge Modelling

8.3.1 Recharge Rates Results

Previous studies have developed analytical models based on annual averaging of rainfall data. These models have proven to be inadequate for developing flow models because the main interest has been studying changes in the aquifer over shorter periods. Since daily data are not available, monthly recharge calculations have been carried out in this study.

The approach used for the monthly recharge estimation is to apply a simple water balance where monthly evapotranspiration (ET) derived from SEBAL and runoff is subtracted from the monthly precipitation (P). Other existing components of recharge such as irrigation, leakage from water supply systems, inter-aquifer connections, and artificial recharge exist in small amounts and therefore are not considered in the calculations. Rainfall recharge is estimated for the winter months only.

Rain is limited to winter months; 70-85% of rainfall occurs between November and February as shown from rainfall data in Chapter 2 (Figure 2.3); usually there is no rain between June and September. The concentration of rainfall within December and January combined with the lowest potential for evapotranspiration is to enhance the potential for recharge in these two months. Aleiwi *et al*., (2006) observed that the month of April each year exhibits the peak of the water levels meaning that the effect of rainfall appearing as recharge in the aquifers is accumulated over the wet season of that year, i.e., in April, the water level will get contributions from March, February, January, December, November and October with the maximum contribution coming from the lagged recharge of the months of December and January in this year of study (2004). It is assumed that the study area is a closed area and hence water storage component is treated as the closing factor of the water balance. Table 8.9 shows the recharge calculation results and Figure 8.4 shows actual surface recharge distribution in January.

Table 8.9: Recharge estimations of the study area from November to January

Month	Mean Recharge (mm month^{-1})	Mean Positive Recharge (MCM month^{-1})
November	12.6	71.1
December	44.5	251.2
January	66.7	376.6
February	0.0	0.0
March	0.0	0.0
Total	**123.8**	**698.9**

There is considerable recharge in the winter period during which the lands are barren and/or crop cover is very thin. The recharge estimations in Table 8.9 show that significant recharge occurs mainly in December and January with some recharge in November and none in February or March. The average annual recharge rate is estimated as 700 MCM yr^{-1}. Rofe and Raffety (1965) has estimated recharge rates ranging between 821-836 MCM yr^{-1}, the Hydrological Service of Israel (1997) estimated recharge to equal to 836 MCM yr^{-1}, and Guttman (1995) has concluded that recharge equals 800MCM yr^{-1} (Table 8.10).

Table 8.10: Comparison of recharge estimates with published figures (SUSMAQ, 2001)

Source	Annual Recharge (MCM yr^{-1})	Estimate Recharge using Remote Sensing (MCM yr^{-1})
Eastern Aquifer Basin		
CDM 1977	140	
CDM 1998	197	
Guttman 1998	125	
Ba'ba' 1996	129	330
EXACT	173	
Article 40, Oslo Agreement	172	
Guttman and Zukerman 1995	119	
North-eastern Aquifer Basin		
EXACT	145	162
Article 40, Oslo Agreement	145	
Western Aquifer Basin		
Bachmat 1995	330 and 332	
EXACT	366	
Goldschmidt	335	208
Tahal	376	
Article 40, Oslo Agreement	362	
West Bank		
Rofe and Raffety 1965	821 and 836	
Israeli Hydrological Service 1997	836	700
Guttman 1995	800	

Thus the annual recharge estimated by using remotely sensed data sets is similar to estimates published in the literature. However, the remote sensing-water balance calculations show that the Western, North-Eastern, and Eastern Aquifer Basins receive 30%, 23%, and 47% of the total calculated recharge, respectively. This indicates that the Eastern and North-Eastern basins are much wetter than the Western areas. This pattern of recharge for the three aquifer basins is inaccurate. The Western Aquifer is a flat area of most developed soil, lowest evapotranspiration rates, and highest precipitation in contrary to the Eastern Aquifer that receives the lowest recharge rates. Also, given that recharge has a similar distribution over the study area as rainfall and land cover, it means that the Western and North-Eastern aquifers should be the highest in recharge. The percentages available in the literature for the Western, North-Eastern, and Eastern are 49%, 22%, and 29%, respectively which is in disagreement to the remote sensing outcome percentages. This disagreement may be credited to the overestimation of

SEBAL ET spatial estimates and underestimation of precipitation derived from the TRMM images in the western area.

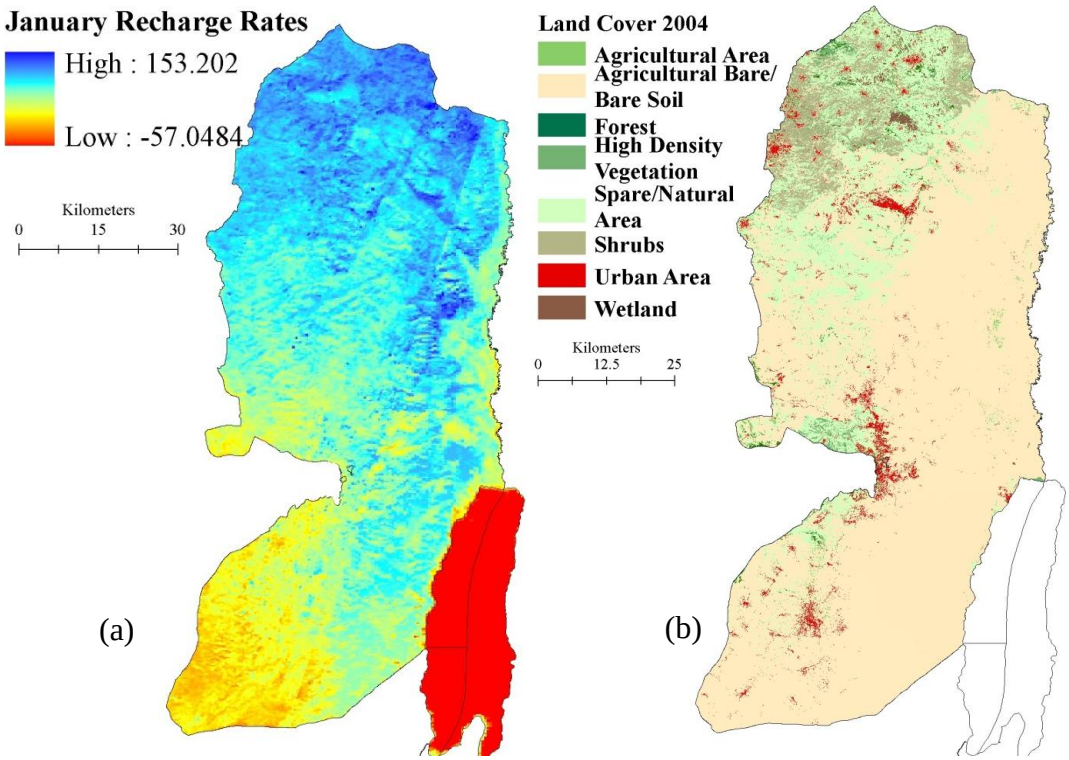

Figure 8.4: Comparison of (a) recharge estimation modelling map and (b) land cover map

In Figure 8.4, recharge is shown to be highest for vegetated land surfaces in the north and west, followed by natural vegetation and bare land in the rest of the area. This is due to the low evapotranspiration and high precipitation rates and to the fact that vegetation retards runoff, hence enhances infiltration and recharge. Areas of recharge are noticed to be present in the Jordan Valley despite its arid climate and low rainfall. This may be explained by the presence of irrigated farmland where irrigation contributes to soil moisture and recharge (Figure 8.5). Also bare land in that area is characterised by its coarse soil that sustain sufficient recharge when it receives runoff from the West Bank hills.

Figure 8.5: Sprinklers in an Israeli settlement in the Jordan Valley (Amnesty International, 2009)

Despite the fact that the winter of 2004 is relatively dry (Chapter 5) and less recharge is to be expected, it is shown that the proposed model results are broadly in line with published estimates of recharge. However, some discrepancies exist. These discrepancies are considered to be mainly due to lack of field data, the overestimation of actual evapotranspiration and underestimation of TRMM precipitation values as will be discussed further in the subsequent two sections. The approach used in this research requires knowledge about the actual field measurements of evapotranspiration, net radiation, rainfall, soil moisture, and water levels and their distribution over the aquifer basins to be used as inputs into the model and validate the results. In addition, there are large areas where there is no soil cover, which makes the soil moisture deficit an inapplicable approach for calculating actual evapotranspiration and comparing it with those derived from SEBAL. And finally, using incomplete and unreliable distributed monthly meteorological data adds an additional factor of uncertainty.

8.4 SEBAL Evapotranspiration

Errors and uncertainties in remotely sensed surface temperature and/or surface air temperature difference have the greatest and most significant impact on sensible heat flux (H) estimates and therefore on ET. It requires subjective specification of representative hot/dry and wet/cool end-member pixels within the scene to define the

model parameters and variables. The selection of pixels representing wet and dry moisture conditions and estimation of evaporative fraction significantly influenced flux predictions. It reflects the regional distribution of relative actual evapotranspiration but not the actual rates as in the case of the West Bank area. Since both MODIS and Landsat TM5 images yielded almost similar ET rates, and then the fault is more likely to be with the method used and not with the sensor. Moreover, the MODIS Level 3 product has shown that variation in surface temperature between “cold” and “hot” pixels from which H and ET are extracted does not exist. Detailed description and analysis is given in Chapter 7.

8.5 TRMM Precipitation Estimates

8.5.1 Results

Over the study area, the spatial distribution of TRMM and rain gauge data are shown to be different. Figure 8.6 below shows TRMM precipitation estimates and the interpolated rainfall of six stations using the inverse distance weighted (IDW) method to cover the study area. The IDW method is used because ground stations are few and given their separation have no spatial correlation, therefore the IDW may produce a more accurate result than the other methods such as the co-kriging, Thiessen polygon, or spline methods (Oliver, 1990). TRMM overestimates the arid area of Jericho and underestimates areas in the north, centre, and south. For instance, rainfall measurements for Jericho in January and February are 30 mm and 23 mm, while TRMM estimates precipitation as 89 mm and 36 mm, respectively. For the Jenin area, rainfall is estimated to equal 176 mm and 95 mm in January and February but TRMM gives an estimation of 158 mm and 95 mm, respectively.

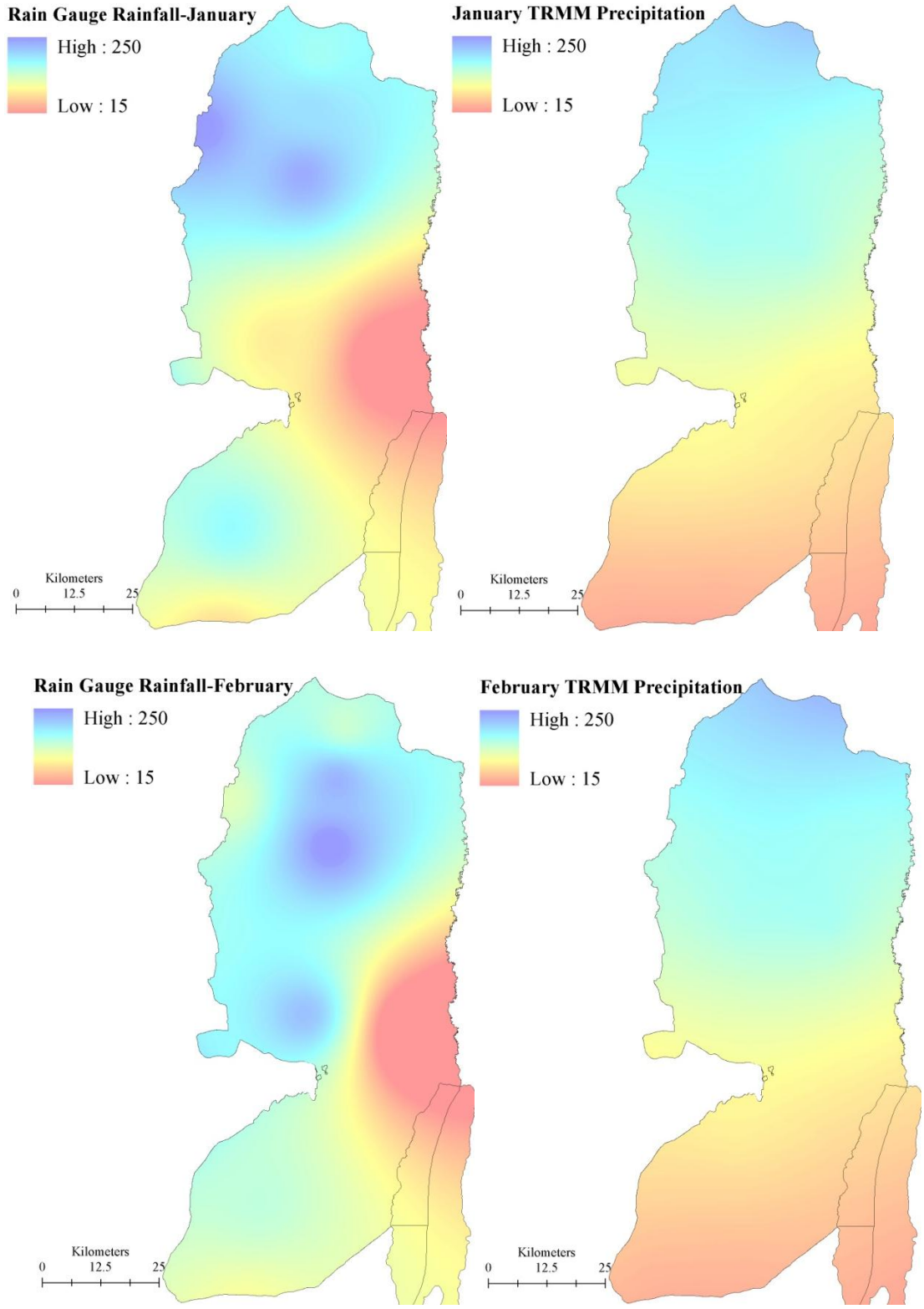

Figure 8.6: Comparison between TRMM precipitation rates and rain gauge data

Such discrepancies in precipitation estimates causes overestimation of recharge rates over the area of Jericho and underestimation in sub-humid areas in the north and west of

the West Bank. It is worth mentioning that there are several other factors that contribute to the differences between TRMM and rain gauge estimates other than TRMM retrieval errors; these are discussed in the following section. However, there are uncertainties that rise from the inadequate spatial representation of the gauge data and by the ways in which the gauge data are used to obtain gridded data. As mentioned in Chapter 2, many of the available rain station records are not complete and there are a substantial number of missing days and gaps throughout 2004 (PCBS,2004). Compared to TRMM estimates, rain gauge measurements are more or less continuous in time but with very small coverage in area, whereas TRMM may provide estimates on non-continuous basis of time but covers larger areas.

8.5.2 TRMM Validation

There have been numerous attempts to validate TRMM estimates with ground measurements in the tropics and the mid-latitudes. There have been efforts to validate TRMM over Asia as well as over the Indian sub-continent. There has been no TRMM inter-comparison carried out for specific regions over the Middle East except for a study carried out by Milewski *et al*., (2009) over the Sinai Peninsula and the Eastern Desert of Egypt. This section will validate the TRMM level 3 (version 6), which is designated as 3B43-V6 product, at a regional scale of a semi-arid to sub-humid area.

To validate the TRMM precipitation estimates over the study area, TRMM is compared with rain gauge station data. The validation of TRMM data will allow the usage of these data in the future in regions of sparse rain gauge stations. TRMM satellite data are provided from January to December (2004) where accumulated monthly precipitation time series from TRMM 3B43-V6 is used. Validation is conducted on monthly basis for six geographical regions (Figure 8.7) with different precipitation regimes are considered: the north (Jenin), northwest (Tulkarm), central (Nablus and Ramallah), south (Hebron), and east (Jericho). A sub-humid climate lies in the north and northwest regions; the central is a transition region between sub-humid and semi-arid climate; the south is characterised by a semi-arid climate; and east and south east by arid climate.

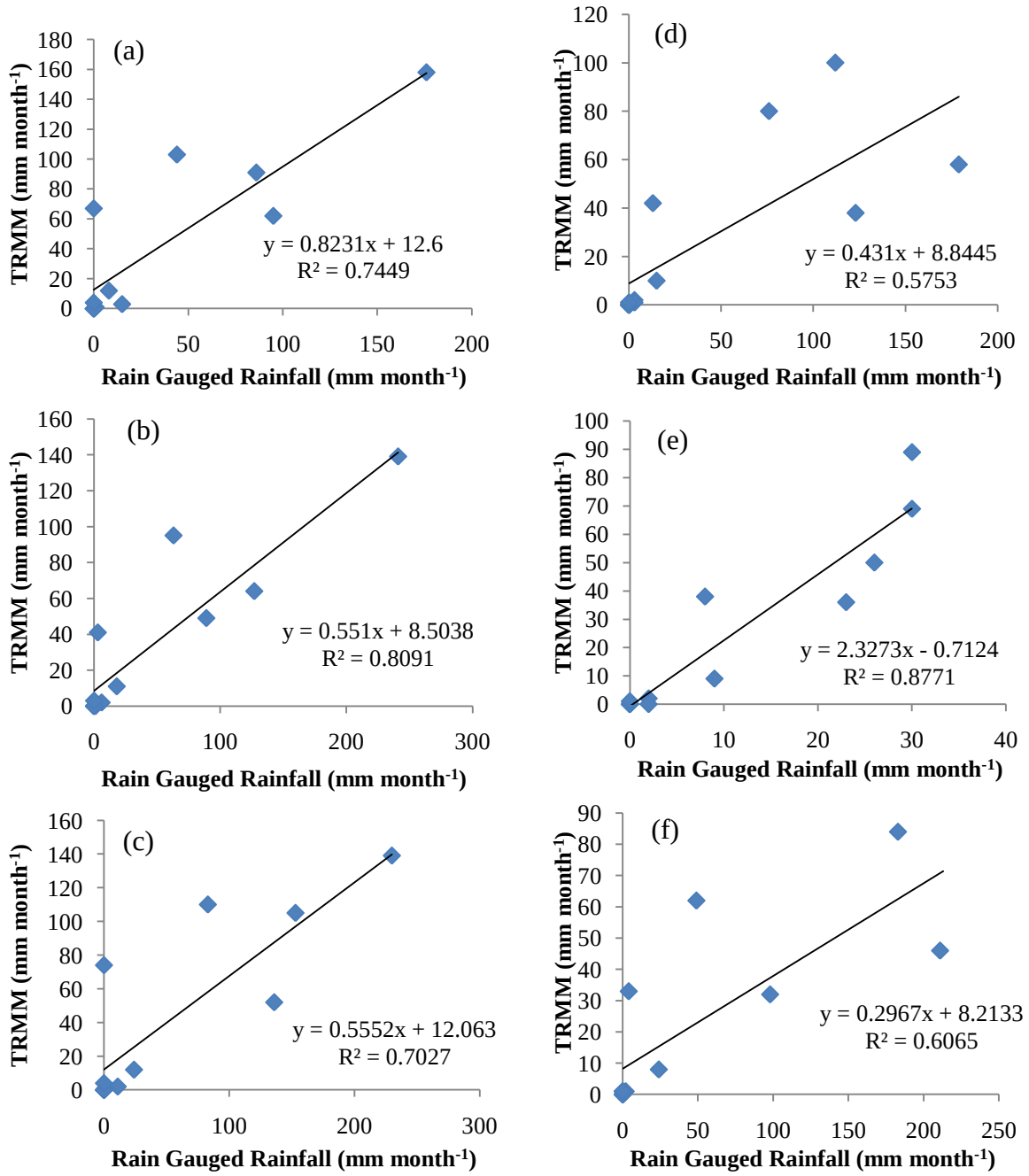

Figure 8.7: Mean annual rainfall from rain gauge stations versus precipitation estimates from TRMM for the six regions (a) Jenin, (b) Tulkarm, (c) Nablus, (d) Ramallah, (e) Jericho, and (f) Hebron. (n=12, p=0.0)

The best agreement between TRMM and rain gauge measurements is obtained in the arid area of Jericho (R^2= 0.88) and sub-humid Tulkarm (R^2= 0.81), and the poorest agreement occurs in the transition area of Ramallah (R^2= 0.58) and semi-arid Hebron

(R^2= 0.61). For Jericho, the mean precipitation is overestimated (by 2.3) while over the rest of the region, mean TRMM precipitation is underestimated. This could be attributed to the pixel size (0.25°×0.25°) and heterogeneity of Jericho area. TRMM in heterogeneous areas creates a superior overview of the synoptic rainfall events, where it produces greater estimates of precipitation than in more homogeneous regions such as the north and northwest, e.g. Tulkarm and Jenin. Thus, TRMM precipitation estimates are considered to be more reliable in regions which are considered sub-humid or humid with mean precipitation is high such as Tulkarm area (TRMM = 0.82 rain gauge estimates). Some studies show that estimates of TRMM are reliable only in the wet season and when the mean precipitation is greater than 120 mm month^{-1} (Franchito *et al*., 2009; Adeyewa and Nakamura, 2003; Nair *et al*., 2009).

The root mean square error (RMSE) (RMSE corresponds to the square root of the average of the squared differences between rainfall estimates and the observed precipitation) for each region is shown in Figure 8.8. RMSE values range between 23.5% in Jericho to 59.6% in Hebron which indicates that TRMM is most bias in the semi-arid region such as Hebron and least in arid Jericho. The average RMSE for the six regions is 40%. Where the RMSE of the TRMM estimates is within 50% of the measured rainfall, such estimates are considered to be reliable in relative terms (Adeyewa and Nakamura, 2003). As a result, TRMM is considered relatively reliable in the study area and most reliable in arid regions (e.g. Jericho). However, it is worth noting that the reliability of the analysis in these areas is affected by the paucity and certainty of rain gauge data and the number of sampling of TRMM as well.

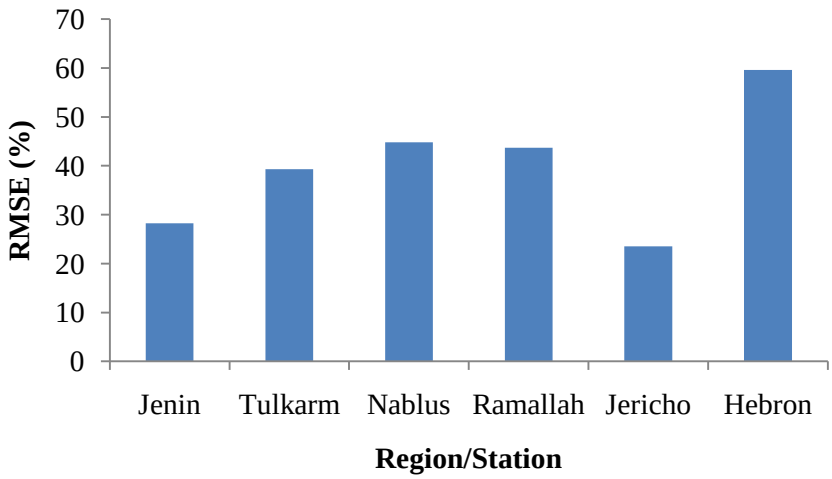

Figure 8.8: Average annual variations of RMSE (%) for the six regions in the West Bank

From the correlation relations and RMSE results, it may be seen that TRMM estimates of precipitation are found to be most inaccurate over semi-arid regions (low correlation and high RMSE). While in arid and sub-humid regions, the estimates are less biased and highly correlated (23.5%, R^2=0.88 and 28%, R^2=0.82 for Jericho and Tulkarm, respectively). In transition areas between sub-humid and arid regions, TRMM has shown to be moderately biased (45% and 44% for Nablus and Ramallah, respectively) and less correlated (R^2=0.55 for Ramallah area).

Despite the reasonable correspondence between TRMM and the six rain gauges data sets, the remote sensing methods used to estimate precipitation from spaceborne instruments are still subject to errors (Franchito *et al*., 2009). As TRMM satellite is a low orbiting satellite (350 km, later in August 2001 orbit boosted to 403 km), its rain sensors sample any region's atmosphere only at discrete time intervals. As sampling frequency is a function of latitude, more samples are collected per month at higher latitudes. Monthly estimates are generated on the basis of arithmetical mean of the observations collected; estimates are underestimated in some regions due to the sampling frequency of the TRMM satellite and the coverage area of the sensor. Moreover since TRMM measurements are acquired every three hours, short events that start and end between two consecutive acquisitions may go undetected. Also in semi-arid regions, satellite-based rainfalls have a tendency to underestimate event-based

precipitation where precipitation events tend to be short and intense (Morrissey and Janowiak, 1996). For the events examined from the six rain gauges, the average TRMM-based precipitation is underestimated for five stations compared to the average precipitation from rain gauge. Earlier findings of studies such as the ones carried in semi-arid environments by Chiu *et al*., (2006) and Chokngamwong and Chiu (2008) show a 15-30% underestimation of precipitation from TRMM compared with rain gauge data. On the other hand, TRMM in some cases may overestimate precipitation owing to its ability to identify events that are not recorded by gauge data (Milewski *et al*., 2009) or in high wind conditions where rain gauges do not properly measure rainfall (Franchito *et al*., 2009). The TRMM sensor can also overestimate rainfall due to the fact that it can sometimes misidentify a variety of Earth surfaces for precipitating clouds (Bauer *et al*., 2002) giving as a result a false indication for light rainfall less than 0.5 mm $hour^{-1}$ (Turk *et al*., 2002). Nevertheless, compared to TRMM estimates, rain gauge measurements provide local measurements, whereas the TRMM integrate observations over much higher domains covering areas of 0.25°×0.25°.

Despite all these weaknesses, TRMM still could be considered one of the most powerful tools to detect and quantify rainfall/precipitation and examine rainfall characteristics especially in regions that have low density of observations (Franchito *et al*., 2009).

8.6 Recharge Mapping Discussion

Recharge is not solely driven by rainfall, but also influenced by other factors such as land cover, soil type, geological conditions, in addition to terrain landscape and the depth to the water tables. Most of these factors, in addition to evapotranspiration derived by SEBAL method, have been taken into account in mapping the actual recharge areas as illustrated in Figure 8.9 for the month of January. High and low weights are described in Table 8.7 (p. 195).

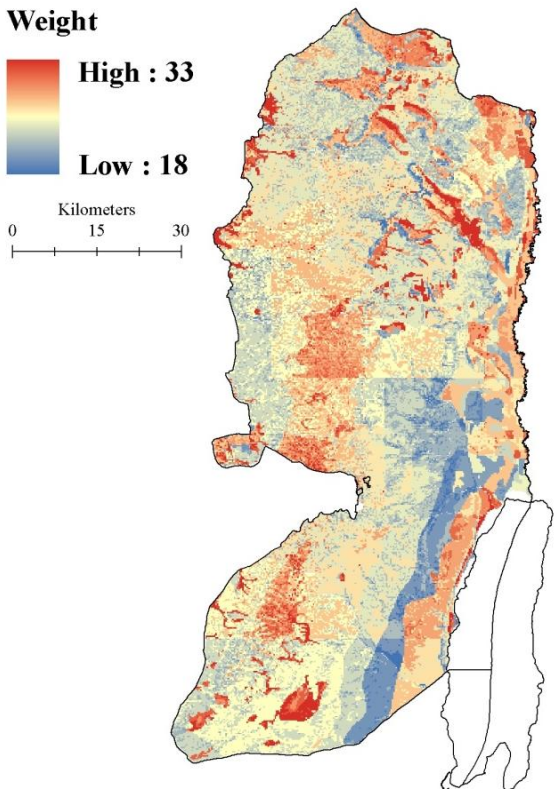

Figure 8.9: Actual areas of recharge for the month of January 2004

January is shown to be the month of highest recharge rates in the West Bank. Since February and March are at the end of the rainy season, so the soil moisture content and the evaporative fraction will significantly decrease, thus changing the amount of water to be recharged.

The areas which are categorized high for actual recharge are areas that have a rating scheme ranging between 31-36 in the final integrated layer; intermediate high ranging from 25 to 30; intermediate low from 19 to 24; and low from 12 to 18. The maximum actual rate in this study occurs in an area categorized as agricultural and the lowest occur in natural grass, shrub, and urban area that have significant role in retarding the recharge process. Human constructions, such as concrete embankments, buildings, roads, etc. create a compacted layer that seals the ground surface, hence reducing rates of recharge. Vegetation cover can be considered to be an enhancing factor. Despite the fact that with higher vegetation cover evapotranspiration rates will be higher, leading to less chances for percolation to the subsurface layers, the vegetation cover helps to confine water under the vegetation, therefore, reducing direct evaporation. In addition,

plants are able to hold soil in place rather than allowing erosion which increases with runoff. The model recharge maps for the month of January versus land cover map are shown in the Figure 8.10.

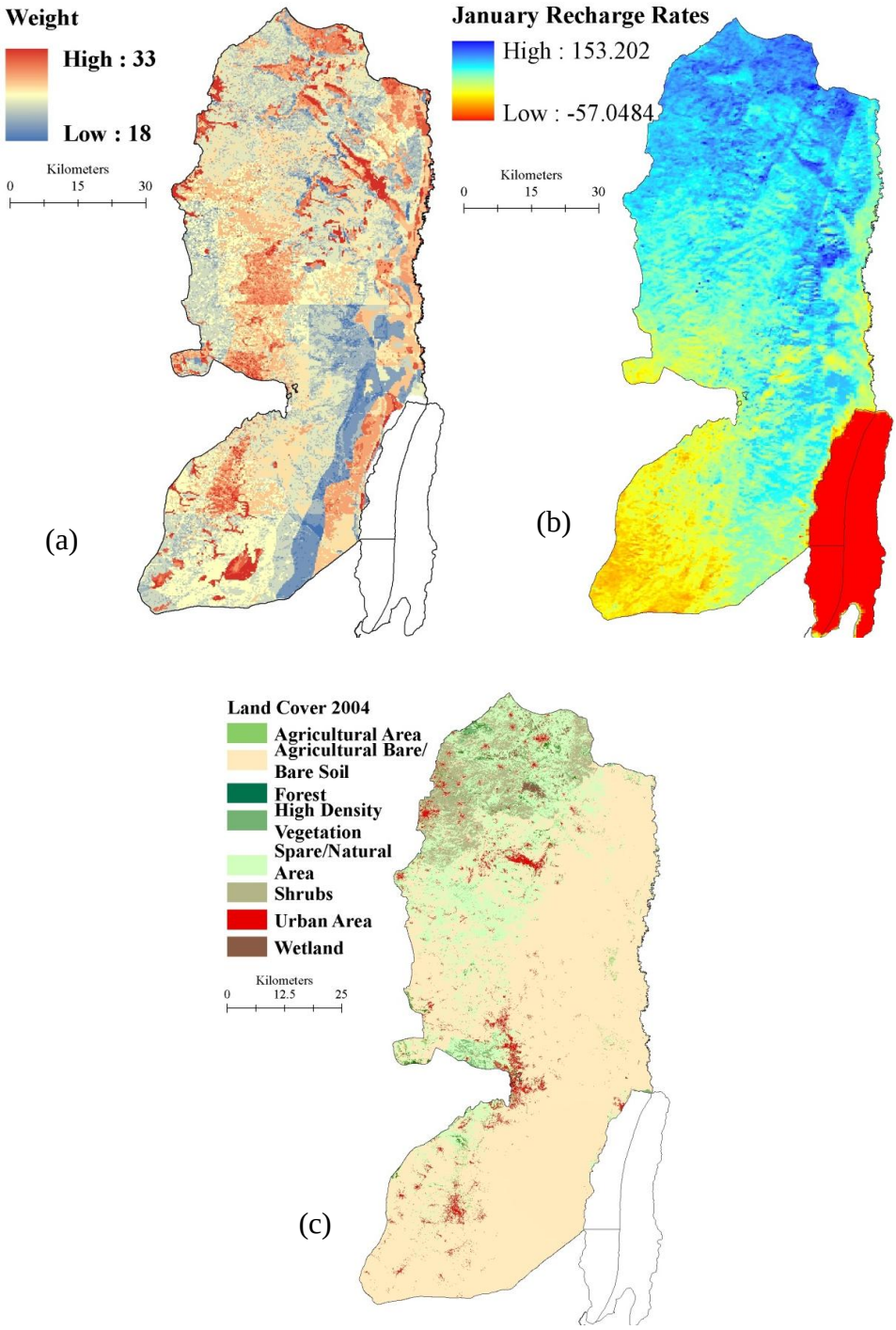

Figure 8.10: (a) Actual recharge areas derived by the mapping model (January, 2004), (b) recharge rates (January 2004), (c) Land cover (May 2004)

It is evident that recharge is not only highest but also originates from vegetated areas. This explains why the north and north-west areas are areas of high recharge, i.e., where vegetation is present. Vegetation is considered an important controlling factor in the recharge process and the interaction between vegetation and recharge is considered critical to the assessment and determination of recharge (Hughes *et al*., 2008). However, the recharge map shows areas of infiltration in the east and south of the West Bank while vegetation is absent in the land cover map. This is attributed to the fact that the land cover map is derived from SPOT-5 image captured in May which is the end of the rain-fed agriculture season. Furthermore, recharge could occur in the east and south areas in the winter season where high-intensity rainfall takes place. Also, the Jordan Valley is characterised by its high intensity of wadis where flow is recharged to the groundwater system through beds.

Studying the maps of long-term average recharge obtained from the Palestinian Water Authority, areas of recharge derived from the application of empirical formulas with the model output show a common pattern. Comparison indicates that the north west of the West Bank receives the maximum amount of recharge and the south-east receives little or no recharge even though it contains a large number of wadis (Figure 2.16). This is explained by the fact that, despite the significance of rainfall, the geology and soil formations are preventing recharge and the transformation of rainfall to runoff.

The map of recharge can be used in groundwater explorations as it gives first-hand information on the spatial distribution of groundwater recharge. Such thematic maps are valuable for assessing the vulnerability of groundwater to pollution, as high recharging zones are the most effective to transmit pollutants to groundwater. However, for regional-scale assessment, no definite approach is known and all studies are considered to be initiatives only (Shaban *et al*., 2006). At the same time, remote sensing has proven to be an effective way of studying recharge; it cannot directly estimate recharge but can help define influencing factors and produce regional maps efficiently.

Other similar models are presented in the literature. One is described by Misstear *et al*., (2009) where effective rainfall using the soil moisture budgeting technique is calculated and then a recharge coefficient that indicates the proportion of effective rainfall

contributing to recharge is applied. This coefficient is determined by the permeability and thickness of the subsoils that overlie the aquifers. This model requires a vulnerability map in addition to data related to soil.

8.6.1 Sensitivity Analysis

In the approach used, the different factors are given equal weight in terms of their influence on recharge. This does not allow the comparative effect of each parameter on recharge to be assessed. To study the influence of each, a weighing approach could be used to incorporate the interactively (Shaban *et al*., 2006). Nonetheless, this is beyond the scope of this research and a simple sensitivity analysis is carried out to present the degree to which recharge mapping is affected by the use of remote sensing-derived data only excluding other thematic field data such as geology and soil type. It aims at understanding how significantly field data could affect the proposed recharge model results.

Two models are presented where the first includes the mapping model presented in section 8.6 which combines data derived from satellite imagery and field data, and the second is a model including only parameters derived from remote sensing including precipitation, evapotranspiration, land cover, slope, and drainage density. The second model is derived by summing the weights that have been assigned to each of the five parameters as described in section 8.2. The final recharge layer has a maximum value of 30 (5 layers multiplied by the highest weight, 6) and a minimum value of 5. The final integrated layer is classed based on the weight ranges shown in Table 8.11.

Table 8.11: Sensitivity model weighing values

Value	Weight
5-9	Very low
10-13	Low
14-17	Intermediate low
18-21	Intermediate high
22-25	High
26-30	Very high

The derived recharge map from the sensitivity analysis and the mapping model (Figure 8.11) share some common areas of recharge in the north and some areas in the south. Nevertheless, the absence of information on geology and soil type leads to

overestimation of recharge areas such as the ones of the Eastern Aquifer Basin and underestimation of areas such as the ones present in the north and west. The hydrological effect of combining all parameters is required to better understand where recharge process. The type of soil leads to the understanding of evapotranspiration rate variation as well as recharge mechanism. For instance, clay soils are made up of fine particles that firmly hold onto soil water, hence high potential for water logging. They therefore have low evapotranspiration, high runoff, and low recharge. As a result, soil type has a significant influence on the hydrological processes and where available should not be excluded from recharge analysis.

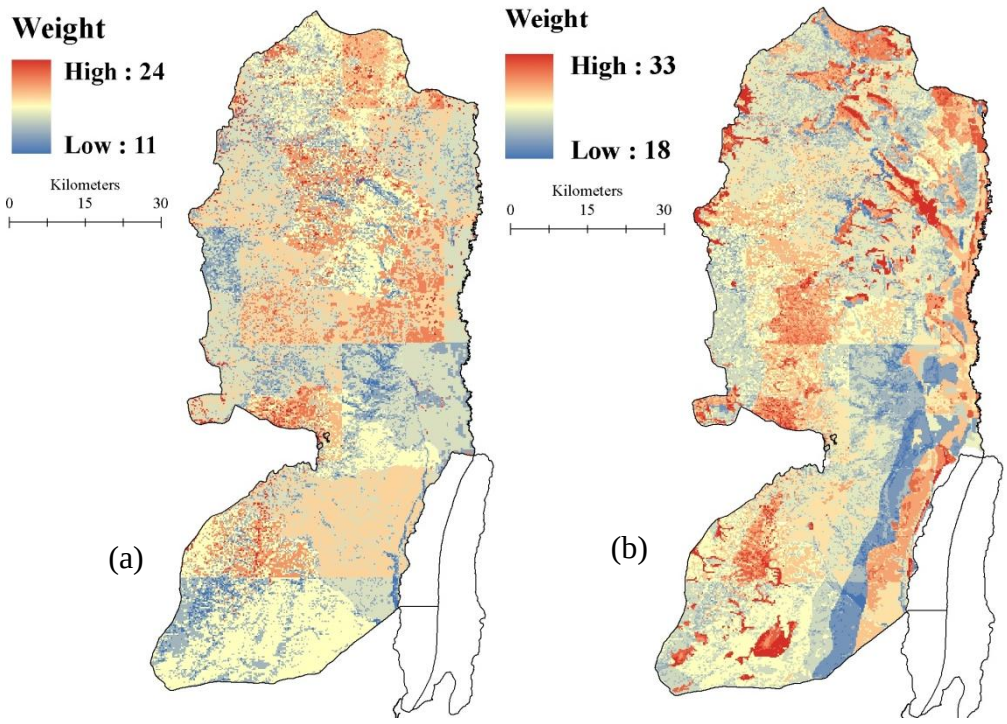

Figure 8.11: recharge map (a) remote sensing-based including precipitation, evapotranspiration, land cover, slope, and drainage density (b) integrated remote sensing and hydrogeological data as described in section 8.6

8.7 Recharge Sustainability

Depletion of water resources in the West Bank and in arid and semi-arid regions is mainly due to population growth, changes in land use, and over-abstraction of the

groundwater system. Recharge is considered an additional critical factor for the sustainable development and preservation of groundwater aquifers.

Recharge processes over the West Bank area are not fully understood as there is a lack of regional modelling techniques and development. Recharge is susceptible to surface conditions and from the recharge map produced, it is evident that recharge is highest where vegetation is present and slope is low. Given this understanding of recharge processes in semi-arid areas, it is necessary to use it to set land management plans to reserve areas of potential recharge and reduce causes hampering its development.

Over the past fifteen years the West Bank has experienced rapid changes in land use and land cover since the creation of the Palestinian Authority and the political de facto changes imposed on the ground. Land cover changes (as described in Chapter 6, Table 6.2) show that high-density vegetation areas have decreased by 75% from 1994 to 2004, permanent/winter agriculture decreased by 76%, forests by 28%, and urban fabric increased by 250% in the same period. Moreover, population has increased by 58% from 1,720,790 in 1994 to 2,716,367 in 2004 (PCBS, 2004) which indicates an increase in water demand reaching beyond the combined Israeli and Palestinian abstractions (SUSMAQ, 2001). Land cover/land use changes, rising population, and the dependency on agriculture for living increases the demand for water and could lead to an unbalanced distribution among users (between Palestinians and Israelis and among Palestinians themselves) and increase conflict in the region. Furthermore, the absence of land management policies to preserve the aquifer basins calls for urgent plans to conserve and develop recharge areas. One of such means of protection is preventing any further land cover/land use changes that would harm the aquifers' replenishment. In order to demonstrate the impact of land cover change on groundwater and natural recharge, an assessment of land cover change impacts on water recharge is carried out. The assessment includes mapping the West Bank area using the two land cover classifications from 1994 and 2004, but with the same fixed parameters of evapotranspiration, precipitation, drainage, slope, soil, and geology (Figure 8.12).

The land cover maps for 1994 and 2004 are given in Chapter 6, Figure 6.3 and a detailed breakdown of the different land cover types are listed in Table 6.2. Whereas

much of the study area is under natural vegetation, shrubs, and bare soil, about 20% of the region is under agricultural land use.

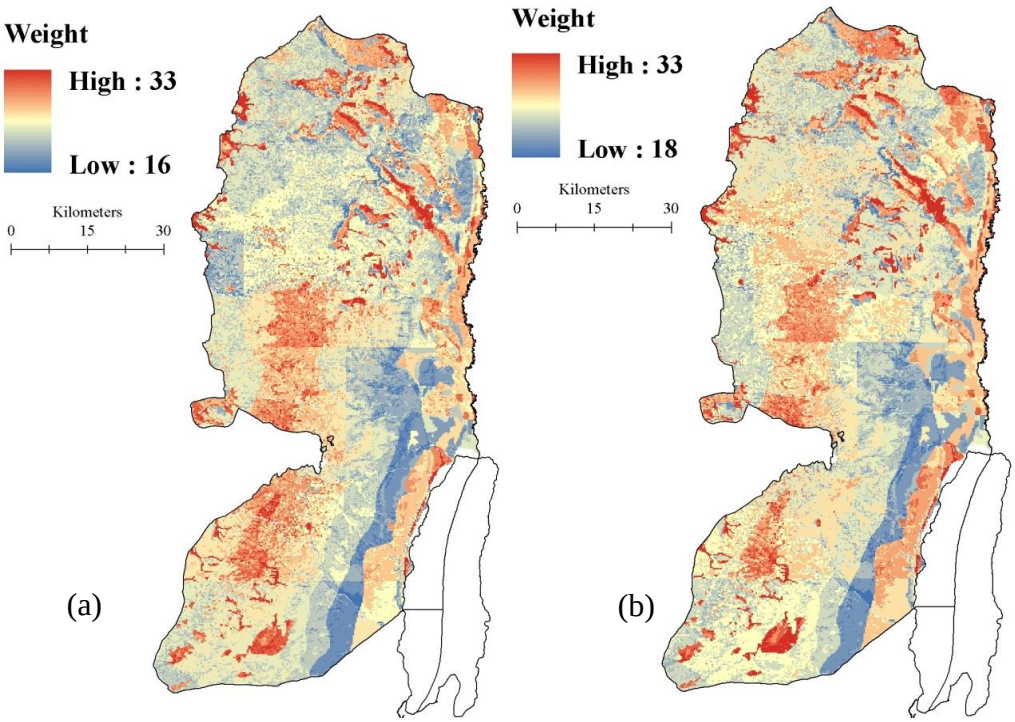

Figure 8.12: Recharge map using land cover classification of year (a) 1994, (b) 2004

The total areas of very high recharge areas are absent in both maps while the high and intermediate high are reduced from 40.25 km^2 and 2462.25 km^2 in year 1994 to 15.5 km^2 and 1994 km^2 in 2004, respectively (Figure 8.13).

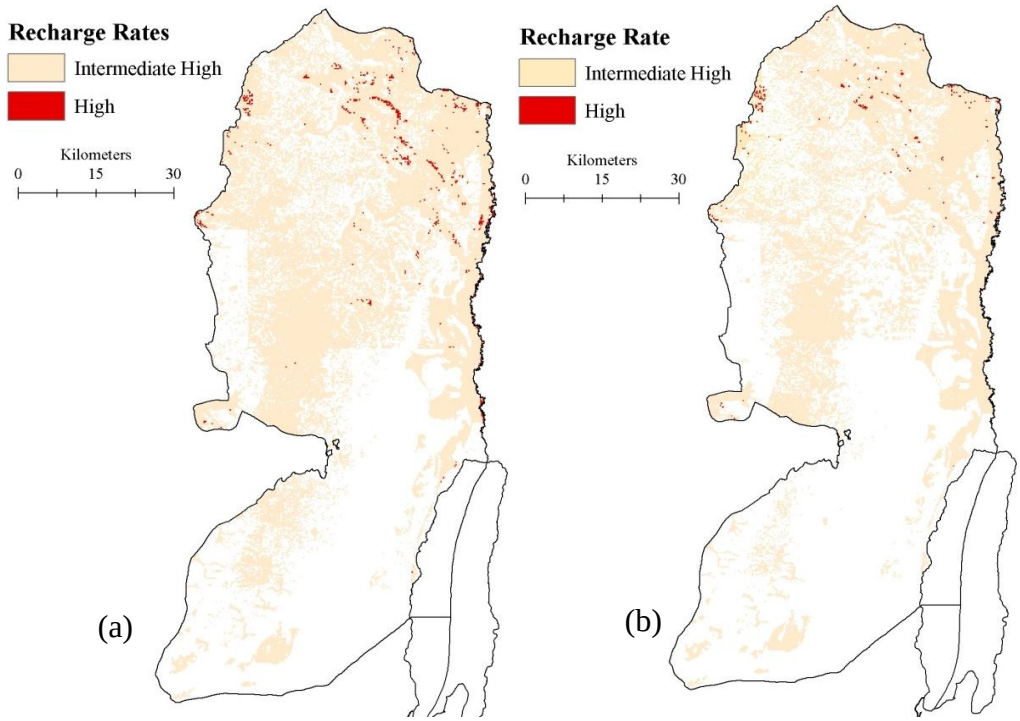

Figure 8.13: Recharge areas in year (a) 1994 and (b) 2004

This illustrates the extent of recharge being influenced by land cover change causing high evapotranspiration triggered by exposure of the soil. To further demonstrate this impact, Ramallah governorate is taken as example. Urban area has increased from 3 km^2 to 15.5 km^2 (417%) and agricultural area decreased from 22.2 km^2 to 4.5 km^2 (-450%) from 1994 to 2004. Corresponding to these changes, recharge has decreased from 1.31 to 0.38 for high recharge and from 433 to 288 for intermediate high (Table 8.12 and Figure 8.14).

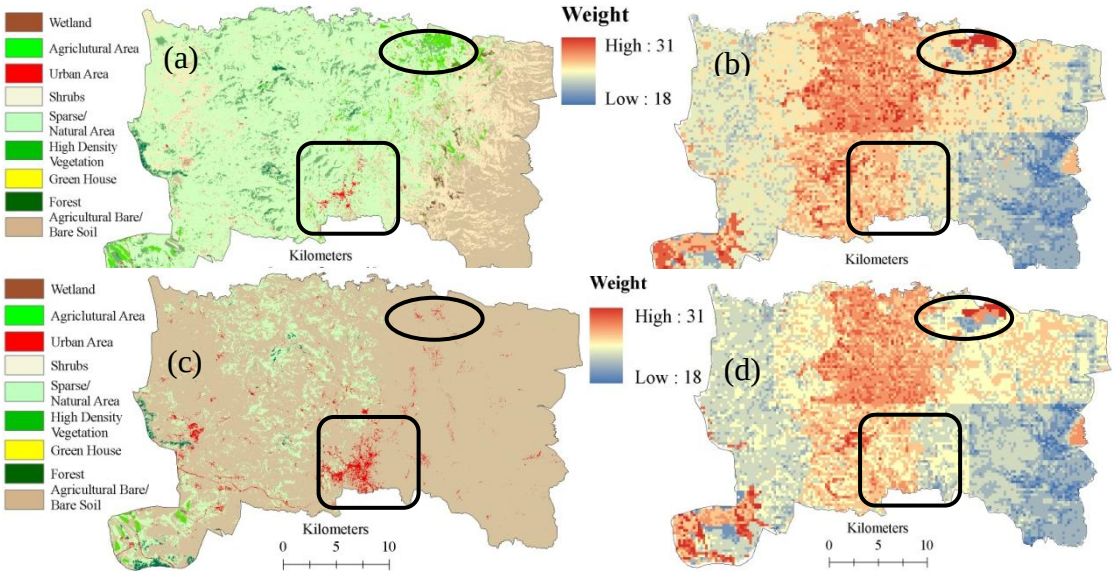

Figure 8.14: Land cover change impact on recharge in Ramallah governorate

If the pattern of land cover change persists, then a considerable threat to water resources in the study area is possible. Hence, integrated land use practices that can support the preservation of water resources should be considered. Such strategies include connecting recharge and land via hydrological modelling. Changes on governorate scale are summarised in Table 8.12:

Table 8.12: Recharge areas changes on governorate scale between 1994 and 2004. Rates are described in Tables 8.8 and 8.11.

Governorate	High (km^2)		Intermediate High (km^2)	
	1994	2004	1994	2004
Tulkarm	3.75	3.75	167.19	82.19
Tubas	14.25	4.69	299.81	292.06
Ramallah	1.31	0.38	432.88	288.00
Qalqiliya and Salfit	1.75	0.69	205.69	155.75
Nablus	1.31	0.50	339.31	276.44
Jerusalem	0.00	0.06	98.38	82.06
Jericho	8.19	1.06	299.56	281.25
Jenin	9.50	4.38	364.75	396.19
Hebron	0.00	0.00	149.38	108.06
Bethlehem	0.19	0.00	105.31	32.00

The greatest reduction in recharge is observed in Tulkarm, Ramallah, and Bethlehem by 51%, 33%, and 70%, respectively. Whilst recharge in Tubas, Jerusalem, and Jericho

remained relatively unchanged; Qalqiliya and Salfit, Nablus, and Hebron experience small changes. Jenin is the only governorate that is experiencing an increase in intermediate high recharge rates. This is attributed to the fact that an increase in vegetation has occurred in 2004 as demonstrated by the land cover classification results presented in Chapter 6 and illustrated in Figure 8.15.

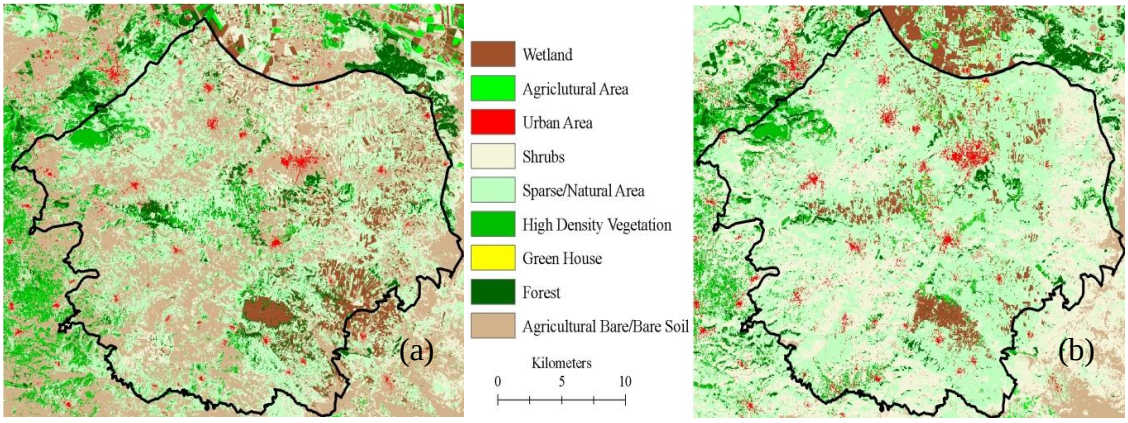

Figure 8.15: Jenin land cover classification (a) 1994, (b) 2004

The numbers presented in Table 8.12 and maps presented in Figures 8.15 regarding recharge change in the Jenin area represent the actual changes on the ground at the date of image capture. The land cover classification for year 1994 is derived from SPOT-2 HRV image captured in January while the 2004 classification is derived from SPOT-5 HRG captured in May. The different dates of capture, sensors used, and imagery spatial resolution (as explained in Chapter 6) explain some of the difference in land cover changes. However, there are major changes in some areas where urban expansion and decrease in agricultural practices have taken place. Such changes are also noticed in other parts of the West Bank area which are causing also changes in areas of groundwater recharge. Consequently, in order to preserve recharge at least at current rates, assuming no changes in rainfall and evapotranspiration rates, an increase of impermeable surfaces and decrease of wetlands and agricultural areas should be avoided.

It is worth noting that recharge calculations presented in this study indicate that the average recharge equals 124 mm year^{-1} while the average annual rainfall of the same year is 480 mm year^{-1}. This suggests an average of 356 mm year^{-1} is lost as

evapotranspiration which is considered the predominant mode of water loss. Hence, decreasing evapotranspiration losses by setting land management strategies is a critical and vital measure for the sustainability and long-term restoration and conservation of limited water resources available.

8.8 Refinements of Precipitation-Recharge Model Estimates

The model presented in this study has overlooked many complexities of recharge in the area such as: the complex geology and the existing of epi-karst zones which may locally result in high rates of recharge, runoff generation during the heavy rainstorms where zones of intense recharge from wadi floors are created, agricultural terracing that would inhibit runoff in steep slopes, recharge from other sources such as leaking pipes, drains, irrigation returns, and wastewater outfalls, the porosity of the three aquifers, and soil moisture storage. Inability to account for such complexities could lead to inaccuracies in the estimation of recharge. For example, in high rainfall intensity, natural recharge may be higher than the estimated as the re-infiltration of water in wadi and epi-karst dominated zones are ignored. A refined approach should be developed where all elements of recharge, direct infiltration of rainfall, infiltration from wadi floors, and leakage and irrigation returns are considered.

The understanding of recharge processes occurring in the West Bank will remain incomplete until the following questions are answered (Hughes and Mansour, 2005):

1. How can the fractures associated with bare rock be determined and what are their implications for recharge?
2. What is the nature of soil pockets and how deep are they?
3. What proportion of runoff reaches wadis? And what percentage of ponding is evaporated?

Nonetheless, the model described in this chapter advances our knowledge of the actual recharge areas and its process in the West Bank. However, it needs further improvements to arrive to a full understanding of recharge to the main aquifers and gain a comprehensive and detailed understanding of its processes. Such refinements include:

i. Satellite sensor data can provide spatial distribution of evapotranspiration which may improve upon the poor network of pan measurements or data derived from meteorological records. Therefore it is essential to use higher spatial resolution satellite imagery for evapotranspiration estimations. The remote sensing energy water and energy flux modelling is determined by a sensor's ability to accurately determine the related terms from the observed reflected and emitted radiances. In order to avoid the dominance of mixed pixels in data with low spatial resolution such as MODIS, higher resolution should be employed instead. Spatial resolution is an important function of ET estimation as different land cover types are defined which have distinctly different heat flux properties, surface roughness, heat capacity, and spectral reflectance (French *et al*., 2005). In this case, MODIS images may not able to make these distinctions over bands with the 1 km resolution. Sufficient spectral resolution is also a requirement to accurately estimate the land surface temperature images, NDVI, and albedo. Moreover, bands with less sensitivity to atmospheric water vapour content are required which is the case only with band 2 in the MODIS sensor (French *et al*., 2005, Kimura *et al*., 2007).

   Despite the fact that the SEBAL model overestimates evapotranspiration rates over the whole year, period; it may still be applicable in the winter months. SEBAL results are equal to potential evapotranspiration rather than actual as shown in Chapter 7 (Table 7.3). Given that actual evapotranspiration is equal to potential in the winter season, the distributed SEBAL evapotranspiration rates could be used to estimate recharge in this period.

ii. Using microwave remote sensing data sets to measure and accommodate soil moisture content to better estimate recharge from the water budget method.

iii. Utilize and combine different satellite and ground data within an integrated framework in order to improve the estimation of land surface hydrological fluxes and their spatial and temporal variability across different scales. Remote sensing data are required for large-scale coverage and field data is essential for the development of algorithms and equations calibrations. Therefore, using remote sensing data sets in addition to ground measurements is required to

improve the estimation of the hydrological parameters especially in regions with poor in-situ data networks such as the West Bank. Field data are also required for data calibration and validation

iv. Run the water balance method with daily rainfalls and ET data. MODIS Level 3 data (combining every 8 days in one image) have shown that surface temperature differences are negligible leading to the assumption that the sensible heat flux (heat used to heat the soil) is zero. This assumption leads to the notion that the evaporative fraction is fixed to a value of 1 indicating a constant supply of water to the soil. As a result, daily data should be considered for the wet season for a refined recharge estimate based on single images data.

v. Obtain time series and extend records of rainfall, ET, net radiation, and heat fluxes. In the absence of such long-term data records from meteorological stations, alternative data can be used such as global data sources even they are at low spatial resolution.

vi. Increase the number of studies on runoff and wadi flows and understand how they are related to rainfall intensities.

vii. Undertake infiltration and recharge experiments

viii. Determine the impact of soil pockets on recharge in rocky areas of the West Bank

The integration of satellite and field measurements is important for a consistent estimation of recharge and land surface water budget variables at a regional scale across the aquifer basins. Precipitation and evapotranspiration data from remote sensing data sets is corrected through using ground observations even if the correction factor is estimated from different years than when it is applied. Remote sensing only approaches are considered weak but with a few available measurements, results could be more accurate (Pan *et al*., 2008).

8.9 Conclusion

Accurate estimation of groundwater recharge is vital for sustainable water resource management and for determining the appropriate levels of groundwater withdrawal, especially in arid and semi-arid regions. It needs to be estimated at a variety of spatial and temporal scales. Delineating areas of recharge, which are considered vulnerable

pathways along which pollutants could move from surface to subsurface, further helps sustain the aquifers by protecting these areas from sources of pollution and preventing the conversion of land into low infiltration uses.

The objective of this chapter was firstly to use the derived water balance components to estimate recharge rates in the winter season of year 2004 based solely on remote sensing data sets. Secondly, to map areas of recharge and understand how land management practices could affect recharge and set some basic recommendations for sustaining it. Thirdly, to apply a sensitivity analysis to illustrate the degree to which the recharge map is affected by using remote sensing-based data only including precipitation, evapotranspiration, land cover, drainage, and slope. The first aim is addressed by applying the water budget method where evapotranspiration and assumed runoff are subtracted from precipitation. This is carried out by using the spatial analysis tool in ArcGIS 9.3. The second aim is addressed by rating elements of the seven parameters into a rating scheme to determine the areas of high potential of recharge. Then in order to assess the comparative impact of land cover changes on recharge, a sensitivity analysis is carried out where the land cover classification of year 1994 is coupled with the same model inputs to map the 2004 recharge areas. The final aim is accomplished through a second sensitivity analysis by mapping the recharge areas with the use of remote sensing datasets only. The results show that soil type is a critical component in mapping recharge areas as it determines where water is infiltrated.

The methodology used in this study for estimating recharge rates has applied geospatial techniques that are used in conjunction with groundwater modelling to define the space-time distribution of groundwater recharge. Data derived from satellite images (land cover, evapotranspiration, precipitation, and DEM derivation) are combined with hydrogeological data in a GIS to identify and map the key surface indicators of recharge areas. Monthly evapotranspiration derived from SEBAL algorithm using MODIS satellite images and precipitations estimates from TRMM sensors during the twelve months of year 2004 have been employed to quantify actual recharge. Runoff has been given assumed values of 1.0 mm month^{-1} in January and 0.5 mm month^{-1} in February. Quantitative analysis reveals an average of annual recharge of 700 MCM yr^{-1} in the year 2004. This estimate is close to published figures from previous estimates. The Western,

North-Eastern, and Eastern Aquifer Basins receive 30%, 23%, and 47% of the total calculated recharge, respectively while percentages available in the literature provide 49%, 22%, and 29%, respectively. This indicates that the Eastern and North-Eastern basins are much wetter than the Western area which is an incorrect outcome. In spite of the good agreement in the total recharge volume, discrepancies in the percentages of each aquifer contribution are due overestimation of actual evapotranspiration and underestimation of TRMM precipitation values.

The recharge map indicates that the most effective groundwater recharge zones are located in the north and west of the area that is characterised by its thick and well developed soil deposits, heavy vegetation, and sub-humid climate with the potential of significant recharge occurring during the wet season. Some areas in the east include concentration of drainage and stream flows which increase recharge of the groundwater system. As water infiltrates in these areas into the aquifer, there is a great need to monitor chemicals and contaminants at the surface and sub-surface. Contaminated recharge will contaminate the aquifer unless barriers or measurements slowing and stopping the downward movement of these materials are taken. Therefore, land use activities and aquifer sensitivity should be continuously monitored and investigated. The least effective areas are in the south and south-west regions that are more arid with much less recharge, mainly due to their isolated thin soil deposits.

It is possible to apply further refinements to the proposed model of recharge estimation. This includes carrying out the proposed methodology over long periods using shorter rainfall intensities such as daily or even hourly, higher resolution datasets, modify SEBAL coefficients with field measurements, and calibrate TRMM values based on long term average rainfalls. These factors could significantly change the estimated proportion of recharge to rainfall events and better understand its process. But for more accurate estimates additional information on crops, soils, and hydrological conditions are required (Kite and Droogers, 2000).

Regional distributed models in the West Bank require a level of spatial data that only remote sensing can provide. The medium resolution MODIS sensor is a good source for regional scale energy and water fluxes such as evapotranspiration. TRMM is also

another good source for rainfall and precipitation distribution. However, despite its promise, distributed remote sensing modelling of hydrological processes currently has its limitations. The major problems are over-parameterization and uncertainty, in the sense that most models have not been validated in all their detail, owing in part to a mismatch between model complexity and the level of data which is available to test and calibrate the models.

Chapter Nine

Conclusions and Recommendations

9.1 Introduction

Recharge estimation is a very important element in water resources studies in Palestine. Of particular interest are modelling studies of the sustainable yields of the Palestinian Aquifers. The reliability of groundwater modelling is constrained by the quality of input data. The point measurements available are poorly distributed and inconsistent. They are considered expensive in the West Bank and unattainable in some cases due to the political circumstances and the lack of equipments. Hence, remote sensing in conjunction with available meteorological data are considered in this study as an option to contribute into quantifying input data for groundwater modelling and thereby improve recharge models reliability. Remote sensing applications in surface hydrology such as estimation of evapotranspiration, rainfall, DEM derivation, and land cover are increasingly used and might be in some cases the only source for providing spatial distributions where point measurements are limited. There is yet no remote sensing-based method that could evaluate and estimate recharge directly in a quantitative way. However, this study shows that remote sensing and GIS methods could contribute to recharge assessment in an indirect way through a GIS-based solution of the water balance equation with inputs derived by remote sensing techniques. The hydrological parameters provided by satellite imagery for recharge assessment include:

- Land cover and land cover change using multispectral SPOT images (Chapter 6)
- Precipitation using thermal radar, the Tropical Rainfall Measuring Mission (TRMM) (Chapter 8)
- Estimation of evapotranspiration using thermal and multispectral Moderate Resolution Imaging Spectroradiometer (MODIS) images (Chapters 4, 5, and 7)
- Digital elevation model derivation from the Advanced Spaceborne Thermal Emission and Reflection Radiometer (ASTER) with 30 m spatial element (Chapter 7)

This chapter integrates the different aspects of the research presented in the thesis. Methodology and results of the recharge model are summarised in section 9.2. Evaluation of research aims is discussed in section 9.3. Limitations of the spatial modelling approach applied are presented in section 9.4. Section 9.5 sets some recommendations for future research and the research conclusions are presented in section 9.6.

9.2 Summary of Methodology and Results

A simplified model of precipitation-recharge into the subsurface media has been employed in this research. Technically, it assumes that some of the precipitation either evaporates or runs on the ground surface in the form of runoff and the remainder percolates through the soil. A summary of the procedural steps of quantifying regional recharge is as follows:

- ***Step 1:*** Monthly evapotranspiration is quantified from MODIS Terra reflectance (MOD09Q1) and land surface temperature and emissivity data (MOD11A2 with temporal granularity of 8 days data by employing the Surface Energy Balance Algorithm for Land (SEBAL) (Chapter 1, objective 1). SEBAL estimates evapotranspiration as the residual of energy balance applied to the land surface for each pixel of the satellite image. Derived evapotranspiration rates are validated using local-scale field measurements of pan evaporation and empirical formulas e.g. Penman-Monteith and Thornthwaite methods. Results from MODIS data have been also validated by those derived from Landsat TM5 of the same date (26th August 2003) to understand the extent of the MODIS sensor bias for its medium spatial resolution (1 km). Validation has also been carried out by comparing the evapotranspiration map with land cover map derived from SPOT-5 HRG image. Validation consists of studying the relation between ET and the surface biophysical variables such as the NDVI.

Results indicate that SEBAL evapotranspiration rates are equal to potential derived from the other methods. In the summer months as actual evapotranspiration decreases to very low rates because of the dry top soil and absence of rainfall, SEBAL results values equal or higher than the potential estimates. While in winter months, SEBAL actual

evapotranspiration has a positive correlation with the other three methods as potential rates in the wet season are equal to the potential.

In general, SEBAL overestimates evapotranspiration rates in the semi-arid, sub-humid, and dry sub-humid areas of the West Bank. However, sub-humid areas have the highest correlation between SEBAL and the other methods in the wet season and the semi-arid areas have the lowest. The overestimation may be contributed to three main factors: (1) MODIS sensor, (2) MODIS product, and (3) SEBAL algorithm. First, in terms of MODIS sensor, the energy flux terms are determined by the MODIS sensor ability to accurately determine them from the observed reflected and emitted radiances. In this study, it has been shown that the spatially distributed surface temperature, NDVI, and evapotranspiration rates from MODIS sensor are higher than those determined by Landsat TM5. This could be due to the lower spatial and spectral resolution of MODIS sensor and the dominance of mixed pixels in its images. Second, in terms of MODIS product, surface temperatures are negligible which indicates low thermal emissions, zero sensible heat fluxes, and an evaporative fraction of 1.0. The product assumes a constant water supply and moist surface throughout the year. This is in contrast to the nature of the West Bank surface where evaporative fraction decreases as the rainy season ends and the atmospheric demand for water increases by the start of the summer season. Finally, in terms of SEBAL algorithm, the model consists of several assumptions (discussed in Chapter 4) that arise uncertainties in the evapotranspiration rates. Also, SEBAL determines evapotranspiration from surface reflectance, vegetation indices, and surface temperature with no data on the soil moisture. One of the major uncertainties is the determination of sensible heat flux (H). Two pixels in the satellite image have to be selected: one that is completely wet for which H~0 and the temperature difference between surface and air temperatures is zero, and the other that is completely dry where H=Rn (net radiation). The selection of these two ends determines the coefficients of a and b that are the internal calibration of SEBAL and is dependent on the user judgement and ability to identify these two points.

Data requirements for SEBAL model is wind speed, humidity, solar radiation, and air temperature. No data on land cover, soil type, or hydrological conditions are required. However, SEBAL computations can only be executed for cloudless days and areas of

abundant agricultural crops. The absence of a wet pixel, resembling a well watered area, unable the estimation of the sensible heat flux and therefore, evapotranspiration. Recalling that sensible heat flux is estimated from wind speed and surface temperature using "internal calibration" (a and b coefficients) of the near surface to air temperature difference. The definition of the coefficients requires the selection of two extreme pixels within the scene where temperature difference can be calculated using a known sensible heat flux at these two pixels.

- ***Step 2:*** Estimation of monthly precipitation from the Tropical Rainfall Measuring Mission (TRMM). Level 3 product (3B43) version-6 with a spatial resolution of 0.25° x 0.25° and 3-hourly footprint is used (Chapter 1, objective 2). The product merges data from TRMM Microwave Imager (TMI), Special Sensor Microwave/Imager (SSM/I), pentad-average adjusted merged-infrared (IR), and monthly accumulated Climate Assessment and Monitoring System (CAMS) or Global Precipitation Climatology Centre (GPCC) rain gauge analysis estimates.

Validation is conducted on monthly basis by comparing TRMM precipitation estimates with six rain gauge stations data with different geographic regions and different rainfall regimes. The highest correlation between TRMM and rain gauge measurements are obtained in the arid area of Jericho (R^2= 0.88) and sub-humid Tulkarm (R^2= 0.81), and the poorest agreement occurs in the dry sub-humid area of Ramallah (R^2= 0.58) and semi-arid Hebron (R^2= 0.61). However, over Jericho area, the mean precipitation is overestimated (by 2.3) while over the rest of the region, mean TRMM precipitation is underestimated. This could be attributed to the pixel size (0.25°×0.25°) and heterogeneity of the area in specific Jericho. TRMM in heterogeneous areas creates a superior overview of the synoptic rainfall events, where it produces more reliable estimates of precipitation in more homogeneous regions such as the north and northwest, e.g. Tulkarm and Jenin. Thus, TRMM precipitation estimates are considered to be more reliable in regions which are considered sub-humid or humid with mean precipitation is high such as Tulkarm area (TRMM = 0.82 rain gauge estimates). From the correlation relations and Relative Mean Square Error (RMSE) results, it may be seen that TRMM estimates of precipitation are found to be most inaccurate over semi-arid regions (low correlation and high RMSE). While in arid and sub-humid regions, the

estimates are less bias and highly correlated (RMSE= 23.5%, R^2=0.88 and RMSE= 28%, R^2=0.82 for Jericho and Tulkarm, respectively). In dry sub-humid areas or transition areas between sub-humid and arid regions, TRMM has shown to be moderately bias (RMSE= 45% and 44% for Nablus and Ramallah, respectively) and less correlated (R^2=0.55 for Ramallah area).

Discrepancies may be due to low spatial resolution of TRMM and also to the inadequate spatial representation of the gauge data, the sampling frequency of the TRMM, and the coverage area of the sensor as explained in Chapter 8, section 8.5.2. Since TRMM measurements are acquired every three hours, short events that start and end in between two consecutive acquisitions may go undetected. On the other hand, TRMM in some cases may overestimate precipitation owing to its ability to identify events that are not recorded by gauge data such as in high wind conditions where rain gauges do not properly measure rainfall.

- ***Step 3:*** Recharge is estimated by applying the water balance method (Chapter 1, objective 4). Recharge estimations in show that significant recharge occurs mainly in the two months of December and January with some recharge in November and none in February or March. The average annual recharge rate is estimated to equal 700 MCM yr^{-1} where empirical models based on long term rainfall measurements result values between 800 MCM yr^{-1} and 836 MCM yr^{-1}. The lower estimated value may be attributed to the overestimation of evapotranspiration over the calculation period and the underestimation of precipitation especially in the high recharge areas north and west of the West Bank. The annual recharge estimated by remote sensing data sets is shown to be similar to numbers published in literature. However, the remote sensing-water balance calculations show that the Western, North-Eastern, and Eastern Aquifer Basins receive 30%, 23%, and 47% of the total calculated recharge, respectively. This indicates that the Eastern and North-Eastern basins are much wetter than the Western areas which are inaccurate. The percentages available in the literature for the Western, North-Eastern, and Eastern are 49%, 22%, and 29%, respectively. Since rainfall is greater in the Western aquifer and the top soil is more developed due to agricultural activities, it has the highest recharge. This disagreement is credited to the overestimation of SEBAL

ET spatial estimates and underestimation of precipitation derived from the TRMM images in the western area.

As results from chapters 7 and 8 indicate, SEBAL model is shown to be applicable in agricultural areas where constant supply of water is provided (Table 9.1). In arid and semi-arid areas, such as Jericho and Hebron, low regressions are observed between SEBAL and field observations. This is due to the fact that the model disregards the moisture content in the soil and evapotranspiration estimates are derived based on radiance and reflectance from the satellite imagery. However, precipitation estimates derived from TRMM are overestimated in arid areas (by 2.3) while are underestimated in semi-arid (Hebron) and almost equal in sub-humid areas (Jenin). Overestimation is may be due to the coarse pixel size and the heterogeneity of the area creating a superior overview of rainfall events.

Table 9.1: Summary results of SEBAL model and TRMM estimates applied in arid Jericho, semi-arid Hebron, and sub-Humid Jenin.

		Arid Jericho	Semi-arid Hebron	Sub-Humid Jenin
SEBAL in winter months	R^2	0.058	0.028	0.148
	Regression with Field Measurement	y=-0.334x	y=0.145x	y=0.467x
TRMM	R^2	0.877	0.607	0.745
	Regression with Field Measurement	y=2.327x	y=0.297x	y=0.823x

9.3 Evaluation of Research Aims

This study has demonstrated successfully that integrated remote sensing and GIS can provide an appropriate platform for data analysis over regional areas. The following two main conclusions are drawn from this research study:

1. **In the present study an integrated remote sensing and GIS based methodology has been developed and demonstrated for estimating surface rainfall-recharge to an aquifer.**

With the application of remote sensing techniques and datasets, regional distribution of evapotranspiration and precipitation is obtained and used as inputs into a surface recharge model. The model results have been validated with numbers introduced in literature based on previous studies and estimates. The outcomes show good agreement as illustrated in Table 8.10 despite the uncertainties and discrepancies of the remote sensing methods used. Recharge results should be used as an indicator to groundwater sustainability. The estimated volume of water recharged may be considered as the upper limit for any assumed future water use scenario assuming that it is equivalent to the annual renewable recharge from rain which falls on the aquifers outcrops of the West Bank area.

2. **The present study has demonstrated that the main recharge sites are situated in the north and north-west of the West Bank, in addition to some wadi areas in the eastern side.**

The recharge map produced has clearly demonstrated the relationship between vegetation and recharge rates. The higher vegetation cover, the higher recharge rates and water tables (Scott & Le Maitre, 1998). As vegetation cover is increased, evapotranspiration and runoff are reduced and therefore recharge is increased. Agricultural practices and vegetative cover manipulation could therefore be an option to preserve groundwater and increase the net recharge of the aquifers in the West Bank. The best land management practice in arid areas of the Jordan Valley is the one which protects the soil from runoff while at the same time requires the lowest amount of water as transpiration. For the semi-arid landscapes, the most appropriate land covers are species that are well adapted to survival with low water availability (Bellor *et al*., 2001). For the rest of the area that is characterised as sub-humid, partial afforestation could increase the annual water recharge to the aquifer systems. However, vegetation effect on recharge and evapotranspiration is complex due to many interactions in the processes involved. For instance, under vegetation mote infiltration could take place due to protection of the soil surface, organic matter content of the soil, and biological activities. Nevertheless, this uptake depends in the species and the environmental factors and has to be determined by field experiments.

The recharge map has also shown that water infiltration is not only dependent on vegetation cover but also on soil type and its hydraulic properties. Soil type determines the water-holding capacity and therefore the amount of water lost through evapotranspiration.

9.4 Limitations of Remote Sensing Application

The main constraint in using remote sensing and GIS in this study is that the methodology and the validation of results are missing field data and measurements. A more accurate estimation of recharge and recharge mapping would be possible if more comprehensive and accurate data on the aquifers climate and hydrogeological characteristics have been available. The lack of reliable field data is due to the poor and sometimes completely absent monitoring facilities. Another principal reason behind the limited application of remote sensing and GIS techniques is the security restrictions on maps and aerial photos imposed by the Israeli Government and their unavailability for genuine uses. As far as the restrictions of remote sensing data are concerned, in view of liberal distribution and relatively easy accessibility of remote sensing data including the high-resolution data, it would be highly beneficial to remove or relax the security restrictions on the remote sensing data and maps for Palestinians. Furthermore, there is an urgent need to develop adequate groundwater-monitoring facilities on a regular and long-term basis throughout the country, and to boost up field investigations in order to ensure effective applications of emerging remote sensing and GIS technologies for the sustainable development and management of vital but shrinking groundwater resources.

The applications of remote sensing technology in hydrology in general and groundwater recharge in specific are very limited compared to other fields of study because of its inherent limitations. Although there is growing interest in exploring this technology, there is a long way to go in order to use remote sensing technology effectively for the development and management of vital groundwater resources. Based on the present review, the focus of future advancements in remote sensing technology should be in the following areas of concern:

- A general problem of using remote sensing in hydrological studies is that very few remotely sensed data can be directly applied in hydrology, they measure only a part of electromagnetic spectrum and different hydrological parameters

are inferred from them. Therefore, there is an urgent need to improve the accuracy and reliability of remote sensing estimates, which are still highly uncertain (Beven, 2001). It could be possible by refining analysis techniques as well as developing new and improved sensors and their applications in conjunction with improved field measurements.

- More remote sensing-based groundwater studies together with field studies should be carried out in order to examine the reliability of remote sensing data. The combined use of multi-spectral data obtained from different sensor systems is necessary to extract more and better information. Future research should also be directed towards developing linkages between surface observations and subsurface phenomena. Such studies will not only enhance and refine remote sensing applications in groundwater hydrology, but will also significantly contribute to the sensor development program.
- The major constraint for the use of remote sensing in hydrogeology is that it can only detect changes at the ground surface or a shallow layer which is less than a metre deep, though the airborne exploration of groundwater using electromagnetic prospecting sensors developed for the mineral industry is reported to map aquifers at depths greater than 200 m (Paterson and Bosschart, 1987). However, with the growing need to explore groundwater, it is often necessary to investigate deep aquifers in which case the usual remote sensing data are of no use, except for the especially acquired data by Ground-Penetrating Radar (GPR) which can penetrate up to about 20 m depth. Although ongoing research activities using GPR, subsurface methods of groundwater investigations, and tracers are expected to enhance the knowledge about complex and hidden subsurface processes, routine use of any of these techniques seems a long way off (Beven, 2001; Lane *et al*., 2000). Future research should focus on the development of easy-to-use techniques to quantify subsurface water storage and visualize fluid flow and transport processes in the subsurface environment. Furthermore, there is a need to have more accurate and reliable non-invasive techniques for monitoring subsurface processes as well as to deal the heterogeneity of aquifer and vadose-zone systems. Future advances in

remote sensing technology in this direction will certainly revolutionize the hydrogeological thinking, theory, and model development.

- There is a need to develop an optimal sensor system including both active and passive microwave techniques for more effective soil-moisture monitoring. It will allow a range of applications and the synergism of the two types of measurements to provide more useful and new information (Jackson *et al*., 1999).
- Recent developments in microwave remote sensing, theory and sensor availability have resulted in new potential and capabilities. Very few studies have revealed the potential to extract and detect subsurface parameters and features using these techniques. More research is required to refine and implement these approaches (Jackson, 2002). The multi-temporal and spatial availability of microwave remote sensing data can complement the monitoring and modelling of groundwater recharge. In addition, through the synergistic use of Earth's gravity-field monitoring satellites (e.g., GRACE and CHAMP) data and satellite microwave remote sensing data, it may be possible to monitor seasonal groundwater recharge over large regions in the near future (Jackson, 2002). Future studies should be carried out in this stimulating direction.

A final recommendation suggests that there must be strong cooperation between space agencies and soil and water scientists (e.g., soil scientists, hydrologists, hydrogeologists, and environmentalists) for the planning and development of sensor systems, which will ensure timely implementation of suitable and efficient sensor systems for the effective mapping of land and water resources. Such cooperation will undoubtedly lead to wide-scale research and applications in the fields of hydrology and hydrogeology, which in turn will ensure efficient land and water management by the promising remote sensing technique.

9.5 Recommendations for Future Research

Recharge may be quantified using conventional data such as chloride method and water table fluctuation. Remote sensing derived parameters may be used in a GIS model to estimate recharge. Apart from rainfall and evapotranspiration data, information about

soil moisture, rooting depth and water holding capacity of the soil has to be estimated in the recharge model. Rooting depth may be judged by vegetation classification while water holding capacity estimates may be based on soil maps and field observations. Also if some recharge data are available, then it may be used to calibrate the model.

Depth to water table is considered to be corresponding to changes in the gravity field where variations in gravity affect the distance between two GRACE (Gravity Recovery and Climate Experiment) satellites.

In order to further estimate the amount of recharge into the aquifer basins of the West Bank during the winter months, there are a number of recommendations for future research. These may be divided into two sections: field investigations and remote sensing modelling.

During field work it was only possible to access certain areas for land cover surveys. Very limited field measurements of hydrogeological, meteorological, and surface parameters exist. In order to estimate the spatial recharge input parameters, field measurements of the model are essential to attain for validation, calibration and reducing the uncertainties accompanied. This indicates that further field measurements and experiments on recharge and its parameters especially in the winter season are required to fill out the general picture of recharge mechanism.

Some of these field measurements include hourly rainfall intensities that should be measured and recorded for soil moisture calculation, runoff generation, and recharge estimation. Long-term rainfall-runoff simulation experiments should be conducted for the three aquifers taking into consideration vegetation patterns and slope. Daily evapotranspiration and precipitation are also important to measure for validation purposes and understanding the water balance mechanism in the surface soil. Other spatially distributed parameters such as heat fluxes, net radiation, and soil moist content are also a requirement.

Second, the remote sensing modelling could be applied to more than one sensor; first, to examine the reliability of the remote sensing data, and second, to obtain different results in order to choose the one with less bias estimates. Choosing data sets with high

resolution could offer more detailed data that could be more useful in heterogeneous areas such as the West Bank. Also, the modelling could use electromagnetic sensors to study and map aquifers at greater depths than surface analysis in addition to microwave sensors to monitor soil moisture and surface water content for better application of the water budget equation.

9.6 Conclusion

Rainfall is the main source of groundwater recharge and evapotranspiration is the major water consumption and both vary spatially even in small areas. Rain gauges and meteorological networks are poorly distributed in the West Bank and typical of many of the developing world which make the determination of spatial rainfall estimation and therefore recharge difficult to attain. Remote sensing is becoming a source for deriving the spatial and temporal distribution of hydrological data inputs such as precipitation, evapotranspiration, and land cover change.

Groundwater recharge estimations and mapping are essential for the management of groundwater aquifers, providing information for sustainable use of groundwater resources. It requires a comprehensive approach that includes all factors influencing recharge such as soil moisture, precipitation, evapotranspiration, and land cover. These inputs can be identified and mapped by remote sensing at different scales but require high spatial and spectral resolution for accurate outcomes. Over the years, increasing population, urbanization and expansion of irrigated agriculture led to the unscientific exploitation of groundwater creating a water stress condition. This alarming situation calls for a cost and time-effective technique for proper evaluation of groundwater resources and management planning.

Different methods for estimating groundwater recharge have been developed for the West Bank areas which are the water balance method and empirical methods. The problems encountered in the water balance method are that it has been applied on small scale catchment areas using potential evapotranspiration and rainfall. The empirical methods rely only on the long term annual rainfall data and/or assuming that recharge equal rainfall plus water discharge. These methods have highlighted the main areas of uncertainty and emphasises the need for improved models to study the variability of

recharge in time and space. This model includes not only climate conditions but also geology, morphology, soil type, and land cover. It is a water balance approach that quantifies groundwater recharge based on remote sensing and GIS techniques.

It is hoped that the findings of this research will contribute to developing future land/water resources management strategies to preserve aquifer systems in the region and maybe beyond. Concerns about the impact of land cover change on the water resources and aquifer sustainability have been raised lately. Consideration of how to adapt land management practices in order to cope with the effects on recharge is required.

References

Adeyewa, Z.D. and Nakamura, K., (2003). Validation of TRMM radar rainfall data over major climatic regions in Africa. *Journal of Applied Meteorology*, 42 (2): 331-347.

Aguera, F., Aguilar, F. and Aguilar, M., (2008). Using texture analysis to improve per-pixel classification of very high resolution images for mapping plastic greenhouses. *ISPRS Journal of Photogrammetry and Remote Sensing*, 63, pp. 635-646.

Akbari, M., Toomanian, N., Droogers, P., Bastiaanssen, W., and Gieske, A., (2007). Monitoring irrigation performance in Esfahan, Iran, using NOAA satellite imagery. *Agricultural Water Management*, 88, pp. 99-109.

Aliewi, A., Abu Saadah, M., Messerschmidt, C., and Kalbouneh, A., (2006). Development of annual and monthly recharge/rainfall estimation models for the Western Aquifer Basin with an application to the Natuf Catchment. *Paper No. 7*, SUSMAQ Project, Ramallah, Palestine.

Allen, R.G., Pereira, L.S., Raes, D., and Smith, M., (1998). Crop evapotranspiration-Guidelines for computing crop water requirements. *FAO Irrigation Paper No. 56*, UN/FAO, Rome.

Allen, R.G., Prueger, J., and Hill, R.W., (1992). Evapotranspiration from isolated stands of hydrophytes: Cattail and Bulrush, *Transactions ASAE*, 35 (2): 1-34.

Allen, R.G., Tasumi, M., and Trezza, R., (2007). Satellite based energy balance for mapping evapotranspiration with internalized calibration (METRIC)- Model. *ASCE Journal of Irrigation and Drainage Engineering*, 133 (4):380-394.

Amnesty International, (2009). Troubled Waters- Palestinians Denied Fair Access to Water. *Amnesty International*, United Kingdom.

Anderson, M.C., Norman, J.M., Diak, G.R., Kustas, W.P., and Mecikalski, J.R., (1997). A two-source time-integrated model for estimating surface fluxes using thermal remote sensing. *Remote Sensing of Environment*, 60: 195-216.

Antea, (1998). Geological Map of Eastern Aquifer Basin. Unpublished report f the Middle East Peace Process. Water Working Group. *Regional Water Data Bank*- Phase 1 and 2 (European Union).

Arad, A., and Michaeli, A., (1967). Hydrogeological investigations in the Western Catchment of the Dead Sea, *Israel Journal of Earth Science*, 16, 181-196.

ARIJ, (1998). Water Resources and Irrigated Agriculture in the West Bank. Applied Research Institute, Jerusalem.

ARIJ, (2007). Status of the Environment in the Occupied Palestinian Territory. *Applied Research Institute-Jerusalem (ARIJ),* Bethlehem, Palestine.

Assaf, K., AlKhatib, N., Kally, E., and Shuval, H., (1993). A proposal for the development of a regional water master plan. *Israel/Palestine Center for Research and Information (IPCRI).*

Ba'ba', M.M., (1996). Hydrogeological investigations in the eastern basin of the West Bank. *Unpublished M.Sc. Thesis*, IHE, Delft.

Bachmat, Y, (1995). Hydrologic Model of the Western Mountain Groundwater Basin for Stage 1 of the Harvard Middle East Water Project. *Institute for Social and Economic Policy in the Middle East, John F. Kennedy School of Government, Harvard University*, USA.

Baker, M.E., Wiley, M.J., and Seelbach, P.W., (2001). GIS-based hydrologic modelling of riparian areas: Implications for stream water quality. *Journal of the American Water Resources Association,* 37 (6):1615-1628.

Bashir, M.A., Tanakamaru, H., Abdelhadi, A.W., and Tada, A., (2008). Satellite-based energy balance model to estimate seasonal evapotranspiration for irrigated sorghum: a case study from the Gezira scheme, Sudan. *Hydrology and Earth System Sciences*, 12, pp. 1129-1139.

Bastiaanssen, W.G.M., (1995). Regionalization of surface flux densities and moisture indicators in composite terrain: A remote sensing approach under clear skies in Mediterranean climate. *PhD. Thesis*, Wageningen University, The Netherlands, 286pp.

Bastiaanssen, W.G.M., Ahmad, M.U.D., and Chemin, Y., (2002). Satellite surveillance of evaporative depletion across the Indus Basin. *Water Resources Research*, 38 (12), Article No. 1273.

Bastiaanssen, W.G.M., (2000). SEBAL-based sensible and latent heat fluxes in the irrigated Gediz Basin, Turkey. *Journal of Hydrology*, 229, pp. 87-100.

Bastiaanssen, W.G.M. and Bos, M.G., (1999). Irrigation performance indicators based on remotely sensed data: a review of literature. *Irrigation and Drainage Systems*, 13: 291-311.

Bastiaanssen, W.G.M. and Chandrapala, L., (2003). Water balance variability across Sri Lanka for assessing agricultural and environmental water use. J. Agric. Water Manage. 58, 171–192.

Bastiannssen, W.G.M., Menenti, M., Feddes, R.A., and Holtslag, A.A.M., (1998). A remote sensing surface energy balance algorithm for land (SEBAL)- Part 1: Formulation. *Journal of Hydrology*, 228: 198-212.

Bastiannssen, W.G.M., Pelgrum, H., Menenti, M., and Feddes, R.A., (1996). Estimation of surface resistance and Priestley-Taylor α-parameter at different scales, In: Stewart et al., (1996) (eds). *Scaling up in hydrology using remote sensing*, J. Wiley and Sons, Chichester, p.255-262.

Bastiannssen, W.G.M., Pelgrum, H., Wang, J., Ma, J., Moreno, J., Roerink, G.J., and Van Der Wal, T., (1998). The Surface Energy Balance Algorithm for Land (SEBAL)- Part 2: Validation. *Journal of Hydrology*, 212-213: 213-229.

Batra, N., Islam, S., Venturini, V., Bisht, G., and Jiang, L., (2006). Estimation and comparison of evapotranspiration from MODIS and AVHRR sensors for clear sky days over the Southern Great Plains. *Remote sensing of Environment*, 103, pp. 1-15.

Bauer, P., Mahfouf, J.F., Olson, W.S., Di Michele, S., Tassa, A., and Mugnai, A., (2002). Error analysis of TMI rainfall estimates over ocean for variational data assimilation. *Quarterly Journal of the Royal Meteorological Society,* 128 (584): 2129-2144.

Ben-Dor, E., Kindel, B., and Goetz, A.F.H., (2004). Quality assessment of several methods to recover surface reflectance using synthetic imaging spectroscopy data. *Remote Sensing of Environment,* 90: 389-404.

Berberoglu, S. and Akin, A., (2009). Assessing different remote sensing techniques to detect land use/land cover changes in the eastern Mediterranean. *International Journal of Applied Earth Observation and Geoinformation*, 11, pp. 46-53.

Berg, W., L'Ecuyer, T., and Kummerow, C., (2006). Rainfall Climate Regimes: The Relationship of Regional TRMM Rainfall Biases to the Environment. *Journal of Applied Meteorological Climate*, 45: 434-454.

Beven, K.J., (2001). How far can we go in distributed modelling. *Hydrology and Earth System Science*, 105: 79-102.

Blake, G.S. and Goldschmidt, M.J., (1947). Geology and Water Resources of Palestine. *Government of Palestine, Department of Land Settlement and Water Commissioner*, Jerusalem.

Bobba, A.G., Bukata, R.P., and Jerome, J.H., (1992). Digitally Processed Satellite Data as a Tool in Detecting Potential Groundwater-Flow Systems. *Journal of Hydrology*, 131 (1-4): 25-62.

Brata, N., Islam, S., Venturini, V., Bisht, G., and Jiang, L., (2006). Estimation and comparison of evapotranspiration from MODIS and AVHRR sensors for clear sky days over the Southern Great Plains. *Remote Sensing of Environment*, 103: 1-15.

Brunner, P., Kinzelbach, W., Li, W.P., and Dong, X.G., (2006). Sustainable irrigation in the Yanqi basin, China. *Sustainable Irrigation Management, Technologies and Policies,* 96: 115-125.

Burt, T. and Shahgedanova, M., (1998). An historical record of evaporation losses since 1815 calculated using long-term observations from the Radcliffe Meteorological Station, Oxford, England. *Journal of Hydrology*, 205: 101-111.

Cai, G.Y., Wu, J., Xue, Y., Hu, Y.C., Guo, J.P., and Tang, J.K., (2005). Soil moisture retrieval from MODIS data in northern China plain using thermal inertia model (SoA-TI). *IEEE International Geoscience and Remote Sensing Symposium*, 1-8: 4501-4504.

Carlson, T.N., Perry, E.M., and Schmugge, T.J., (1990). Remote estimation of soil moisture availability and fractional vegetation cover for agricultural fields. *Agricultural and Forest Meteorology*, 52: 45-69.

CDM, (1997). CDM/Morganti, Task 18: Study of the Sustainable Yield of the Eastern Aquifer Basin: Preliminary Conceptual Model and Initial Estimate of the Sustainable Yield. *PWA/USAID Internal Report*.

CDM, (1998). CDM/Morganti, Study of the Sustainable Yield of the Eastern Aquifer Basin: Final Report. *PWA/USAID Internal Report*.

Chabrillat, S., Goetz, A.F.H., Krosley, L., and Olsen, H.W., (2002). Use of Hyperspectral images in the identification and mapping of expansive clay soils and the role of spatial resolution. *Remote Sensing of Environment*, 82: 480-445.

Chander, G. and Markham, B., (2003). Revised Landsat-5 TM radiometric calibration procedures and postcalibration dynamic ranges. *IEEE Transactions on Geoscience and Remote Sensing*, 41 (11):2674-2677.

Chavez, P.S., (1996). Image based atmospheric corrections revisited and improved. *Photogrammetric Engineering and Remote Sensing*, 62, pp. 1025-1036.

Chemin, Y., (2003). Evapotranspiration of crops by remote sensing using the energy balance based algorithms. *Technical Report B231/2003*, Asian Institute of Technology, Bangkok, Thailand, 16pp.

Chen, S.Y.S., Knaff, J.A., and Marks, F.D., (2006). Effects of vertical wind shear and storm motion in tropical cyclone rainfall asymmetries deduced from TRMM. *Monthly Weather Review*, 134 (11): 3190-3208.

Chen, T.S. and Ohring, G., (1985). On the relationship between clear-sky planetary and surface albedos: a parameterization for simple energy balance climate models. *Advances in Space Research*, 6 (5): 141-144.

Chenini, I., Ben Mammou, A., and El May, M., (2010). Groundwater recharge zone mapping using GIS-based multi-criteria analysis: a case study in central Tunisia (Maknassy Basin). *Water Resources Management*, 24 (5): 921-939.

Chiu, L.S., Liu, Z., Vongsaard, J., Morain, S., Budge, A., Neville, P., and Bales, C., (2006). Comparison of TRMM and water district rain rates over New Mexico. *Advances in Atmospheric Sciences*, 23 (1): 1-13.

Chokngamwong, R. and Chiu, L.S., (2008). Thailand daily rainfall and comparison with TRMM products. *Journal of Hydrometeorology*, 9 (2): 256-266.

Choudhury, B.J., Idso, S.B., and Reginato, R.J., (1987). Analysis of an empirical model for soil heat flux under a growing wheat crop for estimating evapotranspiration by an infrared-temperature based energy balance equation. *Agricultural and Forest Meteorology*, 30: 97-102.

Chowdhury, S.H., Iqbal, M.Z., and Szabo, J.P, (2003). Comprehensive approach of groundwater resources evaluation: A case study in the Chippewa Creek watershed in Ohio. *Ohio Journal of Science*, 103 (5): 134-142.

Clothier, B.E., Clawson, K.L., Pinter, J.R., Moran, M.S., Reginato, R.J., and Jackson, R.D., (1986). Estimation of soil heat flux from net radiation during the growth of Alfalfa. *Agricultural and Forest Meteorology*,37: 319-329.

Compaore, H., Hendrickx, J.M.H., Hong, S., Friesen, J., Van de Giesen, N.C., Rodgers, C., Szaraynski, J., and Vlek, P.L.G., (2008). Evaporation mapping at two scales using optical imagery in the White Volta Basin, Upper East Ghana. *Physics and Chemistry of the Earth*, 33, pp. 127-140.

Congalton, R.G., (1991). A review of assessing the accuracy of classification of remotely sensed data. *Remote Sensing of Environment*, 37, pp. 35-46.

Cook, S.E., Corner, R.J., Groves, P.R., and Grealish, G.J., (1996). Use of airborne gamma radiometric data for soil mapping. *Australian Journal of soil research*, 34 (1): 183-194.

Coppin, P.R. and Bauer, M.E., (1996). Digital change detection in forest ecosystem with remote sensing imagery. *Remote Sensing Reviews*, 13, 207-234.

Cosgrove, B.A., Lohmann, D., Marshall, C.H., Mitchell, K.E., Houser, P.R., Wood, E.F., Schaake, J.C., Robock, A., Sheffield, J., Duan, Q., Luo, L., Higgins, R.W., Pinker, R.T., Tarpley, J.D., and Meng, J., (2003). Real-time and retrospective forcing in the North American Land Data Assimilation System (NLDAS) project. *Journal of Geophysical Research*, 108(D22), 8842, doi:10.1029/2002JD003118.

Cosgrove, B.A., Mitchell, K.E., Houser, P.R., Wood, E.F., Schaake, J.C., Robock, A., Lohmann, D., Sheffield, J., Duan, Q., Luo, L., Higgins, R.W., Pinker, R.T., Tarpley, J.D., and Meng, J., (2003). Land surface model spin-up behaviour in the North American Land Data Assimilation System (NLDAS) project. *Journal of Geophysical Research*, 108(D22), 8842, doi:10.1029/2002JD003118.

Dai, A., (2006). Precipitation characteristics in eighteen coupled climate models. *Journal of Climate*, 19 (18): 4605-4630.

De Bruin, H.A.R., (1987). From Penman to Makkink. In: Hooghart and Warmerdam (1987) (Eds). *Evaporation and weather proceedings and information*, TNO Committee on Hydrological Research, The Hague, The Netherlands, p.5-30.

De Vries, J.J. and Simmers, I., (2002). Groundwater recharge: an overview of processes and challenges. *Hydrogeology Journal*, 10: 5-17.

Di Bella, C.M., Rebella, C.M., and Paruelo, J.M., (2000). Evapotranspiration estimates using NOAA AVHRR imagery in the Pampa region of Argentina. *International Journal of Remote Sensing*, 21 (4): 791-797.

Djorovic, M., (1980). Slope effect on runoff and erosion. In: De Boodt, M., Gabriels, D. (Eds), *Assessment of Erosion.* Wiley-Interscience, Chichester, pp. 215-225.

Doraiswamy, P., Akhmedov, B., Milak, S., and Stern, A., (2008). Remote sensing and modelling methods for crop grain yield assessment. *Proceedings of the IEEE on IGARSS 2008 Geosciences and Remote Sensing: the next generation,* Boston, MA, USA.

Droogers, P., (2000). Estimating actual evapotranspiration using a detailed agro-hydrological model. *Journal of Hydrology,* 229:50-58.

Dudeen, Basim, (2004). The Soils of Palestine (The West Bank and Gaza Strip) Current Status and Future Perspectives. *Options Mediterraneennes,* Serie B, No. 34, pp. 203-233.

Duraiswami, R.A., Dumale, V., and Shetty, U., (2009). Geospatial mapping of potential recharge zones in parts of Pune city. *Journal Geological Society of India,* 73: 621-638.

El Maayar, M. and Chen, J.M., (2006). Spatial scaling of evapotranspiration as affected by heterogeneities in vegetation, topography and soil texture. *Remote Sensing of Environment,* 102: 33-51.

Engman, E.T. and Gurney, R.J., (1991). Remote Sensing in Hydrology. Remote Sensing Applications by Chapman and Hall, London, United Kingdom.

FAO (1998). Evapotranspiration: Guidelines for computing crop water requirements. *UN/FAO Irrigation and Drainage Papers No. 56,* Land and Water Division, FAO Press, Rome Italy. 300pp.

FAO (1977) Guidelines for predicting crop water requirements. *Irrigation and Grainage Paper No. 24, UN-FAO,* Land and Water Development Division, Rome, Italy, 144pp.

Farnsworth, R.K. Barret, E.C., and Dhanju, M.S., (1984). Application of remote sensing to hydrology including ground water. *IHP-II Project A. 1.5,* UNESCO, Paris, France.

Farrar, T.J., Nicholson, S.E., and Lare, A.R., (1994). The influence of soil type on the relationships between NDVI, rainfall, and soil moisture in semiarid Botswana. II. NDVI response to soil moisture. *Remote Sensing of Environment*, 50, pp. 121-133.

Faust, N.L., Anderson, W.H., and Star, J.L., (1991). Geographic information systems and remote sensing future computing environment. *Photogrammetric Engineering and Remote Sensing*, 57 (6): 655-668.

FEWS, (2006). Famine Early Warning Systems Network. www.fews.net

Fox, D.M., Bryan, R.B., and Price, A.G., (1997). The influence of slope angle on final infiltration rate for interrill conditions. *Geoderma*, 80: 181-194.

Franchito, S.H., Rao, V.B., Vasques, A.C., Santo, C.M.E., and Conforte, J.C., (2009). Validation of TRMM precipitation radar monthly rainfall estimates over Brazil. *Journal of Geophysical Research-Atmospheres*, 114, Article No. D02105.

Franklin, J. and Hiernaux, P.H.Y., (1991). Estimating foliage and woody biomass in Sahelian and Sudanian woodlands using a remote sensing model. *International Journal of Remote Sensing*, 12 (6): 1387-1404.

French, A.N., Jacob, F., Anderson, M.C., Kustas, W.P., Timmermans, W., Gieske, A., Su, Z., Su, H., McCabe, M.F., Li, F., Prueger, J., and Brunsell, N., (2005). Surface energy fluxes with the Advanced Spaceborne Thermal Emission and Reflection radiometer (ASTER) at the Iowa 2002 SMACEX site (USA). *Remote Sensing of Environment*, 99, pp. 55-65.

Fu, Baopu, (1998). The differences and variations in components of radiation budget in underlying surfaces of different topographies. *Scientia at Mospherica Sinica*, 22 (3): 178-190.

Fung, T., (1990). An assessment of TM imagery for land cover change detection. *Transactions on Geoscience and Remote sensing*, 28, pp. 681-684

Gao, J., (1999). A comparative study on spatial and spectral resolutions of satellite data in mapping mangrove forests. *International Journal of Remote Sensing*, 20, pp.2823-2833.

Gao, Yanchun, Long, Di and Li, Zhao-Liang, (2008). Estimation of daily actual evapotranspiration from remotely sensed data under complex terrain over the upper Chao river basin in North China. *International Journal of Remote Sensing*, 29:11,3295-3315.

Goetz, S.J., (1997). Multi-sensor analysis of NDVI, surface temperature and biophysical variables at a mixed grassland site. *International Journal of Remote Sensing*, 18 (1): 71-94.

Goldschmidt, (1955). Precipitation and Runoff from Jordan and Litani catchments. Hydrological Paper No. 1, *Hydrological Service of Israel*, Jerusalem.

Goldschmidt and Jacob, (1958). Precipitation and Replenishment of the Yarqon and Nahal Hatteninim underground catchments. Hydrological Paper No. 3, *Hydrological Service of Israel*, Jerusalem.

Gong, P. and Howarth, P.J., (1990). An assessment of some factors influencing multispectral land cover classification. *Photogrammetric Engineering and Remote Sensing*, 56, pp. 597-603.

Gong, P., Marceau, D.J. and Howarth, P.J., (1992). A comparison of spatial feature extraction algorithms for land use classification with SPOT HRV data. *Remote Sensing of Environment*, 40, pp. 137-152.

Granger, R.J., (1997). Summary energy balance at Wolf Creek Research Basin, Yukon. *Proceedings of the Hydro-Ecology Workshop on the Arctic Environmental Strategy Action on Water*, 16:325-341.

Green, E.P., Clark, C.D., Mumby, P.J., Edwards, A.J., and Ellis, A.C., (1998). Remote Sensing techniques for mangrove mapping. *International Journal of Remote Sensing*, 19, pp. 935-956.

Grindley, J., (1969). The calculation of actual evapotranspiration and soil moisture deficit over specified catchment areas. *Hydrological Memorandum No. 38*, Meteorological Office.

Guttman, Y, (1995). The hydrogeology of the Eastern Basin and possibilities for the development of water resources from the Pharaoh Stream to the Judean Desert. *Tahal Water Unit- Hydrological Section*. 01/95/105. TAHAL Consulting Engineers Ltd.

Guttman, Y. and Zukerman, C.H., (1995). Flow model in the Eastern Basin of the Mountains of Judea and Samaria from the Pharaoh Stream to the Judean Desert. *Tahal Water Unit- Hydrological Section*. 01/95/66. TAHAL Consulting Engineers Ltd.

Hafeez, M., Andreini, M., Liebe, J., Friesen, J., Marx, A., and Giesen, N.V.D., (2006). Hydrological parameterization through remote sensing in Volta Basin, West Africa. *International Journal of River Basin Management*, 4:1-8.

Han, H. and Yang, L.Y., (2004). Evaluation of regional scale evapotranspiration using SEBS model in western Chinese loess plateau. *IEEE International Geoscience and Remote Sensing Symposium*, 1-7: 1339-1342.

Haralick, R.M., Shanmugan, K., and Dinstein, I., (1973). Textural features for image classification. *IEEE Transactions on Systems, Man, and Cybernetics*, 3, pp. 610-621.

Heilman, J.L. and Moore, D.G., (1981). Groundwater applications of the heat capacity mapping mission, satellite hydrology. *Proceedings of the Fifth Annual William T. Pecora Memorial Symposium on Remote Sensing*. Sioux Falls, South Dakota, June 1-15, 1979 (1981), pp 446-449.

Herman, A., Kumar, V.B., Arkin, P.A., and Kousky, J.V., (1997). Objectively determined 10-day African rainfall estimates created for famine early warning systems. *International Journal of Remote Sensing*, 18 (10): 2147-2159.

Hinton, J.C., (1996). GIS and remote sensing integration for environmental applications. *International Journal of GIS*, 10 (7): 877-890.

Hong, S.H., Hendrickx, J.M.H., and Borchers, B., (2005). Effect of scaling transfer between evapotranspiration maps derived from Landsat 7 and MODIS images. *Proceedings of International Society for Optical Engineering*, SPIE 5811: 147-158.

Huete, A.R., (1988). A soil adjusted vegetation index (SAVI). *Remote Sensing of the Environment*, 25: 295-309.

Huffman, G.J., Adler, R.F., Bolvin, D.T., Gu, G., Nelkin, E.J., Bowman, K.P., Hong, Y., Stocker, E.F., and Wolff, D.B., (2007). The TRMM Multisatellite Precipitation Analysis (TMPA): Quasi-Global, Multiyear, Combined-Sensor Precipitation Estimates at Fine Scales. *Journal of Hydrometeorology*, 8: 38-55.

Hughes, A.G. and Mansour, M.M., (2005). Recharge modelling for the West Bank aquifers. *British Geological Survey*, Report CR/05/087, Keyworth, Nottingham, United Kingdom.

Hughes, A.G., Mansour, M.M., and Robins, N.S., (2008). Evaluation of distributed recharge in an upland semi-arid karst system: the West Bank Mountain Aquifer, Middle East. *Hydrogeology Journal*, 16 (5): 845-854.

Husary, S., Najjar, T., and Aliewi, A., (1995). Analysis of secondary source rainfall data from the northern West Bank. *Water Resources Management: West Bank and Gaza Strip.* Report WARMP/TEC/J/07. PHG/University Newcastle Upon Tyne.

Hydrological Service of Israel, (1997). Hydrological Yearbook of Israel 1999/2000, Jerusalem, Israel, ISSN 0073-4217.

Immerzeel, W.W., Gaur A., and Zwart, S.J., (2008). Integrating remote sensing and a process-based hydrological model to evaluate water use and productivity in a south Indian catchment. *Agricultural Water Management*, 95, pp. 11-24.

Idso, S.B., Aase, J.K., and Jackson, R.D., (1975). Net radiation and soil heat flux relations as influenced by soil water content variations.

Iqbal, M., (1983). *Introduction to solar radiation*. Academic Press, Montreal, Canada, p.1-83.

Jackson, Thomas, (2002). Remote Sensing of soil moisture: implications for groundwater recharge. *Hydrogeology Journal*, 10: 40-51.

Jackson, R.D., Kustas, W.P., and Choudhury, B.J., (1988). A re-examination of the crop water stress index. *Irrigation Science*, 9: 309-317.

Jackson, T.R., Bras, A., England, E.T., Engman, D., and Entekhabi et al., (1999). *Soil Moisture Research Mission-SMOS*, Earth Observation Quarterly, 66: 18-26.

Jacobsen, A. and Hansen, B.U., (1999). Estimation of the soil heat flux net radiation ratio based on spectral vegetation indexes in high-latitude Arctic areas. *International Journal of Remote Sensing*, 20 (2): 445-461.

Jensen, J.R., (1996). Introductory Image Processing: A Remote Sensing Perspective. Prentice-Hall, Englewood Cliffs, NJ.

Jia, L., Su, Z.B., van den Hurk, B., Menenti, M., Moene, A., De Bruin, H.A.R., Yrisarry, J.J.B., Ibanez, M., and Cuesta, A., (2003). Estimation of sensible heat flux using the Surface Energy Balance System (SEBS) and ATSR measurements. *Physics and Chemistry of the Earth*,28 (1-3): 75-88.

Jiang, L. and Islam, S., (2001). Estimation of surface evaporation map over Southern Great Plains using remote sensing data. *Water Resources Research*, 3 (2): 329 -340.

Kalluri, S.N.V. and Townsend, J.R.G., (1998). A simple layer model to estimate transpiration from vegetation using multi-spectral and meteorological data. *International Journal of Remote Sensing*, 19 (6): 1037-1053.

Karongo, S.K. and Sharma, T.C., (1997). An evaluation of actual evapotranspiration in tropical East Africa. *Hydrological Processes*, 11 (5): 501-510.

Kerr, Y.H., Imbernon, J., Dedieu, G., Hautecoeur, O., Lagouarde, J.P., and Seguin, B., (1989). NOAA AVHRR and its uses for rainfall and evapotranspiration monitoring. *International Journal of Remote Sensing*, 10 (4-5): 847-854.

Kimura, R., Bai, L., Fan, J., Takayama, N., and Hinokidani, O., (2007). Evapotranspiration estimation over the river of the Loess Plateau of China based on remote sensing. *Journal of Arid Environments*, 68, pp. 53-65.

Kite, G.W. and Droogers, P., (2000). Comparing evapotranspiration estimates from satellites, hydrological models and field data. *Journal of Hydrology*, 229, pp. 3-18.

Kongo, V.M. and Jewitt, G.P.W., (2006). Preliminary investigation of catchment hydrology on response to agricultural water use innovations: A case study of the Potshini catchment-South Africa. *Physics and Chemistry of the Earth*, 31, pp. 976-987.

Krishnamurthy, J., Kumar, N.V., Jayaraman, V., and Manivel, M., (1996). An approach to demarcate ground water potential zones through remote sensing and a geographical information. *International Journal of Remote Sensing*, 17 (10): 1867-1884.

Kurc, S.A. and Small, E.E., (2004). Dynamics of evapotranspiration in semiarid grassland and shrubland ecosystems during the summer monsoon season, central New Mexico. *Water Resources Research*, 40 (9), Article No. W09305.

Kustas, W.P. and Daughtry, C.S.T., (1990). Estimation of the soil heat flux/net radiation from spectral data. *Agricultural and Forest Meteorology*, 49: 205-223.

Kustas, W.P., Daughtry, C.S.T., and Van Oevelen, P.J., (1993). Analytical treatment of the relationships between soil heat flux/net radiation ratio and vegetation indices. *Remote Sensing of Environment*, 46: 319-330.

Kustas, W.P., Moran, M.S., Jackson, R.D., Gay, L.W., Duell, L.F.W., Kunkel, K.E., and Matthias, A.D., (1990). Instantaneous and daily values of the surface energy balance over agricultural fields using remote sensing and reference field in an arid environment. *Remote Sensing of Environment*, 32: 125-141.

Kustas, W.P. and Norman, J.M., (1996). Use of remote sensing for evapotranspiration monitoring over land surfaces. *Hydrological Sciences Journal*, 41 (4): 495-516.

Land Research Center, www.lrcj.org

Lane, T.P., Reeder, M.J., Morton, B.R., and Clarke, T.L., (2000). Observations and numerical modelling of mountain waves over the Southern Alps of New Zealand. *Q. J. R. Meteorological Society*, 126: 2765-2788.

Lange J, Greenbaum N, Husary S, Ghanem M, Leibundgut, C, and Schick. A.P., (2003). Runoff generation from successive simulated rainfalls on a rocky, semi-arid Mediterranean hillslope, *Hydrological Processes*, 17, 279-296.

Leduc, C., Favreau, G., and Schroeter, P., (2001). Long-term rise in a sahelian water-table: the Continental Terminal in South-West Niger. *Journal of Hydrology*, 243 (1-2): 43-54.

Lee, D.S., Shan, J., and Bethel, J.S., (2003). Class-guided building extraction from ikonos imagery. *Photogrammetric Engineering and Remote Sensing*, 69, pp. 143-150.

Lee, J. and Philpot, W., (1991). Spectral textures pattern matching: A classifier for digital imagery. *IEEE Transactions on Geoscience and Remote Sensing*, 29, 545.

Leica Geosystems (2003). *ERDAS Imagine Field Guide*, 7th Edition, Atlanta, Georgia, USA.

Leone, A.P. and Escadafal, R., (2001). Statistical analysis of soil colour and spectroradiometric data for Hyperspectral remote sensing of soil properties (example in a southern Italy Mediterranean ecosystem). *International Journal of Remote Sensing*, 22 (12): 2311-2328.

Lerner, D.N., Issar, A.S., and Simmers, I., (1990). Groundwater Recharge: A Guide to Understanding and Estimating Natural Recharge. *International Association of Hydrogeologists*, Hannover.

Li, H., Zheng, L., Lei, Y., Li, C., Liu, Z., and Zhang, S., (2008). Estimation of water consumption and crop water productivity of winter wheat in the North China Plain using remote sensing technology. *Agricultural Water Management*, 95, pp. 1271-1278.

Lillesand, T.M., Kiefer, R.W., and Chipman, J.W., (2008). Remote Sensing and Image Interpretation. John Wiley.

Lin, B., Wielicki, B.A., Minnis, P, Chambers, L., Xu, K.M., Hu, Y.X., and Fan, A., (2006). The effect of environmental conditions on tropical deep convective systems observed from the TRMM satellite. *Journal of Climate*, 19 (22): 5745-5761.

Lippmann, S.B., Lajoie, J., and Moo, B.E., (2005). *C++Primer*, 4th Edition, Pearson Education, Inc. 885pp.

Liu, C. and Zipser, E.J., (2005). Global distribution of convection penetrating the tropical tropopause. Department of Meteorology, University of Utah.

Lloyd, J.W., (1980). Aspects of environmental isotope chemistry in groundwater in eastern Jordan. Advisory Group Meeting on the Application of Isotope Techniques to Arid Zones Hydrology, *IAEA*, Vienna, IAEA-AG-158/14, pp. 193-204.

Lo, S.C.D., Mougin, E., and Gastellu-Etchegorry, J.P., (1993). Relating the global vegetation index to net primary productivity and actual evapotranspiration over Africa. *International Journal of Remote Sensing*, 14: 1517-1546.

Lu, D.S., Mausel, P., Brondizio, E.S., and Moran, E., (2004). Change detection techniques. *International Journal of Remote Sensing*, 25, 2365-2407.

Luk, S.H., Cai, Q., and Wang, G.P., (1993). Effects of surface crusting and slope gradient on soil and water losses in the hilly loess region, North China. *Catena Suppl.*, 24: 29-45.

Lunetta, R.S., Alvarez, R., Edmonds, C.M., Lyon, J.G., Bonifaz, R., Elvidge, C.D. and Garcia, C., (2002). NALC/Mexico land cover mapping results: implications for assessing landscape condition. *International Journal of Remote Sensing*, 23, pp. 3129-3148.

Lyon, J.G. (ed), (2003). GIS for Water Resources and Watershed Management. Taylor and Francis, London. 266 pp.

Ma, L., Hoogenboom, G., Ahuja, L.R., Ascough, J.C., and Saseendran, S.A., (2006). Evaluation of the RZWQM-CERES-Maize hybrid model for maize production. *Agricultural Systems*, 87 (3): 274-295.

Ma, L., Hoogenboom, G., Ahuja, L.R., Nielsen, D.C., and Ascough, J.C., (2005). Development and evaluation of the RZWQM-CROPGRO hybrid model for soybean production. *Agronomy Journal,* 97 (4): 1172-1182.

Ma, Y., Su, Z, Li, Z., Koike, T., and Menenti, M., (2002). Determination of regional net radiation and soil heat flux over a heterogeneous landscape of the Tibetan Plateau. *Hydrological Processes,* 16: 2963-2971.

Maneta, M.P., Schnabel, S., Wallender, W.W., Panday, S., and Jetten, V., (2008). Calibration of an evapotranspiration model to simulate soil water dynamics in a semiarid rangeland. *Hydrological Processes,* 22 (24): 4655-4669.

Mansour, M.M. and Hughes, A.G., (2005). User Manual for the object-oriented recharge model OOBRM. *British Geological Survey* Commissioned Report CR/05/086N.

Marceau, D.J., Howarth, P.J., Dubois, J.M.M. and Gratton, D.J., (1990). Evaluation of the grey level co-occurrence matrix method for land cover classification using SPOT imagery. *IEEE Transactions on Geoscience and Remote Sensing,* 28, pp. 513-519.

Marx, A., Kunstmannm, H., Schuttereyer, D., and Moene, A.F., (2008). Uncertainty analysis for satellite derived sensible heat fluxes and scintillometer measurements over Savannah environment and comparison to mesoscale meteorological simulation results. *Agricultural and Forest Meteorology,* 148, pp. 656-667.

Masunaga. H., LEcuyer, T.S., and Kummerow, C.D., (2006). The Madden-Julian Oscillation recorded in early observations from the Tropical Rainfall Measuring Mission (TRMM). *Journal of Atmospheric Science,* 63: 2777-2794.

Mayers, V.I. and Moore, D.G., (1972). Remote sensing for defining aquifers in glacial drift. *Eighth International Symposium on Remote Sensing of Environment*, volume 1, University of Michigan, pp 715-728.

McCarthy, J., Gumbricht, T., McCarthy, T.S., Frost, P.E., Wessels, K., and Seidel, F., (2004). Flooding patterns in the Okavango Wetland in Botswana between 1972 and 2000. *Ambio,* 7: 453-457.

Meijerink, A.M.J., (2000). Groundwater. In: Schultz G.A., Engman, E.T. (eds) Remote sensing in hydrology and water management. Springer, Berlin Heidelberg New York, pp. 305-325.

Meirovich, L., Ben-Zvi, A., Shentis, I., and Yanovich, E., (1998). Frequency and magnitude of runoff events in the arid Negev of Israel. *Journal of Hydrology*, 207:204-219.

Mekonnen, M.G. and Bastiaanssen, W.G.M., (2000). A new simple method to determine crop-water from satellite data: results from Kenya. *Irrigation and Drainage Systems*, 14 (3): 237-256.

Mekonnen, S.C. (2005) Assessment of catchment water balance using GIS and Remote Sensing: Roxo, Portugal, *MSc. Thesis*, ITC, The Netherlands, 109pp.

Melesse, Assefa M., Frank, Al, Nangia, Vijay and Hanson, (2008). Analysis of energy fluxes and land surface parameters in a grassland ecosystem: a remote sensing perspective. *International Journal of Remote Sensing*, 29:11, pp.3325-3341.

Melesse, A.M. and Nangia, V., (2005). Estimation of spatially distributed surface energy fluxes using remote-sensed data for agricultural fields. *Hydrological Processes*, 19, pp. 2653-2670.

Milewski, A., Sultan, M., Jayaprakash, S.M., Balekai, R., and Becker, R., (2009). RESDEM, a tool for integrating temporal remote sensing data for use in hydrogeologic investigations. *Computers and Geoscience*, 35 (10): 2001-2010.

Milewski, A., Sultan, M., Yan, E., Becker, R., Abdeldayem, A., Soliman, F., and Gelil, K.A., (2009). A remote sensing solution for estimating runoff and recharge in arid environments. *Journal of Hydrology*, 373 (1-2): 1-14.

Milich, L. and Weiss, E., (2000). GAC NDVI images: relationship to rainfall and potential evaporation in the grazing lands of The Gourma (northern Sahel) and in the croplands of the Niger-Nigeria border (southern Sahel). *International Journal of Remote Sensing*, 21 (2): 261-280.

Ministry of Planning, www.mop.gov.ps.

Misstear, B.D.R., Brown, L., and Daly, D., (2009). A methodology for making initial estimates of groundwater vulnerability mapping. *Hydrogeology Journal*, 17 (2): 275-285.

MODIS MOD09 (Surface Reflectance) User Guide (2008). MODIS Land Surface Reflectance Science Computing Facility, March, 2008.

MODIS LST (Land Surface) User Guide (2009). MODIS Land Surface Temperature Products.

MODIS Characterization Support Team (MCST) (2003). *MODIS LUT Information Guide For Level 1B*, MCST Internal Memorandum #M1036, December 1, 2003. The latest release is available on-line at http://www.mcst.ssai.biz/mcstweb/L1B/product.html

Mohamed, Y.A., Bastiaanssen, W.G.M., and Savenije, H.H.G., (2004). Spatial variability of evaporation and moisture storage in the swamps of the upper Nile studied by remote sensing techniques. *Journal of Hydrology*, 289, pp. 145-164.

Morrissay, M.L. and Janowiak, J.E., (1996). Sampling-induced conditional biases in satellite climate-scale rainfall estimates. *Journal of Applied Meteorology*, 35 (4): 541-548.

Morse, A., Tasumi, M., Allen, R.G., and Kramber, W.J. (2000) Application of the SEBAL Methodology for Estimating Consumptive Use of Water and Stream flow Depletion in the Bear River Basin of Idaho through Remote Sensing, *Final Project Report:* 2000, The Raytheon Systems Company, Idaho, USA, pp 1-107.

Murthy, K.S.R., (2000). Ground water potential in a semi-arid region of Andhra Pradesh- a geographical information system approach. *International Journal of Remote Sensing*, 63 (2): 75-95.

Mutiga, J.K., Su, Z., and Woldai, T., (2009). Using satellite remotes sensing to assess evapotranspiration: Case study of the upper Ewaso Ng'iro North Basin, Kenya. *International Journal of Applied Earth Observation and Geoinformation*.

Mutiga, J.K., Su, Z., and Woldai, T., (2010). Using satellite remote sensing to assess evapotranspiration: Case study of the upper Ewaso Ng'iro North Basin, Kenya. *International Journal of Applied Earth Observation and Geoinformation*, 12S: S100-S108.

Nair, S., Srinivasan, G., and Nemani, R., (2009). Evaluation of Multi-Satellite TRMM Derived Rainfall Estimates over a Western State of India. *Journal of the Meteorological Society of Japan*, 87 (6): 927-939.

Narayanan, M.S., Shah, C.M., Kishtawal, V., Sathiyamoorthy, M., Rajeevan, and Kriplani, R.H., (2005). Validation of TRMM merge daily rainfall with IMD raingauge analysis over Indian land mass. *Technical Report*, Space Application Centre, Ahmedabad, India.

Nassif, S. and Wilson, E., (1975). The influence of slope and rain intensity on overland flow and infiltration. *Hydrological Scientific Bulletin*, 20: 539-553.

National Remote Sensing Centre (1987). www.nrsc.gov.in

Nefedov, K.E. and Popova, T.A., (1972). Deciphering of Groundwater from Aerial photographs. Amerind Publishing Co. Pvt. Ltd. New Delhi.

Nemani, P.R. and Running, S.W., (1989). Estimation of regional surface resistance to evapotranspiration from NDVI and thermal IR AVHRR data. *Journal of Applied Meteorology*, 28: 276-557.

Nichol, J. and Lee, C.M., (2005). Urban vegetation monitoring in Hong Kong using high resolution multispectral images. *International Journal of Remote Sensing*, 26, pp. 903-918.

Nicholson, S.E., Some, B., McCollum, J., Nelkin, E., Klotter, D., Berte, Y., Diallo, B.M., Gaye, I., Kpabeba, G., Ndiaye, O., Noukpozounkou, J.N., Tanu, M.M., Thiam,

A., Toure, A.A., and Traore, A.K., (2003). Validation of TRMM and other rainfall estimates with a high-density gauge dataset for West Africa. Part I: Validation of GPCC rainfall product and pre-TRMM satellite and blended products. *Journal of Applied Meteorology*, 42 (10): 1337-1354.

Nicholson, S.E., Some, B., McCollum, J., Nelkin, E., Klotter, D., Berte, Y., Diallo, B.M., Gaye, I., Kpabeba, G., Ndiaye, O., Noukpozounkou, J.N., Tanu, M.M., Thiam, A., Toure, A.A., and Traore, A.K., (2003). Validation of TRMM and other rainfall estimates with a high-density gauge dataset for West Africa. Part II: Validation of TRMM rainfall products. *Journal of Applied Meteorology*, 42 (10): 1355-1368.

Norman, J.M., Anderson, M.C., Kustas, W.P., French, A.N., Mecikalski, J.R., Torn, R.D., Diak, G.R., Schmugge, T.J., and Tanner, B.C.W., (2003). Remote sensing of surface energy fluxes at 10-m pixel resolutions. *Water Resources Research*, 39, DOI:110.1029/2002WR001775.

Oke, T.R., (1997), in A. Perry, R. Thompson (eds). Applied Climatology: Principles and Practices, pp. 273-287.

Oliver, M.A. (1990) Kriging: "A Method of Interpolation for Geographical Information Systems", *Int. Journal of Geographic Information Systems*, 4, (4): 313–332.

Olson, W.S., Kummerow, C.D., Yang, S., Petty, G.W., Tao, W.K., Bell, T.L., Braun, S.A., Wang, Y., Lang, S.E., Johnson, D.E., and Chiu, C., (2006). Precipitation and latent heating distributions from satellite passive microwave radiometry. Part I: Improved method and uncertainties. *Journal of Applied Meteorology and Climatology*, 45(5): 702-720.

Opoku-duah, S., (2007). Remote Sensing of Energy and Water Fluxes over Volta Savannah Catchments in West Africa. *PhD Thesis*, Durham University, Durham, United Kingdom, 281pp.

Opoku-duah, S., Donoghue, D.N.M., and Burt, T.P., (2008). Intercomparison of Evapotranspiration over the Savannah Volta Basin in West Africa using Remote Sensing Data. *Sensors*, 8: 2736-2761.

Paine, J.G. and Collins, E.W., (2003). Applying AEM induction in groundwater salinization and resource studies, west Texas. SAGEEP, Denver, CO, pp. 722-738.

Pan, M., Wood, E.F., Wojcik, R., and McCabe, M.F., (2008). Estimation of regional terrestrial water cycle using multi-sensor remote sensing observations and data assimilation. *Remote Sensing of Environment*, 112 (4): 1282-1294.

Parodi, G.N., (2002). AVHRR Hydrological Analysis System: *Algorithms and Theory (Version 1.3)*, Water Resources Department, ITC, The Netherlands, 31pp.

PASSIA, (2003). Water in Palestine: Problems, Politics, Prospects. *Palestinian Academic Society for the Study of International Affairs*, Jerusalem.

Patel, N.R., Rakhesh, D., and Mohammed, A.J., (2006). Mapping of regional evapotranspiration in wheat using Terra/MODIS satellite data. *Hydrological Sciences*, 51(2).

Paterson, N. and Bosschart, R.A., (1987). Airborne Geophysical Exploration for Ground Water. Ground Water, v. 25, no. 1, pp 41-50.

PCBS, (2004). Meteorological Conditions in the Palestinian Territory-Annual Report. *Palestinian Central Bureau of Statistics*, Ramallah.

PCBS, (2007). Meteorological Conditions in the Palestinian Territory-Annual Report. *Palestinian Central Bureau of Statistics*, Ramallah.

Penman, H.L., (1948). Natural evaporation from open water, bare soil and grass. *Proc. Roy. Soc.* London, A193, 120-146.

Peters-Lidard, G.D., Kumar, S., Tian, Y., Eastman, J., and Houser, P., (2004). Global urban-scale land-atmosphere modelling with land information system. *Symposium on Planning, Nowcasting, and Forecasting in the Urban zone, 84th AMS Annual meeting,* Seattle, WA.

Petersen, W.A., Christian, H.J., and Rutledge, S.A., (2005). TRMM observations of the global relationship between ice water content and lightning. *Geophysical Research Letters,* 32.

Poesen, J., (1984). The influence of slope angle on infiltration rate and Hortonian overland flow volume. *Z. Geomorphol. N.F.,* 49: 117-131.

Powell, R.L., Roberts, D.A., Dennison, P.A. and Hess, L.L., (2007). Sub-pixel mapping of urban land cover using multiple endmember spectral mixture analysis: Manaus, Brazil. *Remote Sensing of Environment,* 106, pp. 253-267.

Price, J.C., (1990), using spatial context in satellite data to infer regional scale evapotranspiration. *IEEE Transactions in Geosciences and Remote Sensing,* 28: 940-948.

Prince, S.D., (1991). A model of regional primary production of air temperature from remotely sensed surface observations. *Remote Sensing of Environment,* 40: 335-346.

Puissant, A., Hirsch, J. and Weber, C., (2005). The utility of texture analysis to improve per-pixel classification for high to very high spatial resolution imagery. *International Journal of Remote Sensing*, 26, pp. 733-745.

Rahman, H. and Sengupta, D., (2007). Preliminary Comparison of Daily Rainfall from Satellites and Indian Gauge Data. *CAOS Technical Report No. 2007ASI,* Center for Atmospheric and Oceanic Sciences, Indian Institute of Science, Bangalore.

Rainey, M.P., Tyler, A.N., Gilvear, D.J., Bryant, R.G., and McDonald, P., (2003). Mapping intertidal estuarine sediment grain size distributions through airborne remote sensing. *Remote Sensing of Environment,* 86 (4): 480-490.

Ramos, J.G., Cratchley, C.R., Kay, J.A., Casterad, M.A., Martinez-Cob, A., and Dominguez, R., (2009). Evaluation of satellite evapotranspiration estimates using ground-meteorological data available for the Flumen District into the Ebro Valley of N.E. Spain. *Agricultural Water Management,* 96, pp. 638-652.

Ravikovitch, S. (1960). *Soils of Israel. Classification of the Soil of Israel*, Hebrew University, Jerusalem, Israel, p. 89.

Rofe and Raffety, (1963). Jerusalem and district water supply: geological and hydrological report. *Hashemite Kingdom of Jordan Central Water Authority*, Amman.

Rofe and Raffety, (1965). West Bank Hydrology 1963- 1965: Analysis. *Hashemite Kingdom of Jordan Central Water Authority*, Amman.

Rogers, J.S., Allen, L.H., and Calvert, D.J., (1983). Evapotranspiration for humid regions: developing citrus grove, grass cover. *Transactions ASAE*, 26 (6):1778-1783, 92.

Roshier, D.A. and Rumbachs, R.M., (2004). Broad-scale mapping of temporary wetlands in arid Australia. *Journal of Arid Environments*, 56 (2): 249-263.

Rushton, K.R., (1988). Numerical and conceptual models for recharge in arid and semiarid zones. In: I. Simmers, (ed), *Estimation of Natural Groundwater Recharge*, Reidel, Dordrecht (1988), pp. 223-238.

Sabbah, W.W., (2004). Developing a GIS and hydrological modelling approach for sustainable water resources management in the West Bank-Palestine. *PhD Thesis*, Brigham Young University, USA.

Saraf, A.K. and Choudhury, P.R., (1998). Integrated remote sensing and GIS for groundwater exploration and identification of artificial recharge sites. *International Journal of Remote Sensing*, 19 (10): 1825-1841.

Scarpa, D.J., (1994). Eastward groundwater flow from the Mountain Aquifer, in Water for Peace in the Middle East, eds. J. Isaac and H. Shuval, pp 193-203, *Elsevier Science Publications*, Amsterdam.

Schneider, W.J., (1965). Areal variability of low flows in a basin of diverse geologic units. *Water Resources Research*, 1: 509-515

Schuttemeyer, D., Schillings, Ch., Moene, A.F., and de Bruin, H.A.R., (2007). Satellite-based actual evapotranspiration over drying semiarid terrain in West Africa. *Journal of Applied Meteorology and Climatology,* 46 (1): 97-111.

Schuurmans, J.M., Troch P.A., Veldhuizen, A.A., Bastiaanssen, W.G.M., and Bierkens, M.F.P., (2003). Assimilation of remotely sensed latent heat flux in a distributed hydrological model. *Advances in Water Resources*, 26, pp. 151–159.

Scott, D.F. and Le Maitre, D.C., (1998). The interaction Between Vegetation and Groundwater: Research Priorities for South Africa. CSIR Report No. ENV/S-C 97161, May 1998.

Seguin, B., Couralt, D., and Guerif, M., (1994). Surface temperature and evapotranspiration: Application of local scale methods to regional scales using satellite data. *Remote Sensing of Environment,* 49: 287-295.

Seguin, B. and Itier, B., (1983). Using midday surface temperature to estimate daily evaporation from satellite thermal IR data. *International Journal of Remote Sensing,* 4: 371-383.

Sener, E., Davraz, A., and Ozcelik, M., (2005). An integration of GIS and remote sensing in groundwater investigations: A case study in Burdur, Turkey. *Hydrogeology Journal,* 13 (5-6): 826-834.

Shaban, M.A. and Dikshit, O., (2001). Improvement of classification in urban areas by the use of textural features: the case study of Lucknow City, Uttar Psadesh. *International Journal of Remote Sensing*, 22, pp. 565-593.

Shaban, A., Khawlie, M., and Abdallah, C., (2006).use of remote sensing and GIS to determine recharge potential zones: the case of Occidental Lebanon. *Hydrogeology Journal,* 14 (4): 433-443.

Shapiro, M.B. (2005). Soils of Israel, *Eurasian Soil Science,* 39 (11): 1170-1175.

Sharama, K., Singh, H., and Pareek, O., (1983). Rainwater infiltration into a bare loamy sand. *Journal of Hydrological Science,* 28: 417-424.

Shaw, E.M., (1994). *Hydrology in Practice*. Chapman and Hall, England (1994); reprinted by Routledge, 2004; 569pp.

Shentis, I., Meirovich, L., Ben-Zvi, A., and Rosenthal, E., (1999). Assessment of transmission losses and groundwater recharge from runoff events in a wadi under shortage of data on lateral inflow, Negev, Israel. Hydrological Processes, 13: 1649-1663.

Shepherd, K.D. and Walsh, M.G., (2002). Development of reflectance spectral libraries for characterization of soil properties. *Soil Science Society of America Journal*, 66: 988-998.

Shuttleworth, W.J., Gurney, R.J., Hsu, A.Y., and Ormsb, J.P., (1989). FIFE: The variation in energy partition at surface flux sites. *In*: Rango, A., (1989) (Ed.) *Remote sensing and large scale global processes*, IAHS Press, Wallingford, p.67-74.

Singh, A., (1989). Digital change detection techniques using remotely sensed data. *International Journal of Remote Sensing*, 10, 989-1003.

Smith, R.C.G. and Choudhury, B.J., (1990). Relationship of multispectral satellite data to land surface evaporation from the Australian continent. *International Journal of Remote Sensing*, 11: 2096-2088.

Snyder, R.L., Lanini, B.J., Shaw, D.A., and Pruitt, W.O., (1989). Using reference evapotranspiration (ETo) and crop coefficients to estimate crop evapotranspiration (Etc) for agronomic crops, grasses, and vegetable crops. *Cooperative Extension, University of California*, Berkeley, CA, Leaflet No. 21427, 12p.

Sobrino, J.A. and Raissouni, N., (2000). Toward remote sensing methods for land cover dynamic monitoring: application to Morocco. *International Journal of Remote Sensing*, 21, pp. 353-366.

Srivastava, S.K., Jayaraman, V., Rao, P.P.N., Manikiam, B, and Chandrasekhar, M.G., (1997). Interlinkages of NOAA/AVHRR derived integrated NDVI to seasonal precipitation and transpiration in dryland tropics. *International Journal of Remote Sensing*, 18 (14): 2931-2952.

Stewart, J.B., Engman, E.T., Feddes, R.A., and Kerr, Y.H., (1998). Scaling up in hydrology using remote sensing: summary of a workshop. *International Journal of Remote Sensing,* 19 (1): 181-194.

Su, Z. (2002) The Surface Energy Balance System (SEBS) for estimation of turbulent heat fluxes. *Hydrology and Earth Systems Sciences* 6(1): 85-99.

Su, Z., Pelgrum, H., and Menenti, M., (1999). Aggregation effects of surface heterogeneity in land surface processes. *Hydrology and Earth Systems Sciences,* 3(4): 549-563.

Sun, R. and Zhu, Q., (1999). Net primary productivity of terrestrial vegetation- A review on related researches *Yingong Shengtai Xuebao,* 10 (6): 757-760.

Sun, Y.Y., Gottsche, F.M., Olesen, F.S., and Fischer, H., (2002). Retrieval of land surface temperature from combined AVHRR data. *Annales Geophysicae,* 20 (8): 1247-1259.

SUSMAQ # 04 (2001): West Bank Aquifers-Conceptual Recharge Estimation. *Working Report SUSMAQ-REC #04 V0.1, Version 0.1,* Ramallah.

SUSMAQ # 20 (2003): West Bank Aquifers-Distribution of Empirical Estimates of Groundwater Recharge by Month. *Working Report SUSMAQ-RED #20 V0.1, Version 0.1,* Ramallah.

SUSMAQ # 64 (2003): Conceptual Model of Wadi Natuf Groundwater Recharge. *Working Report SUSMAQ-NAT #64 V0.3, Version 0.3,* Ramallah.

Tabesh, M., Yekta, A.H.A., and Burrows, R., (2009). An integrated model to evaluate losses in water distribution systems. *Water Resources Management,* 23 (3): 477-492.

Tahal, (1996). Under-ground water storage study, the hydrogeological regime of the Turonian- Cenomanian Aquifer of Central Israel.

Tasumi, M., (2003). Progression in operational estimation of regional evapotranspiration using satellite imagery. PhD. Dissertation, university of Idaho, Moscow, Idaho.

Teixeira, A.H. de C., Bastiaanssen, W.G.M, Ahmad, M.D., and Bos, M.G., (2008). Reviewing SEBAL input parameters for assessing evapotranspiration and water productivity for the Low-Middle Sao Francisco River basin, Brazil. Part A: Calibration and validation. *Agriculture and Forest Meteorology*.

Teixeira, A.H. de C., Bastiaanssen, W.G.M, Ahmad, M.D., and Bos, M.G., (2009). Reviewing SEBAL input parameters for assessing evapotranspiration and water productivity for the Low-Middle Sao Francisco River basin, Brazil. Part B: Application to the regional scale. *Agriculture and Forest Meteorology*, pp. 477-490.

Teixeira, A.H. de C., Bastiaanssen, W.G.M, and Bassoi, L.H., (2007). Crop water parameters of irrigated wine and table grapes to support water productivity analysis in the Sao Francisco river basin, Brazil. *Agricultural Water Management,* 94 (1-3): 31-42.

Timmermans, W.J. and Meijerink, A.M.J., (1999). Remotely sensed actual evapotranspiration: implications for groundwater management in Botswana. *International Journal of Applied Earth Observation and Geoinformation*, V.1, Issue ¾.

Timmermans, W.J., Kustas, W.P., Anderson, M.C., and French, A.N., (2007). An intercomparison of the Surface Energy Balance Algorithm for Land (SEBAL) and the Two-Source Energy Balance (TSEB) modelling scheme. *Remote Sensing of Environment*, 108, pp. 369-384.

Todd, D.K., (1980). Groundwater hydrology (Second Edition): John Wiley and Sons, New York, 535p.

Toll, D.L., (1984). An evaluation of simulated Thematic Mapper data and Landsat MSS data for discriminating suburban and regional land use and land cover. *Photogrammetric Engineering and Remote Sensing,* 50, pp/ 1713-1724.

Torres-Vera, M.A., Prol-Ledesma, R.M. and Garcia-Lopez, D., (2009). Three decades of land use variations in Mexico City. *International Journal of Remote Sensing,* 30, pp. 117-138.

Townshend, J.R.G., and Justice, C.O., (1986). Analysis of the dynamics of African vegetation using the normalized difference vegetation index. *International Journal of Remote Sensing,* 8, pp. 1189-1207.

Trajkovic, S., (2009). Comparison of radial basis function networks and empirical equations for converting from pan evaporation to reference evapotranspiration. *Hydrological Processes*, 23 (6): 874-880.

Tran, N., Zanife, O.Z., Chapron, B., Vandemark, D., and Vincent, P., (2005). Absolute calibration of Jason-1 and Envisat altimeter Ku-band radar cross sections from cross comparison with TRMM precipitation radar measurements. *Journal of Atmospheric and Oceanic*, 22 (9): 1389-1402.

Trishchenko, A.P., Fedosejevs, G., Li, Z.Q., and Cihlar, J., (2002). Trends and uncertainties in thermal calibration of AVHRR radiometers onboard NOAA-9 to NOAA-16. *Journal of Geophysical Research-Atmospheres,* 107 (D24), Article No. 4778.

Turk, F.J., Ebert, E.E., Oh, H.J., and Sohn, B.J., (2002). Validation and applications of a realtime global precipitation analysis. *IEEE International Geoscience and Remote Sensing Symposium and 24th Canadian Symposium on Remote Sensing, VOLS I-VI, Proceedings-Remote Sensing: Integrating our View of the Planet*, 705-707.

UNEP, (2003). Desk Study on the Environment in the Occupied Palestinian Territories. *United Nations Environment Programme*, 2003.

Valiente, J.A., Nunez, M., Lopez-Baeza, E., and Moreno, J.F., (1995). Narrow-Band to Broad-Band Conversion of Meteosat Visible Channel and Broad-Band Albedo using both AVHRR- 1 and 2 Channels. *International Journal of Remote Sensing,* 16 (6):1147-1166.

Van de Griend, A.A., Camillo, P.J., and Gumey, R.J., (1985). Discrimination of soil physical parameters, thermal inertia, and soil moisture from diurnal surface temperature fluctuations. *Water Resources*, 21: 997-1009.

Van de Griend, A.A. and Owe, M., (1993). On the relationship between thermal emissivity and the Normalized Difference Vegetation Index for natural surfaces. *International Journal of Remote Sensing*, 14 (6): 1119-1131.

Verhoef, W., Menenti, M. and Azzali, S., (1996). A colour composite of NOAA-AVHRR-NDVI based on time series analysis. *International Journal of Remote Sensing*, 17, pp. 231-235.

Vermote, E.F. and Vermeulen, A., (1999). Atmospheric correction algorithm: spectral reflectances (MOD09). Algorithm Technical background Document.

Wang, L., Sousa, W.P., Gong, P., and Biging, S., (2004). Comparison of IKONOS and QuickBird images for mapping mangrove species on the Caribbean coast of Panama. *Remote Sensing of Environment*, 91, pp. 432-440.

Waters, P., Greenbaum, P., Smart, L., and Osmaston, H., (1990). Applications of remote sensing to groundwater hydrology. *Remote Sensing Rev*, 4;223-264.

Weszka, J.S., Dyer, C. and Rosenfeld, A., (1976). A comparative study of texture measures for terrain classification. *IEEE Transactions on Systems, Man, and Cybernetics*, SMC, 6, PP.269-285.

Wolfer, J., (1998). Hydrogeological investigations along the Jerusalem-Jericho transect (Wadi et Qilt) Israel/West Bank. *Unpublished Diploma Thesis, Karlsruhe University* (TH).

Woodcock, C.E. and Strahler, A.H., (1987). The factor of scale in remote sensing. *Remote Sensing of Environment*, 21 (3): 311-332.

World Bank, (2009). Assessment of Restrictions on Palestinian Water Sector Development. The International Bank of Reconstruction and Development, Report No. 47657-GZ.

Wythers, K.R., Lauenroth, W.K., and Paruelo, J.M., (1999). Bare soil evaporation under semiarid field conditions. *Soil Science Society of America Journal*, 63 (5): 1341-1349.

World Health Organization: www.who.int

Yamamoto, M.K., Higuchi, A., and Nakamura, K., (2006). Vertical and horizontal structure of winter precipitation systems over the western Pacific around Japan using TRMM data. *Journal of Geophysical Research-Atmospheres*, 111 (D13), Article No., D13108.

Yang, L.M., Wylie, B.K., Tieszen, L.L., and Reed, B.C., (1998). An analysis of relationships among climate forcing and time-integrated NDVI of grasslands over the US northern and central Great Plains. *Remote Sensing of Environment*, 65 (1): 25-37.

Yeh, H.F., Lee, C.H., Hsu, K.C., and Chang, P.H., (2009). GIS for the assessment of the groundwater recharge potential zone. *Environmental Geology*, 58 (1): 185-195.

Zhang, H., Henderson-Sellers, A., Pitman, A.J., McGregor, J.L., Desborough, C.E., and Katzfey, J., (2001). Limited-area model sensitivity to the complexity of representation of the land surface energy balance. *Journal of Climate*, 14 (19): 3965-3986.

Zhang, Q., Wang, J., Gong, P., and Shi, P., (2001). Texture analysis for urban spatial pattern study using SPOT imagery. *IEEE Transactions on Systems, Man, and Cybernetics*, pp. 7033-7036.

Zhang, Y., (1999). Optimisation of building detection in satellite images by combining multispectral classification and texture filtering. *ISPRS Journal of Photogrammetry and Remote Sensing*, 54, pp. 50-60.

Zwart, S.J. and Bastiaanssen, W.G.M., (2007). SEBAL for detecting spatial variation of water productivity and scope for improvement in eight irrigated wheat systems. *Agricultural Water Management*, 89, pp. 287-296.

Appendix 1.1: Monthly Air Temperatures for the West Bank (2004)

Table 1: Mean air temperature (°C)

Month	Jenin	Tulkarm	Nablus	Ramallah	Jericho	Hebron
January	11.7	14.1	10.0	8.8	13.9	7.7
February	12.7	15.0	11.	9.8	15.2	8.6
March	16.5	18.9	15.2	13.9	20.1	13.8
April	18.9	21.5	17.6	16.1	23.2	15.7
May	22.1	24.8	20.0	18.8	26.3	18.5
June	24.7	27.2	22.6	21.3	29.4	21.5
July	27.9	30.0	25.4	23.2	32.4	24.3
August	27.3	29.6	24.2	22.2	31.3	22.9
September	26.1	28.4	23.3	22.0	29.7	22.2
October	24.5	26.8	22.1	20.8	27.2	20.8
November	17.2	21.7	16.2	14.7	20.7	14.4
December	11.7	15.6	10.2	9.4	13.1	9.2

Table 2: Maximum air temperature (°C)

Month	Jenin	Tulkarm	Nablus	Ramallah	Jericho	Hebron
January	19.4	17.8	12.9	11.9	19.6	10.5
February	17.6	19.1	14.7	13.8	21.6	12.1
March	22.6	22.5	19.7	18.9	27.4	17.9
April	25.1	25.5	22.8	21.4	30.6	20.5
May	27.9	28.5	26.0	24.5	33.8	23.0
June	29.8	30.2	28.1	26.8	37.0	26.8
July	33.5	32.9	31.3	28.7	40.1	29.6
August	32.4	32.6	29.8	27.4	38.2	28.1
September	32.0	31.5	29.5	27.5	36.7	28.0
October	31.0	30.6	27.5	25.7	33.8	25.5
November	22.1	25.4	20.3	18.0	26.5	17.4
December	17.2	19.2	14.2	12.5	19.4	12.4

Table 3: Minimum air temperature (°C)

Month	Jenin	Tulkarm	Nablus	Ramallah	Jericho	Hebron
January	8.4	9.8	7.3	6.6	8.8	5.0
February	8.9	9.7	7.4	6.8	9.3	5.1
March	12.1	12.0	11.0	10.7	12.5	9.5
April	13.1	13.3	13.0	12.4	15.5	10.9
May	17.2	17.1	15.3	14.3	18.6	14.0
June	20.6	20.3	18.1	16.5	21.5	16.0
July	22.8	22.4	20.7	18.8	24.3	19.1
August	23.4	22.7	20.4	18.6	23.6	17.6
September	21.7	21.4	19.2	18.3	22.2	17.0
October	20.0	18.7	18.1	17.8	20.1	16.7
November	13.4	14.2	12.8	12.4	14.8	11.3
December	7.9	8.5	7.0	7.2	7.5	6.0

Appendix 1.2: Mean Monthly Rainfall (mm month^{-1}) for the West Bank (2004)

Month	Jenin	Tulkarm	Nablus	Ramallah	Jericho	Hebron
January	175.9	240.8	230.0	112.0	29.8	182.6
February	94.6	89.3	136.2	122.5	23.1	97.7
March	8.1	17.8	24.2	15.4	8.6	24.1
April	15.1	6.0	11.1	3.2	1.7	1.8
May	1.0	0.5	1.2	3.1	2.1	0.0
June	0.0	0.0	0.0	0.0	0.0	0.0
July	0.0	0.0	0.0	0.0	0.0	0.0
August	0.0	0.0	0.0	0.0	0.0	0.0
September	0.0	0.0	0.0	0.0	0.0	0.0
October	0.0	3.0	0.4	12.8	7.6	4.2
November	86.2	127.1	152.8	179.2	26.0	211.2
December	43.9	62.8	82.6	76.1	29.6	49.2

Appendix 1.3: Mean Monthly Relative Humidity (%) for the West Bank (2004)

Month	Jenin	Tulkarm	Nablus	Ramallah	Jericho	Hebron
January	77.0	72.0	74.0	81.0	71.0	78.0
February	74.0	70.0	71.0	79.0	67.0	74.0
March	63.0	60.0	57.0	61.0	52.0	65.0
April	59.0	61.0	49.0	58.0	42.0	64.0
May	58.0	57.0	51.0	58.0	41.0	50.0
June	62.0	60.0	60.0	66.0	45.0	64.0
July	61.0	60.0	56.0	63.0	42.0	61.0
August	64.0	61.0	66.0	71.0	48.0	65.0
September	65.0	60.0	63.0	66.0	49.0	65.0
October	62.0	60.0	59.0	65.0	51.0	64.0
November	67.0	62.0	61.0	73.0	61.0	64.0
December	70.0	60.0	62.0	69.0	69.0	65.0

Appendix 1.4: Mean Monthly Wind Speed (km hour^{-1}) for the West Bank (2004)

Month	Jenin	Tulkarm	Nablus	Ramallah	Jericho	Hebron
January	3.9	5.0	9.5	6.4	5.2	11.0
February	3.8	4.0	8.6	10.8	6.3	6.4
March	2.9	3.3	9.0	9.7	7.8	6.0
April	3.9	3.6	9.0	8.8	10.2	6.3
May	4.6	3.7	9.8	12.0	10.2	9.0
June	5.0	3.8	10.3	9.3	8.6	12.9
July	5.3	3.5	9.8	10.0	8.4	13.0
August	4.8	3.5	10.0	12.9	7.6	13.6
September	3.7	2.5	9.0	13.0	6.4	11.7
October	3.0	2.8	6.7	10.5	5.4	9.8
November	3.5	4.0	8.0	12.2	5.4	13.0
December	1.9	2.9	6.9	10.6	3.4	12.4

Appendix 2.1: Psychometric constant (γ) for different altitudes (z)

Z (m)	γ kPa/°C	Z (m)	γ kPa/°C	Z (m)	γ kPa/°C	Z (m)	γ kPa/°C
0	0.067	1000	0.060	2000	0.053	3000	0.047
100	0.067	1100	0.059	2100	0.052	3100	0.046
200	0.066	1200	0.058	2200	0.052	3200	0.046
300	0.065	1300	0.058	2300	0.051	3300	0.045
400	0.064	1400	0.057	2400	0.051	3400	0.045
500	0.064	1500	0.056	2500	0.050	3500	0.044
600	0.063	1600	0.056	2600	0.049	3600	0.043
700	0.062	1700	0.055	2700	0.049	3700	0.043
800	0.061	1800	0.054	2800	0.048	3800	0.042
900	0.061	1900	0.054	2900	0.047	3900	0.042
1000	0.060	2000	0.053	3000	0.047	4000	0.041

Appendix 2.2: Slope of vapour pressure curve (Δ) for different temperatures (T)

T (°C)	Δ kPa/°C	T (°C)	Δ kPa/°C	T (°C)	Δ kPa/°C	T (°C)	Δ kPa/°C
1.0	0.047	13.0	0.098	25.0	0.189	37.0	0.342
1.5	0.049	13.5	0.101	25.5	0.194	37.5	0.350
2.0	0.050	14.0	0.104	26.0	0.199	38.0	0.358
2.5	0.052	14.5	0.107	26.5	0.204	38.5	0.367
3.0	0.054	15.0	0.110	27.0	0.209	39.0	0.375
3.5	0.055	15.5	0.113	27.5	0.215	39.5	0.384
4.0	0.057	16.0	0.116	28.0	0.220	40.0	0.393
4.5	0.059	16.5	0.119	28.5	0.226	40.5	0.402
5.0	0.061	17.0	0.123	29.0	0.231	41.0	0.412
5.5	0.063	17.5	0.126	29.5	0.237	41.5	0.421
6.0	0.065	18.0	0.130	30.0	0.243	42.0	0.431
6.5	0.067	18.5	0.133	30.5	0.249	42.5	0.441
7.0	0.069	19.0	0.137	31.0	0.256	43.0	0.451
7.5	0.071	19.5	0.141	31.5	0.262	43.5	0.461
8.0	0.073	20.0	0.145	32.0	0.269	44.0	0.471
8.5	0.075	20.5	0.149	32.5	0.275	44.5	0.482
9.0	0.078	21.0	0.153	33.0	0.282	45.0	0.493
9.5	0.080	21.5	0.157	33.5	0.289	45.5	0.504
10.0	0.082	22.0	0.161	34.0	0.296	46.0	0.515
10.5	0.085	22.5	0.165	34.5	0.303	46.5	0.526
11.0	0.087	23.0	0.170	35.0	0.311	47.0	0.538
11.5	0.090	23.5	0.174	35.5	0.318	47.5	0.550
12.0	0.092	24.0	0.179	36.0	0.326	48.0	0.562
12.5	0.095	24.5	0.184	36.5	0.334	48.5	0.574

Appendix 2.3: Number of the day in the year (J)

Day	Jan	Feb	Mar*	Apr*	May*	Jun*	Jul*	Aug*	Sep*	Oct*	Nov*	Dec*
1	1	32	60	91	121	152	182	213	244	274	305	335
2	2	33	61	92	122	153	183	214	245	275	306	336
3	3	34	62	93	123	154	184	215	246	276	307	337
4	4	35	63	94	124	155	185	216	247	277	308	338
5	5	36	64	95	125	156	186	217	248	278	309	339
6	6	37	65	96	126	157	187	218	249	279	310	340
7	7	38	66	97	127	158	188	219	250	280	311	341
8	8	39	67	98	128	159	189	220	251	281	312	342
9	9	40	68	99	129	160	190	221	252	282	313	343
10	10	41	69	100	130	161	191	222	253	283	314	344
11	11	42	70	101	131	162	192	223	254	284	315	345
12	12	43	71	102	132	163	193	224	255	285	316	346
13	13	44	72	103	133	164	194	225	256	286	317	347
14	14	45	73	104	134	165	195	226	257	287	318	348
15	15	46	74	105	135	166	196	227	258	288	319	349
16	16	47	75	106	136	167	197	228	259	289	320	350
17	17	48	76	107	137	168	198	229	260	290	321	351
18	18	49	77	108	138	169	199	230	261	291	322	352
19	19	50	78	109	139	170	200	231	262	292	323	353
20	20	51	79	110	140	171	201	232	263	293	324	354
21	21	52	80	111	141	172	202	233	264	294	325	355
22	22	53	81	112	142	173	203	234	265	295	326	356
23	23	54	82	113	143	174	204	235	266	296	327	357
24	24	55	83	114	144	175	205	236	267	297	328	358
25	25	56	84	115	145	176	206	237	268	298	329	359
26	26	57	85	116	146	177	207	238	269	299	330	360
27	27	58	86	117	147	178	208	239	270	300	331	361
28	28	59	87	118	148	179	209	240	271	301	332	362
29	29	(60)	88	119	149	180	210	241	272	302	333	363
30	30	-	89	120	150	181	211	242	273	303	334	364
31	31	-	90		151		212	243		304		365

*add 1 if leap year

Appendix 2.4: Penman-Monteith evapotranspiration calculations for Jenin

	Jan	Feb	Mar	Apr	May	Jun	Jul	Aug	Sep	Oct	Nov	Dec
Tmin [°C]	8.4	8.9	12.1	13.1	17.2	20.6	22.8	23.4	21.7	20	13.4	7.9
Tmax [°C]	19.4	17.6	22.6	25.1	27.9	29.8	33.5	32.4	32	31	22.1	17.2
Tmean [°C]	11.7	12.7	16.5	18.9	22.1	24.7	27.9	27.3	26.1	24.5	17.2	11.7
Relative Humidity [%]	77	74	63	59	58	62	61	64	65	62	67	70
Wind speed [km/hr^{-1}]	3.9	3.8	2.9	3.9	4.6	5	5.3	4.8	3.7	3	3.5	1.9
Wind Speed [m s^{-1}]	1.08	1.06	0.81	1.08	1.28	1.39	1.47	1.33	1.03	0.83	0.97	0.53
Δ [kPa °C]	0.091	0.096	0.119	0.136	0.162	0.186	0.219	0.212	0.200	0.184	0.124	0.091
γ [kPa °C]	0.0645	0.0645	0.0645	0.0645	0.0645	0.0645	0.0645	0.0645	0.0645	0.0645	0.0645	0.0645
e° (Tmax) [kPa]	2.253	2.013	2.742	3.187	3.758	4.195	5.173	4.863	4.755	4.493	2.660	1.962
e° (Tmin) [kPa]	1.102	1.140	1.412	1.508	1.962	2.427	2.776	2.878	2.596	2.338	1.537	1.065
e_s [kPa]	1.678	1.576	2.077	2.347	2.860	3.311	3.974	3.871	3.675	3.415	2.099	1.514
e_a [kPa]	1.292	1.167	1.309	1.385	1.659	2.053	2.424	2.477	2.389	2.118	1.406	1.060
G [MJ m^{-2} day^{-1}]	0.07	0.336	0.434	0.392	0.406	0.406	0.182	-0.126	-0.196	-0.623	-0.896	-0.385
Gsc [MJ m^{-2} min^{-1}]	0.082	0.082	0.082	0.082	0.082	0.082	0.082	0.082	0.082	0.082	0.082	0.082
J [-]	16	47	76	107	137	168	198	229	260	290	321	351
φ [rad]	0.567	0.567	0.567	0.567	0.567	0.567	0.567	0.567	0.567	0.567	0.567	0.567
dr [rad]	1.032	1.023	1.009	0.991	0.977	0.968	0.968	0.977	0.992	1.009	1.024	1.032
δ [rad]	-0.367	-0.224	-0.033	0.179	0.337	0.408	0.369	0.227	0.023	-0.182	-0.343	-0.408

ωs [rad]	1.333	1.430	1.550	1.682	1.787	1.839	1.810	1.713	1.585	1.458	1.350	1.302
Ra [MJ m-2 day-1]	19.717	24.739	30.905	36.716	40.191	41.422	40.566	37.493	32.180	25.907	20.463	18.196
n [days]	4.1	4.8	6.4	8.2	8.9	8.4	9.6	10.9	10.2	9.8	7	4.5
N [days]	10.181	10.927	11.844	12.847	13.654	14.049	13.827	13.087	12.107	11.137	10.314	9.949
Rs [MJ m^{-2} day^{-1}]	8.899	11.618	16.077	20.896	23.146	22.739	24.224	24.987	21.600	17.875	12.059	8.664
Rns [MJ m^{-2} day^{-1}]	6.852	8.946	12.379	16.090	17.823	17.509	18.652	19.240	16.632	13.764	9.286	6.671
Rso [MJ m^{-2} day^{-1}]	15.132	18.986	23.718	28.177	30.844	31.789	31.132	28.774	24.696	19.882	15.704	13.964
$\sigma T_{max}, K^4$	35.970	34.990	37.470	38.750	40.330	41.410	43.360	42.800	42.520	41.960	37.210	24.750
$\sigma T_{min}, K^4$	30.860	31.080	32.420	32.880	34.750	36.460	37.720	37.980	37.210	36.210	33.110	30.640
Rnl [MJ m^{-2} day^{-1}]	2.683	2.969	3.551	4.087	3.975	3.342	3.465	3.974	4.094	4.600	4.201	2.645
Rn [MJ m^{-2} day^{-1}]	4.169	5.977	8.828	12.003	13.848	14.167	15.188	15.266	12.538	9.163	5.085	4.026
PE [mm day^{-1}]	1.324	1.683	2.645	3.799	4.677	4.929	5.640	5.530	4.513	3.545	2.084	1.272

Appendix 2.5: Penman-Monteith evapotranspiration calculations for Ramallah

	Jan	Feb	Mar	Apr	May	Jun	Jul	Aug	Sep	Oct	Nov	Dec
Tmin [°C]	6.6	6.8	10.7	12.4	14.3	16.5	18.8	18.6	18.3	17.8	12.4	7.2
Tmax [°C]	11.9	13.8	18.9	21.4	24.5	26.8	28.7	27.4	27.5	25.7	18	12.5
Tmean [°C]	8.8	9.8	13.9	16.1	18.8	21.3	23.2	22.2	22	20.8	14.7	9.4
Relative Humidity [%]	81	79	61	58	58	66	63	71	66	65	73	69
Wind speed [km/hr^{-1}]	6.4	10.8	9.7	8.8	12	9.3	10	12.9	13	10.5	12.2	10.6
Wind Speed [m s^{-1}]	1.78	3.00	2.69	2.44	3.33	2.58	2.78	3.58	3.61	2.92	3.39	2.94
Δ [kPa °C]	0.077	0.081	0.103	0.117	0.136	0.155	0.172	0.163	0.161	0.151	0.108	0.079
γ [kPa °C]	0.061	0.061	0.061	0.061	0.061	0.061	0.061	0.061	0.061	0.061	0.061	0.061
e° (Tmax) [kPa]	1.393	1.578	2.184	2.549	3.075	3.524	3.937	3.650	3.671	3.302	2.064	1.449
e° (Tmin) [kPa]	0.975	0.988	1.287	1.440	1.630	1.877	2.170	2.143	2.103	2.038	1.440	1.016
e_s [kPa]	1.184	1.283	1.735	1.994	2.352	2.700	3.053	2.897	2.887	2.670	1.752	1.233
e_a [kPa]	0.959	1.014	1.058	1.157	1.364	1.782	1.924	2.057	1.906	1.736	1.279	0.850
G [MJ m^{-2} day^{-1}]	0.028	0.357	0.441	0.343	0.364	0.308	0.063	-0.084	-0.098	-0.511	-0.798	-0.413
Gsc [MJ m^{-2} min^{-1}]	0.082	0.082	0.082	0.082	0.082	0.082	0.082	0.082	0.082	0.082	0.082	0.082
J [-]	16	47	76	107	137	168	198	229	260	290	321	351
φ [rad]	0.550	0.550	0.550	0.550	0.550	0.550	0.550	0.550	0.550	0.550	0.550	0.550
dr [rad]	1.032	1.023	1.009	0.991	0.977	0.968	0.968	0.977	0.992	1.009	1.024	1.032
δ [rad]	-0.367	-0.224	-0.033	0.179	0.337	0.408	0.369	0.227	0.023	-0.182	-0.343	-0.408

ωs [rad]	1.333	1.430	1.550	1.682	1.787	1.839	1.810	1.713	1.585	1.458	1.350	1.302
Ra [MJ m-2 day-1]	20.273	25.225	31.257	36.876	40.183	41.334	40.523	37.602	32.481	26.362	21.005	18.765
n [days]	4.1	5.5	7.6	9	9.9	11.9	11.8	11.2	10.5	8.3	6.6	6.1
N [days]	10.181	10.927	11.844	12.847	13.654	14.049	13.827	13.087	12.107	11.137	10.314	9.949
Rs [MJ m^{-2} day^{-1}]	9.150	12.654	17.843	22.135	24.613	27.839	27.422	25.490	22.205	16.413	11.972	10.444
Rns [MJ m^{-2} day^{-1}]	7.046	9.744	13.739	17.044	18.952	21.436	21.115	19.627	17.098	12.638	9.218	8.042
Rso [MJ m^{-2} day^{-1}]	15.558	19.359	23.988	28.300	30.838	31.722	31.099	28.857	24.927	20.231	16.120	14.401
$\sigma Tmax,K^4$	32.420	33.340	35.720	36.960	38.490	39.800	40.870	40.060	40.330	39.270	35.240	32.650
$\sigma Tmin,K^4$	31.080	31.520	33.340	34.280	35.720	36.960	37.720	37.210	37.210	36.710	33.810	31.300
Rnl [MJ m^{-2} day^{-1}]	2.860	3.437	4.427	4.763	4.764	4.905	4.816	4.532	4.850	4.404	4.093	4.242
Rn [MJ m^{-2} day^{-1}]	4.186	6.307	9.313	12.281	14.189	16.531	16.299	15.096	12.247	8.234	5.125	3.800
PE [mm day^{-1}]	1.191	1.732	3.283	4.191	5.210	5.448	5.922	5.260	4.954	3.846	2.369	1.763

Appendix 2.6: Penman-Monteith evapotranspiration calculations for Hebron

	Jan	Feb	Mar	Apr	May	Jun	Jul	Aug	Sep	Oct	Nov	Dec
Tmin [°C]	5	5.1	9.5	10.9	14	16	19.1	17.6	17	16.7	11.3	6
Tmax [°C]	10.5	12.1	17.9	20.5	23	26.8	29.6	28.1	28	25.5	17.4	12.4
Tmean [°C]	7.7	8.6	13.8	15.7	18.5	21.5	24.3	22.9	22.2	20.8	14.4	9.2
Relative Humidity [%]	78	74	65	64	60	64	61	65	65	64	65	65
Wind speed [km/hr^{-1}]	11	6.4	6	6.3	9	12.9	13	13.6	11.7	9.8	13	12.4
Wind Speed [m s^{-1}]	3.06	1.78	1.67	1.75	2.50	3.58	3.61	3.78	3.25	2.72	3.61	3.44
Δ [kPa °C]	0.072	0.076	0.103	0.114	0.133	0.157	0.182	0.169	0.163	0.151	0.106	0.078
γ [kPa °C]	0.06	0.06	0.06	0.06	0.06	0.06	0.06	0.06	0.06	0.06	0.06	0.06
e° (Tmax) [kPa]	1.270	1.412	2.051	2.412	2.809	3.524	4.147	3.802	3.780	3.263	1.987	1.440
e° (Tmin) [kPa]	0.872	0.878	1.187	1.304	1.599	1.818	2.211	2.013	1.938	1.901	1.339	0.935
e_s [kPa]	1.071	1.145	1.619	1.858	2.204	2.671	3.179	2.907	2.859	2.582	1.663	1.188
e_a [kPa]	0.835	0.847	1.053	1.189	1.322	1.709	1.939	1.890	1.858	1.653	1.081	0.772
G [MJ m^{-2} day^{-1}]	-0.042	0.427	0.497	0.329	0.406	0.406	0.098	-0.147	-0.147	-0.546	-0.812	-0.469
Gsc [MJ m^{-2} min^{-1}]	0.082	0.082	0.082	0.082	0.082	0.082	0.082	0.082	0.082	0.082	0.082	0.082
J [-]	16	47	76	107	137	168	198	229	260	290	321	351
φ [rad]	0.697	0.697	0.697	0.697	0.697	0.697	0.697	0.697	0.697	0.697	0.697	0.697
dr [rad]	1.032	1.023	1.009	0.991	0.977	0.968	0.968	0.977	0.992	1.009	1.024	1.032
δ [rad]	-0.367	-0.224	-0.033	0.179	0.337	0.408	0.369	0.227	0.023	-0.182	-0.343	-0.408

ωs [rad]	1.333	1.430	1.550	1.682	1.787	1.839	1.810	1.713	1.585	1.458	1.350	1.302
Ra [MJ m-2 day-1]	15.055	20.592	27.781	35.080	39.867	41.736	40.524	36.257	29.450	22.000	15.899	13.440
n [days]	4.9	5.8	7.6	8.9	9.5	12.6	12.5	11.8	10.2	8.2	6	5.9
N [days]	10.181	10.927	11.844	12.847	13.654	14.049	13.827	13.087	12.107	11.137	10.314	9.949
Rs [MJ m^{-2} day^{-1}]	7.386	10.613	15.859	20.921	23.836	29.149	28.448	25.410	19.768	13.599	8.599	7.345
Rns [MJ m^{-2} day^{-1}]	5.687	8.172	12.211	16.109	18.354	22.445	21.905	19.565	15.221	10.471	6.621	5.656
Rso [MJ m^{-2} day^{-1}]	11.554	15.803	21.320	26.922	30.596	32.030	31.100	27.825	22.601	16.883	12.202	10.314
σTmax,K^4	31.740	32.420	35.240	36.460	37.720	39.800	41.410	40.330	40.330	39.010	34.990	32.650
σTmin,K^4	29.350	29.350	31.300	31.970	33.340	34.280	35.720	34.990	34.750	34.750	32.190	29.780
Rnl [MJ m^{-2} day^{-1}]	3.323	3.630	4.274	4.481	4.463	5.108	4.950	4.905	4.652	4.352	3.928	4.141
Rn [MJ m^{-2} day^{-1}]	2.364	4.542	7.937	11.628	13.891	17.337	16.955	14.660	10.569	6.119	2.694	1.515
PE [mm day^{-1}]	1.077	1.329	2.489	3.551	4.674	5.916	6.541	5.628	4.520	3.285	2.280	1.617

Appendix 2.7: Penman-Monteith evapotranspiration calculations for Jericho

	Jan	Feb	Mar	Apr	May	Jun	Jul	Aug	Sep	Oct	Nov	Dec
Tmin [°C]	8.8	9.3	12.5	15.5	18.6	21.5	24.3	23.6	22.2	20.1	14.8	7.5
Tmax [°C]	19.6	21.6	27.4	30.6	33.8	37	40.1	38.2	36.7	33.8	26.5	19.4
Tmean [°C]	13.9	15.2	20.1	23.2	26.3	29.4	32.4	31.3	29.7	27.2	20.7	13.1
Relative Humidity [%]	71	67	52	42	41	45	42	48	49	51	61	69
Wind speed [km/hr^{-1}]	5.2	6.3	7.8	10.2	10.2	8.6	8.4	7.6	6.4	5.4	5.4	3.4
Wind Speed [m s^{-1}]	1.44	1.75	2.17	2.83	2.83	2.39	2.33	2.11	1.78	1.50	1.50	0.94
Δ [kPa °C]	0.103	0.111	0.146	0.172	0.202	0.236	0.274	0.260	0.240	0.211	0.150	0.099
γ [kPa °C]	0.067	0.067	0.067	0.067	0.067	0.067	0.067	0.067	0.067	0.067	0.067	0.067
e° (Tmax) [kPa]	2.281	2.580	3.650	4.391	5.260	6.275	7.415	6.697	6.173	5.260	3.462	2.253
e° (Tmin) [kPa]	1.133	1.172	1.449	1.761	2.143	2.564	3.038	2.913	2.676	2.353	1.684	1.037
e_s [kPa]	1.707	1.876	2.550	3.076	3.702	4.420	5.227	4.805	4.425	3.807	2.573	1.645
e_a [kPa]	1.212	1.257	1.326	1.292	1.518	1.989	2.195	2.306	2.168	1.941	1.569	1.135
G [MJ m^{-2} day^{-1}]	0.147	0.434	0.56	0.434	0.434	0.427	0.133	-0.189	-0.287	-0.63	-0.987	-0.476
Gsc [MJ m^{-2} min^{-1}]	0.082	0.082	0.082	0.082	0.082	0.082	0.082	0.082	0.082	0.082	0.082	0.082
J [-]	16	47	76	107	137	168	198	229	260	290	321	351
φ [rad]	0.697	0.697	0.697	0.697	0.697	0.697	0.697	0.697	0.697	0.697	0.697	0.697
dr [rad]	1.032	1.023	1.009	0.991	0.977	0.968	0.968	0.977	0.992	1.009	1.024	1.032
δ [rad]	-0.367	-0.224	-0.033	0.179	0.337	0.408	0.369	0.227	0.023	-0.182	-0.343	-0.408

ωs [rad]	1.333	1.430	1.550	1.682	1.787	1.839	1.810	1.713	1.585	1.458	1.350	1.302
Ra [MJ m-2 day-1]	15.055	20.592	27.781	35.080	39.867	41.736	40.524	36.257	29.450	22.000	15.899	13.440
n [days]	5.7	6.9	8	9.3	9.8	11.9	11.8	11.3	10.6	8.2	6.6	5.5
N [days]	10.181	10.927	11.844	12.847	13.654	14.049	13.827	13.087	12.107	11.137	10.314	9.949
Rs [MJ m^{-2} day^{-1}]	7.978	11.649	16.328	21.467	24.274	28.109	27.422	24.717	20.254	13.599	9.062	7.075
Rns [MJ m^{-2} day^{-1}]	6.143	8.970	12.572	16.530	18.691	21.644	21.115	19.032	15.596	10.471	6.977	5.448
Rso [MJ m^{-2} day^{-1}]	11.554	15.803	21.320	26.922	30.596	32.030	31.100	27.825	22.601	16.883	12.202	10.314
$\sigma Tmax,K^4$	36.018	37.010	40.010	41.740	43.510	45.670	47.200	46.060	45.180	43.510	39.530	35.920
$\sigma Tmin,K^4$	31.010	31.230	32.650	34.040	35.530	36.960	38.380	38.030	37.310	36.260	33.720	30.420
Rnl [MJ m^{-2} day^{-1}]	3.627	4.029	4.442	4.979	4.774	4.917	4.767	4.548	4.747	4.262	3.934	3.646
Rn [MJ m^{-2} day^{-1}]	2.516	4.941	8.130	11.551	13.917	16.727	16.348	14.484	10.849	6.208	3.043	1.801
PE [mm day^{-1}]	1.231	1.977	3.799	5.962	7.070	7.631	8.142	6.937	5.438	3.685	2.212	1.032

Appendix 3.1: SEBAL code for MATLAB-based processing of MODIS Level 1B (26 August, 1992)

```
%%JULIAN DAY NUMBER (JD)
JD=226;
%%DAY ANGLE (DA)
DA=2.*3.1428571.*(JD-1)./365;
%%ECCENTRICITY CORRECTION FACTOR (Eo)
Eo=1+0.33.*cos(2.*PI.*JD./365);
%%EQUATION OF TIME (ET)
ET=229.18.*(0.000075+0.001868.*cos(DA)-0.032077.*sin(2.*DA)-
0.014615.*cos(2.*DA)-0.04089.*sin(2.*DA));
%%LOCAL APPARENT TIME (LAPT)
LAPT=8.92+4.*(29.3823./60)+(ET./60);
%%SOLAR DECLINATION (DE)
DE=0.006918-(0.399912.*cos(DA))+(0.070257.*sin(DA))-
(0.006758.*cos(2.*DA))+(0.000907.*sin(2.*DA))-
(0.002697.*cos(3.*DA))+(0.00148.*sin(3.*DA));
%%HOUR ANGLE (OME)
OME=15.*(LAPT-12).*(3.1428571./180);
%%COSINE OF SOLAR ZENITH ANGLE (CSZ)
CSZ=sin(DE).*sin(32.627./57.29577951)+cos(DE).*cos(32.627./57.29577951).*cos
(OME);
%%EXO ATMOSPHERIC SOLAR RADIATION (Kexo)
Kexo=1367.*Eo.*CSZ;
%%EARTH SUN DISTANCE (D)
D=1.01253;
%%PLANETARY ALBEDO (Rp)
if 0.035+(0.545.*rfc1)+(0.32.*rfc2)<0;
Rp=0;
else
Rp=0.035+(0.545.*rfc1)+(0.32.*rfc2);
end
```

```
%%SURFACE ALBEDO (Ro) BASED ON Rp AND ATMOSPHERIC TRANSMISSIVITY CONSTANTS SPECIFIC TO WEST BANK
Ro=(Rp-0.115)./0.5929;
%%INSTANTANEOUS ATMOSPHERIC TRANSMISSIVITY (ATR_ins)
ATR_ins=sqrt((Rp-0.115)./Ro);
%%SOIL ADJUSTED VEGETATION INDEX (SAVI)
savi=1.5.*(rfc2-rfc1)./(rfc2+rfc1+0.5);
%%THERMAL INFRARED BROADBAND EMISSIVITY (SE)
if ndvi<0.16;
SE=0;
else
SE=1.009+0.047.*log(ndvi);
end
%%SURFACE TEMPERATURE (Ts) derivative of bt and SE
Ts=0.39.*bt31.^2+2.34.*bt31-0.78.*bt31.*bt32-1.34.*bt32+0.39.*bt32.^2+0.56;
%%AIR TEMPERATURE (Ta) DAY SPATIAL AVERAGE FROM FIELD LOGGER DATA
Ta=26.5.*Ts./Ts;
%%APPARENT EMISSIVITY (Ea) EMPIRICALLY DERIVED
Ea=SE./1.3025;
%%INSTANTANEOUS INCOMING LONG WAVE RADIATION (LW_IN_ins)
LW_IN_ins=Ea.*0.0000000567.*(Ta+273.15).^4;
%%INSTANTANEOUS OUTGOING LONG WAVE RADIATION (LW_OUT_ins)
LW_OUT_ins=SE.*0.0000000567.*Ts.^4+(1-SE).*LW_IN_ins;
%%INSTANTANEOUS INCOMING SHORT WAVE RADIATION (SW_IN_ins)
SW_IN_ins=Kexo.*ATR_ins;
%%INSTANTANEOUS NET SHORT WAVE RADIATION (SW-NE_ins)
SW_NE_ins=(1-Ro).*SW_IN_ins;
%%INSTANTANEOUS NET RADIATION (Rn_ins)
Rn_ins=SW_NE_ins+LW_IN_ins-LW_OUT_ins;
%%INSTANTANEOUS SOIL HEAT FLUX (Go_ins)
```

```
Go_ins=(Ts-273.15).*(0.0032.*1.1.*Ro+0.0062*(1.1*Ro).^2).*(1-
0.978*(ndvi.^4)).*(Rn_ins./Ro);
%%EMPIRICAL ESTIMATION OF LEAF AREA INDEX (LAI) FROM SAVI
if savi>0.689;
LAIf=6.0;
else
LAIf=-log((0.689-savi)./0.5369);
end
LAI=real(LAIf);
%%ROUGHNESS LENGTH FOR MOMENTUM TRANSPORT (Zom)
DETERMINED AFTER BY FAO
Zom=exp(-5.809+5.62.*savi);
%%ROUGHNESS LENGTH FOR HEAT TRANSPORT (Zoh) FAO EMPIRICAL
RELATIONSHIP
Zoh=0.1*Zom;
%%DISPLACEMENT HEIGHT (DIS)
DIS=1.*(1-((1-exp(-((20.6.*LAI).^0.5)))./((20.6.*LAI).^0.5)));
%%DISPLACEMENT AT BLENDING HEIGHT OR MIXING LAYER (Ubl)
WINDSPEED FROM
%%GROUND DATA AT 2m AND APPROX. MIXING LAYER OF 100m
Ubl1=2.15.*(log(100-DIS)-log(Zom))./(log(2-Zom)-log(Zom));
Ubl=real(Ubl1);
%%ATMOSPHERIC AIR DENSITY (ADD) MODEL EMPIRICALLY
DETERMINED
AAD=((99.190-1.59)./Ts.*2.87)+(1.59./Ts.*4.61);
%%FRICTION VELOCITY (Usta) BASED ON BLENDING HEIGHT, VON
KARMAN'S CONSTANT
%%(0.41) AND ASSUMED NULL STABILITY
Usta1=0.41*Ubl./log((100-DIS)./Zom);
Usta=real(Usta1);
%%AERODYNAMIC RESISTANCE (rah)
rah1=(log((2-DIS)./Zoh))./(0.41.*Usta);
rah=real(rah1);
```

```
%%SUN RISE-SET HOUR (WS)
WS=acos(-tan(32.627.*3.1428571./180).*tan(DE));
%%DAILY INCOMING SHORT WAVE RADIATION AT THE TOP OF THE ATMOSPHERE (SW_day_TOA)
SW_day_TOA=24.*1367.*0.0036.*Eo.*sin(32.627.*3.1428571./180).*sin(DE).*(WS-tan(WS))./3.1428571;
%%day time duration (N)
N=WS.*24./3.1428571;
%%DAILY ATMOSPHERIC TRANSMISSIVITY (TAU)
TAU=0.25+0.5.*11.4./N;
%%DAILY INCOMING SHORT WAVE RADIATION AT GROUND (SW_day_GR)
SW_day_GR=11.57441.*TAU.*SW_day_TOA;
%%DAILY NET RADIATION (RN_day)
RN_day=(1-1.1.*Ro).*SW_day_GR-110.*TAU;
%%TEMPERATURE DIFFERENCE (Tdel) AIR TEMPERATURE IS SPATIALLY REFERENCED
%%FROM GROUND DATA AND EMPIRICAL FORMULA APPLIED
if (-118.047+0.335.*Ts)<0;
Tdel=0;
else
Tdel=(-118.047+0.335.*Ts);
end
%%CORRECTED SENSIBLE HEAT FLUX (H_ins)
H_ins=(1004.*AAD.*Tdel./rah);
%%EVAPOTRANSPIRATION (PET_24) THIS IS RELATED TO Rn_24
PET_ins=Rn_ins-Go_ins-H_ins;
%%EVAPORATIVE FRACTION
if PET_ins./(Rn_ins-Go_ins)<0;
   EF=0;
else
EF=PET_ins./(Rn_ins-Go_ins);
end
```

```
%%DAILY ACTUAL EVAPOTRANSPIRATION (ETa_day)
ETa_day=EF.*RN_day./28.356;
```

Appendix 3.2: SEBAL code for MATLAB-based processing of Landsat TM5 (26 August, 1992)

```
%%JULIAN DAY NUMBER (JD)
JD=215;
%%DAY ANGLE (DA)
DA=2.*PI.*(JD-1)./365;
%%ECCENTRICITY CORRECTION FACTOR (Eo)
Eo=1+0.033.*cos(2.*3.1428571.*JD./365);
%%EQUATION OF TIME (ET)
ET=229.18.*(0.000075+0.001868.*cos(DA)-0.032077.*sin(2.*DA)-
0.014615.*cos(2.*DA)-0.04089.*sin(2.*DA));
%%LOCAL APPARENT TIME (LAPT)
LAPT=7.32+4.*(35.388./60)+(ET./60);
%%SOLAR DECLINATION (DE)
DE=0.006918-(0.399912.*cos(DA))+(0.070257.*sin(DA))-
(0.006758.*cos(2.*DA))+(0.000907.*sin(2.*DA))-
(0.002697.*cos(3.*DA))+(0.00148.*sin(3.*DA));
%%HOUR ANGLE (OME)
OME=15.*(LAPT-12).*(3.1428571./180);
%%COSINE OF SOLAR ZENITH ANGLE (CSZ)
CSZ=sin(DE).*sin(31.742./57.29577951)+cos(DE).*cos(31.742./57.29577951).*cos
(OME);
%%EXO ATMOSPHERIC SOLAR RADIATION (Kexo)
Kexo=1367.*Eo.*CSZ;
%%RADIANCE PER BAND
L1=(B1+1.52)./0.602431;
L2=(B2+2.84)./1.1751;
L3=(B3+1.17)./0.805765;
L4=(B4+1.51)./0.814549;
L5=(B5+0.37)./0.108078;
```

```
L6=(B6-1.2378)./0.055158;
L7=(B7+0.15)./0.05698;
%%EARTH SUN DISTANCE (D)
D=1+0.0167.*sin(2.*3.1428571.*(JD-93.5)/365);
%%REFLECTANCE PER BAND
R1=3.1428571.*L1.*(D.^2)./(1957.*CSZ);
R2=3.1428571.*L2.*(D.^2)./(1825.*CSZ);
R3=3.1428571.*L3.*(D.^2)./(1557.*CSZ);
R4=3.1428571.*L4.*(D.^2)./(1033.*CSZ);
R5=3.1428571.*L5.*(D.^2)./(214.9.*CSZ);
R7=3.1428571.*L7.*(D.^2)./(80.72.*CSZ);
%%NORMALIZED DIFFERENCE VEGETATION INDEX (NDVI)
ndvi=(R4-R3)./(R4+R3);
%%SOIL ADJUSTED VEGETATION INDEX (SAVI)
savi=1.5.*(R4-R3)./(R4+R3+0.5);
%%PLANETARY ALBEDO(Rp)
Rp=(1957.*R1+1825.*R2+1557.*R3+1033.*R4+214.9.*R5+80.72.*R7)./(1957+182
5+1557+1033+214.9+80.72);
%%SURFACE ALBEDO (Ro) BASED ON Rp AND ATMOSPHERIC TRANSMISSIVITY CONSTANTS SPECIFIC TO WEST BANK
Ro=(Rp-0.03613)./0.5929;
%%INSTANTANEOUS ATMOSPHERIC TRANSMISSIVITY (ATR_ins)
ATR_ins=sqrt((Rp-0.03613)./Ro);
%%BRIGHTNESS TEMPERATURE (BT)
BT=1284.30./log((671.62./L6)+1);
%%THERMAL INFRARED BROADBAND EMISSIVITY (SE)
if ndvi<0.16;
SE=0.92;
else
SE=1.009+0.047.*log(ndvi);
end
%%SURFACE TEMPERATURE (Ts) derivative of bt and SE
Ts=BT.*SE.^(-0.25);
```

```
%%AIR TEMPERATURE (Ta) DAY SPATIAL AVERAGE FROM FIELD LOGGER DATA
Ta=25.34.*Ts./Ts;
%%APPARENT EMISSIVITY (Ea) EMPIRICALLY DERIVED
Ea=0.85.*(-log(ATR_ins)).^0.09;
%%INSTANTANEOUS INCOMING LONG WAVE RADIATION (LW_IN_ins)
LW_IN_ins=Ea.*0.0000000567.*(Ta+273.15).^4;
%%INSTANTANEOUS OUTGOING LONG WAVE RADIATION (LW_OUT_ins)
LW_OUT_ins=SE.*0.0000000567.*Ts.^4+(1-SE).*LW_IN_ins;
%%INSTANTANEOUS INCOMING SHORT WAVE RADIATION (SW_IN_ins)
SW_IN_ins=Kexo.*ATR_ins;
%%INSTANTANEOUS NET SHORT WAVE RADIATION (SW_NE_ins)
SW_NE_ins=(1-Ro).*SW_IN_ins;
%%INSTANTANEOUS NET RADIATION (Rn_ins)
Rn_ins=SW_NE_ins+LW_IN_ins-LW_OUT_ins;
%%INSTANTANEOUS SOIL HEAT FLUX (Go_ins)
Go_ins=(Ts-273.15).*(0.32.*1.1.*Ro+0.62.*(1.1*Ro).^2).*(1-
0.978*(ndvi.^4)).*(Rn_ins./100.*Ro);
%%EMPIRICAL ESTIMATION OF LEAF AREA INDEX (LAI) FROM SAVI
if savi>0.689;
LAIf=6.0;
else
LAIf=-log((0.689-savi)./0.5369);
end
LAI=real(LAIf);
%%ROUGHNESS LENGTH FOR MOMENTUM TRANSPORT (Zom) DETERMINED AFTER BY FAO
Zom=exp(-5.809+5.62.*savi);
%%ROUGHNESS LENGTH FOR HEAT TRANSPORT (Zoh) FAO EMPIRICAL RELATIONSHIP
Zoh=0.1*Zom;
%%DISPLACEMENT HEIGHT (DIS)
```

```
DIS=1.*(1-((1-exp(-((20.6.*LAI).^0.5)))./((20.6.*LAI).^0.5)));
%%DISPLACEMENT AT BLENDING HEIGHT OR MIXING LAYER (Ubl) WINDSPEED FROM
%%GROUND DATA AT 2m AND APPROX. MIXING LAYER OF 100m
Ubl1=3.6.*(log(100-DIS)-log(Zom))./(log(2-Zom)-log(Zom));
Ubl=real(Ubl1);
%%FROM GROUND DATA AND EMPIRICAL FORMULA APPLIED
%%ATMOSPHERIC AIR DENSITY (ADD) MODEL EMPIRICALLY DETERMINED
AAD=((99.190-1.59)./Ts.*2.87)+(1.59./Ts.*4.61);
%%FRICTION VELOCITY (Usta) BASED ON BLENDING HEIGHT, VON KARMAN'S CONSTANT
%%(0.41) AND ASSUMED NULL STABILITY
Usta1=0.41*Ubl./log((100-DIS)./Zom);
Usta=real(Usta1);
%%AERODYNAMIC RESISTANCE (rah)
rah1=log((2-DIS)./Zoh)./(0.41.*Usta);
rah=real(rah1);
%%SUN RISE-SET HOUR (WS)
WS=acos(-tan(31.742.*3.1428571./180).*tan(DE));
%%DAILY INCOMING SHORT WAVE RADIATION AT THE TOP OF THE ATMOSPHERE (SW_day_TOA)
SW_day_TOA=24.*1367.*0.0036.*Eo.*sin(31.742.*3.1428571./180).*sin(DE).*(WS-tan(WS))./3.1428571;
%%day time duration (N)
N=WS.*24./3.1428571;
%%DAILY ATMOSPHERIC TRANSMISSIVITY (TAU)
TAU=0.25+0.5.*11.84./N;
%%DAILY INCOMING SHORT WAVE RADIATION AT GROUND (SW_day_GR)
SW_day_GR=11.57441.*TAU.*SW_day_TOA;
%%DAILY NET RADIATION (RN_day)
RN_day=(1-1.1.*Ro).*SW_day_GR-110.*TAU;
```

```
%%TEMPERATURE DIFFERENCE (Tdel) AIR TEMPERATURE IS SPATIALLY REFERENCED
if (-998.8+3.265.*Ts)<0;
Tdel=0;
else
Tdel=(-998.8+3.265.*Ts);
end
%%CORRECTED SENSIBLE HEAT FLUX (H_ins)
H_ins=(1004.*AAD.*Tdel./rah);
%%CALCULATION OF EVAPOTRANSPIRATION (PET_24) THIS IS RELATED TO Rn_24
PET_ins=Rn_ins-Go_ins-H_ins;
%%EVAPORATIVE FRACTION METHOD
if PET_ins./(Rn_ins-Go_ins)<0;
   EF=0;
else
EF=PET_ins./(Rn_ins-Go_ins);
end
%%DAILY ACTUAL EVAPOTRANSPIRATION (ETa_day)
ETa_day=EF.*RN_day./28.356;
```